AD-A059 726 EG AND G INC ALBUQUERQUE N MEX F/G 19/6
MUZZLE DEFLECTION MEASUREMENT SYSTEM.(U)
JUL 78 R M BLAKNEY DAAK11-77-C-0051
UNCLASSIFIED EG/G-AG-1340 ARBRL-CR-00376 NL

1 OF 3
AD A059726

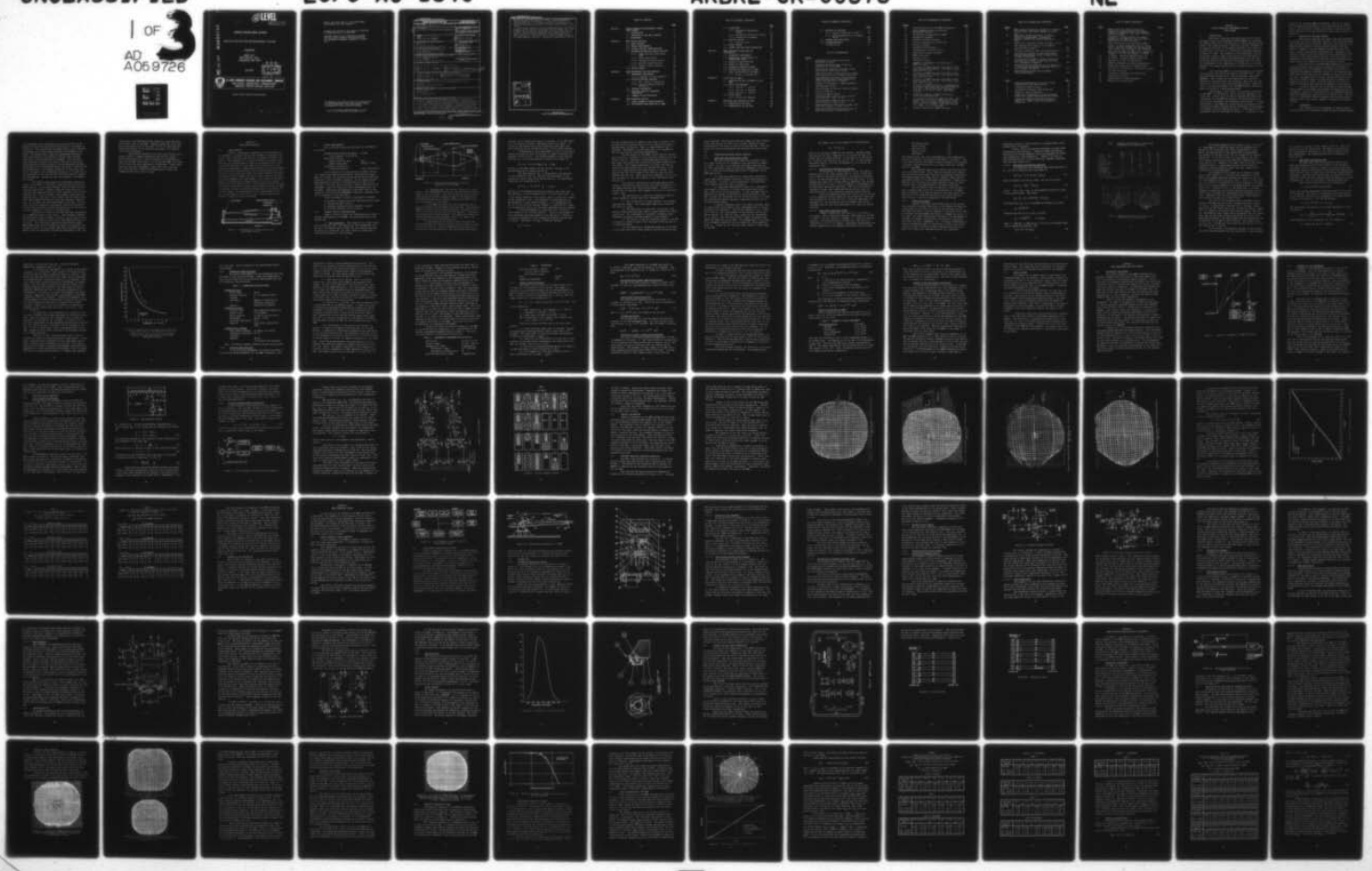

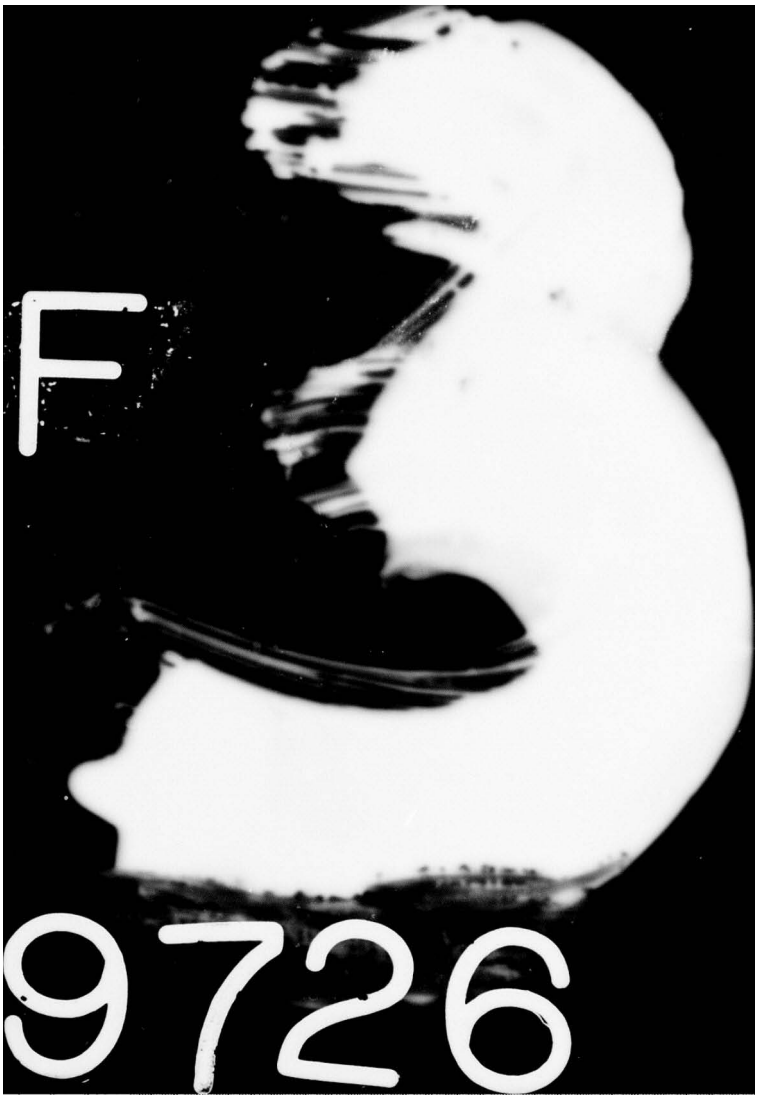
F
9726

CONTRACT REPORT ARBRL-CR-00376

MUZZLE DEFLECTION MEASUREMENT SYSTEM

Prepared by

EG&G, Inc.
9733 Coors Rd., N.W.
Albuquerque, NM 87114

July 1978

US ARMY ARMAMENT RESEARCH AND DEVELOPMENT COMMAND
BALLISTIC RESEARCH LABORATORY
ABERDEEN PROVING GROUND, MARYLAND

Destroy this report when it is no longer needed.
Do not return it to the originator.

Secondary distribution of this report by originating or sponsoring activity is prohibited.

Additional copies of this report may be obtained from the National Technical Information Service, U.S. Department of Commerce, Springfield, Virginia 22161.

The findings in this report are not to be construed as an official Department of the Army position, unless so designated by other authorized documents.

The use of trade names or manufacturers' names in this report does not constitute indorsement of any commercial product.

UNCLASSIFIED

SECURITY CLASSIFICATION OF THIS PAGE (When Data Entered)

REPORT DOCUMENTATION PAGE

READ INSTRUCTIONS BEFORE COMPLETING FORM

1. REPORT NUMBER: CONTRACT REPORT ARBRL-CR-00376
2. GOVT ACCESSION NO.:
3. RECIPIENT'S CATALOG NUMBER:

4. TITLE (and Subtitle): MUZZLE DEFLECTION MEASUREMENT SYSTEM
5. TYPE OF REPORT & PERIOD COVERED: Final Report, July 1977-April 1978
6. PERFORMING ORG. REPORT NUMBER: AG-1340

7. AUTHOR(s): Dr. R.M. Blakney, Ph.D.
8. CONTRACT OR GRANT NUMBER(s): DAAK 11-77-C-0051

9. PERFORMING ORGANIZATION NAME AND ADDRESS:
EG&G, Inc.
9733 Coors Rd. N.W.
Albuquerque, New Mexico 87114

10. PROGRAM ELEMENT, PROJECT, TASK AREA & WORK UNIT NUMBERS:
61102 A
1L161102AH43
002 AJ

11. CONTROLLING OFFICE NAME AND ADDRESS:
US Army Ballistic Research Laboratory
(ATTN: DRDAR-BLB)
Aberdeen Proving Ground, MD 21005

12. REPORT DATE: JULY 1978

13. NUMBER OF PAGES: 194

14. MONITORING AGENCY NAME & ADDRESS (if different from Controlling Office):
US Army Armament Research & Development Command
Ballistic Research Laboratory
(ATTN: DRDAR-BL)
Aberdeen Proving Ground, MD 21005

15. SECURITY CLASS. (of this report): Unclassified

15a. DECLASSIFICATION DOWNGRADING SCHEDULE: N/A

16. DISTRIBUTION STATEMENT (of this Report):
Approved for public release; distribution unlimited.

18 ARBRL, SBIE
19 CR-00376, AD-E430 201

17. DISTRIBUTION STATEMENT (of the abstract entered in Block 20, if different from Report)

12 204 p.
14 EG/G-AG-1340

18. SUPPLEMENTARY NOTES:
To be presented at second U.S. Army Symposium on Gun Dynamics
Institute on Man and Science
Rensalaerville, NY

19. KEY WORDS (Continue on reverse side if necessary and identify by block number):
Muzzle Deflection
Muzzle Jump
Muzzle Motion Measurement
Tank Gun Accuracy

20. ABSTRACT (Continue on reverse side if necessary and identify by block number):
A system for measuring the angular motion of the muzzle of artillery weapons during firing is described. The system provides a continuous (analog) recording of the angular deflection of the muzzle referred to the breech of the gun with an angular resolution of 0.1 mrad and a frequency response in excess of 6 kHz. The technique of measurement involves reflecting a beam of light from a mirror on the tube muzzle to an analog, two axis position sensing detector; both the light source and detector are

DD FORM 1 JAN 73 1473 EDITION OF 1 NOV 65 IS OBSOLETE

UNCLASSIFIED

SECURITY CLASSIFICATION OF THIS PAGE (When Data Entered)

388 376

mounted at the breech end of the tube. The displacement of the light beam at the detector is a direct measure of the angular deflection of the muzzle relative to the breech. A detailed description is given of the system design and calibration.

Tests were conducted with the system mounted on statically mounted, 105 mm tank gun at Aberdeen Proving Ground, MD. Nine firings were recorded in which data on muzzle motion were obtained. These data were digitized with a time resolution of 5μsec and used to produce graphical representations of the muzzle motion for a period of 15 ms, which included the period of round emergence and exit. The data are presented in detail.

TABLE OF CONTENTS

TABLE OF CONTENTS (CONTINUED)

TABLE OF CONTENTS (CONTINUED)

LIST OF ILLUSTRATIONS

LIST OF ILLUSTRATIONS (CONTINUED)

TABLE OF ILLUSTRATIONS (CONTINUED)

LIST OF TABLES (CONTINUED)

SECTION 1
MUZZLE DEFLECTION MEASUREMENT SYSTEM
FINAL REPORT

1.1 INTRODUCTION

This report describes the design and test of a prototype Muzzle Deflection Measurement System (MDMS) for measuring the angular deflection of the muzzle of a 105 mm tank gun during firing. The system provides a continuous (analog) recording of the angular deflection of the muzzle referred to the breech of the gun with a resolution of 0.1 mrad and a frequency response in excess of 6 kHz. The technique of the measurement involves reflecting a beam of light from a mirror on the tube muzzle to an analog, two-axis position sensing detector; both the light source and detector are mounted at the breech end of the tube. The displacement of the light beam at the detector is a direct measure of the angular deflection of the muzzle relative to the breech.

The prototype MDMS was tested successfully at Aberdeen Proving Ground, MD, during the week of 5 December 1977. Tests were conducted at Range 18 on a 105 mm tank gun, code named MOONSHOT. Nine firings were recorded during this period in which data on muzzle motion were obtained. Note that the test vehicle for this test was a statically mounted gun. Modification to the mounting hardware for the MDMS would be required to mount the system on a tank-mounted weapon.

The purpose of this report is to describe the design of the MDMS, its calibration, and the results obtained in the field test. Section 2 of the report discusses the design considerations for the MDMS and presents the design analysis for the critical components--the transmitter and receiver. A breadboard model of the MDMS was constructed for the purpose of optimizing the design approach and for evaluating the performance of candidate position sensing detectors. The results of the breadboard tests are discussed in Section 3. In Section 4, the

design of the prototype MDMS is described. Results of laboratory evaluation and calibration of the system is given in Section 5. Section 6 and 7 contain the results of the field test, and an analysis of the data obtained in these tests in given in Section 7.

1.2 OBJECTIVE OF THE MDMS PROGRAM

The need for improved fire control has been identified by the Army for the M-60 and XM-1 systems. Tests with the M60A3 tank have shown that a potential significant error source in the muzzle motion caused by continuous rapid firing of the main weapon or changes in the environmental conditions due to sun, rain, or other environmental discontinuities. A method is required to measure the actual muzzle motion to determine its contribution to the observed miss distance. Once this effect is understood, the method could become the basis for measuring the muzzle vector for feedback into the fire control system.

The objective of the EG&G MDMS Program was to develop a prototype muzzle motion sensing system which is capable of measuring both the slow changes of the muzzle vector due to changing environmental conditions as well as the rapid motions which occur during and after the passage of the projectile down the tube. The design objective was a system sensitivity of 0.1 mrad over a dynamic range of ±5 mrad and with a frequency response in excess of 5 kHz. Reliable operation was to be obtained in the shock and vibration environment of a 105 mm gun.

A further objective was to provide an analog sensing system capable of recording continuously the angular motion of the muzzle. Analysis of the motion was to be accomplished after digitally sampling the analog data at a suitable rate. The object is to demonstrate that the sampled data could be used for feedback into a fire control computer to improve the accuracy of fire.

1.3 BACKGROUND

The technique for the measurement of muzzle angular deflection was first developed by EG&G during the HITVAL Program.

The requirement was to determine the vector position of the muzzles of rapid fire anti-aircraft artillery at the moment of round exit. One contribution to muzzle motion is the twisting and bending of the tube during and after the passage of the round. The method used to make this measurement employed a HeNe laser mounted at the breech of the gun with its beam directed to a mirror mounted on the muzzle. The reflected laser beam was returned to an optical receiver at the breech and focused onto a matrix array of silicon detectors (Reticon). Linear motion of the reflected beam in the plane of the detector was proportional to the angular deflection of the mirror and, hence, the muzzle, with a maximum resolution of 0.4 mrad set by the parameters of the receiver optics and the detector element size and spacing. The Reticon was time sampled at 100 samples per second.

The HITVAL muzzle deflection measurement system was shown to be capable of providing a quantitative description of muzzle motion. It was found, however, that the muzzle motions contained significant frequency components which were well beyond the high-frequency detection limit imposed by the 100 sec^{-1} sampling rate. For this reason, valid muzzle motion data was obtained only in that part of the firing cycle following round exit, where damped oscillatory motion was observed, characteristic of the first few vibrational modes of the tube. Furthermore, the severe mechanical environment (shock and vibration) on the breech resulted in system malfunction at an unacceptable rate due primarily to failure of the HeNe laser.

Solutions to these two problems have been implemented in the MDMS described in this report. High-frequency response was obtained by using an analog, two-axis, silicon position sensitive detector (PSD) in place of the time-sampled matrix silicon array. In an internal research and development program, EG&G showed that the silicon PSD was capable of accurately following the motion of the focused light spot reflected from the muzzle mirror at sinusoidal frequencies approaching 10 kHz. The

large area of the PSD implied that relatively large amplitude deflections could be recorded. Spatial resolution of the spot motion was shown to be on the order of 10^{-4} cm, implying that angular deviations of the muzzle on the order of 0.1 mrad or less could be detected.

The problems imposed by the shock and vibration environment require a rugged transmitter and receiver system. Particularly sensitive to this environment in the HITVAL program was the HeNe laser source. In the present MDMS, the transmitter source has been redesigned to incorporate a laser diode, which has intrinsic ruggedness, small size, and a low mass. This has permitted a transmitter design which is small and rugged and relatively easy to align.

SECTION 2
MDMS DESIGN ANALYSIS

2.1 MDMS FUNCTION

Figure 1 illustrates schematically the configuration of the MDMS. A transmitter/receiver assembly is mounted at the breech end of the tube, and a mirror is rigidly attached to the muzzle. The transmitter is an optical projection system which projects a collimated beam of light to the muzzle mirror, where it is reflected back into the aperture of the receiver. The receiver is basically a camera which focuses the collimated beam onto a position sensing detector in the focal plane of the camera lens. As the gun tube bends, the vector defining the muzzle pointing direction changes, and the (vector) normal to the muzzle mirror undergoes the same change. This causes the reflected beam to be deflected by an amount equal to twice the angular deflection of the muzzle vector. The angular motion of the beam causes the focused spot on the position sensitive detector (PSD) to translate linearly a distance proportional to the muzzle deflection angle. By measuring the vector displacement of the spot on the PSD as a function of time, a direct quantitative measure of muzzle motion is obtained.

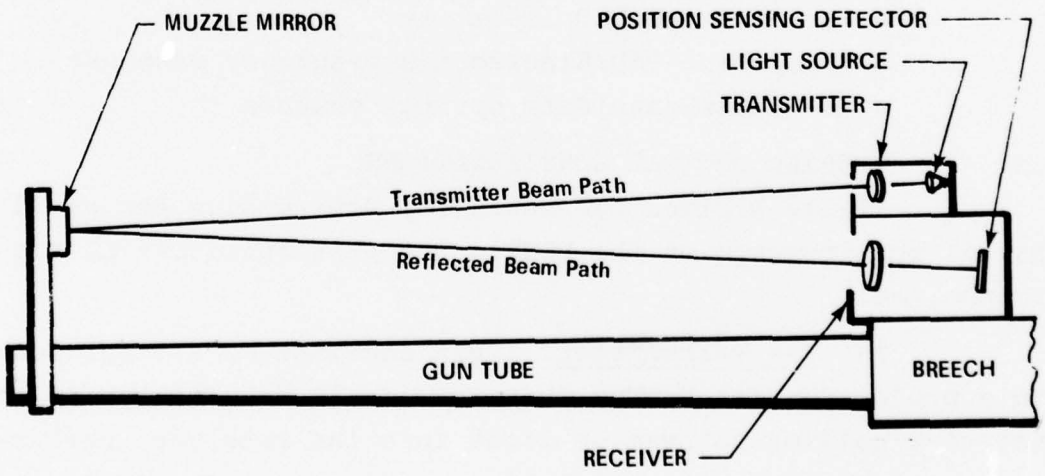

Figure 1. Configuration of Muzzle Deflection Measurement System

2.2 DESIGN REQUIREMENTS

The contractual design specification on the MDMS are as follows:

Maximum Angular Deflection Amplitude of Muzzle of 105 mm Gun	±5 mrad
Shock and Vibration	
Muzzle Along Gun Axis	500 g
Muzzle Cross Axis	1000 g @ 5 kHz
Turret/Gun Interface for Electronics/Optics	3 psi overpressure

In the absence of a specification on angular resolution, EG&G established with Government concurrences a design goal of 0.1 mrad. No specification was given for the shock and vibration at the turret/gun interface. To the extent possible, EG&G designed the system to withstand 500 g @ 5 kHz at this interface. This goal was an estimate, verbally supplied by the Government, since the results of actual measurement were not available. Subsequent measurements of the shock level on the trunnion of the 105 mm gun (MOONSHOT) indicated a maximum shock of 100 g parallel to the tube axis.

Other contractual technical requirements included:

- Evaluate candidate position sensing detectors (PSD)
- Determinate PSD linearity
- Determine PSD/Electronics frequency response
- Evaluate candidate optical sources

2.3 OVERALL OPTICAL CONSIDERATIONS

Figure 2 gives the basis for determining the overall optical requirements on the MDMS. The principal optical subsystems are:

1) The Transmitter. This consists of a light source and a projection lens. The function of the transmitter is to project a collimated beam of light into the receiver aperture. By virtue of collimation, the light source is effectively at infinity with respect to the receiver.

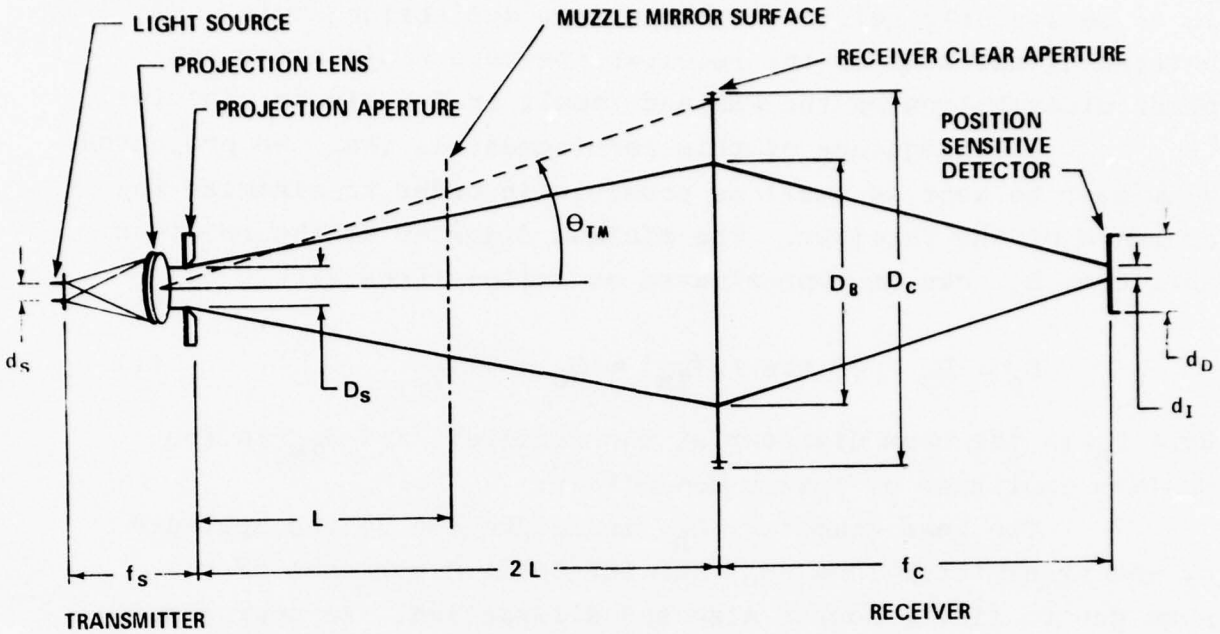

Figure 2. Schematic Representation of Optical Requirements on the MDMS

2) The Receiver. The receiver consists of a high quality, fast photographic lens with a position sensing detector (PSD) in its focal plane. The receiver lens focuses the collimated beam onto the PSD, forming an image of the light source. The PSD and associated electronics senses the centroid of the power distribution in this image.

In the MDMS prototype, both the transmitter and receiver are mounted at the breech end of the tube. The projected beam is aimed at a mirror rigidly attached to the muzzle, which reflects the beam back into the receiver aperture. In Figure 2, this folded path is shown unfolded. The separation between the transmitter/receiver and the muzzle mirror is L; hence, the total length of the projected beam is 2L.

A requirement on the system is that the entire projected beam enter the receiver aperture over the range of muzzle deflection specified. Since the PSD measures the centroid of the incident light distribution, this distribution must remain

constant for all deflection angles of interest, if the PSD output is to be linearly related to the muzzle deflection angle. Vinetting of the beam by the receiver aperture would alter the power distribution on the PSD and result in non-linear behavior.

A consequence of this requirement is that the projected beam must be kept as small as possible in order to minimize the aperture of the receiver. The minimum diameter of the receiver aperture, D_c, can be approximated as follows (see Figure 2):

$$D_c \approx D_b + 2L \tan (2\theta_{TM}) \approx D_b + 4L\theta_{TM} . \qquad (1)$$

Here D_b is the beam diameter at the receiver, and θ_{TM} is the maximum amplitude of muzzle deflection.

The beam diameter, D_b, is determined by the aperture of the transmitter lens, D_s, and the total divergence of the beam due to finite source size and diffraction. An approximate expression for estimating D_b is:

$$D_b \approx D_s + 2L (2 \tan \theta_D + d_s/f_s) \qquad (2)$$

Here θ_D is the Fraunhofer diffraction angle to the first minimum and d_s/f_s is the divergence due to a finite source size. d_s is the linear dimension of the source, and f_s is the focal length of the transmitter lens. The expression in parentheses is an approximation to total beam divergence. It is recognized that Eq. (2) is not strictly correct; however, it suffices as a means for estimating D_b and D_c for the cases considered in this program.

If the beam diameter is neglected, Eq. (1) gives a lower bound for the receiver aperture. Early in the program it was established from measurements on the gun that L = 380 cm is a practical separation of the transmitter/receiver and the muzzle mirror. Therefore, for θ_{TM} = 5 mrad one obtains:

$$D_c > 7.6 \text{ cm}$$

The beam diameter must be added to this value to arrive at the minimum receiver aperture which will not vignette the beam at maximum muzzle deflection. Hence, a large diameter lens is required. Furthermore, the lens must have a low f/number as can be seen from the following consideration:

The PSD chosen for the MDMS (United Detector Technology SC-10D) has a diameter 1.0 cm, with best linearity over the central 0.25 cm. Therefore, the maximum angular deflection must cause the focused spot to move no more than 0.125 cm from the center. For a muzzle deflection of 5 mrad, the beam reflected from the muzzle mirror will deflect 10 mrad. If the spot is to remain within the linear region of the PSD, this implies that the focal length of the receiver lens can be no greater than 12.5 cm. Since the receiver diameter, $D_c > 7.6$ cm, the conclusion is that the f/number of the lens must be less than f/1.6.

The receiver lens must also have high quality with respect to aberrations, which affect the power distribution in the image and hence the centroid measurement. A highly corrected lens is required, which suggests the use of a good photographic lens.

The realization of a practical transmitter/receiver system depends on several practical considerations:

1) The availability of large aperture, low f/number, high quality lenses. This requirement drastically restricts the choice of lenses.

2) The availabity of high power, solid state light sources (light emitting diode (LED) or laser diodes) with small source size. The requirement is necessary to minimize beam divergence and hence the beam diameter at the receiver.

3) The ability to deliver sufficient power to the PSD to achieve a signal-to-noise ratio consistent with the goal of 0.1 mrad resolution.

4) The reduction of background radiation on the PSD to the point where both linear behavior and the resolution goal

can be achieved. The receiver lens will image the solar illuminated scene beyond the mirror onto the PSD, adding the power distribution of the scene to that of the focused spot. This can affect the centroid measurement and introduce non-linear behavior.

2.4 TRANSMITTER/RECEIVER DESIGN ANALYSIS

2.4.1 Light Emitting Diode Source (LED)

The light emitting diode (LED) was considered first as a light source for the transmitter and rejected on a number of counts. In spite of its obvious advantages (availability, low cost, high power, ease of operation, ruggedness, reliability, etc.), it has two shortcomings which make it unuseable in the MDMS application:

1) High power LEDs have a large source size which causes high beam divergence and hence a large beam diameter at the receiver. In order to avoid vignetting, an unreasonably large diameter receiver lens is required.

2) High power LEDs generally emit into a hemisphere which makes it difficult to collect and project more than a small fraction of the emitted power. It was concluded that an LED would not permit the delivery of sufficient power to the PSD to permit the achievement of the revolution goal of 0.1 mrad. The following discussion provides a quantitative basis for rejecting the LED source.

A typical high-power LED is the Texas Instrument TIXL-12, which emits 40 milliwatts into a hemisphere with an on-axis intensity of 15 mwatt/str. The emitter diameter is d_s = 0.036 in. = 0.09 cm. The beam diameter of the receiver can be estimated from Eq. (2), once the focal length for the transmitter, f_s, is chosen. This choice involves a trade-off between beam power and image size on the PSD. For maximum power in the beam, a low f/number transmitter lens is called for, which implies a small f_s. A small f_s, on the other hand, implies a large image on the PSD.

The image size, d_I (see Figure 2) is determined by:

$$d_I = (f_c/f_s)\, d_s \qquad (3)$$

where f_c is the focal length of the receiver. The PSD chosen (see Section 3-4) has a diameter of 1.0 cm with the best linearity over the central 0.25 cm. If one sets $d_I < 0.25$ cm and $d_s = 0.09$ cm, then from Eq. (3), $f_c/f_s < 2.8$. It has already been shown that $f_c < 12.5$ cm, which gives $f_s > 4.5$ cm for the transmitter lens.

2.4.1.1 Beam Diameter and Receiver Aperture

If one uses $d_s = 0.09$ cm and $f_s = 5$ cm, the beam divergence due to the finite source size is $\sim d_s/f_s = 0.018$ rad. For L = 380 cm, this gives $2L\,(d_s/f_s) \approx 14$ cm as the contribution to the beam diameter due to the source size alone. It has already been shown that if beam width is neglected, the receiver aperture must be at least 7.6 cm in diameter to accommodate the ±5 mrad muzzle deflection amplitude. Thus the total aperture required to accept this beam would thus be ~22 cm, plus the contribution due to the transmitter aperture and diffraction.

These considerations alone rule out the use of the LED as the transmitter source because of the excessively large aperture required for the receiver lens. Given the additional requirements for low aberration and low f/number, one quickly concludes that the lens being described is at least not readily available.

2.4.1.2 Beam Power and Power on PSD

Assume a transmitter lens with $D_s = 1.0$ cm and $f_s = 5$ cm (f/5). Such a lens would subtend a solid angle at the LED of $\pi/4F^2 = 0.03$ str, where F = f/number = 5. Since the on-axis intensity of the TIXL-12 LED is 15 mwatt/str, the lens will intercept 15 x 0.03 = 0.45 mwatts. Reasonable transmissions for several components of the transmitter/receiver are as follows:

Transmitter Lens	0.9
Muzzle Mirror	0.8
Optical Filter	0.8
Receiver Lens	0.6
PSD Window	0.9

With these values, the total transmission of the system would be 0.30, giving the total power on the PSD of 0.14 mwatts. This is at the low end of the range of power estimated to be required to obtain a system resolution of 0.1 mrad, which was a design goal for the MDMS.

The estimates made in this section have been based on use of the TIXL-12 LED. Other LEDs are available with smaller chip size which would reduce the receiver aperture requirements. The reduced power from these devices, however, makes them unacceptable because of the PSD power requirements. Higher power LEDs are also available with larger emitters; these are unacceptable due to the demand made on the receiver aperture.

The conclusion from this analysis is that the LED is not a suitable light source for the transmitter of the MDMS. What is required is an emitter having a very small source size with most of its radiation emitted in the forward direction. Such a source is the room temperature, CW laser diode.

2.4.2 Laser Diode Source

Properly selected, laser diodes have all the properties required to produce high power in the transmitter beam and a beam width on the order of 1-2 cm at the receiver aperture. This makes possible a receiver diameter of less than 10 cm, which is available in photographic objectives, although the choice is not wide. The laser diode emitter has most of the advantages of the LED; for example: Off-the-shelf availability, high power, relatively low cost, ruggedness, etc. Its major disadvantage is that its temperature must be controlled to within close limits (1-2°C) in order to obtain reliable operation and long life. While this complicates implementation of the transmitter,

temperature control to this accuracy is straightforward using thermoelectric techniques.

Table 1 gives the operating parameter of Laser Diode Laboratories (LDL) emitters. These are GaAlAs multiheterostructures with stripe geometry, which are designed for continuous operation at room temperature. Figure 3 (a) and (b) show the distribution of output radiation, somewhat idealized. Note the small source size.

2.4.2.1 Beam Width and Receiver Aperture

The expression for estimating beam width was given in Eq. (2) and is repeated below (see Figure 2).

$$D_b \approx D_s + 2L\,(2 \tan \theta_D + d_s/f_s). \tag{2}$$

Since the angles involved are small, this may be written

$$D_b \approx D_s + 4L\theta_D + 2Ld_s/f_s, \tag{4}$$

where $\theta_D = 1.22\ \lambda/D_s$ is the Fraunhofer diffraction angle to the first minimum. This gives

$$D_b \approx D_s + 4L\,(1.22\lambda)/D_s + 2L\,d_s/f_s. \tag{5}$$

The beam width, D_b, is at a minimum with respect to D_s when

$$D_s = \sqrt{4.88\ \lambda L}\ .$$

Substituting this for D_s in Eq. (5) gives

$$D_b \approx 2\sqrt{4.88\ \lambda\ L} + 2L\,d_s/f_s.$$

With λ = 850 nm, L = 380 cm, D_s = 0.4 cm is the optimum diameter of transmitter aperture, and

$$D_b \approx 0.8 + 2L\,d_s/f_s. \tag{6}$$

TABLE 1. OPERATING CHARACTERISTICS OF LASER DIODE LABORATORIES (LDL) LASER DIODES

		Symbol	Min.	Typ.	Max.	Units
Total Radiant	LCW5	Pom	5	7	10	mW
Flux at Rated I_m	LCW10	Pom	10	14	20	mW
Forward Current		I_m	150	300	500	mA
Threshold Current		I_{th}	100	200	350	mA
Wavelength of Peak Intensity		λ	800		890	nm
Spectral Width at 50% pts.		$\Delta\lambda$		2.5		nm
Source Size				.01X.5		mils
Rise Time of Radiant Flux		Tr		100		PS
Operating Temperature		To	0		65	°C
Storage Temperature		Ts	−196		+140	°C
Forward Voltage	at 50ma	Vb		1.5		volts
	at I_m	V_m		1.8		volts

*Pom, I_m & I_{th} information furnished with each device

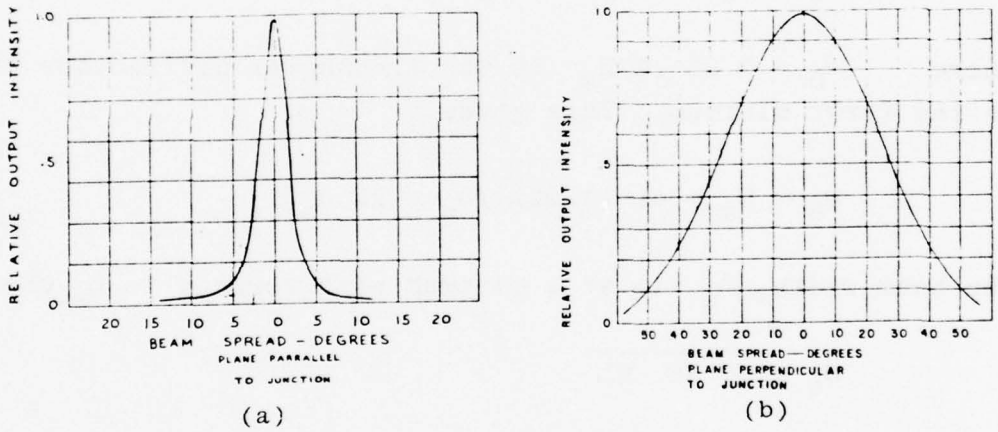

Figure 3. Radiation Distribution from Laser Diode Laboratories (LDL) Laser Diodes

The maximum dimension of the source is $d_s = 1.3 \times 10^{-3}$ cm. Measurements at EG&G have shown that the aspheric lens chosen for the transmitter can resolve approximately 15 μm; hence, the emitting area of the laser diode is unresolvable. The diameter of the blur circle for the transmitter is thus assumed to be 1.5×10^{-3} cm, and it is the image of the blur circle that is projected onto the PSD with a magnification of f_c/f_s (See Eq. 3). Because of the small size of the blur circle ("emitting area"), a large magnification can be tolerated. Therefore, one has freedom to choose the focal length of the transmitter for high-beam power.

The transmitter lens chosen was an aspheric singlet with a focal length $f_s = 1.2$ cm and clear aperture of 1.8 cm. Since the optimum transmitter aperture was found to be $D_s = 0.4$ cm, the transmitter will operate at f/3.0. With $f_s = 1.2$ cm and $d_s = 1.5 \times 10^{-3}$ cm (transmitter blur circle diameter), the beam width at the receiver aperture as estimated from Eq. (6) becomes $D_b \approx 1.6$ cm. In Section 2.2.1, it was shown that if the beam diameter is neglected, the receiver aperture would have to be at least 7.6 cm in diameter to accommodate ±5 mrad muzzle deflection. Therefore, with the laser diode source, the diameter of the receiver lens must be at least 9.2 cm.

The size of the irradiated area on the PSD is determined by the magnification of the transmitter/receiver optics, $m = f_c/f_s$. As described in Section 2.3.2.1, the most linear region of the PSD chosen occurs over the central 0.25 cm. Therefore, the image of the source should be much smaller than 0.25 cm. The receiver focal length can be estimated from the requirement that the amplitude of muzzle deflection is ±5 mrad (±10 mrad beam deflection), and this should cause the centroid of the focused spot on the PSD to move ±0.125 cm. This implies that $f_c = 12.5$ cm. The PSD spot size would then be (See Eq. 3) 1.5×10^{-3} (12.5/1.2) = 0.013 cm.

At this point, the essential features of the receiver lens have been determined; the lens should have a clear aperture

of at least 9.2 cm with a focal length of 12.5 cm. Thus, one requires an f/1.36, 125 mm lens. The analysis to this point has not considered the quality of the lens in terms of allowable aberrations. This characteristic will be discussed in Section 2.4.4.

2.4.2.2 Beam Power and Power on PSD

The beam power from the transmitter using a laser diode was estimated from the specification on the intensity distribution from the emitter. Figure 3 (a) and (b) show the approximate radiation distribution from Laser Diode Laboratories (LDL) emitters; both of these curves can be well approximated by a gaussian. Measured distributions show variations from these idealized curves, but their general shape is Gaussian to a first approximation. This form was used in estimating beam power.

The intensity distribution can be expressed as:

$$I = I_o \exp(-\theta^2/2a^2) \exp(-\phi^2/2b^2). \qquad (7)$$

Here θ and ϕ define orthogonal directions relative to the axis of the emitter. The angle θ is measured in the plane parallel to the emitter junction and ϕ is measured in the plane perpendicular to the junction. For the LDL emitters:

$$a = 3.08 \times 10^{-2} \text{rad}, \quad b = 0.41 \text{ rad}.$$

The total power contained in a solid angle defined by θ and ϕ, is given by:

$$P_s = 4 I_o \int_0^{\theta_1} \exp(-\theta^2/2a^2)\, d\theta \int_0^{\phi_1} \exp(-\phi^2/2b^2) d\phi \qquad (8)$$

Upon completion of the integration, Eq. (8) reduces to:

$$P_s = 8\pi ab I_o \text{ Erf } (\theta_1/a) \text{ Erf}(\phi_1/a), \qquad (9)$$

where Erf( ) is the error function. For the circularly symmetrical transmitter lens, $\theta_1 = \phi_1$.

To evaluate the beam power, P_s, a value of the on-axis intensity, I_o, is required. This could be calculated from Eq. (8) by setting the upper integration limits at infinity. This gives the total power emitted by the diode, which is published by the manufacturer, and hence allows I_o to be computed. However, the on-axis intensity derived in this manner is overestimated, since the actual intensity distribution tends to have broader wings and more structure than that shown in Figure 3. Therefore, EG&G used data for I_o previously measured in its laboratories. The value of I_o varies considerably from device to device, suggesting that suitable laser diodes for the MDMS transmitter need to be selected. Laboratory measurements on a limited number of diodes indicated that a value for $I_o \geq 40$ mw/str can be reasonably expected if the devices are suitably selected. Figure 4 is a plot of P_s from Eq. (9) against the f/number of the transmitting lens (f/no = 1/2 tan θ_1), with I_o = 40 mw/str.

As shown above, the transmitter will operate at f/3 in order to produce the minimum beam width at the receiver aperture. With this aperture, the transmitter will collect one milliwatt for collimation into the beam. In Section 2.4.1.2, the total transmission of the transmitter/receiver was estimated at 0.30, indicating that ~0.30 mwatt will be incident on the PSD. As will be shown later, this is sufficient power to produce a signal-to-noise ratio consistent with achieving the goal of 0.1 mrad resolution.

The value of the calculation made above is that it provides one basis for selecting suitable laser diodes. On this basis, laser diodes were ordered with the requirement that at least 1.5 mwatts were contained in an f/3 cone. The circled data points in Figure 4 represent measurements made during this program with a laser diode selected according to this criterion. Note that for this particular device, 1.7 mwatts were observed

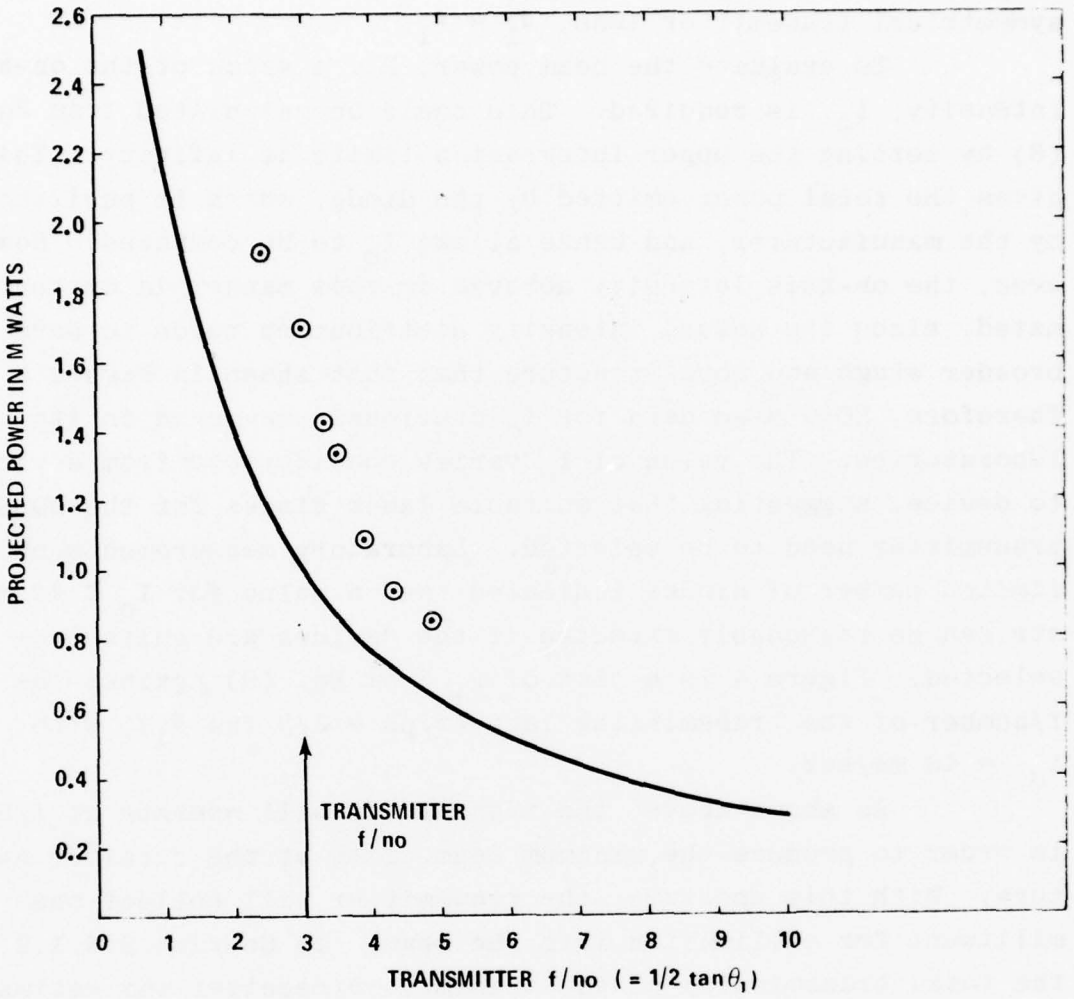

Figure 4. Power Collected as Function of f/no from a Laser Diode with I_o = 40 mwatt/str. Solid Line Computed (See Text). Circled Points Measured Using Laser Diode Laboratories Laser Diode Emitting 7.2 mwatts

in an f/3 cone. This is typical of the laser diodes used in this program.

2.4.3 Transmitter Specifications

The optical requirements on the transmitter have been developed in the previous sections. These are summarized in this section along with the non-optical requirements and form the transmitter specifications.

TABLE 2. TRANSMITTER SPECIFICATIONS

Transmitter Lens	
Focal Length	12 mm
Aperture Diameter	0.4 cm (Aperture Stop)
f/number	3
Lens Shape	Aspheric (corrected for spherical aberration)
Supplier	Melles-Griot 01LAG111
Transmitter Source	
CW Laser Diode	Room Temperature Operation
Radiant Flux	5 mw minimum
Axial Intensity	1.5 mw in f/3 cone (min.)
Wavelength	820 nm ±15 nm
Operating Temperature	27°C
Supplier	Laser Diode Laboratories LCW-5
Thermoelectric Element	
Heat Pumped (maximum)	25 BTU/hr (8.5 watts)
Temperature Difference (maximum)	67.5°C
Supplier	Melcor FC 07-32-05 (two required)

Note: Two Melcor elements required; series wired factory.

2.4.4 Receiver Specifications

In the preceding paragraphs, an analysis was made of the critical design parameters for the MDMS transmitter, and

quantitative values of these parameters were derived. This analysis also produced the basic specification of the receiver lens. It was shown that this lens should be f/1.4 with a focal length of 125 mm. A standard focal length for photographic lenses is 135 mm. The only lenses found to be available that came close to meeting these specifications were:

1) Aero Ektar f/2.5, 300 mm. This is an aerial camera lens, containing seven elements and weighing twelve pounds. It has a clear aperture of 12 cm which is more than adequate for the MDMS application. The focal length, however, is 2.4 times the 125 mm deduced from the preceding analysis, which would cause the spot on the PSD to move out of the most linear region of the PSD for muzzle deflection angles in excess of ±2 mrad. This lens was rejected for this reason primarily, and because another choice was available.

2) Noritar f/1.4, 135 mm. This lens was manufactured in Japan and used on the HITVAL program. It comes very close to meeting the requirements deduced above and has the further advantage of having shown that it can withstand the shock environment associated with a large caliber artillery weapon. While manufacture of this lens was discontinued several years ago and it is currently unavailable in the market, the HITVAL lens was made available by BRL for this program and used in the MDMS.

The requirements on lens quality are difficult to specify in terms of the angular resolution goal of 0.1 mrad. However, a commentary on required performance can be made based on the following observations. The diameter of the blur circle of the transmitter lens was estimated to be 1.5×10^{-3} cm; since its focal length is 1.2 cm, its angular resolution is 1.3×10^{-3} rad. A good 135 mm photographic lens operating at f/1.4 can resolve ~50 lp/mm which implies an angular resolution of 1.5×10^{-4} rad. Hence, the angular resolution of the transmitter/receiver from the standpoint of image formation is $\sim 1.3 \times 10^{-3}$ rad. This makes the spot size on the PSD $\sim 1.7 \times 10^{-2}$ cm. It

is the centroid of light distribution within this spot that is sensed by the PSD. Changes in this distribution due to aberrations will cause the centroid to shift.

The question to be answered relates to the constancy of the aberrations over the lens aperture, rather than their magnitude, since the diameter of the illuminated area on the PSD is about ten times the resolution capabilities of the lens itself. A 0.1 mrad change in mirror tilt corresponds to a translation of the centroid of 1.35×10^{-3} cm, which is about ten percent of the blur circle diameter. Thus, the requirement on the lens is that the residual aberrations cause a differential shift in the centroid distribution of no more than 0.1×10^{-3} cm to 0.2×10^{-3} cm, as the transmitter beam traverses the lens aperture. A shift of this magnitude would be observable, since it has been shown that the spatial resolution of the PSD is $\sim 0.5 \times 10^{-4}$ cm (EG&G internal research result, reported in the Proposal to BRL AL-P- 75-20, dated 4 March 1975). While the magnitude of the centroid shift resulting from a change in aberrations across the lens aperture cannot be predicted, such a shift is sure to occur, and because of the high resolution of the PSD, it is likely to be detected. Given a sufficiently high signal-to-noise ratio, one would expect this effect would limit the angular resolution of the MDMS. This limit can only be determined by an independent measurement.

The position sensitive detector chosen for the MDMS is the United Detector Technology, Inc. PIN-SC/10D with the typical performance parameters given in Table 3. The basis for this selection is discussed in Section 3.4.

TABLE 3. PERFORMANCE PARAMETERS UDT PIN-SC/10D

Active Area	1.0 cm x 1.0 cm
Spectral Range	350 nm - 1100 nm
Responsivity, Peak λ	0.55 amp/watt
NEP (Peak λ ,1 kHz)	10^{-11} watt/Hz$^{\frac{1}{2}}$
Uniformity of Responsivity	2%
Position Sensitivity, Peak λ	1 amp/watt/cm

TABLE 3. (CONTINUED)

Position Linearity - Center to point 25% of distance from center to edge	0.5%
Drift	2 μm/°C
Operating Temperature	27°C

2.4.5 Signal-to-Noise Analysis

The signal-to-noise ratio for a muzzle mirror tilt of 0.1 mrad will be estimated in this section. The signal of interest is the difference between the two photogenerated currents flowing out of the two terminals defining one axis of the PSD. If these currents are represented by i_1 and i_2, then the signal current for a spot movement ΔX is:

$$i_s = i_1 - i_2 = (2\beta/L)\,(P_o/2)\,\Delta X = 2.3 \times 10^{-7} \text{ amp.} \quad (10)$$

In this expression:

β = PSD responsivity, 0.47 amp/watt at λ = 820 nm

L = Dimension of the PSD = 1.0 cm

P_o = Laser power incident on the PSD = 0.2 mw

ΔX = Displacement of the centroid for a mirror tilt of 0.1 mrad = 2.7×10^{-3} cm

There are several contributions to the total noise current:

1) Noise equivalent power, NEP, of the PSD. For the United Detector Technology SC/10D, Table 3 gives NEP = 10^{-11} watt/$Hz^{\frac{1}{2}}$. The mean square of the noise current corresponding to NEP will be designated $\langle i_{NEP}^2 \rangle$.

2) There will be a contribution to noise due to fluctuations in the photocurrent generated by the laser power incident on the PSD. This will be $\langle i_p^2 \rangle$.

3) The solar illuminated background will be imaged on the PSD and produce a noise contribution $\langle i_B^2 \rangle$.

4) The preamplifier following the PSD will have a noise contribution at its input: $\langle i_{PA}^2 \rangle$.

The signal bandwidth of the MDMS was chosen to be 10 kHz (3 dB down), and the prototype was so adjusted. The corresponding noise bandwidth, B_N, is larger by a factor of $\pi/2$. Hence,

$$B_N = 1.5 \times 10^{+4} \text{ Hz} \tag{11}$$

Noise Equivalent Power (NEP Contribution)

The NEP of the PSD is given in Table 3 as NEP = 10^{-11} watt/$Hz^{\frac{1}{2}}$, so that the corresponding mean squared current noise is:

$$\langle i_{NEP}^2 \rangle = B_N[(NEP)/\beta]^2 = 6.8 \times 10^{-18} \text{ amp}^2 \tag{12}$$

Photocurrent Fluctuation Noise

The photocurrent generated by the laser power, P_o, incident on the PSD is $i_p = \beta P_o$. The noise due to fluctuations in this current contribute:

$$\langle i_p^2 \rangle = 2e \beta P_o B_N = 4.5 \times 10^{-19} \text{ amp}^2 \tag{13}$$

Here e = 1.6×10^{-19} coul, the charge on the electron.

Preamplifier Noise

The preamplifier is an LF 155 operational amplifier operated in the transimpedance mode. The input current noise specification is $i_{PA} = 10^{-14}$ amp/$Hz^{\frac{1}{2}}$, and this makes a contribution:

$$\langle i_{PA}^2 \rangle = i_{PA}^2 B_N = 1.5 \times 10^{-24} \text{ amp}^2 \tag{14}$$

Noise Due to Solar Illuminated Background

The solar illuminated background imaged onto the PSD is composed of two parts: 1) The scene forward of the gun which is not blocked by the muzzle mirror and its mounts; and 2) The scene behind the gun as reflected into the receiver by the muzzle mirror. The presence of these images on the PSD contributes unwanted photocurrent which adds to the noise. A second undesirable effect of this image is that it can alter the

distribution of light on the PSD which can cause an error in the measurement of the desired centroid.

In order to minimize both the noise and centroid error due to the background radiation, the following steps were taken:

1) A 0.5 cm diameter field stop was placed in contact with the PSD window. This has the effect of reducing the total power from the background and defining a small circular field of view for the receiver. The 0.5 cm diameter field stop accommodates the ±0.135 cm motion of the focused spot (±5 mrad mirror tilt) with enough area left over to allow for alignment and focusing errors.

2) Circular baffles were placed around the muzzle mirror and behind the transmitter. The diameter of these baffles was chosen to fill the field of view of the receiver as defined by the field stop. Because the background radiation from behind the gun is reflected into the receiver by the muzzle mirror, the image of this scene will move across the PSD as the muzzle mirror tilts. Hence, the diameter of the rear baffle was increased to block the background for the full ±5 mrad dynamic range of muzzle deflection (±10 mrad due to reflection). Similarly, the front baffle (around muzzle mirror) was oversized to account for as much as ±2 cm translational motion of the muzzle during firing. Both the baffles and the front face of the receiver were given matte black finishes to reduce reflection. The reflectivity of these surfaces was not measured. For the purposes of estimating noise due to the solar background, a conservative estimate of reflectivity, $\rho = 0.2$ was made.

In order to reduce further the background signal, an optical interference filter was placed in front of the receiver objective. This filter was designed to have a peak transmission of 0.8 at a wavelength of 820 nm, with a bandpass of 25 nm at the 50% transmission points.

With these design features, the noise due to the solar illuminated background can be estimated. The background now

is assumed to be a uniformly scattering surface with a reflectivity $\rho = 0.2$. Therefore, the background power on the PSD may be written as:

$$P_B = \rho H_\lambda B_o T_R d_c^2/4F^2 = 8 \times 10^{-6} \text{ watts} \qquad (15)$$

Here, $\rho = 0.2$

H_λ = 1 w/m^2 nm is the solar spectral irradiation in the neighborhood of 820 nm.

B_o = 25 nm is the optical filter bandpass.

T_R = 0.5 is the transmission of the receiver (see Table 1).

d_c = 0.5 cm is the diameter of the field stop.

F = 1.4 is the f/number of the receiver objective.

The fluctuaion in the photocurrent generated by this irradiation of the PSD gives a background noise contribution:

$$\langle i_B^2 \rangle = 2e \beta P_B B_N = 1.9 \times 10^{-20} \text{ amp}^2$$

Signal-to-Noise Ratio (SNR)

Table 4 summarizes the several contributions to the noise. Only the first two components in the table contribute significantly to the noise.

TABLE 4. SUMMARY OF NOISE COMPONENTS

Noise Contribution	$\langle i^2 \rangle$ amp^2
PSD NEP	6.8×10^{-18}
Photocurrent	4.5×10^{-19}
Solar Background	1.9×10^{-20}
Preamplifier	1.5×10^{-24}

Note that the contribution due to solar background appears to be insignificant. The square root of the sum of the components in the table constitute the RMS noise current, designated by $\langle i_n^2 \rangle^{\frac{1}{2}}$. The signal produced by a mirror deflection of 0.1 mrad was computed in Eq. (10). Thus, the signal-to-noise ratio at this signal level may be estimated as:

$$SNR = i_s / \langle i_n^2 \rangle^{\frac{1}{2}} = 85 \quad (@\ 1\ kHz)$$

This value of SNR is based on a value of PSD NEP measured at 1 kHz (see Table 3) with no indication by the manufacturer as to the bandwidth of the measurement. Since it most likely does not account for low frequency noise, the value of SNR estimated here is probably an overestimate.

Comment on S/N and Angular Resolution

In the preceding analysis, it was implicitly assumed that the noise power spectrum was flat with frequency, which is a good assumption for frequencies above a few hundred hertz. However, the bandpass of the MDMS extends from DC to 10 kHz. With photodetectors such as the PSD, the noise power is known to increase at low frequencies approximately as the inverse of the frequency. Thus, if the frequency bandpass of the system extends to DC, as in the case of the MDMS, the total noise power in the band would be expected to be higher than that given in Table 4 for the PSD NEP. No quantitative data are available describing the behavior of the noise power spectrum for the PSD at low frequency. However, it is not unreasonable to expect that the total noise power in the 10 kHz bandpass for the MDMS could be increased by a factor of 3-4 by the low frequency contribution. Assuming this to be the case, the SNR as computed above would be too high by this factor, and a value of S/N ~20-30 is more to be expected. While no quantitative SNR measurements were made, a S/N value for the MDMS in this range is consistent with the data taken.

This result suggests that from the standpoint of the SNR, an MDMS resolution of 0.1 mrad should be easily obtained. The system resolution, however, depends not only on the SNR but also on system linearity, which depends in turn on PSD linearity and the residual aberrations of the receiver lens. A high SNR is a necessary, but not sufficient, condition for high system resolution. The measurements on the MDMS breadboard and prototype reported in Sections 3 and 4 indicate a high SNR, as

predicted, but also show that the resolution is not much better than 0.1 mrad. The reason for this is believed to be due primarily to the effect of residual aberrations in the NORITAR.

2.5 MUZZLE MIRROR

The purpose of the muzzle mirror is the reflect the transmitter beam into the receiver. The principle criteria for the mirror are that it be of sufficient size so that the transmitter beam will not be vignetted due to lateral motion of the muzzle during firing and that it be rugged enough to withstand the shock environment at the muzzle.

It was estimated by BRL personnel that the total lateral translation of the muzzle during firing is approximately one inch. The diameter of the transmitter beam at the mirror was estimated by the methods described previously to be about 1 cm. Thus, a two-inch diameter mirror was considered the smallest safe diameter. Note that if vignetting of the beam at the mirror is to be prevented, care must be taken in system alignment to put the transmitter beam at the center of the mirror.

A stainless steel mirror was selected after consideration of the shock and vibration environment expected at the muzzle. The reflectivity of polished stainless steel is less than 0.9. In view of its exposed position and vulnerability to contamination by muzzle gases, a reflectivity of 0.8 for this component of the MDMS has been assumed. To maintain this level of reflectivity, adequate maintenance of the mirror surface must be performed.

SECTION 3
MDMS BREADBOARD AND TEST RESULTS

3.1 BREADBOARD ARRANGEMENT

The primary purpose of the MDMS breadboard was to evaluate candidate position sensitive detectors (PSD) and to aid in the design of the position sensing computer. At the time that the breadboard studies were initiated, the laser diode transmitter was not available and a HeNe laser with no external optics was used as a substitute. By adjusting the distance between the receiver lens and the output of the HeNe laser, the spot size of the laser beam at the receiver aperture was made approximately 1.6 cm in diameter. This was the expected beam diameter from the laser diode transmitter.

Figure 5 gives the schematic arrangement of the breadboard. In order to accomodate on a single optical table the 380 cm separation required between the receiver (NORITAR lens) and the muzzle mirror, a folded optical system was required. The "muzzle" mirror was mounted in a two-axis mount which could be moved by micrometer adjustment in both the X-direction (in the plane of the figure) and Y-direction (plane perpendicular to figure). The PSD was contained in a mount with provision for motion along the X-, Y- and Z-axis, as well as a rotation about the Z-axis; the Z-axis was colinear with the optical axis of the NORITAR.

Angular tilt of the muzzle mirror was measured with a Kollmorgan Model K222 Dual Axis Autocollimator. This instrument measures directly angular tilt of the mirror and has a sensitivity and repeatability of 0.1 sec of arc with a field of view of 26 min of arc. As shown in Figure 5, the muzzle mirror is viewed by the autocollimator via a turning mirror. This arrangement was made for the sake of convenience in making the various measurements, since it placed the autocollimator at the same end of the optical table as the positioning controls for the "muzzle" mirror and PSD.

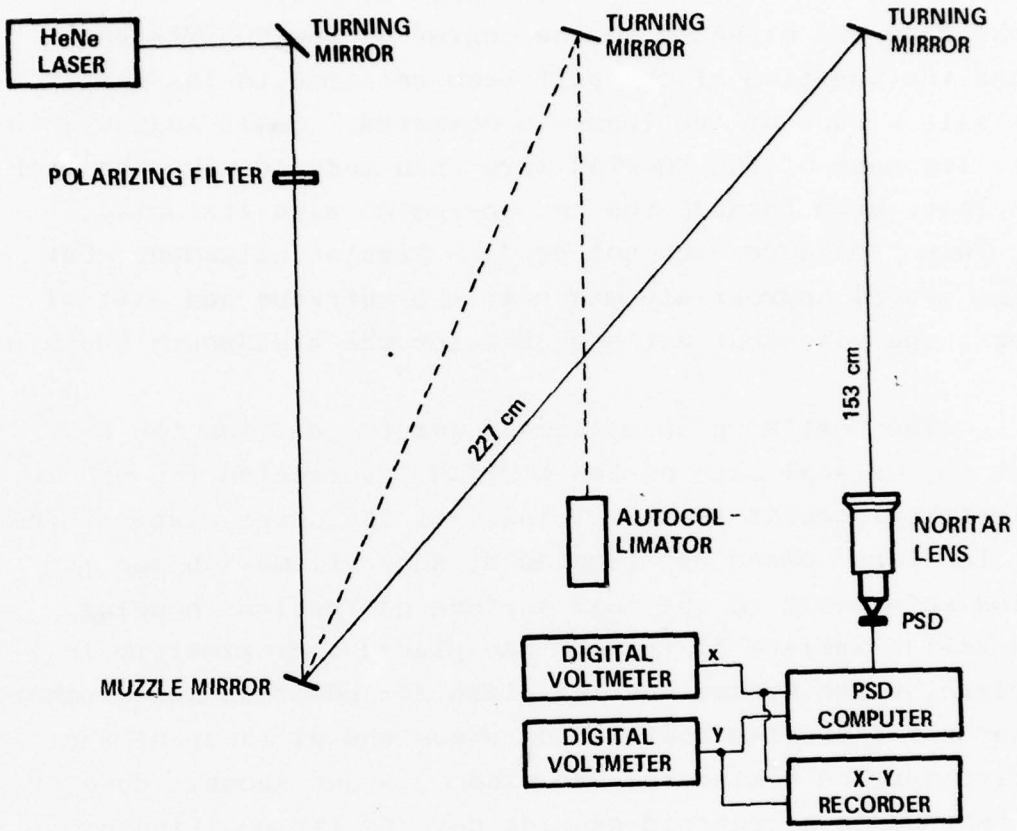

Figure 5. Schematic Arrangement of MDMS Breadboard

3.1.2 Alignment of the Breadboard

Alignment of the breadboard was made to the optical axis of the NORITAR. This lens was mounted in a V-block, aligned by eye with one edge of the optical table and leveled. The HeNe beam was directed to the center of the NORITAR aperture and the position of the exit beam relative to the center of the exit window of the lens was observed. Small adjustments in the alignment of the NORITAR were then made to make the path of the laser beam through the lens coincide with its optical axis. This procedure does not produce precise alignment, but with the aid of appropriate masks at the entrance and exit of the lens, the alignment was adequate for the breadboard measurements.

The next step in alignment was to position the PSD so that the optical axis of the NORITAR intersected the PSD at its electrical center in the vicinity of the focal plane of the lens. The focal plane was located by autocollimation and its position referenced to the rear surface of the lens housing. The sensitive surface of the PSD was placed approximately in this plane, which became the X-Y plane for position measurement. This was not a precise positioning since the distance of the sensitive surface behind the PSD window is not known. However, since the PSD is a centroid sensing device, its positioning relative to the focal plane should not be too critical. Once the X-Y plane was established, the PSD was moved in this plane until a null reading on the X- and Y- digital voltmeters (DVM) was obtained. This established the electrical center of the PSD on the optical axis of the NORITAR.

The final adjustment was to align the axes of the PSD with the X- and Y-axes defined by the dual-axis mirror mount. This was accomplished by rotating the PSD about the Z-axis in small increments and sweeping the laser beam across the NORITAR aperture in the X-Z plane, while observing the output of the Y-DVM. When properly aligned, a sweep of the laser beam produced no change in the null reading of the Y-DVM. As a check on

the alignment, the beam was scanned in the Y-Z plane while observing the reading on the X-DVM. This reading remained null, indicating that the axes of the PSD were orthogonal and aligned with the axes defined by the dual axis mirror mount.

3.2 POSITION SENSING COMPUTER

3.2.1 PSD - Theory of Operation

The PSD chosen for the MDMS is the United Detector Technology SC/10D; the reasons for this selection are described in Section 3.4. The SC/10D is a planar diffused type PIN photodiode, with four contacts defining the X- and Y-axes made to the n-type base. A fifth electrode provides a means for biasing the device negatively. The dimensions of the active area are 1 cm x 1 cm.

Light absorbed at a point on the surface of the PSD causes electrons to be injected into the depletion layer, where they are drawn by the applied field into the n-region, establishing a current which flows out through the four contacts. The n-region may be considered a distributed resistance which functions as a resistive divider, so that the current flowing to any electrode is inversely proportional to the resistance between the point of charge injection and the electrode. Hence, the magnitude of the photocurrent at each electrode is related to the distance between that electrode and the point of electron injection. Strictly speaking, this is a three dimensional problem. However, an adequate description of the PSD for the purpose of this discussion can be developed using a one dimensional approximation.

An approximate equivalent circuit for one axis of the PSD is shown in Figure 6. The current source represents the photocurrent generated by a light spot incident on the detector at a point X cm from the electrical center of the detector. C_D is the cell (barrier) capacitance, and $R_S = R_1 + R_2$ is the distributed resistance between detector electrodes, 1 and 2, which are separated by a distance, L. The distance from the centroid of the light spot to electrodes 1 and 2 is (L/2 + X) and (L/2 -

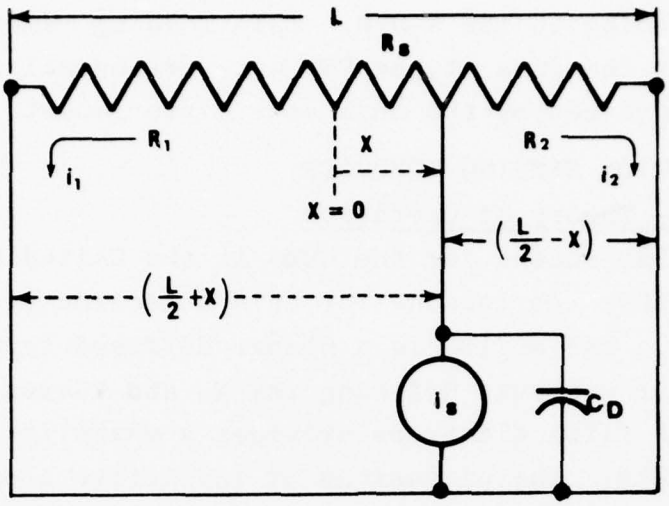

Figure 6. PSD Equipment Circuit

X), respectively. In the one-dimensional approximation, $R_1 = (1/2 + X/L)R_s$, $R_2 = (1/2 - X/L)R_s$ and the currents in R_1 and R_2 are

$$i_1 = (1/2 - X/L)i_s$$
$$i_2 = (1/2 + X/L)i_s \qquad (16)$$

The difference between the two currents is then proportional to the coordinate of the light spot,

$$i_2 - i_1 = \frac{X}{L/2} \; i_s \; ; \qquad (17)$$

and the sum of the currents is equal to the total photocurrent:.

$$i_1 + i_2 = i_s \qquad (18)$$

The position of the centroid of the light spot is then found by taking the ratio of Equations (18) and (17).

$$X = \frac{i_2 - i_1}{i_2 + i_1} \quad \frac{L}{2} \qquad (19)$$

Since both the sum and difference currents are proportional to the total photocurrent, which in turn is proportional to the light power absorbed by the detector, the position measurement of the centroid of the light spot is independent of the

incident light power. For the two-axis detector, this simple analysis is less credible. Intuitively, however, one would expect the X- and Y-coordinates of the centroid to be proportional to the ratio of the difference and sum currents in the X- and Y-axes, respectively, as given by Eq. (19). This is what is found empirically.

3.2.2 Position Sensing Computer Operation

A block diagram of the position sensing computer is given in Figure 7. The four PSD currents are first transformed to voltages which are transmitted to the position computer. For each electrode pair the difference and sum of the voltages V_{x+} and V_{x-} are then formed and the ratio taken, in accordance with the prescription of Eq. (19). The output voltage of the computer is thus

$$V_x = K\,(V_{x+} - V_{x-})/(V_{x+} + V_{x-}) \qquad (20)$$

where K is a scale factor determined by the amplifier buffer to give a convenient voltage range at the output.

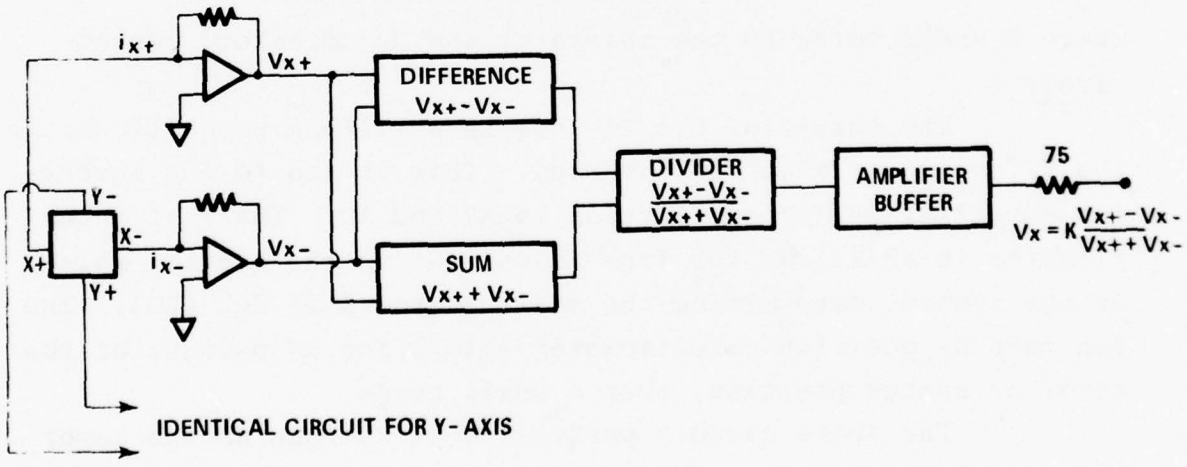

Figure 7. Block Diagram of Position Sensing Computer

Figure 8 gives the circuit diagram of the computer and Figure 9 shows the component layout on the wire-wrapped board. In describing the operation of this circuit, only the X portion of the computer will be referred to; the Y computation is identical.

The difference $V_{x+} - V_{x-}$ is computed in A5 (top) of Figure 8, the difference amplifier. The 20 KΩ potentiometer at A6 provides a means for nulling the output of the amplifier when $V_{x+} = V_{x-} = 0$. Equalization of the gain for V_{x+} and V_{x-} is accomplished by means of the 2 KΩ potentiometer in A6. Thus, with equal voltages at +x and -x, the output may be adjusted to zero.

The sum $V_{x+} + V_{x-}$ is computed in A5 (bottom). Again the 20 KΩ potentiometer in A4 zeros the output with +x and +y equal to zero. The 500Ω potentiometer in A4 equalizes the gain so that +x and +y have exactly the same effect on the output.

Division is performed by a Burr-Brown divider (BB 4291) at A8. For proper operation of the divider, the denominator must always remain positive and be larger (in magnitude) than the numerator. The transfer function for the divider is

$$E = 10\ N/D$$

where N and D refer to the numerator and denominator, respectively.

The output of the divider is a voltage proportional to the X- position, which is inverted. This is fed to the inverting amplifier-buffer combination in A3 and A9. The 2 kΩ potentiometer in A3 allows for fine adjustment in the overall gain of the system, determining the scale factor K in Eq. (20). The ten turn X- position potentiometer allows for adjustment of the zero, or center position, over a small range.

The above circuit performs well as long as the laser beam power does not vary by more than a factor of about five below the design value of 0.8 mwatts. When the beam position reaches the angular limits of ±5 mrad set by the diameter of the receiver aperture, vignetting occurs and the power incident in

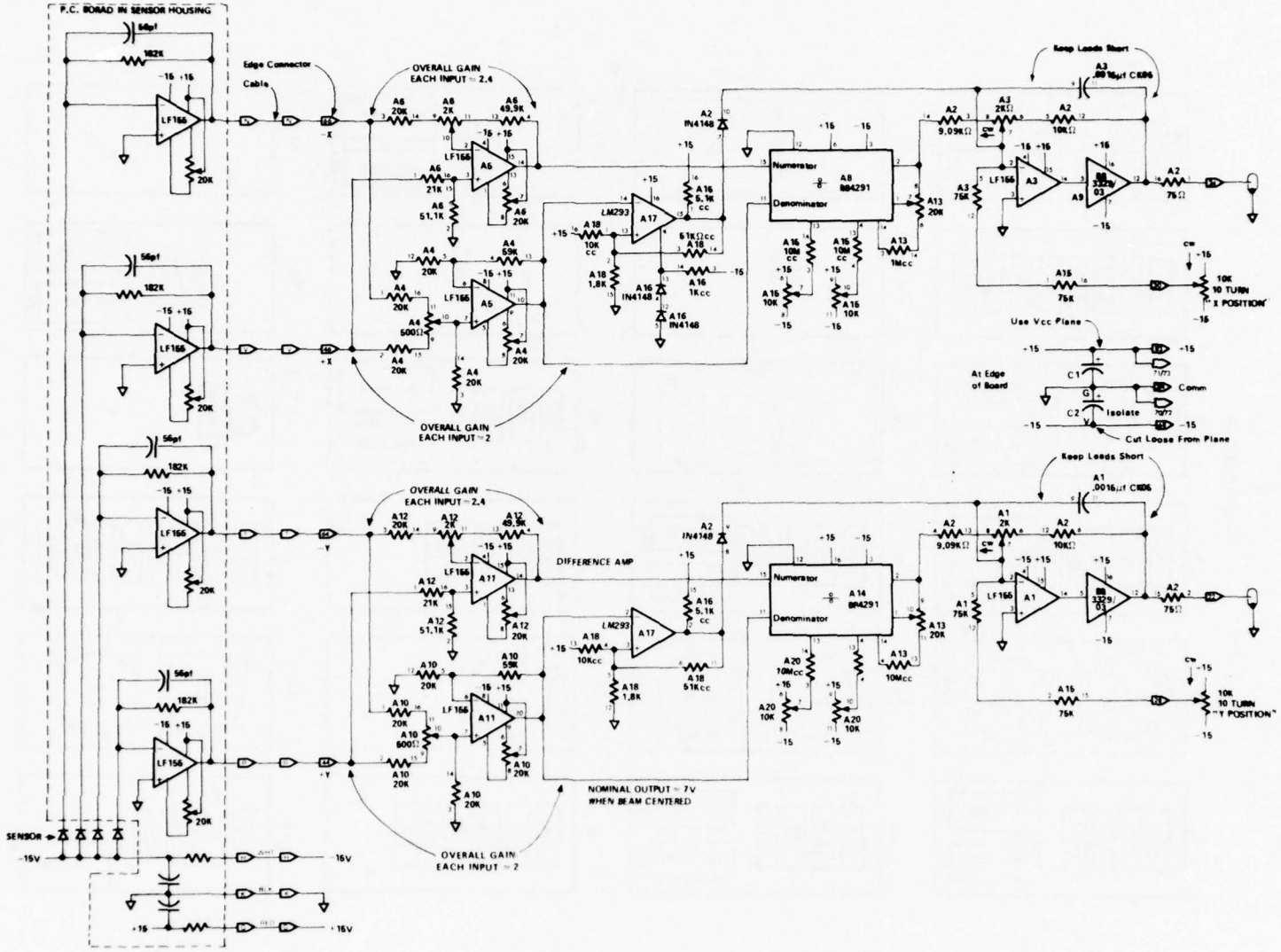

Figure 8. Position Computer

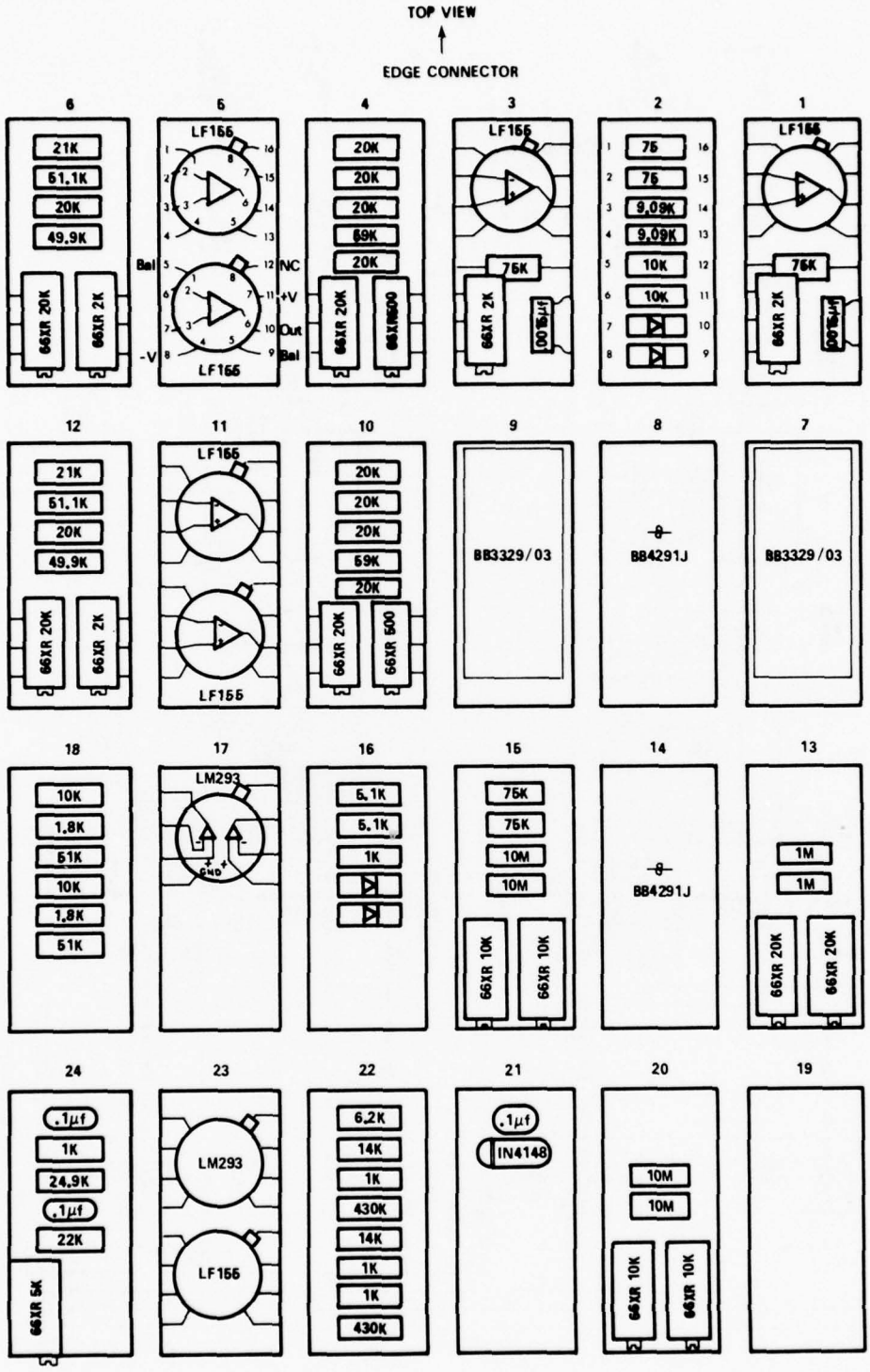

Figure 9. Position Computer Layout

the PSD is reduced. Should the power reduction become large enough to impair the measurement, comparator A17 causes the amplifier-buffer combination in A3 and A9 to go to its negative saturation voltage (~-13.5 V). A17 accomplishes this by monitoring the sum of the two input voltages (denominator). Should the sum fall below a predetermined value, the comparator forces the output to negative saturation.

Note that the output impedance is 75Ω. Should the output be terminated in 75Ω, all voltage values will be one-half of the open circuit values.

3.3 ANGULAR CALIBRATION

Angular calibration of the MDMS breadboard was accomplished using the Kollmorgan Model K222, Dual Axis Autocollimator, which measures directly the angular tilt of the "muzzle" mirror. The procedure used to evaluate the linearity of response of the PSD was to rotate the "muzzle" mirror in either the X-Z or Y-Z plane, using the autocollimator to measure the amount of mirror rotation. The standard increment of rotation was one minute of arc (0.29 mrad). After setting the mirror tilt increment along one axis, the mirror was rotated to sweep the laser beam along the other axis, with the output of the PSD computer recorded on an X-Y recorder. By repeating this procedure for both axes, a grid was traced, with the grid lines spaced at one minute intervals. From these traces, the degree of linearity (or non-linearity) could be determined with considerable precision.

3.4 POSITION SENSITIVE DETECTOR EVALUATION

Two PSD's were obtained for evaluation: 1) United Detector Technology (UTD) SC/10D; and 2) Quantrad Corp, (QC) PS-200-1. The purpose of the evaluation was to examine linearity of response and the procedure used for both detectors was the same.

Each detector was mounted behind the NORITAR and aligned by the procedure described in Section 3.1.2. The HeNe

laser beam power was set to produce the same photocurrent in the PSD which would result if a GaAlAs laser at 820nm were used to give 0.3mw incident on the PSD. The measurement procedure used for assessing linearity is that described in Section 3.3. Figures 10 through 13 show the X-Y traces for the two PSD devices.

Figures 10 and 11 are traces for the UTD SC/10D PSD, operated at 15 volts and 0 volts bias, respectively. Figures 12 and 13 are similar traces for the QC PS-200-1, again at 15 volts and 0 volts bias, respectively. In each figure, the electrical center of the device is marked by a circle, and the grid interval is one minute of arc. The voltage sensitivity of the X-Y recorder was 0.5 v/cm in all cases.

A cursory glance at these figures shows that of the four traces, the one in Figure 10 for the UDT SC/10D at 15 volts bias has the best linearity. When the bias is removed, as in Figure 11, considerable non-linearity appears, and, as might be expected, the output sensitivity decreases.

The character of the two traces for the QC PS-200-1 (Figures 12 and 13) is considerably different. Under both biased and non-biased operating conditions, a dominant feature of these traces is barrel distortion, which appears to be enhanced when the PSD is biased.

A qualitative examination of these traces makes it clear that the UDT SC/10D PSD has the most linear performance, and no further consideration was given to the Quantrad device. It is possible that under a different set of operating conditions, this PSD might perform more satisfactorily. Since, however, the conditions of test were arranged to simulate those expected to be found in the MDMS prototype, it is unlikely that minor changes within the constraints of these conditions would greatly improve the PS-200-1 performance. Therefore, the SC/10D was chosen as the PSD to be used in the MDMS.

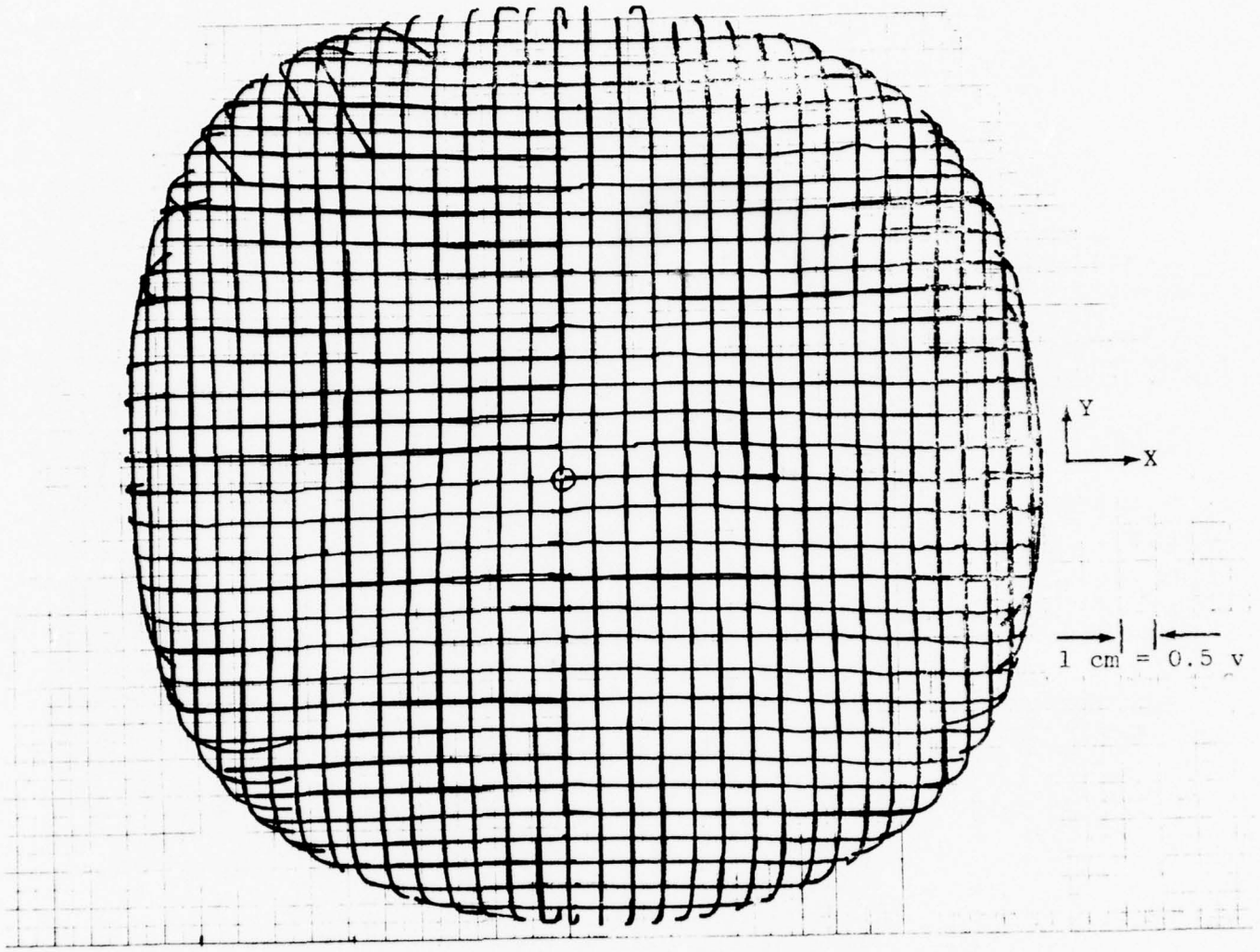

Figure 10. UDT SC/10D PSD Linearity Scan; 15V Bias Grid Interval: 1 Min. of Arc

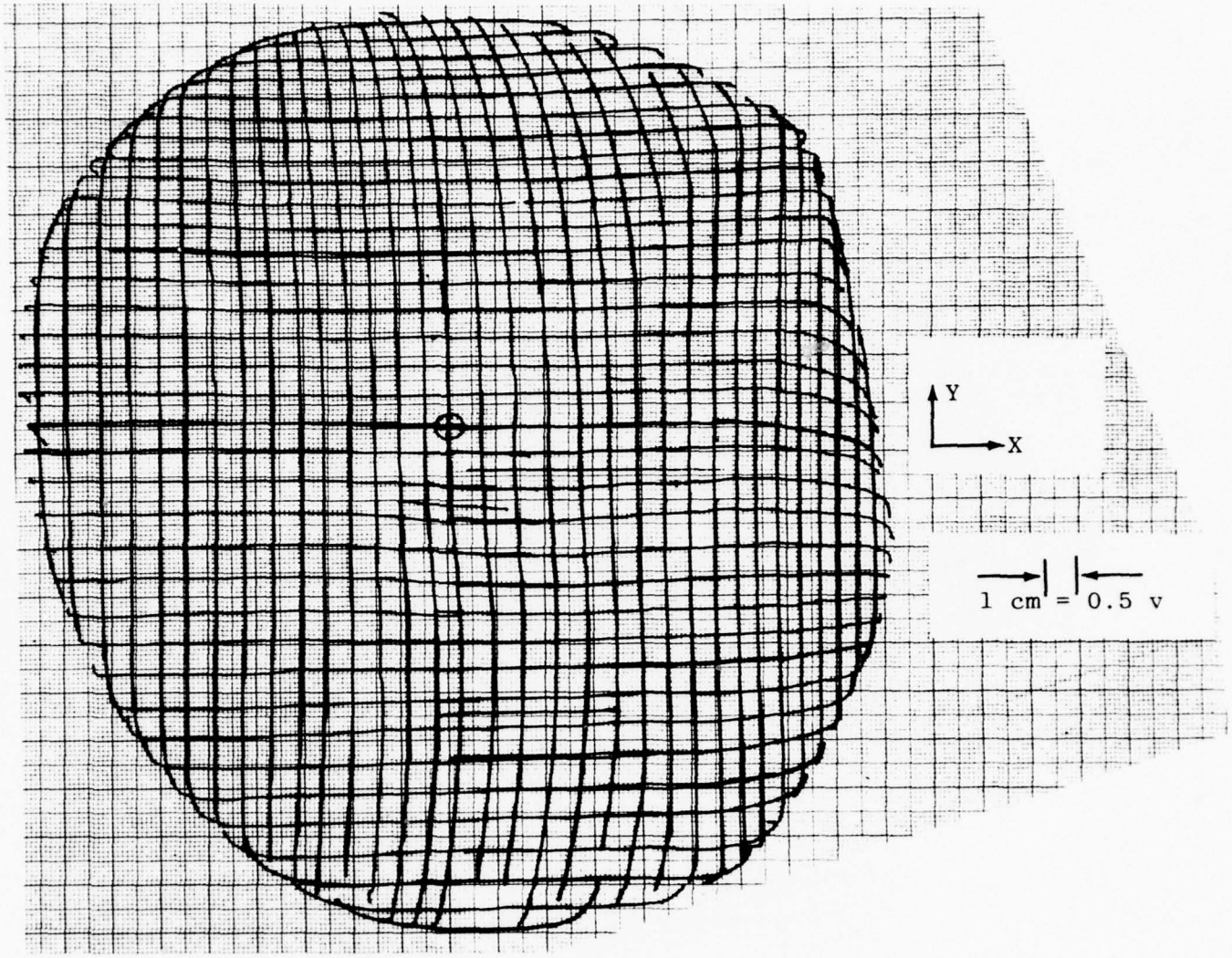

Figure 11. UDT SC/10D PSD Linearity Scan; 0V Bias Grid Interval: 1 Min. of Arc

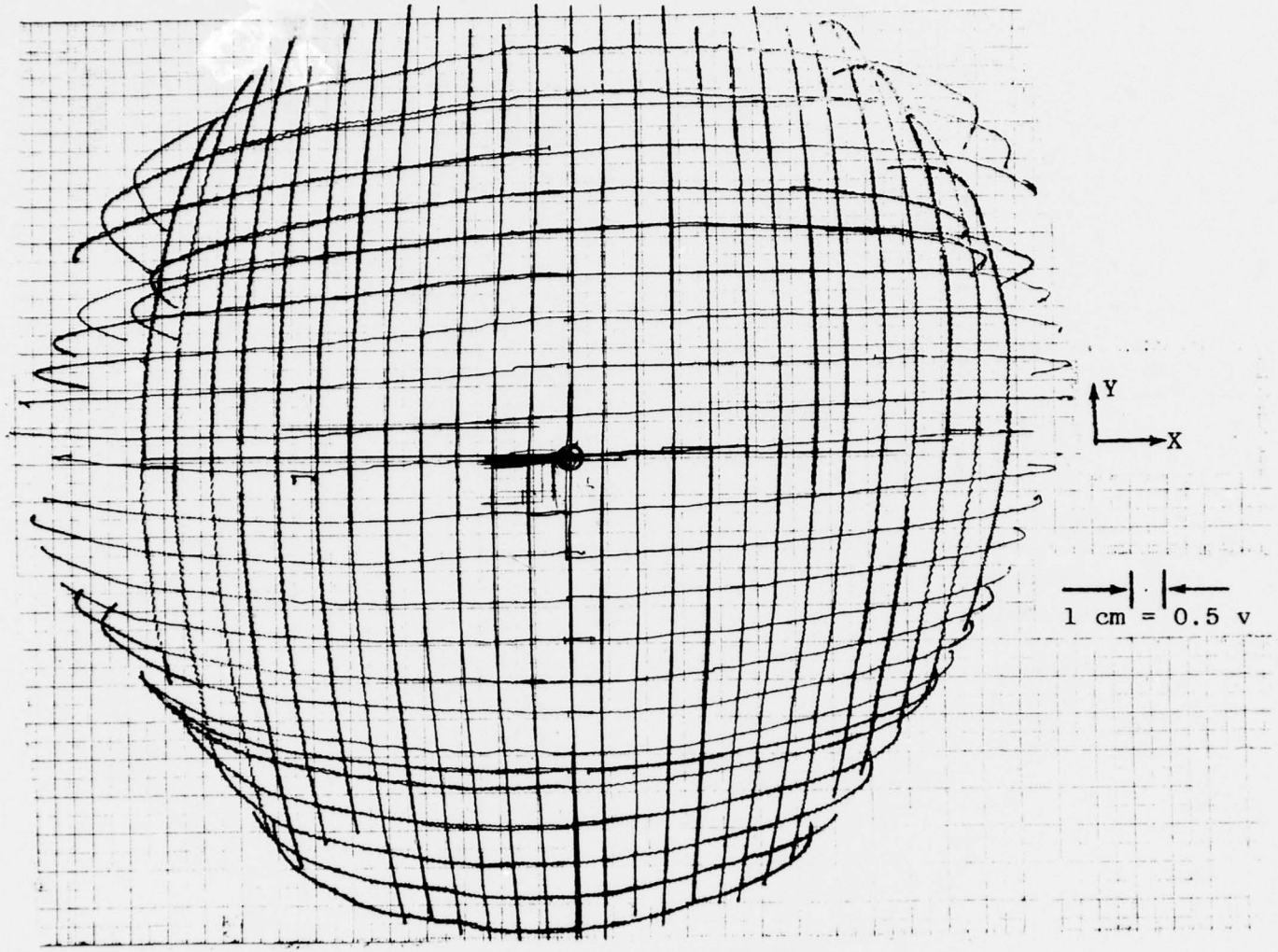

Figure 12. Quantrad PS-200-1 PSD Linearity Scan; 15V Bias Grid Interval: 1 Min. of Arc

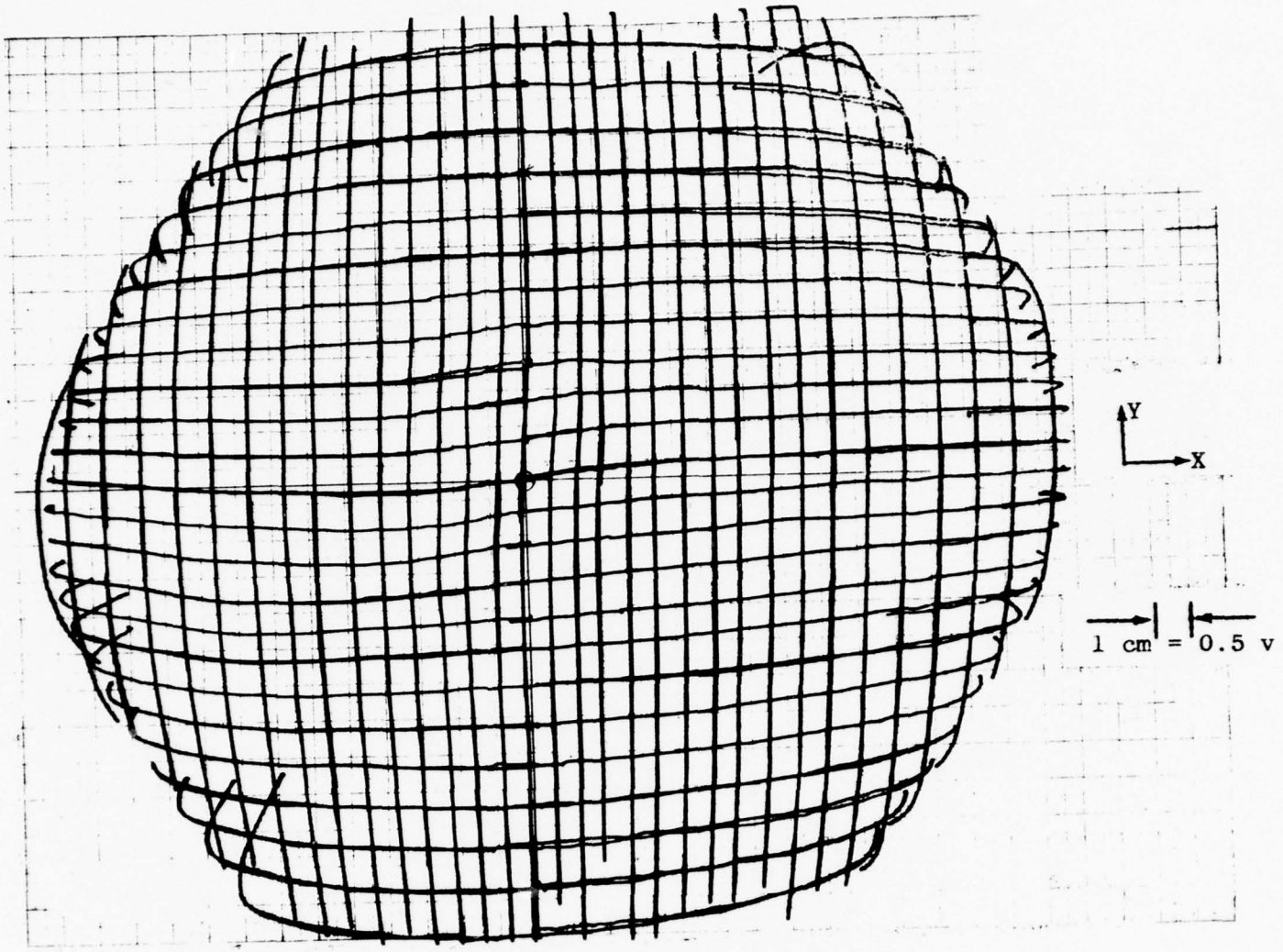

Figure 13. Quantrad PS-200-1 PSD Linearity Scan; 0V Bias Grid Interval: 1 Min. of Arc

A quantitative analysis of the linearity of the UDT SC/10D may be made by the following procedure. Figure 14 is a plot of the output voltage of the position sensitive computer against the muzzle mirror tilt angle, Θ_T, as measured by the autocollimator. The plotted points represent scans along both the X-axis (+) and Y-axis (⊙). This curve is assumed to represent the transfer function of the MDMS system, and will be used to compare the angular deflection at non-axial points as measured by the MDMS, with the same points measured by the autocollimator.

The transfer function of Figure 14 is well represented by the following expression:

$$V = 7.85 \sin (5.5 \times 10^{-2} \Theta_T) \qquad (21)$$

where V = voltage output from the PSD computer, and Θ_T = angular deflection of the muzzle in minutes of arc. The argument of the sine function is in radians. This function applies to both the X- and Y-axis, as indicated in Figure 14.

Using the transfer function of Eq. (21), the values of muzzle tilt angles, Θ_{TCX}, Θ_{TCY} and $\Theta_{TC} = (\Theta_{TCX}^2 + \Theta_{TCY}^2)^{\frac{1}{2}}$ can be computed; these are the angles as determined by the PSD output. Θ_{TC} can then be compared with the tilt angle as measured by the autocollimator, Θ_{TM}, where $\Theta_{TM} = (\Theta_{TMX}^2 + \Theta_{TMY}^2)^{\frac{1}{2}}$, and Θ_{TMX} and Θ_{TMY} are the angles along the X- and Y-axes measured with the autocollimator. Table 5 presents this comparison for angular displacements along the X- and Y-axes. Table 6 gives the comparison of the computed and measured values for non-axial mirror tilt occurring along the diagonals of Figure 10.

An examination of the data in the tables shows that the angles as measured on the breadboard with the PSD computer agree closely with those measured with the autocollimator. In all cases, the difference between the two values is well under 0.1 mrad. Therefore, the conclusion is that the accuracy of the mirror tilt measurement as made by the breadboard MDMS is better than 0.1 mrad.

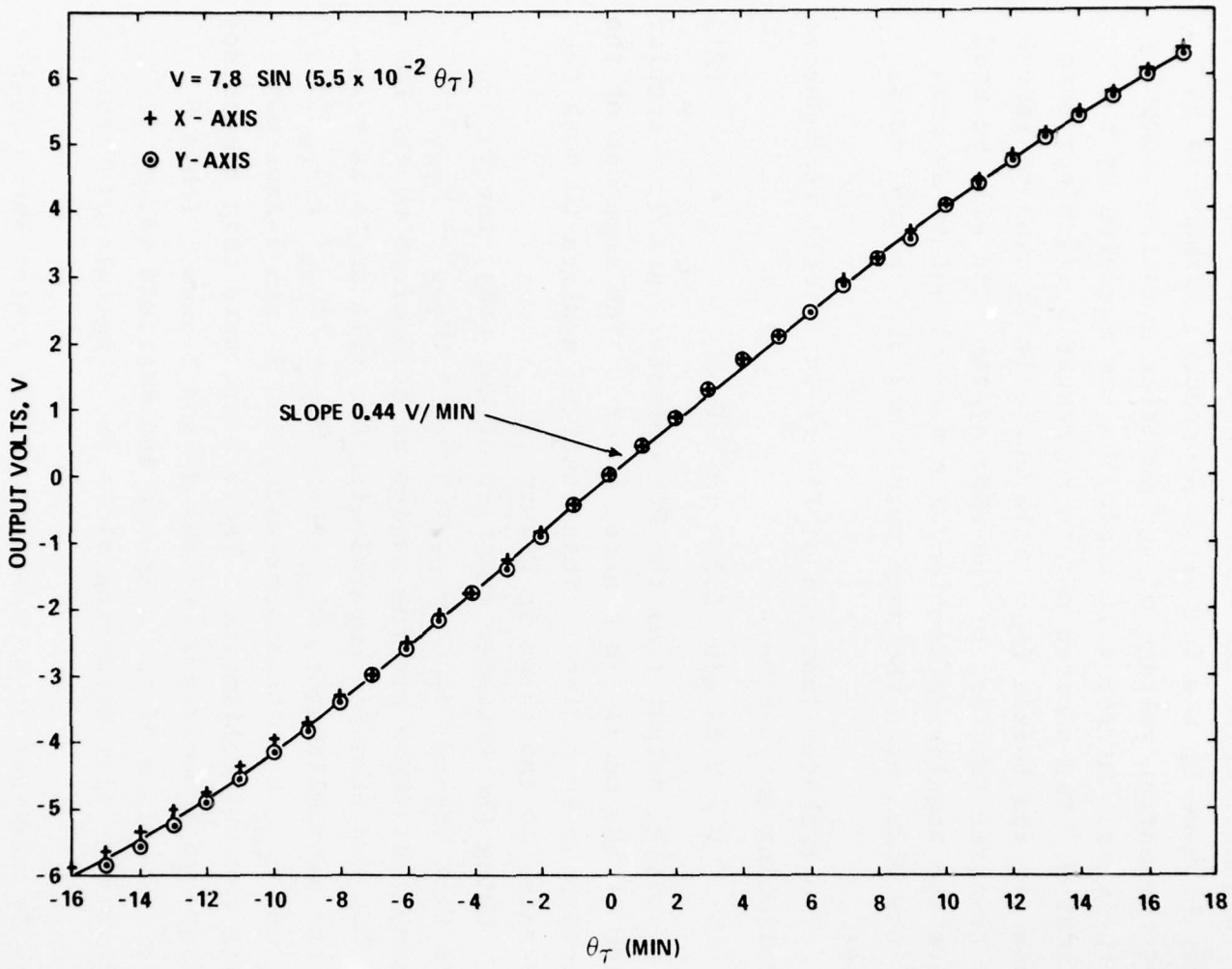

Figure 14. Transfer Function of the MDMS Breadboard

TABLE 5

Comparison of Measured and Computed Muzzle Mirror Tilt Angles Along the X- and Y-Axes

Θ_{TX}, Θ_{TY}, Θ_{TM} Measured by Autocollimator

Θ_{TC} Computed by MDMS Breadboard

$\Theta_{TY} = 0, \Theta_{TX}$ (Min)	POSITIVE X-AXIS								
	1	2	4	6	8	10	12	14	16
Θ_{TM} (mrad)	0.29	0.58	1.16	1.74	2.32	2.90	3.48	4.06	4.64
Θ_{TC} (mrad)	0.30	0.59	1.19	1.74	2.25	2.86	3.47	4.05	4.69

$\Theta_{TY} = 0, -\Theta_{TX}$ (Min)	NEGATIVE X-AXIS								
	1	2	4	6	8	10	12	14	16
Θ_{TM} (mrad)	0.29	0.58	1.16	1.74	2.32	2.90	3.48	4.06	4.64
Θ_{TC} (mrad)	0.30	0.57	1.15	1.71	2.29	2.84	3.41	3.95	4.48

$\Theta_{TY} = 0, \Theta_{TY}$ (Min)	POSITIVE Y-AXIS								
	1	2	4	6	8	10	12	14	16
Θ_{TM} (mrad)	0.29	0.58	1.16	1.74	2.32	2.90	3.48	4.06	4.64
Θ_{TC} (mrad)	0.30	0.57	1.12	1.67	2.24	2.84	3.41	4.00	4.59

$\Theta_{TX} = 0, -\Theta_{TY}$ (Min)	NEGATIVE Y-AXIS								
	1	2	4	6	8	10	12	14	16
Θ_{TM} (mrad)	0.29	0.58	1.16	1.74	2.32	2.90	3.48	4.06	4.64
Θ_{TC} (mrad)	0.30	0.61	1.19	1.80	2.36	2.94	3.55	4.16	-

TABLE 6

Comparison of Measured and Computed Muzzle Mirror Tilt Angles Along the Diagonals of Figure 10.

Θ_{TX}, Θ_{TY}, Θ_{TM} Measured by Autocollimator

Θ_{TC} Computed by MDMS Breadboard

$\Theta_{TX} = \Theta_{TY}$ (Min)	1st QUADRANT						
	1	2	4	6	8	10	12
Θ_{TM} (mrad)	0.41	0.82	1.64	2.46	3.28	4.10	4.92
Θ_{TC} (mrad)	0.43	0.82	1.63	2.42	3.24	4.03	4.86

$-\Theta_{TX} = -\Theta_{TY}$ (Min)	3rd QUADRANT						
	1	2	4	6	8	10	12
Θ_{TM} (mrad)	0.41	0.82	1.64	2.46	3.28	4.10	4.92
Θ_{TC} (mrad)	0.43	0.83	1.65	2.48	3.29	4.09	4.84

$\lvert-\Theta_{TX}\rvert = \Theta_{TY}$ (Min)	2nd QUADRANT						
	1	2	4	6	8	10	12
Θ_{TM} (mrad)	0.41	0.82	1.64	2.46	3.28	4.10	4.94
Θ_{TC} (mrad)	0.43	0.81	1.60	2.39	3.21	4.02	4.84

$\Theta_{TX} = \lvert-\Theta_{TY}\rvert$ (Min)	4th QUADRANT						
	1	2	4	6	8	10	12
Θ_{TM} (mrad)	0.41	0.82	1.64	2.46	3.28	4.10	4.92
Θ_{TC} (mrad)	0.43	0.85	1.68	2.51	3.31	4.10	4.85

The non-linearity of response of the MDMS breadboard as exhibited by Figure 14 is due, in part, to the vignetting of the laser beam by the edge of the NORITAR lens aperture. When part of the beam is vignetted, the centroid of light distribution on the PSD shifts toward the center. Thus, the incremental change of centroid position with mirror angle becomes progressively less as more of the beam is vignetted. This accounts, in part, for the deviation in linearity. For a smaller beam diameter, one would expect the transfer function to be linear over a larger range of muzzle mirror tilt.

The range of spot motion on the PSD was ~±0.135 cm from the electrical center. This is determined by the 135 mm focal length of the NORITAR and the fact that the laser beam swings through ±10 mrad for a ±5 mrad tilt of the muzzle mirror. According to the UDT specification for the SC/10D, which has a 1 cm square sensitive area, the position linearity is typically 0.5% for the central ±0.125 cm. Thus, for most of the ±5 mrad range of "muzzle" mirror tilt, the focussed laser spot moves within this area.

3.5 SUMMARY OF PSD EVALUATION

The linearity of response of the UDT SC/10D and QC PS-200-1 position sensitive detectors were examined. By inspection of the results, the UDT SC/10D was chosen as the superior device. A transfer function for the SC/10D was developed which permits a conversion of the PSD computer output voltage to mirror tilt angle. It was shown that the angles computed with the transfer function agree well with the measured mirror tilt angles, with the error being a few hundreths of a milliradian. The conclusion is: 1) The transfer function, as defined, represents the behavior of the PSD over the area scanned by the focused laser spot; 2) the MDMS breadboard is capable of measuring muzzle mirror tilt angles with an accuracy of at least 0.1 mrad.

SECTION 4
MDMS PROTOTYPE DESIGN

In this section, the design of the MDMS prototype will be described. The emphasis of the discussion will be to describe the system and its major components, with the objective of assisting the reader to understand their functions, operation and alignment. The design of the prototype is based on the analysis prsented in Section 2 and the results of this analysis are used in the system design. A repetition of the material in Section 2 will be kept at a minimum in order to emphasize the functional aspects of the system.

4.1 BLOCK DIAGRAM OF MDMS PROTOTYPE

A block diagram of the MDMS is shown in Figure 15. There are three major subsystems: 1) Transmitter; 2) Receiver; and 3) Control Subsystem.

The transmitter consists of a laser diode source, the radiation from which is collimated by an aspheric lens and projected toward the receiver, via the muzzle mirror. Temperature control of the laser diode is provided by thermoelectric elements mounted in the transmitter housing. Adjustments are provided for collimation and alignment of the laser diode axis with the optical axis of the projection lens.

The Receiver sub-system is composed of the NORITAR f/1.4, 135 mm lens with the PSD in its focal plane. It also contains the preamplifiers for the PSD outputs which buffer these signals for transmission to the Position Computer located off the gun in the Control Box. Adjustments are provided for positioning the electrical center of the PSD on the optical axis of the NORITAR and for aligning its axes in the X-Z and Y-Z planes.

The control sub-system contains the Position Computer, all power supplies and control elements (such as switches potentiometers and indicator lights, etc.) for remote control of the MDMS.

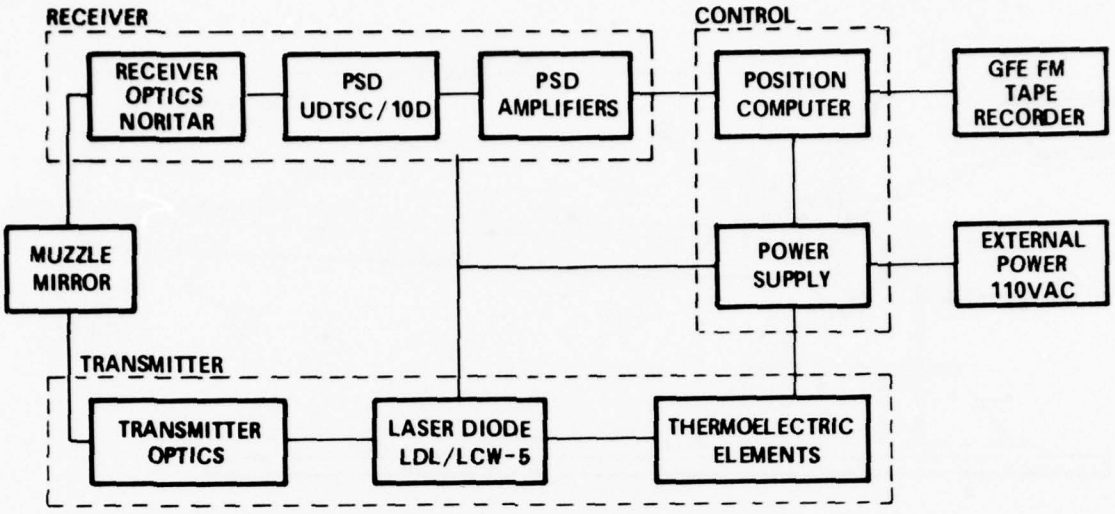

Figure 15. Block Diagram of Muzzle Deflection Measurement System

4.2 GUN-MOUNTED CONFIGURATION OF MDMS

Figure 16 shows the configuration of the MDMS mounted on the 105 mm gun, MOONSHOT; the major subsystems are identified by numbers on the figure. The receiver and transmitter are shown at (2) and (4), respectively, and are mounted on a heavy steel bracket, (1). The bracket, in turn, is bolted to the yoke of the gun, which is assumed to be rigidly attached to the breech mechanism. The muzzle mirror mount, shown at (3), is bolted to an existing sleeve on the muzzle.

As shown, the transmitter is mounted on the receiver, with its axis at an angle of 1.915° with respect to the receiver optical axis. The receiver axis makes the same angle with the tube axis. These angles are constrained by the permissible mounting positions of the several subsystems and were chosen so that the transmitter beam would be incident on the muzzle mirror at its center and the reflected beam would be coaxial with the receiver optical axis after proper alignment. With this arrangement, the separation of the receiver aperture and muzzle

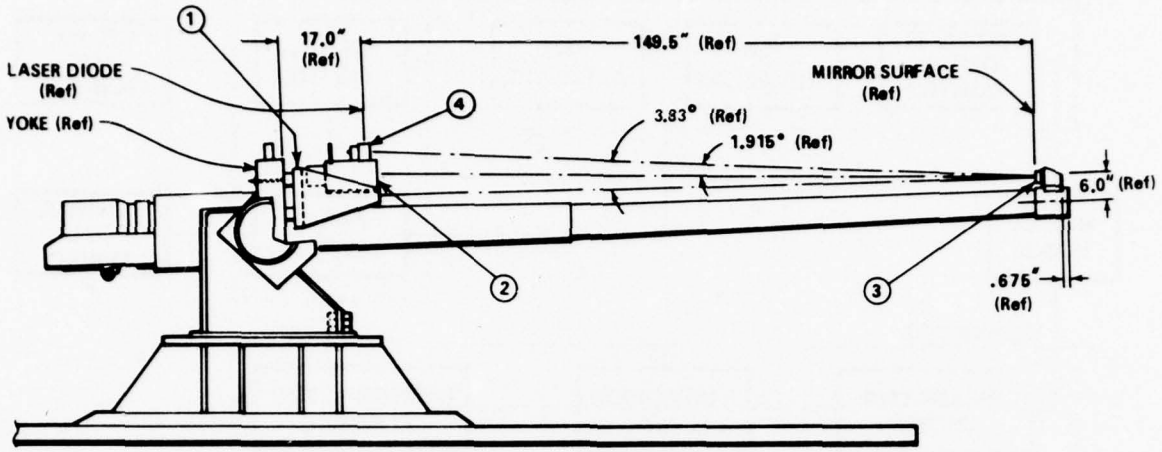

Figure 16. Gun Mounted Configuration of MDMS

mirror was 380 cm. Provision was made at the interface between the receiver (2) and bracket (1) for adjusting the receiver position so that this separation could be set within 0.5 cm.

4.3 TRANSMITTER

4.3.1 Transmitter Mechanical Design

An assembly drawing of the transmitter is shown in Figure 17. This assembly fits into a mounting attached to the top of the receiver housing, which is constructed so as to depress the axis of the transmitter downward (see Figure 16) at an angle such that the beam intercepts the muzzle mirror at its center. The transmitter housing (10) is constructed from a phenolic block to provide thermal isolation between the ambient thermal environment and the laser diode assembly (8).

There are four sub-assemblies in the transmitter which will be described below according to the numbers in Figure 17: a) Projection lens and assembly (9); b) Laser diode and heat sink (8); c) Thermoelectric elements and heat sink (13) and (6)

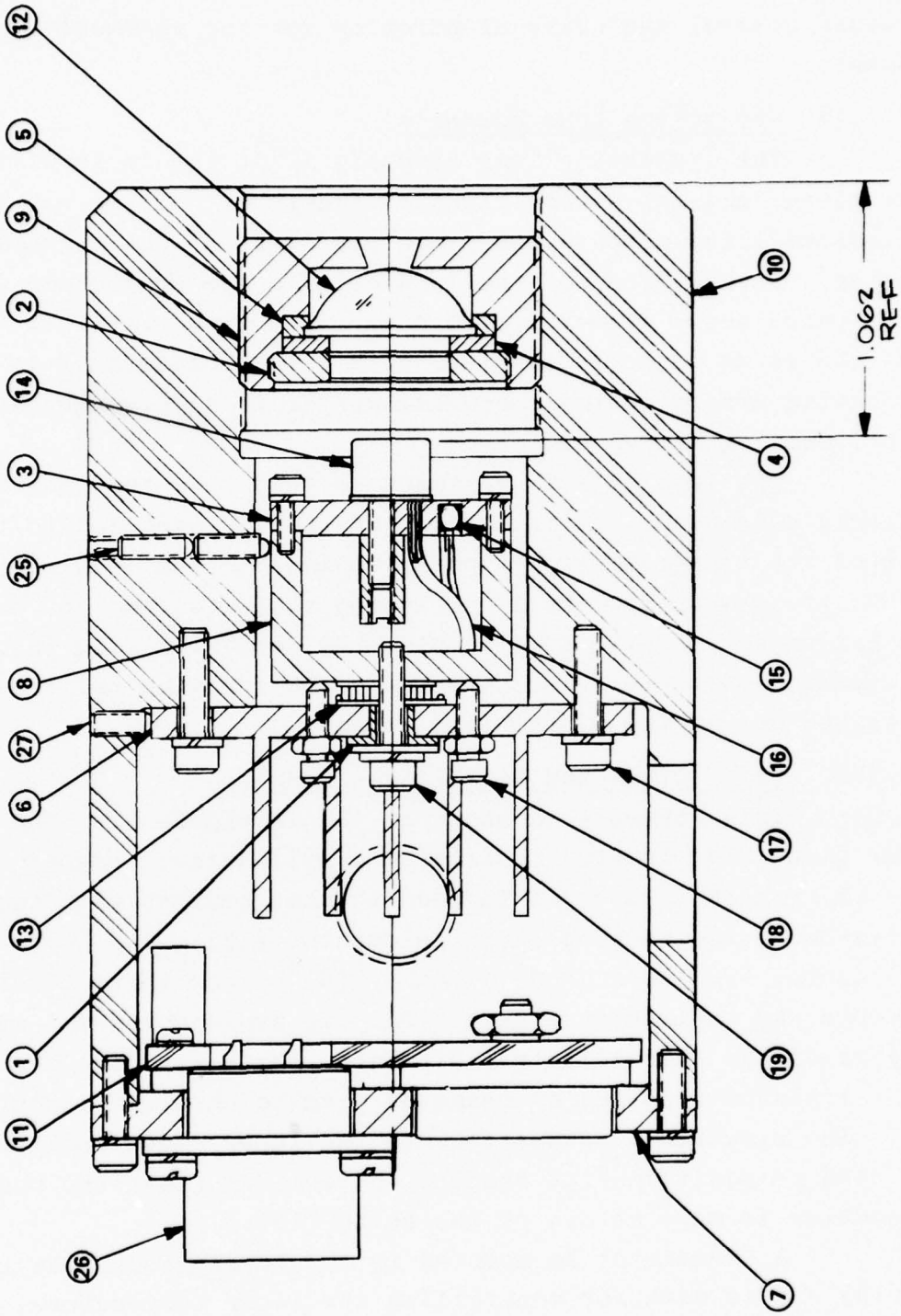

Figure 17. Transmitter Assembly

and d) printed circuit board assembly (11) containing the temperature control and drive electronics for the thermoelectric element.

4.3.1.1 Projection Lens Assembly

The projection lens assembly is at the front of the transmitter housing on the right of Figure 17. It is contained in lens cell (9) which screws into the front of the transmitter housing. At the front of the lens cell is the projection aperture, which has a diameter of 0.4 cm. The lens itself is at (12) and is an aspheric singlet, with a focal length of 1.2 cm, and having zero spherical aberration. It is supplied by Melles Griot, Catalog Number 01LAG111.

The lens cell is designed so that when the lens is properly assembled, its axis is automatically parallel to the axis of the transmitter. In order to isolate the lens from shock, it is supported by two mylatron rings (4) and (5), and the entire assembly is held in place by retaining ring (2). Collimation adjustment is accomplished by screwing the lens cell in to and out of the transmitter housing.

4.3.1.2 Laser Diode and Heat Sink Assembly

This assembly is shown at (8) in Figure 17. The laser diode (14) is stud mounted to a cylindrical, copper heat sink (3) and (8), which is in good thermal contact with two series-connected thermoelectric elements, (13). Two bolts at (19) fasten the laser diode assembly (8) to the thermoelectric elements and their heat sink at (6). To avoid a thermal short-circuit of the thermoelectric elements, the bolts (19) are thermally isolated from (6) by means of plastic shoulder washers at (1). The electrical connections to the laser diode require that the stud be positive with respect to terminal (16); the positive connection is made at one of the bolts (19).

A thermister is mounted in the laser diode heat sink at (15) and is used for controlling the laser temperature. All leads from the thermister and negative terminal of the laser are brought through a hole (not shown) at the bottom of the laser

diode assembly. These leads, plus those to the thermoelectric elements pass through another hole (not shown) in the heat sink (6) and are connected to terminals on the printed circuit board at (11).

Four bolts at (18) provide mechanical support for the laser diode assembly (8). Once the assembly (8) has been tightened against the thermoelectric elements according to the manufacturer's specifications, bolts (18) are adjusted to bear firmly against assembly (8). Their function is to protect the thermoelectric elements from excessive pressure due to longitudinal shock when the gun is fired. In order to prevent thermal short circuiting of the thermoelectric elements, these bolts bear against phenolic pads (not shown) cemented to (8).

Once the laser diode assembly has been aligned to place its radiating axis on the projection lens axis, the set screws (25) are adjusted to bear on the assembly (8). The set screws are spaced at 120° around the periphery of the transmitter assembly and function to stabilize the assembly (8) against vibration.

4.3.1.3 Thermoelectric Elements and Heat Sink

The thermoelectric elements (13) are sandwiched between the laser diode assembly (8) and the heat sink (6). They are manufactured by MELCOR and designated FRIGICHIP FC 0.7-32-05. Two FRIGICHIPS connected in series were used in order to handle the heat pumping requirements.

Care must be exercised in mounting the FRIGICHIPS, since they are relatively fragile ceramic elements. The manufacturers mounting instructions must be followed closely to prevent exerting excess pressure.

The heat sink for the thermoelectric elements is at (6) and is constructed of copper with several fins to radiate the heat generated by the laser and FRIGICHIPS. It is mounted to the transmitter housing by means of three bolts at (17). The laser diode assembly (8) and the heat sink (6) form a mechanically rigid assembly, and alignment of the diode radiating axis

to the optical axis requires that the entire structure be moved in the plane perpendicular to the optical axis. This is accomplished by means of three set screws at (27), which are spaced 120° apart around the periphery of the transmitter. The clearance holes for bolts (17) are oversized and allow adequate motion for (6) during alignment. Alignment procedure will be described in Section 4.3.3.

4.3.1.4 Printed Circuit Board

The electronic components required to control the laser diode temperature and drive the FRIGICHIPS are contained on the printed circuit (PC) board at (11). This also contains the pin connections for the laser diode and thermister (15). A power amplifier for supplying current to the FRIGICHIPS is also mounted on the PC board which requires a heat sink for power dissipation. The aluminum back cover of the transmitter at (7) functions as this heat sink. All external connections to the PC board are made through the connector (26).

4.3.2 Transmitter Electrical Design

4.3.2.1 Laser Diode Thermal Control

The schematic diagram of Figure 18 gives the laser diode thermal control circuitry which is contained in the PC board mounted at the rear of the transmitter. One function of the circuit is to supply current to the FRIGICHIP thermoelectric elements in the proper direction to cause heating or cooling, as required, of the laser diode assembly. A second function is to protect the laser diode by turning it off when its temperature falls outside the range 27°C ±1°C. This is particularly important in the initial start-up, when the diode temperature is likely not to be within this range.

The diode temperature is sensed by thermister R3. This actually consists of two temperature sensitive resistors: one resistor senses the temperature for control purposes and the second is used to control the temperature at which the laser is turned on. This latter function will be described in Section 4.3.2.2, below.

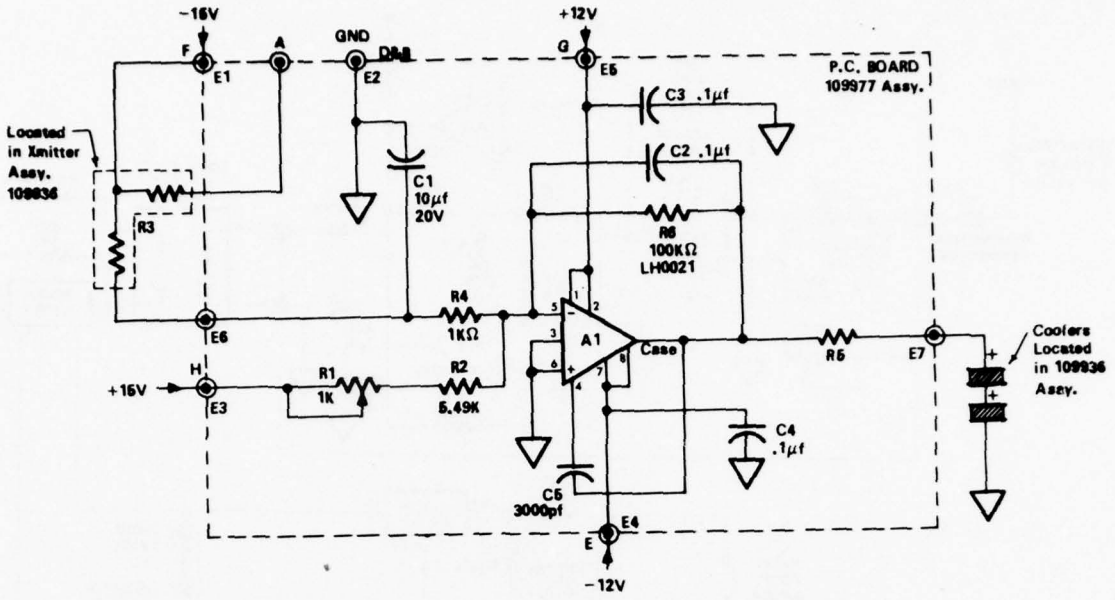

Figure 18. Assembly Transmitter Board

The current through the thermoelectric coolers is controlled by A1 in Figure 18. Current through thermister R3 is substracted from a fixed current supplied by R1 and R2. This fixed current is adjustable by means of R1 and represents a pre-selected temperature. When this temperature is reached by R3, the two currents are equal and the output of A1 drops to zero. The closed loop gain of A1 determines how close the actual temperature will be to the pre-set temperature when the output of A1 goes to zero under worst case conditions. This circuit provides full output with a temperature difference of 1°C, thus providing temperature control of the laser over a range of ±1°C.

4.3.2.2 Laser Diode Drive

The schematic for the laser diode drive circuitry is shown in Figure 19, and is composed of two separate circuits. One circuit determines if the laser is at the pre-selected temperature and the other controls the current to the laser.

The temperature sensing circuit is shown within the dotted lines at the left of the figure. Operation of the LF 155 (A23) amplifier circuit is quite similar to that of the

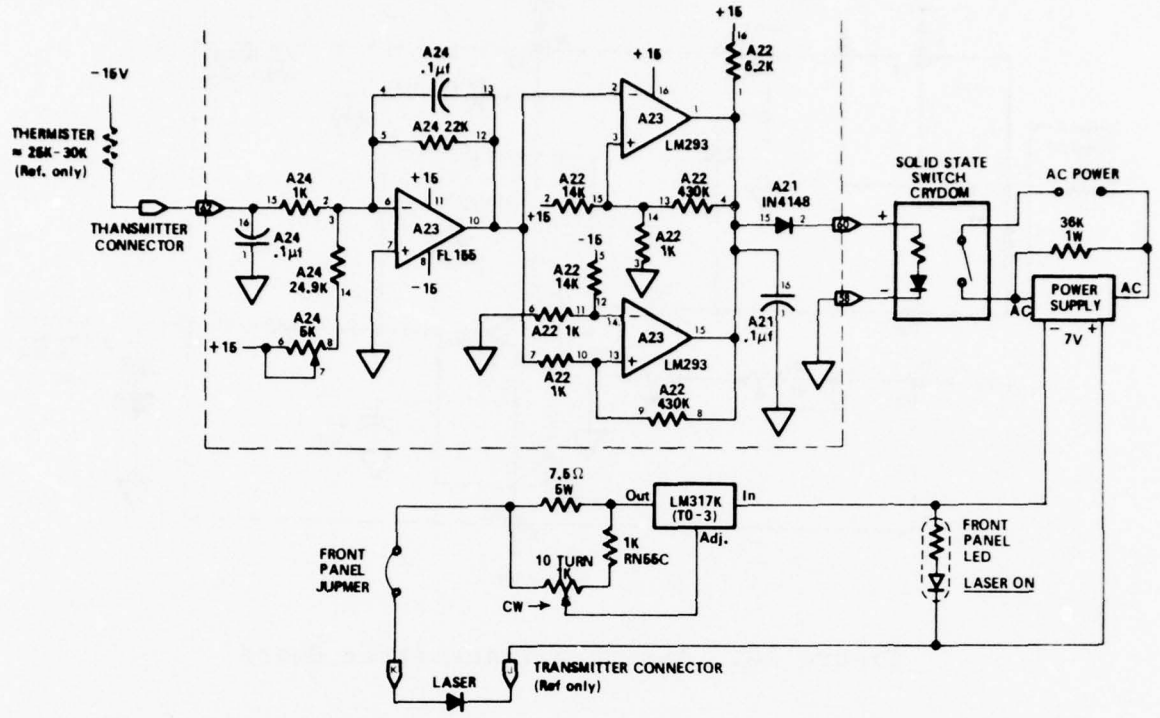

Figure 19. Position Computer Laser Power Circuit

laser thermal control circuit. The temperature sensing thermister is housed in the same head with the thermal control thermister and has one lead in common with it. When the thermal control circuit has brought the laser diode to the pre-selected temperature of 27°C, as indicated by zero output from power amplifier (A1 in Figure 18), the 5K potentiometer in A24 is adjusted to make the output of the LF 155 (A23) zero. This output is fed to the two comparators in the lower half of A23, which comprise a "window" circuit. As long as the input stays within the specified window (corresponding to 27°C ±1°C), the output will be high and the laser power circuit will be turned on. If the input to the window circuit strays out of the prescribed limits, either above or below, the output will go negative and turn off the laser supply. The gain of the amplifier and the window limits have been set to allow a maximum temperature variation of ±1°C about 27°C within which the laser will be turned on.

The current from the temperature sensing circuit (within the dotted lines) flows through the diode A21 to the CRYDOM solid state switch and turns the switch on, causing AC power to be applied to the power supply (7EB45). Once the supply is on, the control circuit for the laser is powered up and the front panel light on the Control Box lights up.

The control circuit for the laser consists of an LM 317 K voltage regulator connected as a constant current regulator. The circuit senses the current through the 7.5Ω resistor and maintains the voltage drop constant. Current through the laser may be preset via the ten turn potentiometer, and can be monitored at the front panel of the Control Box by replacing the jumper with a current meter. This permits the power output from the laser to be pre-set. The current may be varied from 170 ma to 330 ma, which is a sufficient range to cover the current demands of LCW-5 laser diodes.

4.3.3 Transmitter Alignment

Alignment of the transmitter requires three procedures: 1) Co-aligning the laser radiating axis with the axis of the projection lens; 2) Beam collimation; and 3) Aligning the beam to intercept the muzzle mirror at its center. Steps 2 and 3 usually require some iteration. The principal objective of these procedures is to achieve maximum beam power, minimum beam divergence and symmetrical distribution of power in the beam.

4.3.3.1 Laser Radiation Axis

The radiation axis of the laser is not usually co-linear with the mechanical axis of symmetry of the TO-5 package in which it is mounted. Deviations of as much as 7 degrees have been observed. The radiation pattern in the plane perpendicular to the junction is broad and typically ±50 degrees (10% points). In the plane parallel to the junction, the pattern is narrow and typically ±5 degrees at the 10% points. Since the radiation axis can differ by more than 5 degrees from the mechanical axis, it is important to align the radiation axis with the optical axis of the projection lens.

To accomplish this alignment, the direction of peak intensity relative to the mechanical axis of the TO-5 mount must be determined. This is best done on an optical bench with the laser fixed in a mount with a graduated circle. A photodetector with a small aperture is placed at a distance such that the aperture subtends less than a degree at the laser, but close enough so that a convenient photo-signal is developed. The radiation pattern can thus be plotted and the radiation axis established.

In order to align this axis to the optical axis of the lens, the laser must be appropriately cocked when mounted on its heat sink. This was accomplished by fabricating two horseshoe shaped washers with the correct wedge angle. The slot in the horseshoe is large enough to fit around the stud with its long dimension parallel to the line joining the stud and negative electrode. The orientation of the slot is such that its long dimension is parallel to the apex of the wedge angle. One washer is placed between the laser package and heat sink and the other on the opposite side between the heat sink and locking washer. This procedure aligns the laser and lens axes to within a degree. Thermal grease should be applied to all surfaces to ensure good thermal conductivity.

4.3.3.2 Beam Collimation

Collimation of the beam is accomplished by moving the lens cell along the axis of the lens barrel to achieve minimum beam divergence. This is best done by performing a preliminary alignment of the beam so that it reflects from the muzzle mirror back to the plane of the receiver aperture. The beam pattern can be observed on a diffusely reflecting surface in the receiver aperture by use of a suitable infra-red viewing device. By adjusting the lens, the minimum beam diameter can be readily found.

It will be observed that the beam moves around at the receiver aperture as the lens is screwed in and out. This occurs because the laser source is not yet on the axis of the lens.

It is difficult to eliminate this effect entirely, because the mechanical axis of the lens cell is not precisely colinear with the axis of the lens. However, by iterating the collimation and beam alignment procedures (to be described in the next section), this effect can be minimized.

4.3.3.3 Beam Alignment

Beam alignment is accomplished with the three set-screws at (27) in Figure 17. These are placed at 120 degree intervals around the circumference of the transmitter housing and cause the laser to be moved in the plane perpendicular to the transmitter axis. Prior to adjusting these set-screws, the set-screws at (25) must be backed out to free the laser diode assembly. Bolts (17) must also be loosened slightly to allow the heat sink to be moved. By adjusting set-screws (27) in small increments, the laser can be positioned on the lens axis. The adjustment is complete when the beam pattern is most symmetric. When this occurs, the pattern will have a bright center surrounded by two or three rings; it will be slightly elongated in the direction of the x-axis, and will be approximately 1.5 to 2 cm in diameter.

When the transmitter is properly aligned, the beam power should be 0.8 m watt or more. This assumes that the laser has been chosen to radiate at least 1.5 m watt into the f/3 cone of the transmitter. It may also be necessary to adjust the position of the transmitter/receiver assembly slightly in the X-Z plane to have the beam intercept the muzzle mirror at its center. Adjustment in the Y-Z plane can be made, if required, by using shims under the transmitter/receiver or between the bracket and the trunnion of the gun. These latter adjustments should only be necessary when the MDMS is first mounted on the gun.

4.4 RECEIVER DESIGN

An assembly drawing of the receiver/transmitter is shown in Figure 20. The transmitter (1) is shown mounted on top of the receiver in mount (8), which is slotted at the top.

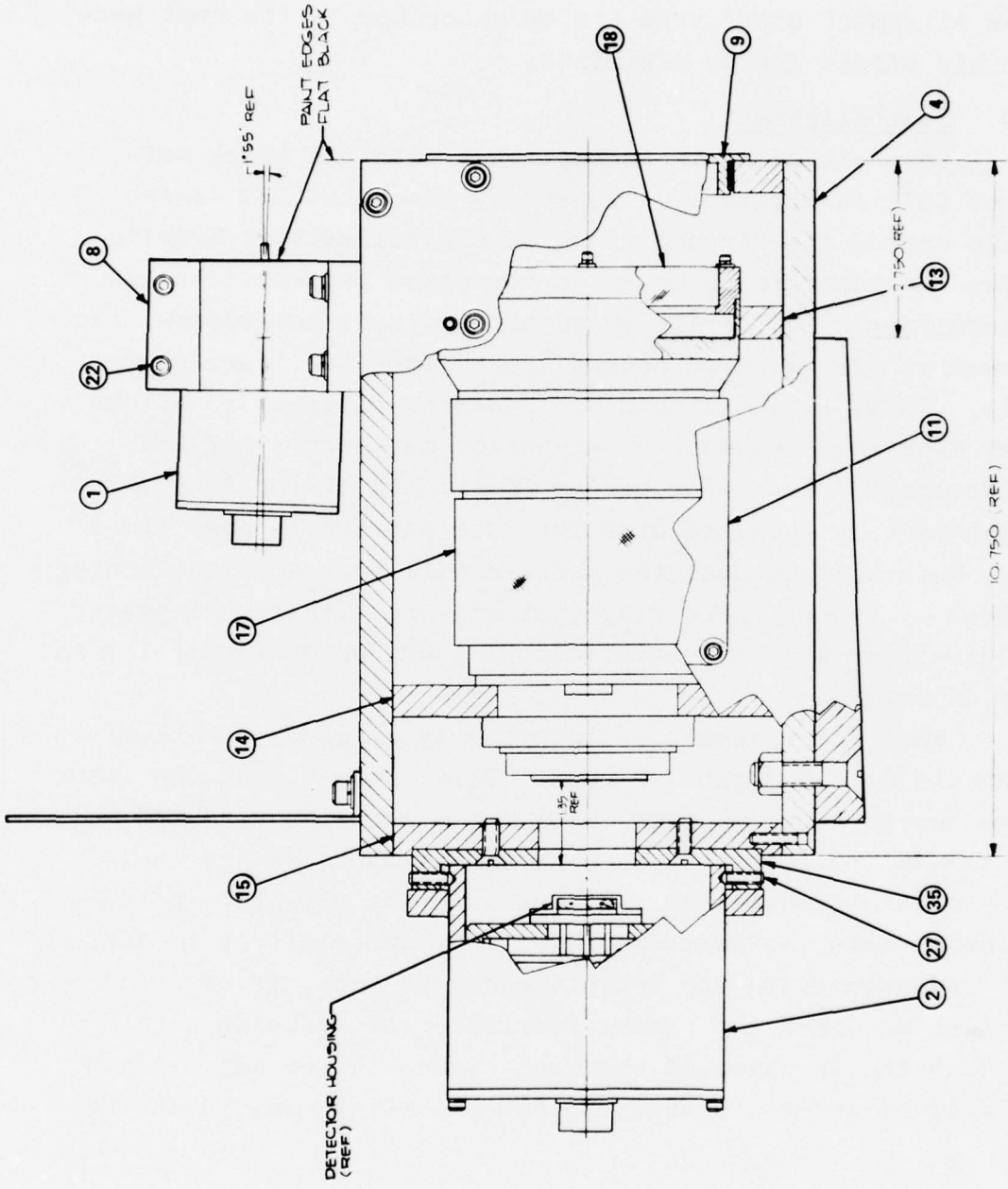

Figure 20. Receiver Assembly

After the transmitter is inserted into the mount, it is clamped tightly by tightening bolts (22).

The main body of the receiver (4) holds the NORITAR lens (17), the optical interference filter (18) and a lens cover at (9). The lens is held by the two members (13) and (14). Member (14) is constructed with a clamp which clamps the front of the lens barrel and fixes the lens axis relative to the receiver housing. Back support (14) stabilizes the lens against longitudinal shock. The focusing and aperture adjustment rings of the lens are set for infinity and f/1.4, respectively, and then taped in place. Access ports (11) are provided on the sides of the housing so that these settings can be checked and readjusted as required.

The detector assembly (2) is mounted at the rear of the receiver. It is held in place by a mounting ring (not numbered) which bolts to plate (35), which, in turn, is rigidly attached to the receiver assembly. The clearance holes in the mounting ring are oversized to allow the entire detector assembly to be moved in the X-Y plane, permitting the detector to be centered on the optical axis. This motion is accomplished by four set-screws at (27), spaced at 90° intervals; two of these allow motion in the Y-directon and the other two permit motion in the X-direction. These set-screws ride in a V-groove cut around the circumference of the detector assembly, allowing the detector to be rotated around the optical axis of the lens, so that the detector X- and Y-axes can be aligned with the X-Y axes defined for the gun. (This alignment is made in the laboratory).

The PSD is mounted, as shown, on a cylindrical mount coaxial with the detector assembly. This can be moved along the axis to place the detector in the focal plane of the NORITAR. Once this position is found (a laboratory procedure), the assembly carrying the detector is locked in place by two bolts (not shown) extending through slots in (2).

Alignment of the receiver consists in placing the electrical center of the PSD on the optical axis of the NORITAR and orienting its X- and Y-axes. The procedure for doing this was described in Section 3.1.2, as part of the discussion concerning the MDMS Breadboard. The performance of the PSD with respect to linearity was found to be sensitive to its focal position, and the optimum position was obtained by trial. This will be discussed in a later section.

The detector assembly also contains a printed circuit board containing the preamplifiers for the PSD. Their function is to convert the PSD currents to voltages at a level which can be transmitted at low impedance to the position computer located off the gun. Figure 21 gives the circuitry for the four preamplifiers and shows the layout of the printed circuit board. The operation of the position sensitive computer was described in Section 3.2, as part of the discussion of MDMS breadboard.

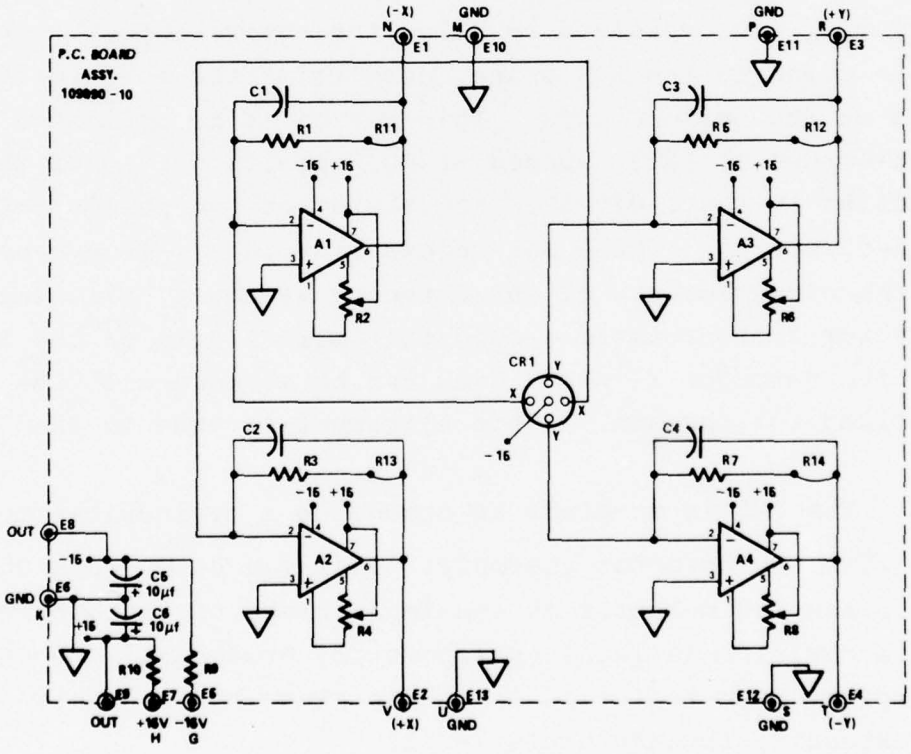

Figure 21. Assembly Detector Board

At the top rear of the receiver assembly is mounted a baffle, as shown in Figure 20. The purpose of the baffle is to block the solar illuminated scene behind the gun, which would otherwise be imaged on the PSD by reflection in the muzzle mirror. The diameter of the baffle is such that it fills the receiver field of view for all angles of muzzle mirror deflection up to ±5 mrad. It is painted black with a matte finish to minimize scattering of solar energy into the receiver aperture.

4.4.1 Optical Filter

The function of the optical filter is to reduce the amount of solar background power incident on the PSD. Figure 22 gives the transmission function of the filter. As can be seen from the curve, it has a transmission of 0.8 or greater for wavelengths lying between 817 nm and 831 nm, with a bandpass of 220 nm at the 50% transmission points. The blocking range of the filter (transmission of 10^{-3} or less) extends to wavelengths below 400 nm and on the long wavelength side to beyond 1000 nm. In order to be consistent with this filter function, the laser diodes were specified to radiate within the wavelength range 817 nm - 831 nm at an operating temperature of 27°C. The diode temperature was controlled to within ±1°C of this value.

4.5 MUZZLE MIRROR

An assembly drawing of the muzzle mirror mount is shown in Figure 23. It is designed to be mounted on the muzzle sleeve of the 105 nm gun, MOONSHOT. A 2 in. diameter by 0.5 in. thick stainless steel mirror (7) is held in retainer (2), which is attached to the mirror bracket (3) by means of three bolts (4). The mirror retainer (2) bears against a ball bearing (6) which is seated in conical holes in the center of the rear surface of the bracket. The diameter of the ball bearing is such that the retainer and bracket are separated, allowing the mirror to be tilted about the center of the ball bearing. The three bolts (4) are 1/4 - 80 and are spaced at 120 degree intervals

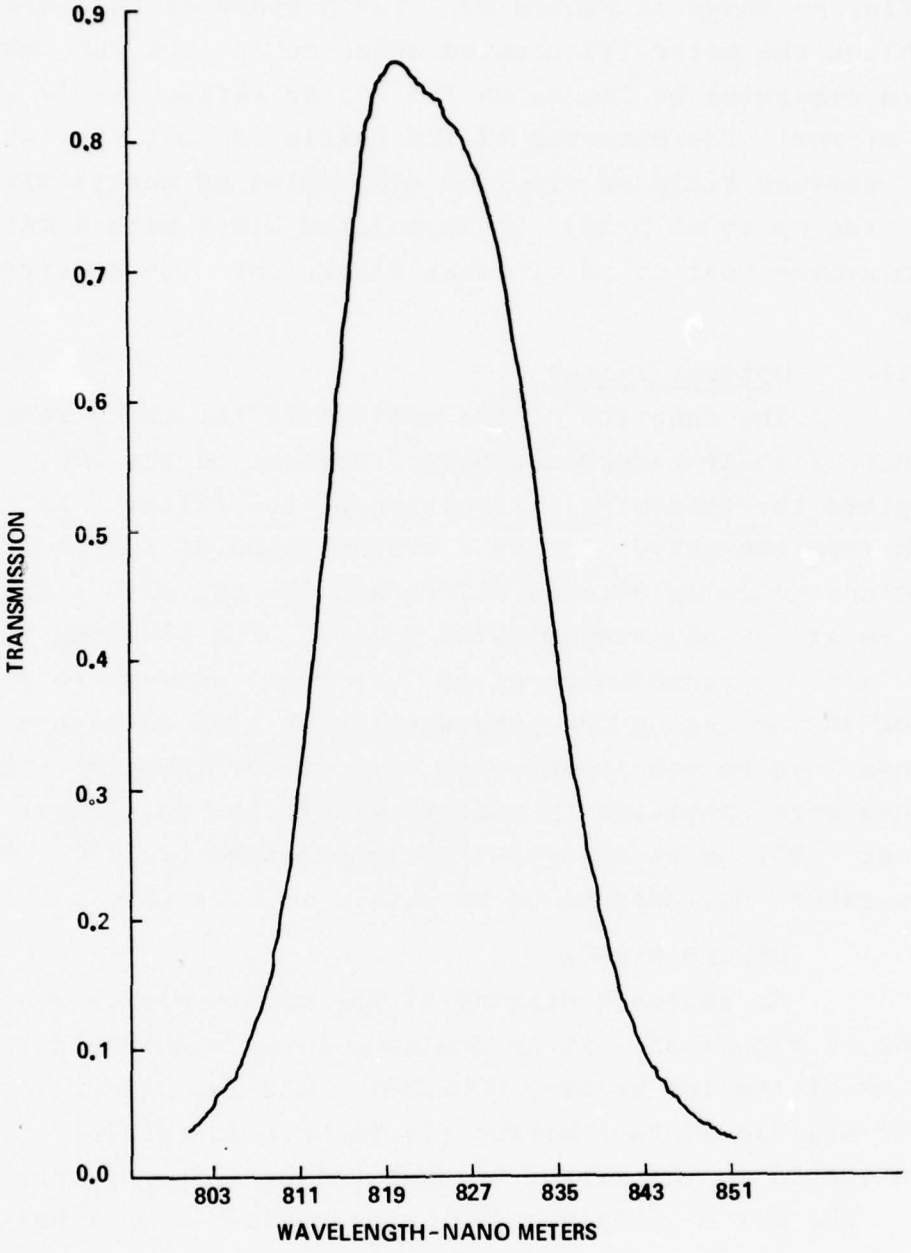

Figure 22. Transmission of Optical Filter

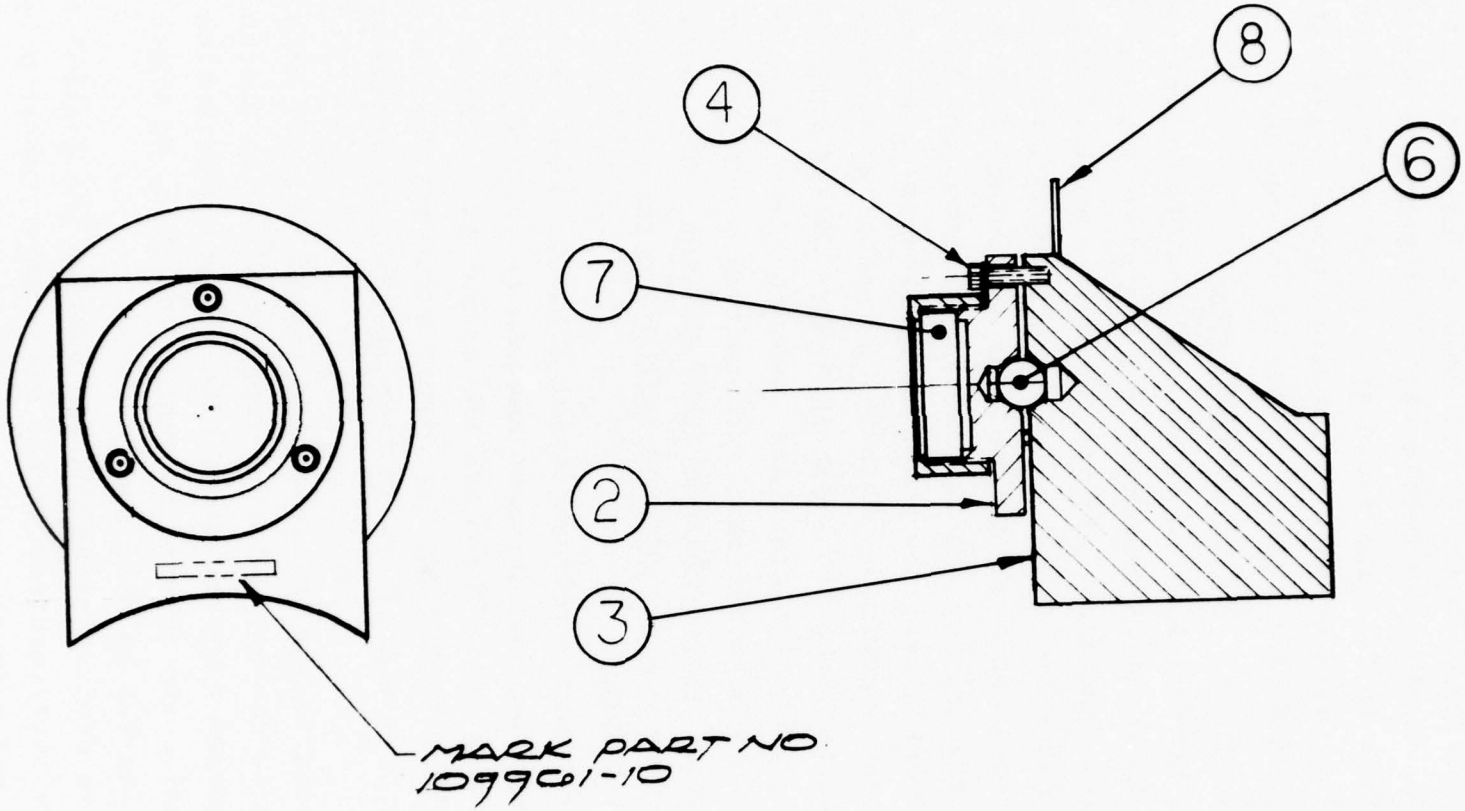

Figure 23. Muzzle Mirror Mount Assembly

about the circumference of the mirror retainer. The fine thread permits accurate positioning of the beam on the center of the receiver axis. A circular baffle (8) is attached to the mirror mount and serves to fill the field of view of the receiver. It is painted black with a matte finish and serves to provide a uniform, low reflecting surface viewed by the receiver.

4.6 CONTROL BOX AND CABLE CONNECTIONS

The Control Box houses most of the MDMS electronics. It contains the position computer, all the power supplies and various control functions. Figure 24 shows the front panel layout which makes the function of the Control Box essentially self explanatory. When the Control Box is connected to the receiver and transmitter via the cable connectors on the upper left of the front panel, the power switch powers up the whole MDMS system when energized. When the preset laser temperature of 27°C is reached, the front panel light, labeled LASER ON, will light up, indicating that the laser is emitting power. Laser current can be monitored by connecting a current meter at the banana jacks labeled LASER CURRENT MONITOR. The current through the laser can be adjusted by the ten-turn potentiometer labeled LASER CURRENT.

The X- and Y-voltage output from the position computer can be monitored by connecting voltmeters to the X-POSITION and Y-POSITION connectors. These are BNC connectors. The X- and Y-POSITION OFFSET potentiometers permit adjustment of the position voltages over a small range corresponding to approximately ±0.3 mrad.

Access to the internal electronics is quite simple, as everything is connected to the front panel which can be unbolted and removed from the case. The control electronics are operational while the chassis is out of the case, so that trouble shooting can be done conveniently.

There are two signal cables between the control box and the transmitter/receiver on the gun. These cables provide all the power and control signals required, as well as bringing

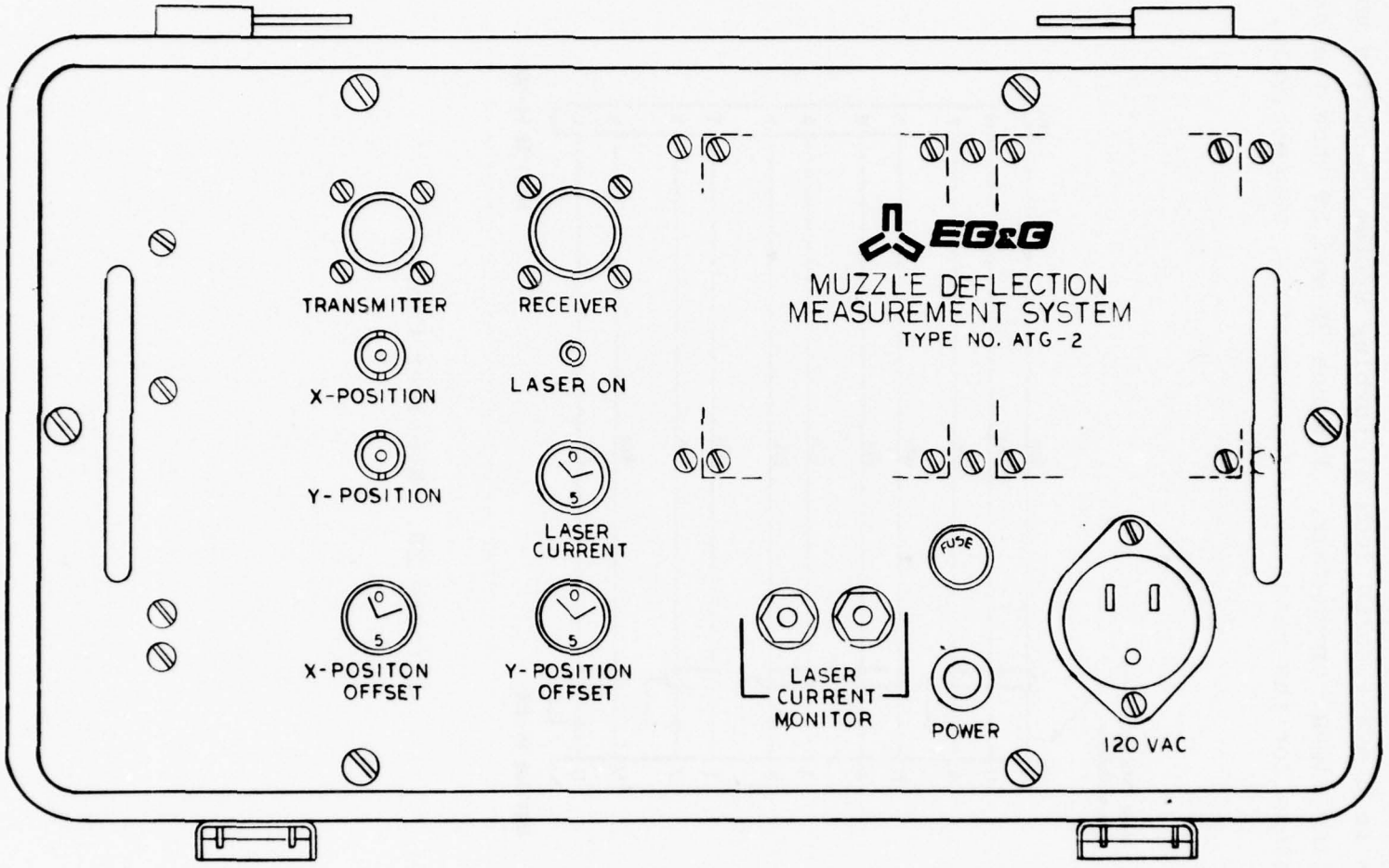

Figure 24. MDMS Front Panel

the position signals back to the computer. They have external shields to prevent noise from disturbing system operation and preventing signal cross-talk. Figures 25 and 26 show the cable connections for the receiver and transmitter, respectively.

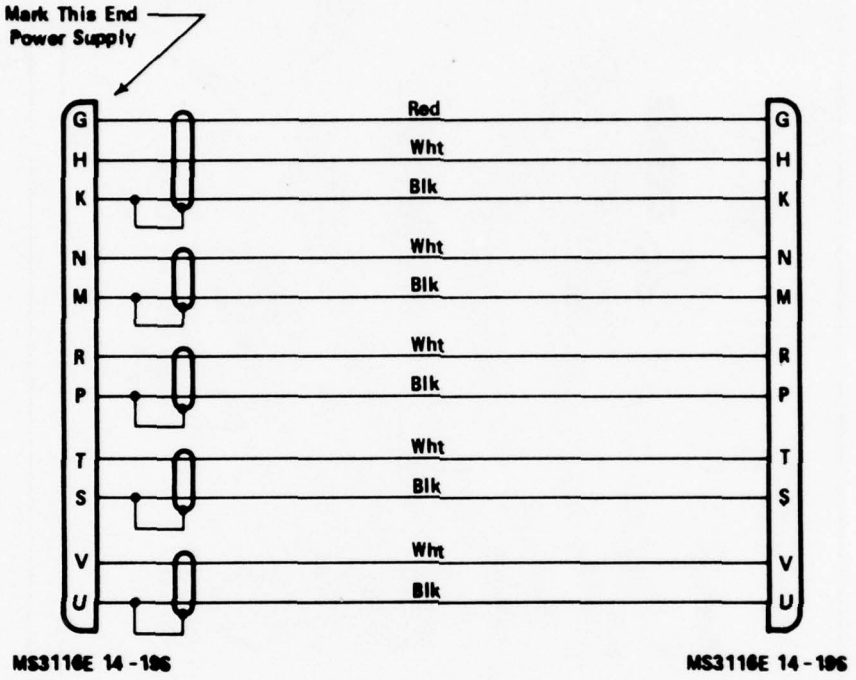

Figure 25. Receiver Cable

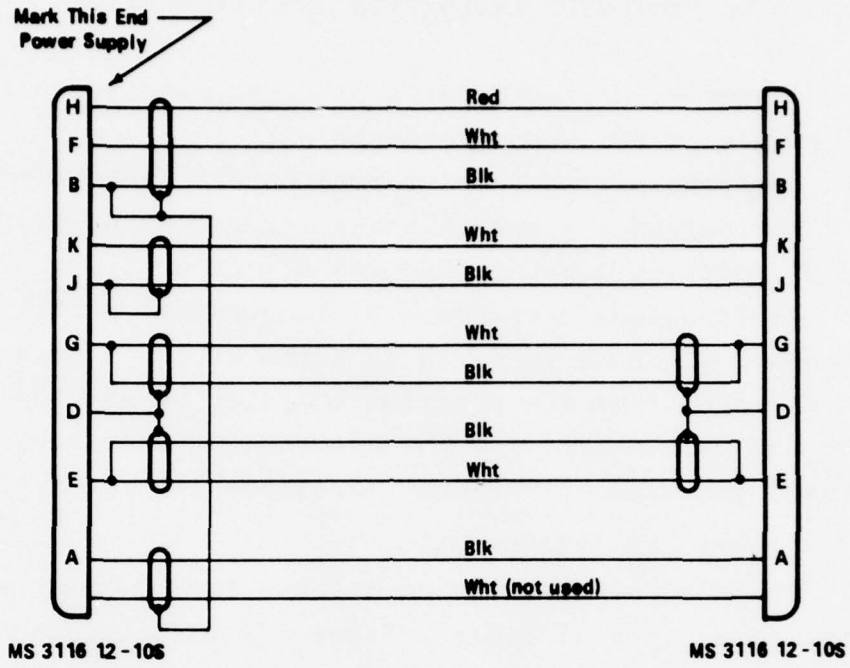

Figure 26. Transmitter Cable

SECTION 5
MDMS PROTOTYPE EVALUATION AND CALIBRATION

A summary of the results of tests made to evaluate the performance of the MDMS prototype will be presented in this Section. The principal tests performed were: 1) Performance stability against variations in transmitter beam power; 2) Optimum focal position for the PSD; 3) Effect of a field stop at the PSD; 4) Frequency response; 5) Temperature stability. A calibration of the MDMS is given in terms of the X- and Y-position voltages from the position computer versus the angular motion of the muzzle mirror. The accuracy of this measurement is discussed in terms of residual non-linearity and system noise.

5.1 LABORATORY ARRANGEMENT

The MDMS was mounted on a three inch I-beam, which was bolted to an optical table. Figure 27 gives a schematic plan view of the laboratory arrangement. The geometrical relationship of the receiver/transmitter to the muzzle mirror was the same as it would be if the system were mounted on the gun. This relationship was shown in Figure 16. The 2 inch diameter, stainless steel muzzle mirror was mounted in a two-axis, National Research Corporation mount at one end of the I-beam at a distance of 380 cm from the receiver aperture.

Measurement of the angular motion of the muzzle mirror was accomplished in the same way as described in Section 3.3, in the discussion of the MDMS breadboard. In the present case, however, the autocollimator beam was reflected twice from the muzzle mirror. This was done primarily for convenience in making the measurements and had the effect of increasing the angular sensitivity of the measurement by a factor of two, because of the double reflection at the muzzle mirror.

During the system calibration, the Control Box was connected to the transmitter/receiver with the 30 foot cables supplied for the field test. Thus, the MDMS calibration was performed with all the components to be used in the field test.

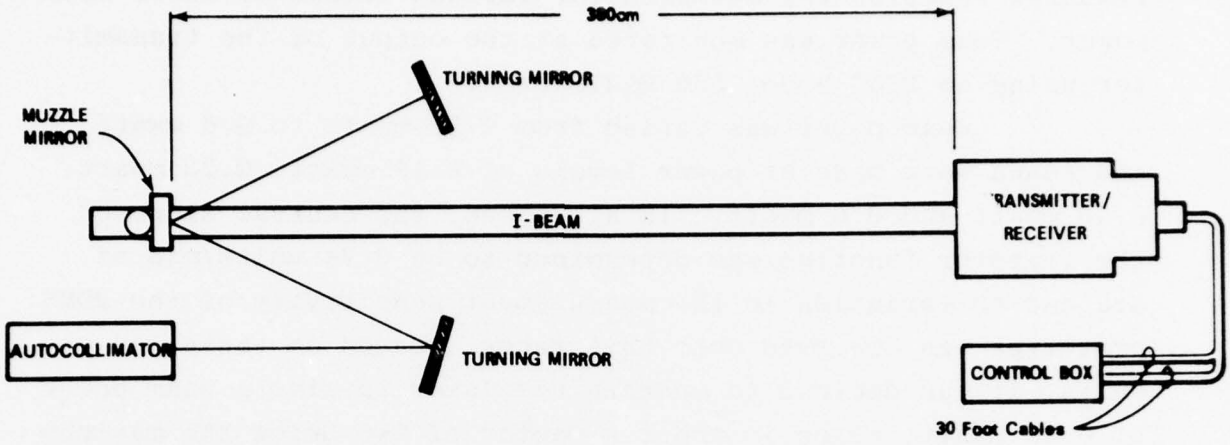

Figure 27. Schematic Arrangement for Evaluation of MDMS Prototype

The rest of the test apparatus (i.e., X-Y recorder, digital voltmeters, etc.) required for the calibration is the same as that used for the breadboard evaluations described in Section 3 (see also Figure (5)).

5.2 SENSITIVITY TO VARIATIONS IN TRANSMITTER POWER

The purpose of this test was to determine the allowable variations in laser power without degradation of measurement accuracy. The PSD was centered on the optical axis of the receiver and placed at a focal position which gave the most linear response. At this point in the evaluation program, the optimum focal position had not been determined. For this test, however, the focal position was near the optimum.

The procedure was to make an X-Y scan as previously described, with the grid lines spaced at one minute of arc intervals. The transfer function was then determined by the

method described in Section 3.4 and the central slope of the transfer function was measured for various levels of laser beam power. Beam power was monitored at the output of the transmitter using an EG&G Model 550 Radiometer.

Beam power was varied from 0.12 mwatt to 0.6 mwatt, and scans were made at power levels of 0.12 mwatt, 0.23 mwatt, 0.46 mwatt and 0.6 mwatt. In all cases, the central slope of the transfer function was determined to be 0.74 volts/min of arc and no variation in the measurement sensitivity of the MDMS prototype was observed over this range. Based on these results, it was decided to operate the laser to give a beam power of 0.46 mwatt, which is about a factor of two below the maximum permissable power rating. This decision was made primarily in the interest of laser lifetime. Thus, a downward variation in beam power by at least a factor of four could be tolerated. Variations of beam power could result from changes in muzzle mirror reflectivity due to surface contamination, muzzle exhaust gases in the beam path, etc.

It should be noted at this point that the MDMS, as delivered to BRL, had a voltage sensitivity in the central part of the transfer function of 0.62 volts/minute in the open circuit mode. The difference between this calibration and that of 0.74 volts/minute obtained above is that the system gain in the two measurements were not the same. When the above measurements were made, the gain of the position computer was such that at mirror deflection angles in excess of ±4 mrad, the output voltage exceeded 10 volts, which is the upper limit for linear operation specified by the manufacturer of the output buffer amplifier. Subsequently, the gain settings were changed to keep the output within the ±10 volts limit. Hence, the lower sensitivity value.

The conclusion from this test is that the MDMS measurement accuracy is not affected by beam power variations between 0.6 mwatts and 0.1 mwatts.

5.3 EFFECT OF FOCAL POSITION

Because the laser diode radiates at 820 nm, the determination of the focal plane position for the NORITAR could not be conveniently made at this wavelength by the usual visual methods. It was found, however, that the linearity of the X-Y scan was a sensitive function of the focal position of the PSD. The technique adopted to find the best focal position was to take several scans at different axial points and locate the optimum position as that providing the most linear scan.

Figures 28, 29, and 30 show three scans taken at back focal distances of 5.38 cm, and 5.84 cm and 5.70 cm respectively. The back focal distance was measured between the front surface

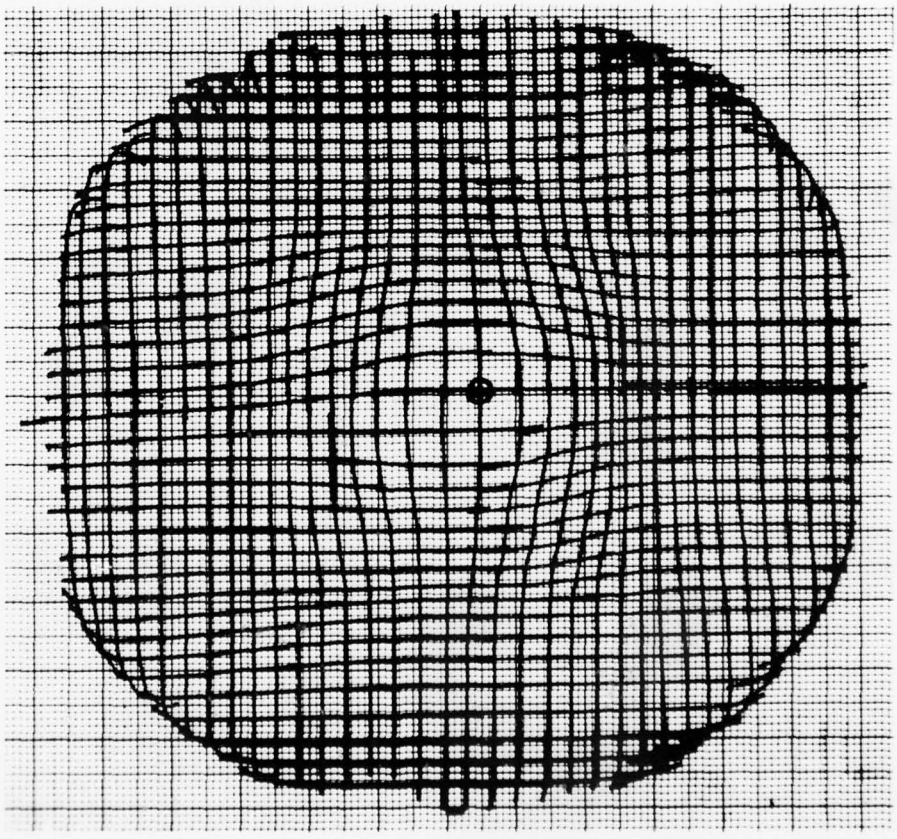

Figure 28. X-Y Scan for MDMS Prototype with PSD at Back Focal Distance of 5.38 cm. Plot Scale 1 V/cm Beam Power 0.43 mw.

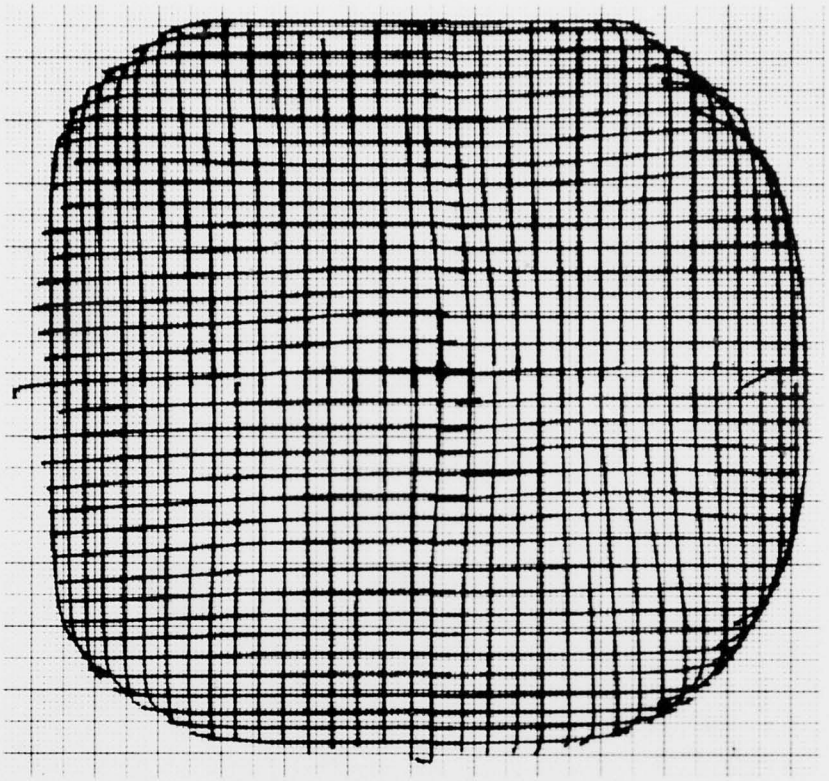

Figure 29. X-Y Scan for MDMS Prototype with PSD at Back Focal Distance of 5.84 cm. Plot Scale 2 V/cm Beam Power 0.43 mw.

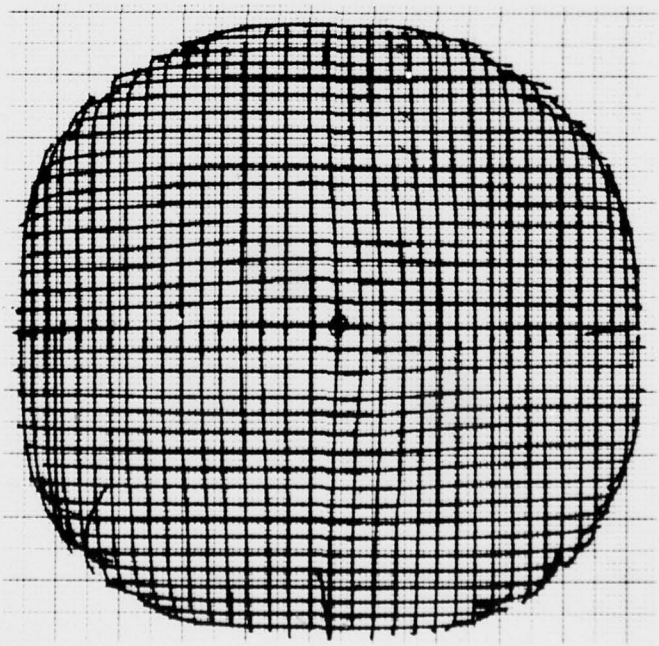

Figure 30. X-Y Scan for MDMS Prototype with PSD at Back Focal Distance of 5.70 cm. Plot Scale 2 V/cm Beam Power 0.43 mw.

of the PSD window and the rear surface of the window at the output end of the NORITAR. All plots were made with a beam power of 0.43 mw. Note the difference in the scale of the plots.

The plot of Figure 28 was taken with a back focal distance of 5.38 cm and a plot scale of 1 volt/cm. Considerable barrel distortion is evident at the center of the grid. Figure 29 was made at a back focal distance of 5.84 cm and with a plotting scale of 2 volt/cm. Here the distortion is greatly reduced, there being only a slight tendency toward pincushion distortion near the periphery. The optimum back focal distance was found at 5.70 cm, and the pattern for this position is shown in Figure 30, with a plotting scale of 2 volt/cm. There is still a small amount of distortion near the center. As will be shown in the next section, this residual distortion is removed for all practical purposes, by placing a field stop at the PSD window.

The large change in sensitivity for a small change in focal position is a notable feature of these traces. For example, with an angular displacement of 10 minutes of arc, the linear displacement of the centroid on the PSD increased by more than a factor of two as the PSD was moved from 5.38 cm to 5.84 cm, a distance of 0.46 cm. At the same time the linearity of the pattern greatly improved. The most probable explanation for this behavior is that when the PSD is not in the focal plane, out-of-focus aberrations modify the position of the centroid of the illuminated area. The high distortion shown in Figure 28 is one piece of evidence for this.

The low sensitivity exhibited in Figure 28, suggests that the out-of-focus aberrations act generally to move the centroid toward the center of the PSD. This is a large effect: For an angular deflection of 10 minutes of arc, for example, the centroid displacement at the back focal position of 5.38 cm is less than half the displacement occurring at the focal position of 5.84 cm. A displacement of the centroid of ~0.8 mm

would be expected for a 10 minute angular (mirror) displacement. The data suggests that out-of-focus effects cause the centroid to displace less than 0.4 mm when the PSD is at 5.38 cm. As the focal plane is approached, this effect decreases because the out-of-focus aberrations also decrease. At the optimum focal position (5.70 cm), the residual lens aberrations are low enough so that non-linearities in the scan is not observable.

5.4 EFFECT OF FIELD STOP

As indicated in the discussion on the signal-to-noise ratio (Section 2.4.5), a field stop at the PSD functions to reduce the radiation from the solar illuminated background incident on the PSD. A 0.5 cm diameter stop was placed over the window of the PSD after the scan of Figure 30 was taken, and the pattern of Figure 31 was made. This scan should be compared to that in Figure 30, noting the significant improvement in linearity.

The reason for this improvement can be speculated on. The preceding measurements were made with the laboratory lights full on, with the optical filter and baffle behind the transmitter in place. Without the field stop in place, the field of view of the MDMS was determined by the 1 cm x 1 cm dimension of the PSD. Thus, it is possible that the PSD was receiving background illumination reflected from the laboratory walls, which added to the light distribution in the PSD caused by the focused spot on the PSD. Since the PSD measures the centroid of light distribution on its surface, the presence of the background illumination would be expected to change the centroid. Furthermore, this change would be dependent on the angular position of the (muzzle) mirror.

By restricting the field of view of the MDMS with a field stop at the PSD, most of this non-uniform background was eliminated. The remaining background was due to radiation scattered from the uniform low-reflectance baffle. Thus, one might expect an improvement in linearity with the field stop in place.

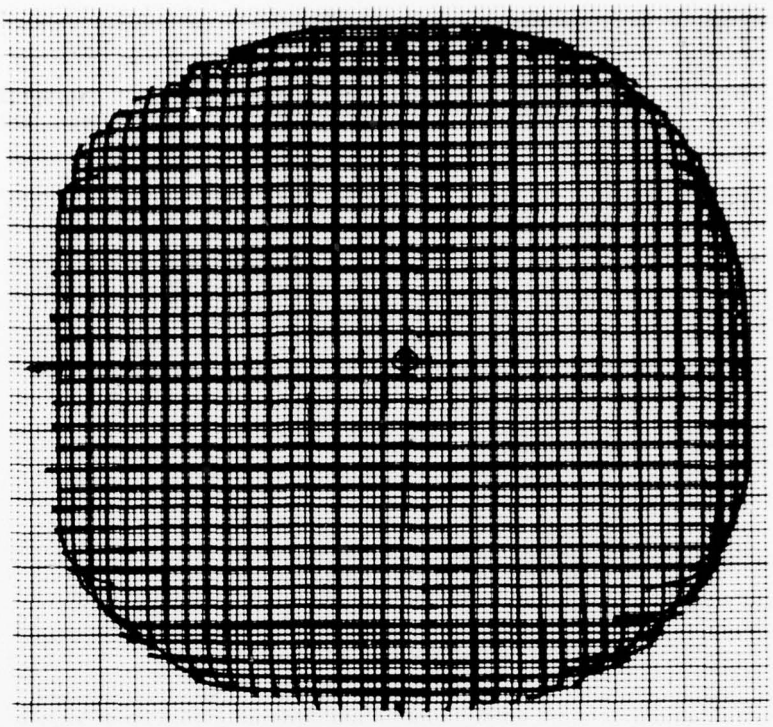

Figure 31. X-Y Scan for MDMS Prototype. A 5 mm Diameter Field Stop was placed over the PSD Window for this Scan. PSD at Back Focal Distance of 5.70 mm. Plot Scale 2 V/cm. Beam Power 0.43 mw.

5.5 FREQUENCY RESPONSE OF MDMS

The frequency response of the MDMS was measured by reflecting a HeNe laser beam from a sinusoidally oscillating mirror into the receiver aperture. The beam was caused to move along the X-axis of the MDMS, and its amplitude was kept constant as a function of frequency. Results from this measurement are shown as circled data points in Figure 32.

The frequency response of the MDMS electronics was set to roll off at about 10 kHz. In Figure 32, the solid line represents a single time constant response for which the response is down 3 dB at 16 kHz. The measured points (circled) fall on this curve, indicating that the frequency response of the MDMS is limited by the response of the electronics and not the PSD.

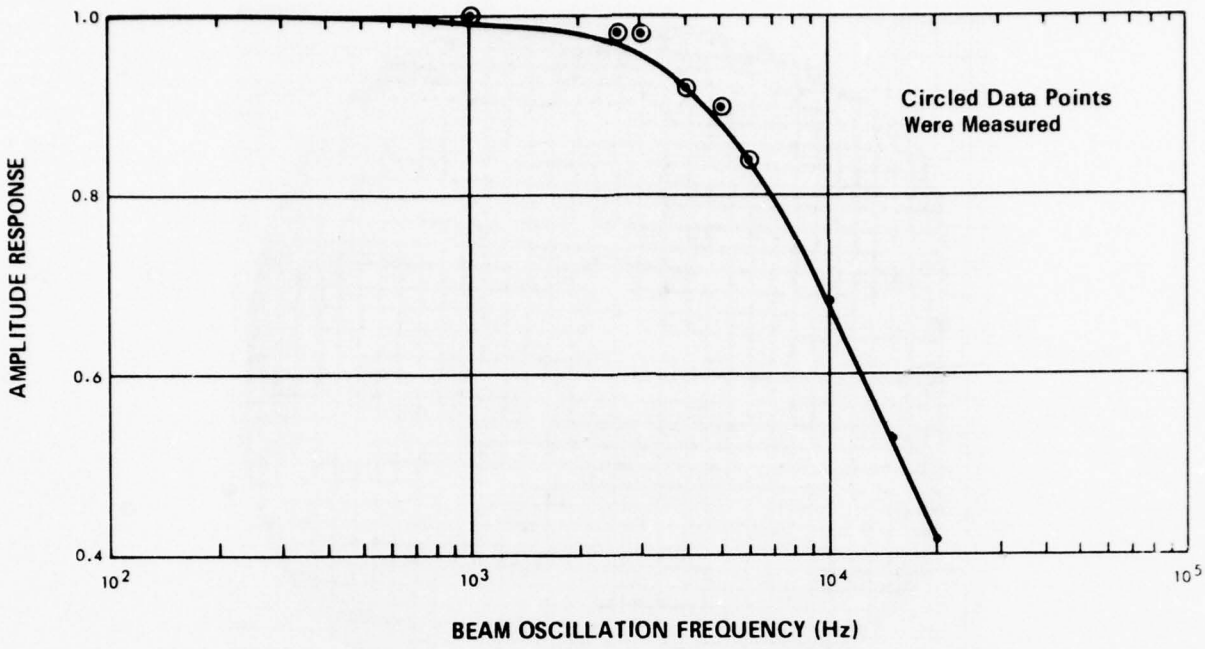

Figure 32. Frequency Response of MDMS Circled Data Points (⊙) were Measured

5.6 TEMPERATURE STABILITY OF MDMS

Temperature stability of the MDMS was evaluated by measuring the drift of the electrical zero of the PSD as a function of temperature. The test was performed by placing the PSD, its mount and the position computer electronics in an oven whose temperature could be controlled. The PSD was uniformly illuminated by an incandescent, light bulb with a frosted envelope, which was also in the oven and placed about 18 inches from the PSD. Since the PSD was uniformly illuminated, the centroid of illumination occurred at the electrical center of the detector; the position of the light bulb relative to the PSD was not critical. Current in the light bulb was adjusted to give the same photocurrent through the PSD that would occur if it were being irradiated by the focused laser spot.

The position of the light bulb was adjusted to achieve a null on the X- and Y- axes at room temperature (20°C). Oven

temperature was then changed and the output of the position computer observed. Sufficient time was allowed for the system to reach thermal equilibrium and the output from the position computer to stabilize. Measurements were made over the temperature range -6°C to 43°C.

The system was first cooled from room temperature to -6°C and then heated in several steps to 43°C. During cooling the X-output became more negative and the Y-output moved in the positive direction. On heating, the trend was reversed. Over the temperature range - $6°C \leq T \leq 43°C$, $\Delta T = 49°C$, the total drift on each axis was about 0.3 volts. Since the transfer function of the PSD in this case was 0.62 volt/min, this change corresponds to approximately $\sqrt{2}$ x 0.5 min $\approx$ 0.7 minutes of arc or 0.2 mrad. The average temperature coefficient over this temperature range is therefore, approximately 0.004 mrad/°C.

5.7 FINAL CALIBRATION OF THE MDMS

Final calibration of the MDMS was made after the gains in the X- and Y-channels of the position computer were adjusted optimally. The calibration was made using the full system as it was to be used in the field, with the position computer terminated in 75Ω. Figure 33 shows the X-Y scan, in which the plot scale is 1 volt/cm and the grid line intervals are one minute of arc (0.291 mrad).

The transfer function for the system is shown in Figure 34. Here the plotted points represent measured values along the X- and Y-axes. For each grid line parallel to the X-axis, the measured angle θ_{TMY} (minutes of arc) was set using the autocollimator, with θ_{TMX} set at zero. The output voltage of the position computer was then recorded, giving V_{TMY} (volts), and the muzzle mirror was scanned in the X-direction. This was repeated for values of θ_{TMY} between -17 minutes of arc to +17 minutes of arc. The same procedure was followed for the scan lines parallel to the Y-axis. Points on the graph of Figure 33 marked + represent measured points on the X-axis; points marked

θ_T Min	V_{MX} Volt	V_{MY} Volt
17	4.85	4.99
16	4.75	4.87
15	4.54	4.71
14	4.27	4.45
13	4.01	4.16
12	3.70	3.85
11	3.43	3.54
10	3.15	3.21
9	2.84	2.90
8	2.53	2.58
7	2.20	2.25
6	1.88	1.93
5	1.57	1.58
4	1.24	1.26
3	0.92	0.95
2	0.61	0.62
1	0.28	0.32
-1	0.32	0.31
-2	0.65	0.63
-3	0.98	0.95
-4	1.28	1.26
-5	1.57	1.58
-6	1.90	1.88
-7	2.20	2.19
-8	2.53	2.52
-9	2.85	2.83
-10	3.16	3.16
-11	3.47	3.44
-12	3.76	3.73
-13	4.05	4.02
-14	4.34	4.29
-15	4.61	4.55
-16	4.85	4.79
-17	5.04	4.97

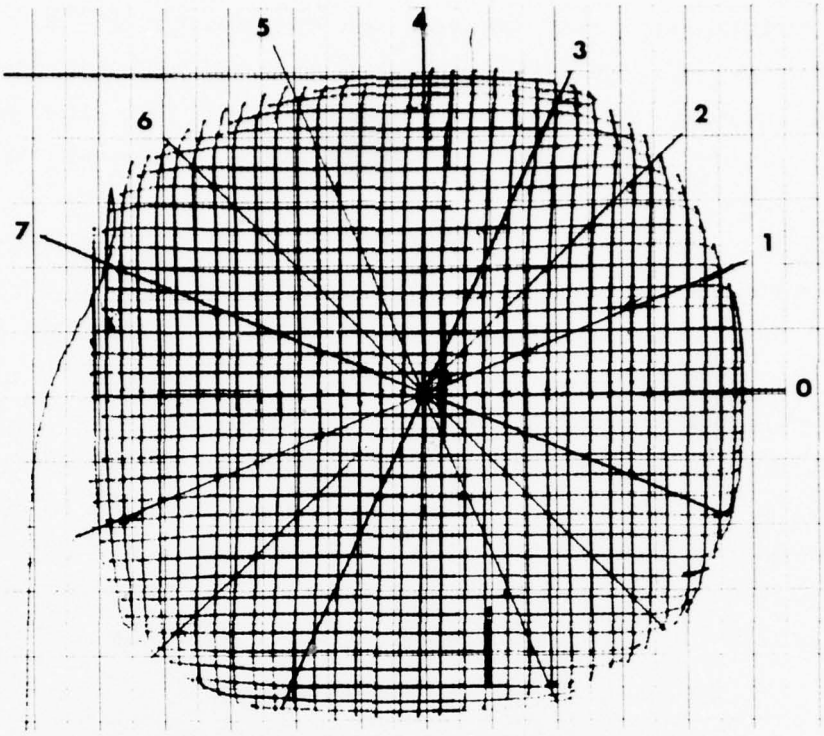

Figure 33. X-Y Calibration Scan for MDMS Prototype. This Calibration is for full system used in Field Tests. Position Computer Terminated in 75Ω. Plot Scale is 1 volt/cm. Grid Line Interval is 1 Minute of Arc (0.29 mrad).

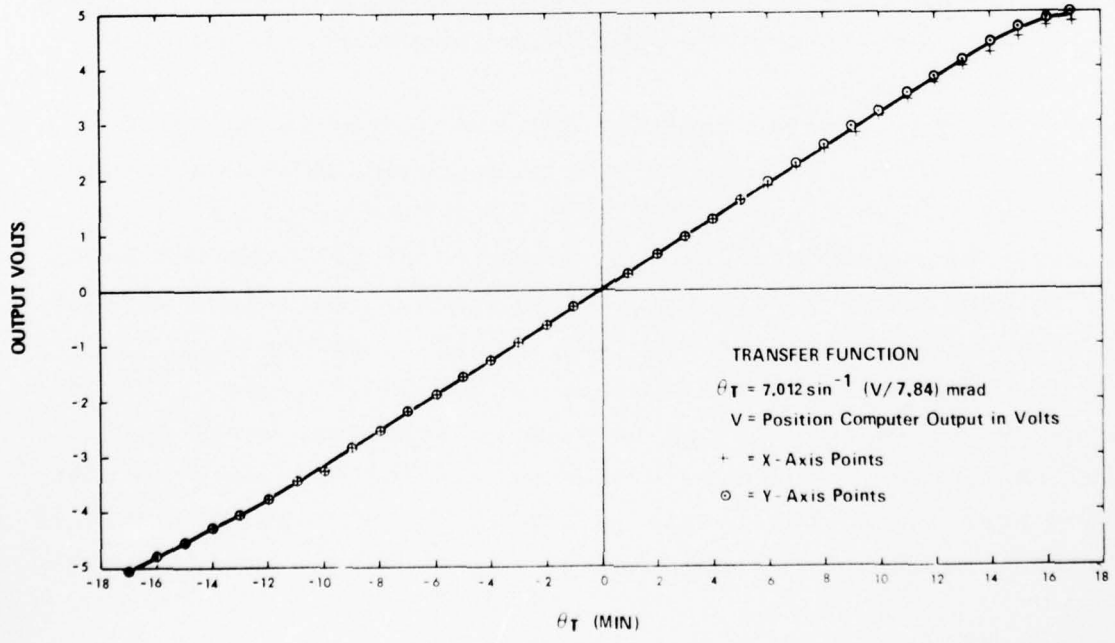

Figure 34. Transfer Function for MDMS Prototype

⊙ are for the Y-axis. The values for these points are given on the left of the figure.

These data are represented by the transfer function:

$$V_{M\gamma} = 7.844 \sin (0.143\ \theta_{TC\gamma}) \qquad (22)$$

Here γ = X or Y, $V_{M\gamma}$ is the output of the position computer for the γ channel and $\theta_{TC\gamma}$ is the computed mirror tilt angle along the γ axis. For data reduction, Eq. (22) is inverted to give

$$\theta_{TC\gamma} = 7.012 \sin^{-1} (V_{M\gamma}/7.844) \qquad (23)$$

Equation (23) was used to compute the tilt angles represented by intersections of the grid lines in the X-Y plane. The results are tabulated in Table 7, and represent computations along the numbered lines in Figure 33. For each of these lines, the values of the measured axial tilt angles, θ_{TMX}, θ_{TMY} were read from Figure 33; these are listed long the top row in each sub-table and are given in minutes of arc. For each intersection thus represented, the voltages V_{MX} and V_{MY} were read from the calibration scan using a pair of dividers, the values are tabulated in the second tow of each sub-table. With these voltage values, the mirror tilt angles θ_{TCX} and θ_{TCY} were computed using Eq. (23).

The composite tilt angle $\theta_{TC} = (\theta_{TCX}^2 + \theta_{TCY}^2)^{\frac{1}{2}}$ is given in the third row of each sub-table, and represents the tilt angles as measured by the position computer. Note that the units θ_{TC} are given in milliradians. The fourth row in each sub-tabl gives the composite tilt angle, θ_{TM}, as measured by the autocollimator: $\theta_{TM} = (\theta_{TMX}^2 + \theta_{TMY}^2)^{\frac{1}{2}}$. Thus, a comparison can be made between the computed and measured tilt angles by comparing the last two numbers in each column in a given sub-table. It is to be noted that the computed values agree well with the measured values over the entire X-Y plane of Figure 32.

TABLE 7

MDMS Calibration (Figures 32 and 33)
Comparison of Muzzle Mirror Tilt Angles Computed by MDMS with same Angles Measured by Autocollimator

θ_{TMX}, θ_{TMY}, θ_{TM} are Angles Measured by Autocollimator

V_{MX}, V_{MY} are Voltage Outputs Measured by MDMS

θ_{TC} is Angle Measured by MDMS
(Refer to Figure 32)

LINE 0 (X-AXIS)

$\theta_{TMX}/\theta_{TMY}$ (min)	-15/0	-10/0	-5/0	5/0	10/0	15/0
V_{MX}/V_{MY}	-4.61/0	-3.16/0	-1.59/0	1.57/0	3.15/0	4.54/0
θ_{TC} (mrad)	4.39	2.90	1.43	1.41	2.89	4.31
θ_{TM} (mrad)	4.35	2.90	1.45	1.45	2.90	4.35

LINE 1

$\theta_{TMX}/\theta_{TMY}$ (min)	-15/-6	-10/-4	-5/-2	5/2	10/4	15/6
V_{MX}/V_{MY}	-4.65/ -1.90	-3.20/ -1.30	-1.60/ -0.65	1.55/ 0.65	3.20/ 1.35	4.50/ 2.00
θ_{TC} (mrad)	4.75	3.16	1.55	1.51	3.18	4.63
θ_{TM} (mrad)	4.69	3.12	1.56	1.56	3.12	4.69

LINE 2 (DIAGONAL)

$\theta_{TMX}/\theta_{TMY}$ (min)	-12/-12	-8/-8	-4/-4	4/4	8/8	11/11
V_{MX}/V_{MY}	-3.75/ -3.65	-2.60/ -2.56	-1.35/ -1.25	1.27/ 1.27	2.60/ 2.60	3.49/ 3.47
θ_{TC} (mrad)	4.86	3.31	1.65	1.61	3.34	4.54
θ_{TM} (mrad)	4.92	3.28	1.64	1.64	3.28	4.51

TABLE 7. (CONTINUED)

LINE 3

$\theta_{TMX}/\theta_{TMY}$ (min)	-6/-15	-4/-10	-2/-5	2/5	4/10	6/15
V_{MX}/V_{MY}	-2.03/ -4.50	-1.40/ -3.17	-0.73/ -1.53	-0.70/ 1.60	1.30/ 3.20	2.00/ 4.50
θ_{TC} (mrad)	4.65	3.17	1.52	1.57	3.16	4.63
θ_{TM} (mrad)	4.69	3.12	1.56	1.56	3.12	4.69

LINE 4 (Y-AXIS)

$\theta_{TMX}/\theta_{TMY}$ (min)	0/-15	0/-10	0/-5	0/5	0/10	0/15
V_{MX}/V_{MY}	0/-4.50	0/-3.16	0/-1.58	0/1.58	0/3.20	0/4.60
θ_{TC} (mrad)	4.26	2.90	1.42	1.42	2.94	4.39
θ_{TM} (mrad)	4.35	2.90	1.45	1.45	2.90	4.35

LINE 5

$\theta_{TMX}/\theta_{TMY}$ (min)	-6/15	-4/10	-2/5	2/-5	4/-10	6/-15
V_{MX}/V_{MY}	-1.90/ 4.59	-1.32/ 3.23	-0.66/ 1.57	0.61/ -1.57	1.31/ -3.13	1.91/ -4.48
θ_{TC} (mrad)	4.69	3.19	1.53	1.51	3.10	4.58
θ_{TM} (mrad)	4.69	3.12	1.56	1.56	3.12	4.69

LINE 6 (DIAGONAL)

$\theta_{TMX}/\theta_{TMY}$ (min)	-12/12	-8/8	-4/4	4/-4	8/-8	12/-12
V_{MX}/V_{MY}	-3.79/ 3.74	-2.60/ 2.60	-1.30/ 1.32	1.30/ -1.30	2.52/ -2.52	3.65/ -3.65
θ_{TC} (mrad)	4.95	3.34	1.66	1.65	3.23	4.78
θ_{TM} (mrad)	4.92	3.28	1.64	1.64	3.28	4.92

TABLE 7. (CONTINUED)

LINE 7

$\theta_{TMX}/\theta_{TMY}$ (min)	-15/6	-10/4	-5/2	5/-2	10/-4	15/-6
V_{MX}/V_{MY}	-4.67/ 2.02	-3.15/ 1.29	-1.62/ 0.66	1.53/ 0.65	3.14/ -1.25	4.55/ 1.84
θ_{TC} (mrad)	4.81	3.11	1.57	1.49	3.09	4.63
θ_{TM} (mrad)	4.69	3.12	1.56	1.56	3.12	4.69

It will be observed that there is some distortion in the first quadrant of the grid pattern in Figure 33. The origin of this is not known: We can only note that this appeared when the position computer was terminated in 75Ω and the 30 ft. cables used in the field were connected. Otherwise, the condition of the MDMS was the same as that which produced the pattern shown in Figure 31. The effect of this distortion on the measurement accuracy is examined in Table 8. Here, the angles measured by the MDMS are compared to the same angle measured using the autocollimator in the range 2 min $\leq \theta_{TMX} \leq$ 9 min and 8 min $\leq \theta_{TMY} \leq$ 14 min. This is the region of greatest distortion. The data indicate that the largest error incurred is in the order of 0.1 mrad and that this occurs only when the composite tilt angle is ~4 mrad or greater.

5.7.1 Effect of System Noise

Uncertainties will occur in the computed values of mirror tilt angle due to system noise. The effect of this source of error is considered in this section.

The transfer function for the MDMS prototype was given in Eq. (23) and has the form:

$$\theta_{TC\gamma} = A \sin^{-1} (V_{M\gamma}/V_o), \qquad (24)$$

TABLE 8

Comparison of Muzzle Mirror Tilt Angles Computed by the MDMS with the same Angles Measured by the Autocollimator

θ_{TMX}, θ_{TMY}, θ_{TM} are Angles Measured by Autocollimator

V_{MX}, V_{MY} are Voltage Outputs Measured by MDMS

θ_{TC} are Angles Measured by MDMS

(Refer to Figure 32)

$\theta_{TMX}/\theta_{TMY}$ (min)	2/8	3/8	4/8	5/8	6/8	7/8	8/8	9/0
V_{TMX}/V_{TMY}	0.62/ 2.57	0.92/ 2.57	1.30/ 2.57	1.61/ 2.57	1.92/ 2.57	2.25/ 2.58	2.60/ 2.59	2.90/ 2.59
θ_{TM} (mrad)	2.40	2.49	2.60	2.75	2.90	3.09	3.29	3.50
θ_{TC} (mrad)	2.41	2.49	2.62	2.75	2.91	3.11	3.34	3.55

$\theta_{TMX}/\theta_{TMY}$ (min)	2/10	3/10	4/10	5/10	6/10	7/10	8/10	9/10
V_{TMX}/V_{TMY}	0.67/ 3.20	0.98/ 3.20	1.30/ 3.22	1.65/ 3.23	1.99/ 3.24	2.25/ 3.25	2.60/ 3.25	2.90/ 3.25
θ_{TM} (mrad)	2.97	3.04	3.13	3.25	3.39	3.55	3.73	3.92
θ_{TC} (mrad)	3.01	3.08	3.19	3.33	3.49	3.62	3.82	4.00

$\theta_{TMX}/\theta_{TMY}$ (min)	2/12	3/12	4/12	5/12	6/12	7/12	8/12	9/12
V_{TMX}/V_{TMY}	0.67/ 3.78	1.00/ 3.78	1.35/ 3.79	1.70/ 3.79	2.00/ 3.84	2.32/ 3.83	2.63/ 3.84	2.95/ 3.84
θ_{TM} (mrad)	3.54	3.60	3.68	3.78	3.90	4.04	4.20	4.37
θ_{TC} (mrad)	3.58	3.64	3.74	3.85	4.02	4.15	4.32	4.49

$\theta_{TMX}/\theta_{TMY}$ (min)	2/14	3/14	4/14	5/14	6/14	7/14	8/14	9/14
V_{TMX}/V_{TMY}	0.70/ 4.39	1.07/ 4.39	1.42/ 4.39	1.74/ 4.39	2.04/ 4.39	2.33/ 4.37	2.60/ 4.32	2.90/ 4.28
θ_{TM} (mrad)	4.12	4.17	4.24	4.33	4.43	4.56	4.69	4.84
θ_{TC} (mrad)	4.21	4.27	4.36	4.45	4.56	4.65	4.73	4.84

where γ = X or Y, and

$$A = 7.012 \text{ mrad}, \quad V_o = 7.844 \text{ volts}. \tag{25}$$

If the mean-squared fluctuation in voltage output from the X- and Y-channels is denoted by $(\Delta V_{MX})^2$ and $(\Delta V_{MY})^2$, respectively the uncertainty in the measured angle is given by

$$\Delta\theta_{TC} = \left[\left(\frac{\partial\theta_{TC}}{\partial V_{MX}} \right)^2 \left(\Delta V_{MX} \right)^2 + \left(\frac{\partial\theta_{TC}}{\partial V_{MY}} \right)^2 \left(\Delta V_{MY} \right)^2 \right]^{\frac{1}{2}} \tag{26}$$

With $V_M = (V_{MX}^2 + V_{MY}^2)^{\frac{1}{2}}$, the partial derivatives in Eq. (26) have the form:

$$\frac{\partial\theta_{TC}}{\partial V_{MD}} = \frac{A \, V_{MD}}{V_M \, (V_o^2 - V_M^2)^{\frac{1}{2}}} \tag{27}$$

Using the values of A and V_o given in Eq. (25), the uncertainty in the angle measurement by the MDMS can be estimated for given values of V_{MD}.

A measurement of system noise was not made during the laboratory tests; however, an estimate of system noise is available from the field test data given in BRL Report IMR 591,"Performance Data for the EG&G Laser Muzzle Position Indicator Taken on the M-68 Tank Gun", February 1978. Data for the present estimate was obtained from shot 041-13-36 (12/6/77); the counts for the first two milliseconds of recorded data were averaged and the variance determined. The first data point occurred at 7.145 ms before the time of fire, and it is assumed that the succeeding two milliseconds represented a steady state for the MDMS-gun system. The variance of these readings was assumed to be a measure of the root-mean-squared (RMS) system noise. Thus, the RMS voltage fluctuation was determined by applying the calibration factors for each channel to the variance of counts. This gave $\Delta V_{MX} = 0.037$ volts and $\Delta V_{MY} = 0.045$ volts.

AD-A059 726 EG AND G INC ALBUQUERQUE N MEX F/G 19/6
MUZZLE DEFLECTION MEASUREMENT SYSTEM.(U)
JUL 78 R M BLAKNEY DAAK11-77-C-0051
UNCLASSIFIED EG/G-AG-1340 ARBRL-CR-00376 NL

2 OF 2
AD A059726

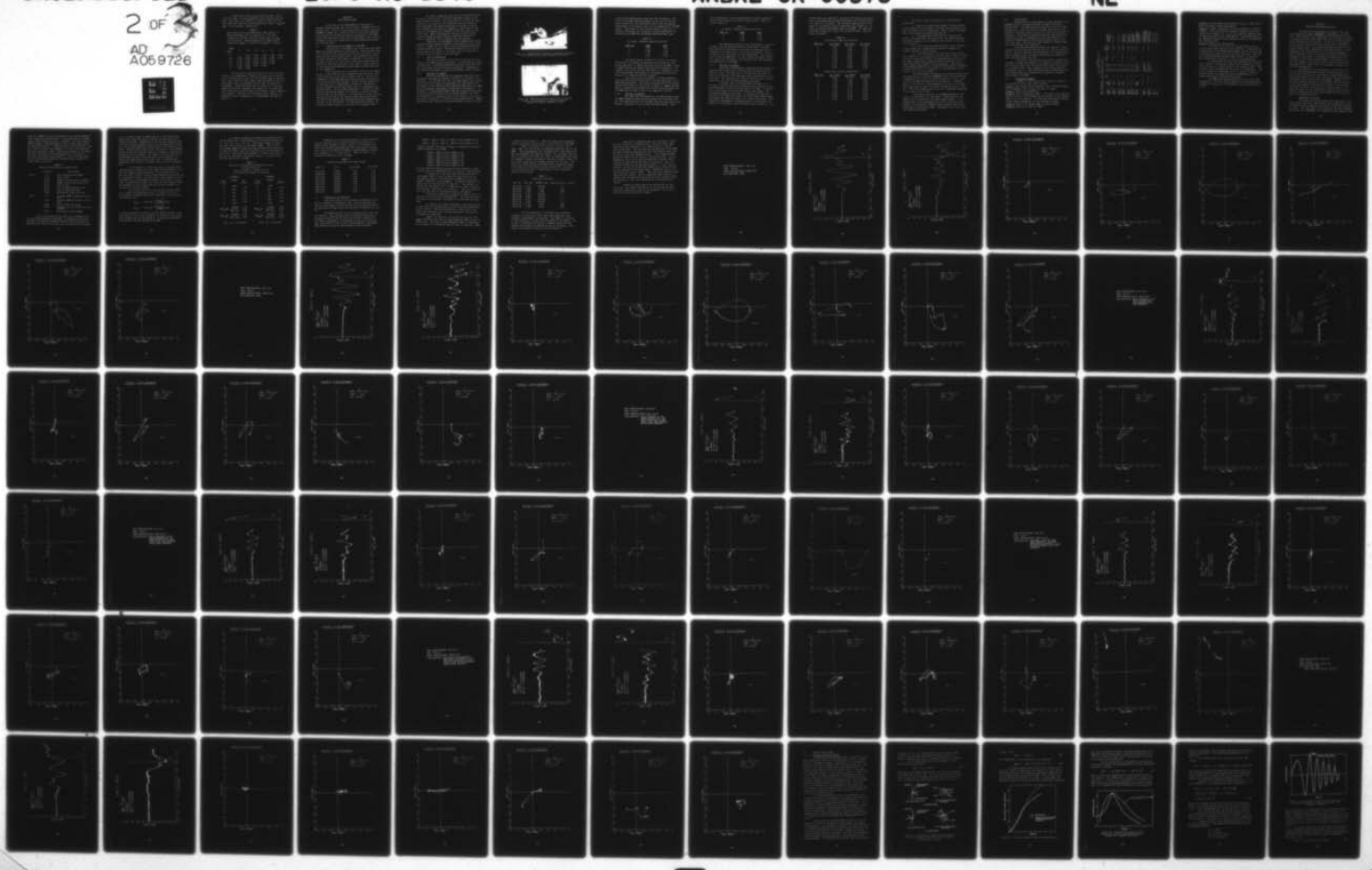


972

Using these values for the noise voltages, the uncertainty, $\Delta\theta_{TC}$, in angle measurement were computed using Eq. (26). The results are tabulated in Table 9, where the rows and columns are labeled by the measured axial angles, θ_{TMX} and θ_{TMY}, in milliradians, respectively.

TABLE 9

Table entries give the uncertainty, $\Delta\theta_{TC}$ (mrad), in angle measurement due to system noise. Rows and columns are labled by the axial angles θ_{TMX} and θ_{TMY} in milliradians. Mean-squared noise voltage values assumed are $(\Delta V_{MX})^2 = (0.037)^2$ and $(\Delta V_{MY})^2 = (0.045)^2$.

θ_{TMY} ↓ / θ_{TMX} →	0	0.9	1.8	2.7	3.6	5
0	0	0.033	0.034	0.035	0.038	0.042
0.9	0.040	0.037	0.036	0.037	0.039	0.043
1.8	0.042	0.040	0.039	0.040	0.042	
2.7	0.043	0.043	0.043	0.044	0.046	
3.6	0.047	0.047	0.047	0.049		
5	0.052	0.052				

The conclusion from this analysis is that the uncertainty in the measurement of muzzle tilt angle due to system noise is ±0.05 mrad or less over the dynamic range of measurement. Note that the noise figures used correspond to the test environment, which is probably noisier than the laboratory environment. Where PSD distortion is severe, as in the outer reaches of the first quadrant (see Figure 32), an additional error occurs and can be as high as 0.1 mrad in a small region of this quadrant. Over most of the angular range, however, the distortion error is negligible, as evidenced by the data in Table 7.

SECTION 6
FIELD TEST OF MDMS

Field tests of the EG&G MDMS were conducted at Aberdeen Proving Ground, Md. in the period 1 December 1977 to 9 December 1977. Prior to firing tests using the 105 mm tank gun MOONSHOT at Range 18, a series of static tests were conducted in an attempt to validate the angular calibration of the MDMS. These tests and their results will be described in this section. A summary of the nine firing tests in which EG&G participated will also be given.

6.1 INSTALLATION AND ALIGNMENT OF THE MDMS

Installation of the MDMS on the 105 mm tank gun (MOONSHOT) was accomplished with no difficulty. The gun bracket was first mounted on the trunnion directly above the recoil system, using the four existing bolt holes. The transmitter/receiver was then attached to the bracket, connected to the control box by means of the thirty foot control and signal cables and powered up to check the operation of the laser. Normal operation of the system was determined by measuring the laser beam power at the transmitter.

After installation of the muzzle mirror on the muzzle collar, it was found that the transmitter beam was about three inches above and to the right of mirror center. Initial misalignment of this magnitude had been anticipated and means for its correction had been provided. Lateral angular adjustment of the beam can be accomplished by moving the transmitter/receiver assembly on the gun bracket prior to tightening the mounting bolts. Vertical beam adjustment is provided by shimming the gun bracket against the trunnion; a series of shims was provided for this purpose. Fine adjustment of the vertical position of the beam at the muzzle mirror can be made using thin shim stock between the transmitter/receiver assembly and the base of the gun bracket. By employing these methods, the beam was brought readily to the center of the muzzle mirror.

In order to align the axis of the reflected beam with the axis of the receiver, the three adjustment screws on the muzzle mirror were used. The first step was to place the beam visually at the center of the transmitter/receiver aperture. Final adjustment was made by observing the outputs of the X- and Y-channels of the position computer, using voltmeter indicators at the appropriate terminals on the front panel of the control box. Small adjustments at the muzzle mirror permit accurate nulling of these outputs, indicating that the reflected transmitter beam is coaxial with the receiver.

Figure 35 is a photograph of the transmitter/receiver assembly and gun bracket attached to the trunnion of the 105 mm tank gun. Figure 36 is a view of the gun from the breech end looking toward the muzzle. The muzzle mirror with its baffle can be seen in the center of the figure and the transmitter/receiver, with its baffle, is to the right.

6.2 STATIC MEASUREMENTS

The initial purpose of the static tests was the validation of the MDMS angular calibration. In the course of accomplishing this, it was discovered that play existed in the linkage between gun tube and the base of gun mount. Measurements were made in an attempt to locate the sources of this looseness.

6.2.1 Test No. 1, 12/2/77

This test was made on the assumption that the breech mechanism of the gun was rigidly connected to the base of the gun mount. If this were the case, one would expect that angular deflections of the muzzle would produce the same angular displacements of the reflected laser beam when measured by the MDMS and an independent measurement referenced to the gun base. Accordingly, a tripod-mounted HeNe laser was placed on the ground behind the gun and trained onto the muzzle mirror. The beam was reflected to a measuring scale on the back wall of the gun barricade, a distance of 11.32 m from the muzzle mirror. Muzzle deflections were induced by raising (bending) the gun tube with

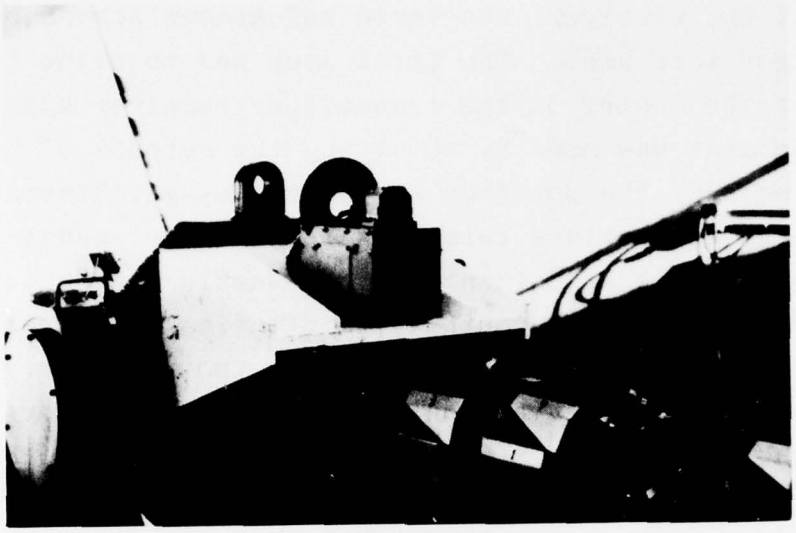

Figure 35. MDMS Transmitter/Receiver Assembly on Trunnion of 105 mm Gun; Note Steel Bracket at Interface

Figure 36. MDMS Muzzle Mirror Mounted on 105 mm Gun (Center of Photograph). Transmitter/Receiver Assembly on Trunnion Showing at Right

a jack placed approximately four feet from the muzzle. The ratio of the HeNe beam displacement on the scale to the distance between the scale and muzzle mirror gives the angular displacement of the muzzle, and is to be compared with the MDMS output. The results of this test are given in Table 10, in which are tabulated the Y-component of beam displacement as measured by the MDMS and the ground-referenced HeNe laser.

TABLE 10

θ_Y (mrad) - Measured Angular Deflection

DEFL. No.	MDMS	HeNe
1	0.56	1.25
2	0.83	1.52
3	1.49	2.30
4	2.01	3.05

The results given in Table 10 show that the angular deflection of the muzzle as measured with reference to the ground (gun base) is larger than that given by the MDMS. Since the MDMS measures the muzzle deflection with reference to the trunnion, this result implies that there is a component of the total displacement with respect to the ground which involves motion of the trunnion and tube together.

As a check on this conclusion, the HeNe measuring scale was moved from the back wall of the gun barricade to the EG&G mounting bracket. The results obtained with this configuration were similar to those given in Table 10, suggesting that there is indeed motion between the trunnion and gun base which the MDMS does not detect (and is not expected to detect).

6.2.2 Test No. 2, 12/2/77

The HeNe laser was mounted on the EG&G bracket beside the MDMS transmitter/receiver and trained onto the muzzle mirror. The measuring scale for the HeNe laser spot was also on the bracket, a distance of 4.21 m from the muzzle mirror. With

this configuration, the two measurements of muzzle angular deflection were expected to yield the same results; these are shown in Table 11.

TABLE 11

θ_Y (mrad) - Measured Angular Deflection

DEFL. No.	MDMS	HeNe
1	1.26	1.43
2	2.85	3.00
3	3.18	3.16

The agreement between the two measurements is seen to be good, with the maximum difference being about 0.15 mrad. This difference corresponds to an error in measuring the displacement of the HeNe spot of less than a millimeter, which is as good as one could expect for this measurement. The conclusion is that the MDMS does, in fact, measure the muzzle deflection angle with reference to the trunnion; this test validates the calibration of the MDMS.

6.2.3 Test No, 3, 12/2/77

The previous measurements indicated motion between the trunnion and the gun base as the gun tube was raised and lowered by a jack. The major part of this motion was traced to play in the bearing on the gun mount which establishes the tube elevation. This looseness was observed directly with a feeler gauge while the tube was being jacked up and down.

A further series of measurements was made in an attempt to identify and isolate other sources of motion in the gun system which would not be detected by the MDMS. In particular, play between the breech and trunnion was sought. The following arrange ment was used: 1) A mirror was cemented to the rear of the EG&G gun bracket and a HeNe laser beam (ground referenced) was reflected from it to a scale 7.20 m away. This permitted a measurement of angular motion of the bracket with respect to the gun base, and is denoted by θ_B in Table 12. 2) A

second mirror was cemented to the end of the tube in the breech and a second HeNe beam (ground referenced) was reflected from it to a scale 6.11 m distant. This allowed angular motion of the breech to be detected, which is denoted by θ_G in Table 12. θ_T gives the angular measurement made by the MDMS. The tube was deflected by means of a jack, as in previous tests. Table 12 gives the results.

TABLE 12

Deflection of Tube in Y-Direction

DEFL. No.	θ_{TY} (mrad)	θ_{BY} (mrad)	θ_{GY} (mrad)
1	1.50	1.25	1.23
2	2.47	2.08	1.80
3	3.20	2.50	2.25
4	4.15	2.90	2.87
5	-0.81	-0.25	-0.25
6	-1.53	-0.44	-0.49
7	-2.39	-0.63	-0.65
8	-2.91	-0.88	-0.94
9	-3.73	-0.94	-1.18

Deflection of Tube in X-Direction

DEFL. No.	θ_{TX} (mrad)	θ_{BX} (mrad)	θ_{BY} (mrad)
1	0.87	0.16	0.32
2	1.94	0.28	0.59
3	3.12	0.98	0.38
4	3.93	1.18	0.42
5	-1.15	-0.11	-0.33
6	-1.82	-0.14	-0.37
7	-2.34	-0.17	-0.65
8	-2.95	-0.19	-0.55
9	-3.44	-0.19	-0.60

The data in Table 12 gives rise to the following conclusions:

1) Both the trunnion (gun bracket) and breech move in the Y-direction with respect to the gun base (ground) as the tube is deflected in the Y-direction. This is direct confirmation of the conclusion reached from Test No. 1.

2) The magnitude of deflection of trunnion and breech is an appreciable fraction of the tube deflection measured with reference to the trunnion, particularly in the positive Y-direction.

3) The trunnion and breech appear to move together in the Y-direction, suggesting that these two members are rigidly attached in the Y-Z plane.

4) The breech end of the tube and the gun bracket do not appear to move together in the X-Z plane. However, these motions are much smaller than the corresponding motions in the Y-Z plane, suggesting a tighter mechanical coupling in this plane between these members and the gun mount. Some play between breech and trunnion is evident which apparently disappears at higher deflections, as indicated by the saturation of the values in the last two columns.

The measurements reported in this section clearly show that tube motion in this gun (MOONSHOT) stems from two sources: 1) Bending of the tube (1st column in Table 12), which is measured by the MDMS and referred to the trunnion. 2) Angular motion of the tube as a rigid member due to play in the mechanism connecting the gun to its mount (columns 2 and 3 in Table 12). This latter angular motion can be of comparable magnitude to the bending of the tube.

An ultimate objective of the MDMS measurement technique is to determine if a knowledge of tube distortion can improve the hit probability for tank weapon systems. It is obvious that if this measurement is to be of value for this purpose, the mechanical linkage between trunnion and gun carriage must be essentially rigid. Presumably this is the case for operational systems.

6.3 FIRING TESTS

Opportunities to participate in eleven firings of the MOONSHOT gun were available between 6 December 1977 and 9 December 1977. The MDMS functioned properly on nine of these opportunities. For the first six firings, data was lost for periods of a millisecond or less in the vicinity of the time of round exit. The cause of these data drop-outs was finally determined to be due to obscuration of the laser beam by the ejection of burned gases from the bore evacuator hole at the top of the tube. Once this hole was blocked, no further drop--outs were observed near round exit.

Late time data drop-outs were also observed. These appeared to occur when the tube was near its limit of travel in recoil. When the tube was in this position, it is quite likely that the muzzle mirror no longer intercepted the transmitter beam, and hence signal was lost.

It should be recalled that the position computer was designed to clamp each channel at its negative saturation voltage should the beam power fall below about twenty five percent of its normal value. Thus, whenever the data show negative saturation, this is a clear indication that the beam power has been reduced below the minimum level required for accurate functioning of the MDMS.

6.3.1 Firing Test Summary

A summary of the firing tests is given in Table 13. The contents of this table are as follows:

Column 1: Shot identification and date; also includes designation of magnetic tape on which raw data in stored.

Column 2: Round type designation.

Column 3: Time to Round Exit (TRE). All times in the table are given in units of milliseconds and are referred to the leading edge of the time fiducial. All time data were taken from visicorder traces produced at the time the shot occurred.

Column 4: Time to the leading edge of drop-out (TDO).

Column 5: Duration of drop-out (DOD).

TABLE 13

MDMS SHOT SUMMARY AND GENERAL OBSERVATION

TRE: Time to Round Exit TDO: Time to Leading Edge of Dropout
DOD: Duration of Dropout RE: Round Exit
All times in milliseconds referred to leading edge of time fiducial.

Shot ID	Round	TRE (ms)	TDO (ms)	DOD (ms)	Muz.Retr. @ RE (cm)	Voltage Calibration (mv/count)	Comments
041-13-36 12/6/77 Tape PD 240	APDS M392A2 Standard	29.7	28.8 99.0 103.4 122.7	0.6 0.2 0.1 0.5	2.8	X: 3.61 Y: 3.45	MDMS Power Cord Failure after Data obtained.
042-09-56 12/7/77 Tape PD 240	Same - No Magnet	33	31.7 33.5 80 86.9	1.1 0.7 1.0 3.0	No Doppler	X: 3.75 Y: 3.43	Data at RE
045-10-57 12/8/77 Tape PD 240	Same - Standard	29.1	28.1 29.7 79.3	1.0 0.9 2.0	3.0	X: 3.68 Y: 3.45	Data at RE (?)
046-13-55 12/8/77 Tape PD 240	Same - Standard	36	34.9 36.5 65.9 92.6	1.1 1.1 1.3 1.9	No Doppler	X: 3.69 Y: 3.64	Data at RE (?) Disconnected Y Drop-out Clamp
047-14-49 12/8/77 Tape PD 240	Proof Slug	34.3	33.3 35.3 56.3	1.0 0.3 10.6	2.8	X: 3.74 Y: 3.67	Data at RE Y Drop-out Clamp Disconnected
048-15-07 12/8/77 Tape PD 244	Proof Slug	30.5	29.8 31.3 55.4	0.8 0.15 17	No Doppler	X: 3.77 Y: 3.73	No Data at RE Y Drop-out Clamp Disconnected
047-10-38 12/9/77 Tape PD 244	APDS M392A2 Standard	29.4	No Dropouts Near TRE. 1st DO - Muzzle Retracted 29 cm.		2.8	X: 3.69 Y: 3.63	3" Diam. Mirror on Muzzle. Plugged Top Bore Evacuator Hole Y Drop-out Clamp Disconnected
049-11-24 12/9/77 Tape PD 244	Proof Slug	30.9	No Dropouts Near TRE. 1st DO - Muzzle Retracted 29 cm.		2.8	X: 3.74 Y: 3.72	Standard 2" Muzzle Mirror. Bore Evacuator Hole Plugged. Y Drop-out clamp disconnected
050-11-37 12/9/77 Tape PD 244	Proof Slug	31.6	No Dropouts Near TRE. 1st DO - Muzzle Retracted 21 cm.		2.8	X: 3.74 Y: 3.69	Bore Evacuator Hole Plugged. Y Drop-out Clamp Disconnected
043 12/7/77	----	----	----		----	----	MDMS Laser Failed
044 12/7/77	----	----	----		----	----	MDMS Under Repair

Column 6: Distance muzzle had traveled in recoil at TRE; determined from doppler radar measurements.

Column 7: Voltage calibration of X- and Y-channels of position computer. These calibrations represent averages for the four calibration voltages, -3v, -1v, 1v, 3v, and were computed from the data print-outs given in BRL IMR 591, "Performance Data for the EG&G Laser Muzzle Position Indicator taken on the M-68 Tank Gun", February 1978.

Column 8: Comments and observations.

Note that on the first six firings, data drop-outs occurred just before and just after round exit. These were due to obscuration of the laser beam by gases ejected into the beam from the bore evacuator hole at the top of the tube. This hole was blocked beginning with 047-10-38, 12/9/77; no drop-outs were observed near round exit on this or succeeding shots.

It should also be noted that beginning with shot 046-13-55, 12/8/77, the drop-out clamp in the Y-channel was disconnected and was left disconnected for the remaining shots. This was done during the search for the cause of the drop-outs. Data in the Y-channel corresponding to the X- drop-out interval is invalid because the signal was below threshold and will be ignored during data reduction and analysis.

The MDMS laser diode failed just prior to shot 043. Replacement of the laser and realignment of the system resulted in EG&G not being able to participate in shots 043 and 044 on 12/7/77.

SECTION 7
REDUCTION AND ANALYSIS OF DATA

The data collected during the firings of the statically mounted 105 mm gun (MOONSHOT) is presented in this section. Data reduction was accomplished in the Computer Facility at Kirtland Air Force Base, which was used to produce two graphical representations of the data. In the first, the angular deflection of the muzzle mirror in the X- and Y- directions is plotted against time. The second presentation consists of six graphs in which the Y-deflection of the muzzle mirror is plotted against the X-deflection in one millisecond intervals. These constitute a type of polar plot showing the angular displacement of the muzzle. The graphs are grouped into sets, according to shot identification number. For each shot, the first two graphs in the set give the X- and Y- deflections of the muzzle mirror versus time; the following six graphs give the polar presentation.

The purpose of the discussion in this section is to present these data and describe their salient features. As will be seen, the motion of the muzzle is complex during and after round transit of the tube, indicating that the mechanisms responsible for the motion are also complex. However, there are some striking similarities in the muzzle motion from shot to shot which appear to be related to forces on the tube generated by the forced rotation of the round in transit. An hypothesis based on this mechanism is examined and is found to predict torquing forces which could account for the gross features of the observed motion.

7.1 REDUCTION OF THE DATA

The analog data from each shot were digitized at five microsecond intervals by BRL personnel and transmitted to EG&G on keypunch cards, along with a print-out of the digitized data in counts. The count range of the digitized data was originally specified to be $-999 \leq 0 \leq 999$, corresponding to the maximum voltage

swing of $-5 \leq 0 \leq +5$ volts at the output of the position computer. After examining the analog data, it was found that the voltage signals never exceeded ±3 volts. Therefore, the count range of ±999 was made to span approximately this voltage range during the digitizing process. During periods of data drop-outs, when the X- and Y- outputs were clamped at -5 volts, the digitized data were recorded as -999. Fifteen milliseconds of the analog data were digitized, starting approximately 10 ms prior to round exit and ending 5 ms thereafter. The set of data cards for each shot were preceded by two header cards, having the format shown in Table 14.

TABLE 14

Format and Description of Header Cards

	Column No.	Description
Card 1	1-10	Shot Identification Number
	11-20	Date of Shot
	21-30	Number of data Points in Channel
	31-40	Sample rate (ms per data point)
	41-50	Time of Fire
	51-60	Time of Round Emergence (ms)
	61-70	Time of Round Exit (ms)
	71-80	Calibration (Volts per step)
Card 2	1-10	X-channel MDMS calibration (volts/min)
	11-20	Y-channel MDMS calibration (volts/min)
	21-30	Time of first data point
	31-60	Average value of calibration steps (counts)
	72-80	Shot Identification Number

Prior to entering the raw data into a permanent file, the following adjustments were made: A program was written to determine the mean and standard deviation of the first 400 digitized points (first 2 ms) and to set all drop-out data points

(i.e. all counts equal to -999) equal to a 4-Hollerith (4-H) blank field, which was used to identify the drop-out data in further processing. Examination of the raw data indicated that the first two milliseconds of raw data fluctuated about a mean value which represented the initial offset of the position computer. The data were corrected for this off-set. The standard deviation from this mean was taken as a measure of system noise during each of the firings. The values of off-set and noise in milliradians for each firing are given in the legend of the graphs for angular deflection versus time. Following these adjustments the raw data, in counts, were stored in a permanent file.

In an attempt to isolate the cause of the data drop-outs during the firing tests, the clamp in the Y-channel of the position computer was disconnected. This was done first on Shot 047-14-49, 12/8/77, and the clamp remained disconnected for all subsequent firings. For these shots, data drop-outs in the Y-channel were not designated by -999 in the raw data. Therefore, in processing the data, all values in the Y-channel which corresponded in time to data drop-outs in the X-channel were set equal to 4-H blank fields.

The primary function of the data processing program was to convert the adjusted raw data in counts to units of milliradians of angular deflection, according to the prescription (See Eq. 23):

$$\theta_{TCX} = 7.012 \ \mathrm{Sin}^{-1} \left[\frac{k_x \ C_x}{7.844} \right] \ \text{mrad},$$

$$\theta_{TCY} = 7.012 \ \mathrm{Sin}^{-1} \left[\frac{k_y \ C_y}{7.844} \right] \ \text{mrad}.$$

In these expressions, C_x and C_y are the adjusted values of raw data counts in the X- and Y-channels; k_x and k_y are the calibration constants for the two channels. k_x and k_y are different for each shot and were derived as follows:

A voltage calibration of the BRL data acquisition system was made prior to each firing at the following voltage levels: -5v, -3v, -1v, 1v, 3v, 5v. The average number of counts for each level is given in the header cards. Table 2 gives the average number of counts for each calibration voltage level for shot 041-13-36, along with the ratio of millivolts/count at each level. These were then averaged, as shown in the table, to develop the calibration constants k_x and k_y. A similar procedure was used for all firings.

TABLE 15

Derivation of Calibration Constants k_x and k_y for Shot 041-13-36

V_{CAL} = Calibration voltage in volts

k = Calibration constant in mv/count

X-CHANNEL			Y-CHANNEL		
V_{CAL} (volts)	COUNTS	k_x (mv/CT)	V_{CAL} (volts)	COUNTS	k_y (mv/CT)
-5	-1390		-5	-1338	
		3.79			3.72
-3	-863		-3	-801	
		3.61			3.51
-1	-309		-1	-231	
		3.45			3.60
1	220		1	324	
		3.77			3.24
3	750		3	942	
		3.25			3.40
5	1365		5	1530	
$-5 \leq V_{CAL} \leq 5$	Average	3.57	$-5 \leq V_{CAL} \leq 5$	Average	3.49
	Std. Dev.	0.23		Std. Dev.	0.18
$-3 \leq V_{CAL} \leq 3$	Average	3.61	$-3 \leq V_{CAL} \leq 3$	Average	3.45
	Std. Dev.	0.16		Std. Dev.	0.19
Used:	k_x = 3.61 mv/CT		Used:	k_y = 3.45 mv/CT	

Examination of the raw data from all firings indicated that the absolute value of output voltage from the position computer never exceeded 3 volts. Hence, the calibration constants used in data processing were those derived from an average of the four calibration constants corresponding to calibration voltages -3, -1, 1 and 3 volts. Table 16 tabulates the calibration constants for all firings.

TABLE 16

Calibration Constants for Each Firing

SHOT ID	Date	k_x (mv/CT)	k_y (mv/CT)
041-13-36	12/6/77	3.61	3.45
042-09-56	12/7/77	3.75	3.43
045-10-56	12/8/77	3.68	3.45
046-13-55	12/8/77	3.69	3.64
047-10-38	12/9/77	3.69	3.63
048-15-07	12/8/77	3.77	3.73
049-11-24	12/9/77	3.74	3.72
050-11-37	12/9/77	3.74	3.69
047-14-49	12/2/77	3.74	3.67

7.2 PRESENTATION OF THE DATA

Data from eight of the firings are presented in this section, primarily in graphical form. They are grouped into sets of eight graphs for each firing; the sets are separated by an identification page giving the pertinent information for the set.

The graphs in each set are labeled with the shot number and date. θ_{TCX} and θ_{TCY} denote the angular deflection of the muzzle mirror in the X- and Y- directions, respectively. The order of appearance of the graphs in each set is given below, along with the time interval corresponding to each graph. TRE1 denotes the time of round emergence from the muzzle.

Graph 1 θ_{TCX} vs. Time (t) TRE1-7.0 ms $\leq$ t $\leq$ TRE1+1.5 ms

Graph 2 θ_{TCY} vs. Time (t) TRE1-7.0 ms $\leq$ t $\leq$ TRE1+1.5 ms

Graphs 3 through 8 give θ_{TCX} vs θ_{TCY} in consecutive one millisecond intervals, as follows:

Graph 3 TRE1-4.5 ms $\leq$ t $\leq$ TRE1-3.5 ms
Graph 4 TRE1-3.5 ms $\leq$ t $\leq$ TRE1-2.5 ms
Graph 5 TRE1-2.5 ms $\leq$ t $\leq$ TRE1-1.5 ms
Graph 6 TRE1-1.5 ms $\leq$ t $\leq$ TRE1-0.5 ms
Graph 7 TRE1-0.5 ms $\leq$ t $\leq$ TRE1+0.5 ms
Graph 8 TRE1+0.5 ms $\leq$ t $\leq$ TRE1+1.5 ms

For shot 046-13-55 Graph 8 has been omitted because of insufficient data for a meaningful plot as a result of data drop-out.

In addition to the shot identification and date on each graph, Graphs 1 and 2 in each set give the off-set in milliradians applied to the data and the RMS noise for each channel, expressed in milliradians. In Graphs 3 through 8, T_o identifies the starting time for the plot. For example, in Graph 3 for shot 050-11-17, T_o = TRE1-4.5 ms; TRE1 = 31.520 ms for this shot; therefore, T_o = 27.020 ms. The plot begins at this time and ends one millisecond later at 28.020 ms.

The time of round exit is marked on Graphs 1 and 2 in each set by the vertical line marked RE. The time axis gives the time in milliseconds, referenced to an arbitrary starting time.

In each of the Graphs 3 through 8, the starting point of the trace is indicated by the letter S and the ending point by the letter E. The starting point on a given plot is the same as the ending point of the preceding plot; the scales of the graphs are identical.

Graph 7 of each set is the polar plot for the time range centered on the time of round emergence: TRE1-0.5 ms $\leq$ t $\leq$ TRE1+0.5 ms. The time of round emergence, TRE1, is indicated by the symbol X, if recorded, and the time of round exit, TRE2,

is denoted by the symbol O. These two events were measured by sensors existing on the gun prior to installation of the MDMS.

Table 17 tabulates the round exit interval, REI = TRE2 - TRE1, for each firing, as measured during the test of the MDMS. These measurements were analyzed by Mr. Jimmy Schmidt of BRL, who designed the round exit sensor. He concluded that only four of the REI in the table are valid, as indicated in the table. Mr. Schmidt's results are shown in the third column of Table 7-4. The fourth column gives the muzzle velocity of the shell. The round exit sensor detects the discontinuity between the metal shell casing and the plastic collars at each end. The length of the round exit pulse is proportional to this separation, which is ≈5.25 inches.

TABLE 17

Round Exit Intervals

Shot ID	REI (ms)	SCHMIDT (ms)	Muzzle Velocity (m/sec)
041-13-36	0.035	Invalid	----
042-09-56	0.070	0.078	1710
045-10-57	0.080	0.088	1520
046-13-55	0.160	Invalid	----
047-10-38	0.885	Invalid	----
048-15-07	0.175	Invalid	----
049-11-24	0.055	Invalid	----
050-11-37	0.120	0.105	1270
047-14-49	0.086	0.091	1470

The time resolution in the polar plots (Graphs 3 through 8) is high and in many cases small amplitude, high frequency displacements are observed. This makes it difficult in some instances to follow the gross motion of the muzzle. As an aid to visualizing the motion, a summary figure has been prepared which shows the smoothed motion of the muzzle. This figure is presented in Section 7.3.2 as Figure 42.

Eight sets of graphical data are presented, of which the first seven are considered valid. Shot 047-10-38, dated 12/9/77, differs radically in its characteristics from the other seven shots. For this shot the configuration of the MDMS had been altered by replacing the two inch diameter muzzle mirror with a three inch diameter mirror. This change was made during the search for the cause of the data drop-out. One hypothesis at the time was that the amplitude of muzzle deflection was so great during the time of the drop-out, that the transmitter beam was not hitting the mirror. To test this hypothesis, the two inch mirror was removed and a three inch mirror was cemented to the mirror mount. During the firing, the mirror was torn from the mount. This fact alone makes the data from this shot suspect. While no drop-outs were observed, it appears that the cement did not hold the mirror rigidly during the observation time, thus producing the non-characteristic results.

During the digitizing of the analog data for Shot 047-14-49, some unspecified difficulty was encountered which resulted in data which could not be processed. As a result, plots of this data could not be made.

SHOT IDENTIFICATION: 050-11-37

DATE: 12/9/77

ROUND IDENTIFICATION: PROOF SLUG

DATA DROP-OUTS: NONE

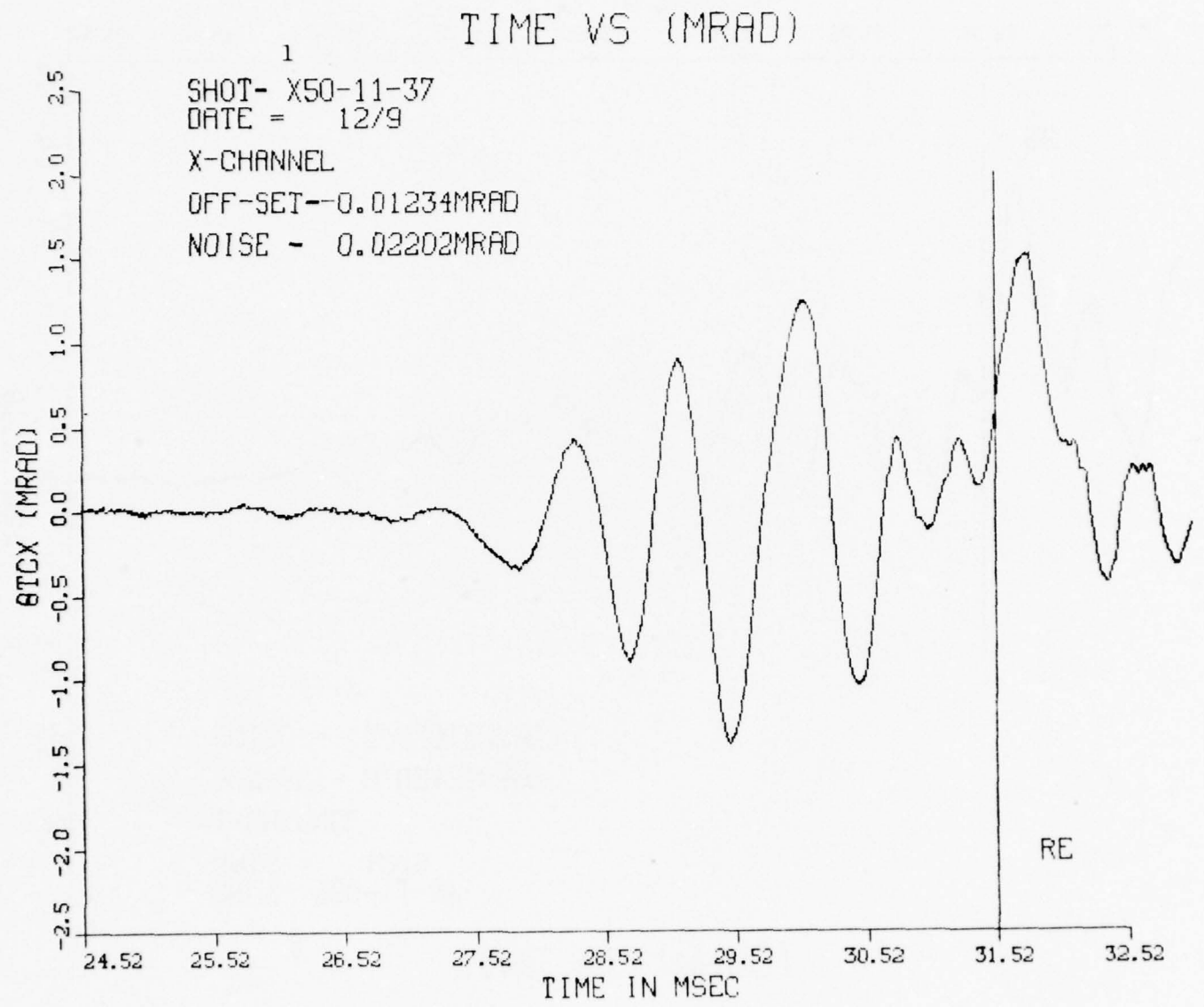
TIME VS (MRAD)
1
SHOT- X50-11-37
DATE = 12/9
X-CHANNEL
OFF-SET--0.01234MRAD
NOISE - 0.02202MRAD
θTCX (MRAD)
2.5
2.0
1.5
1.0
0.5
0.0
-0.5
-1.0
-1.5
-2.0
-2.5
RE
24.52
25.52
26.52
27.52
28.52
29.52
30.52
31.52
32.52
TIME IN MSEC

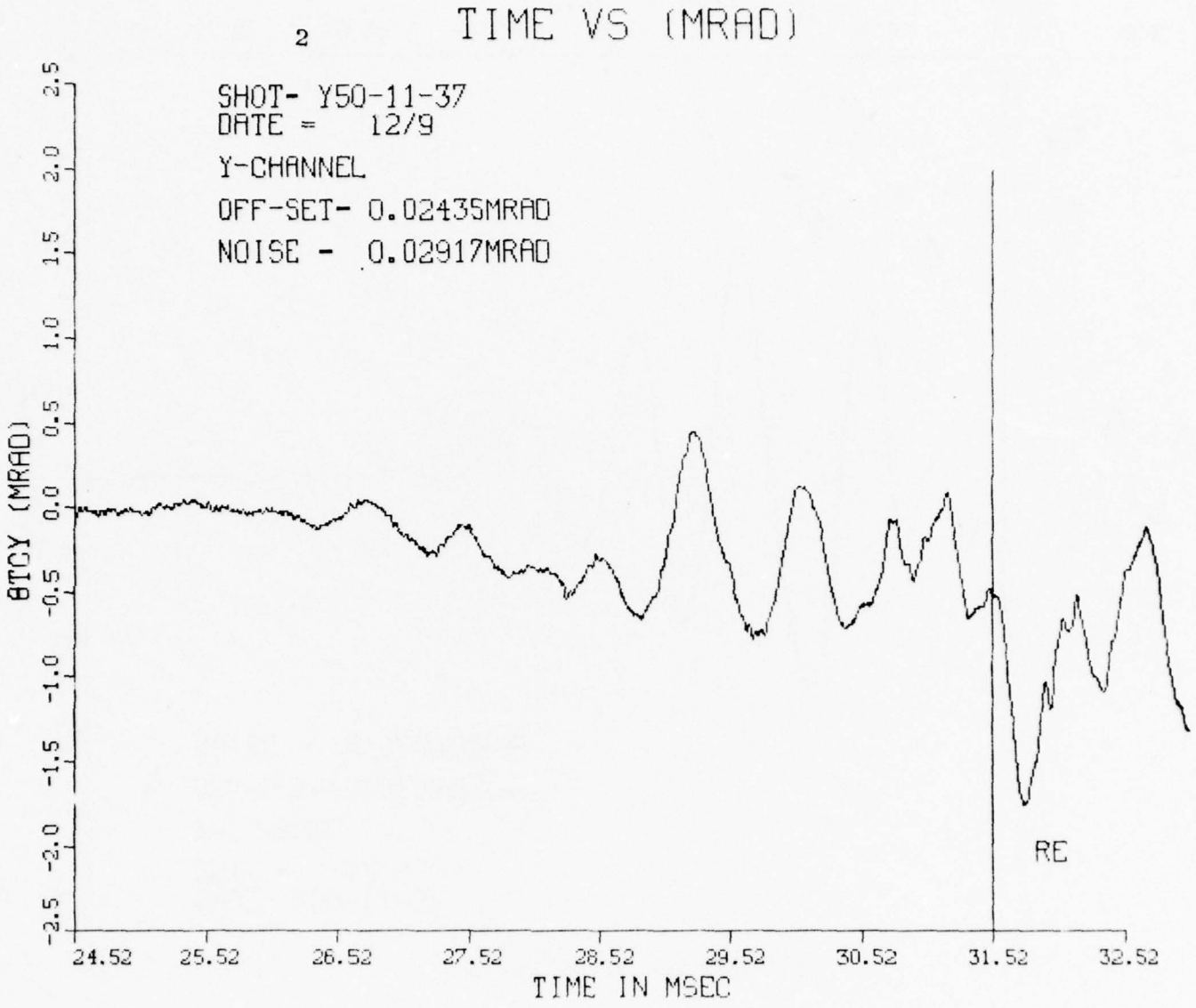
TIME VS (MRAD)
2
SHOT- Y50-11-37
DATE = 12/9
Y-CHANNEL
OFF-SET- 0.02435MRAD
NOISE - 0.02917MRAD
θTCY (MRAD)
2.5
2.0
1.5
1.0
0.5
0.0
-0.5
-1.0
-1.5
-2.0
-2.5
RE
24.52
25.52
26.52
27.52
28.52
29.52
30.52
31.52
32.52
TIME IN MSEC

MUZZLE DISPLACEMENT

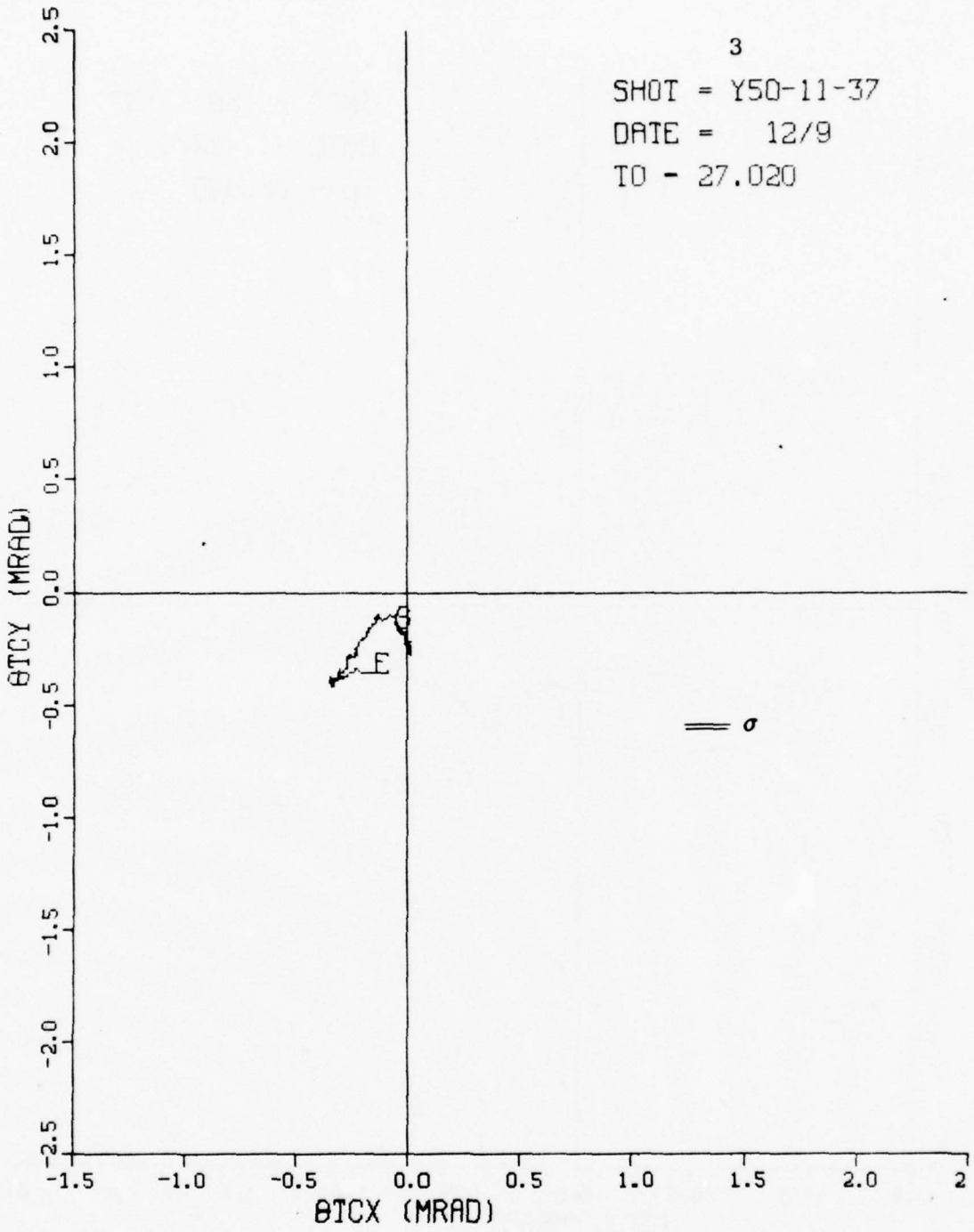

MUZZLE DISPLACEMENT

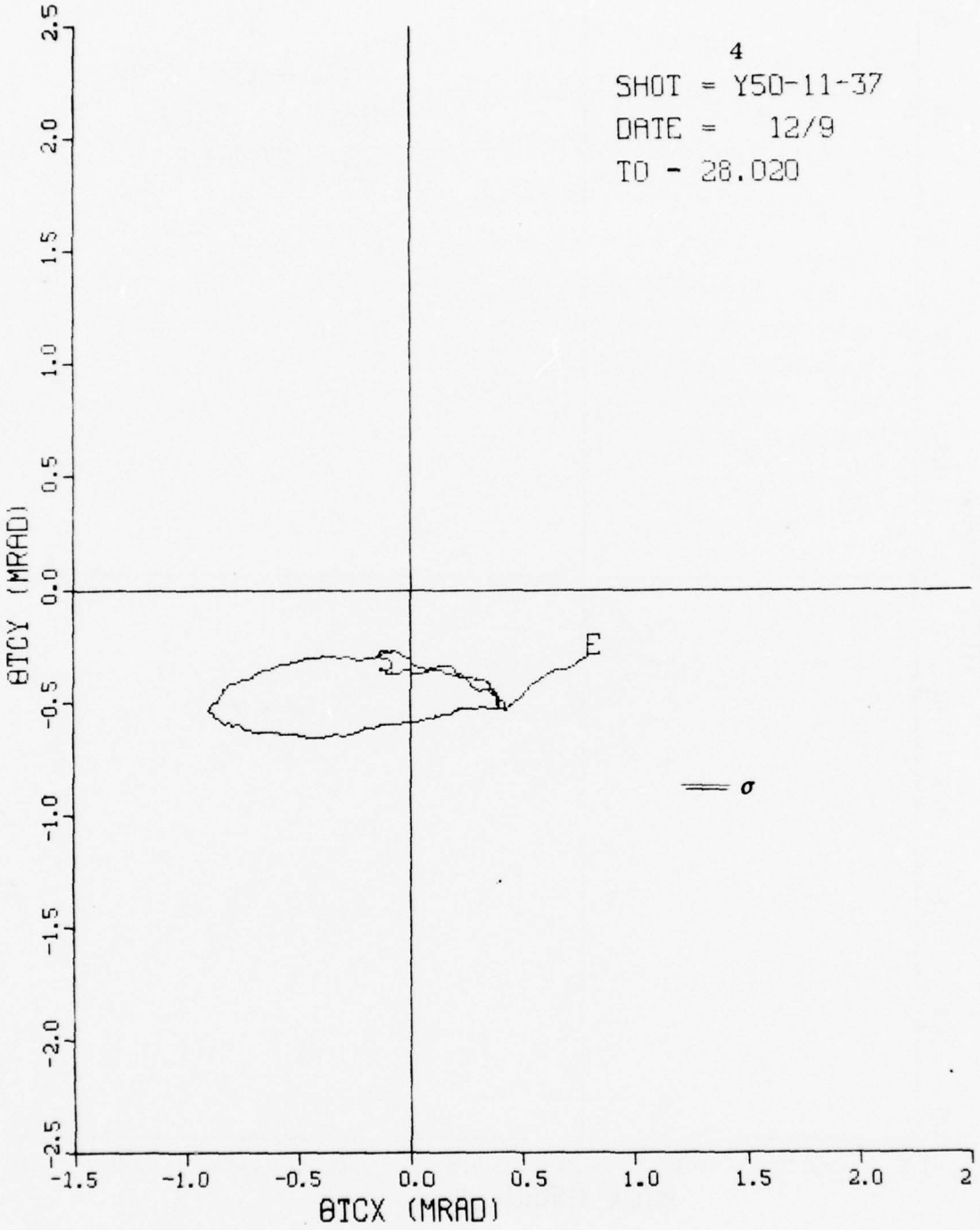

MUZZLE DISPLACEMENT

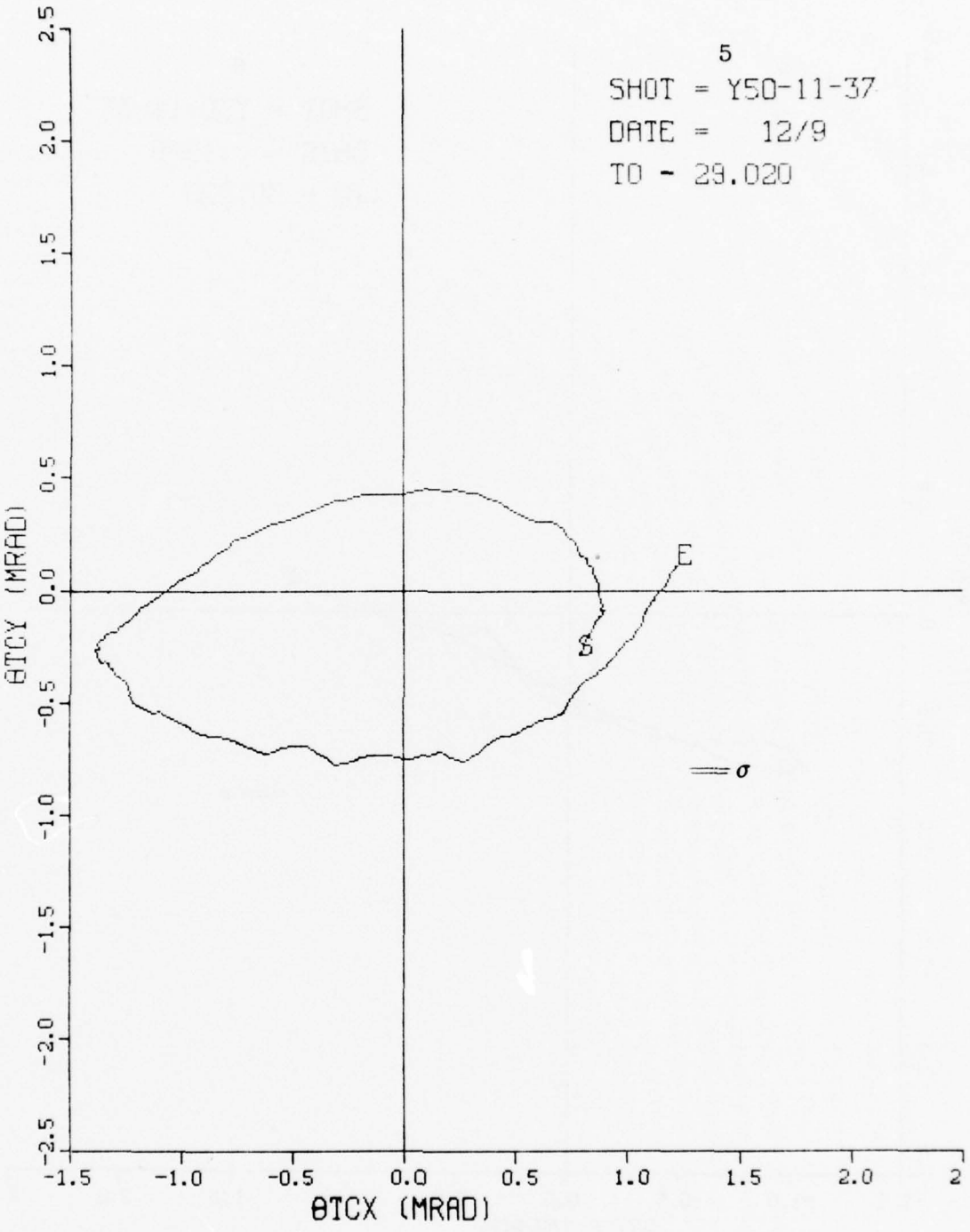

MUZZLE DISPLACEMENT

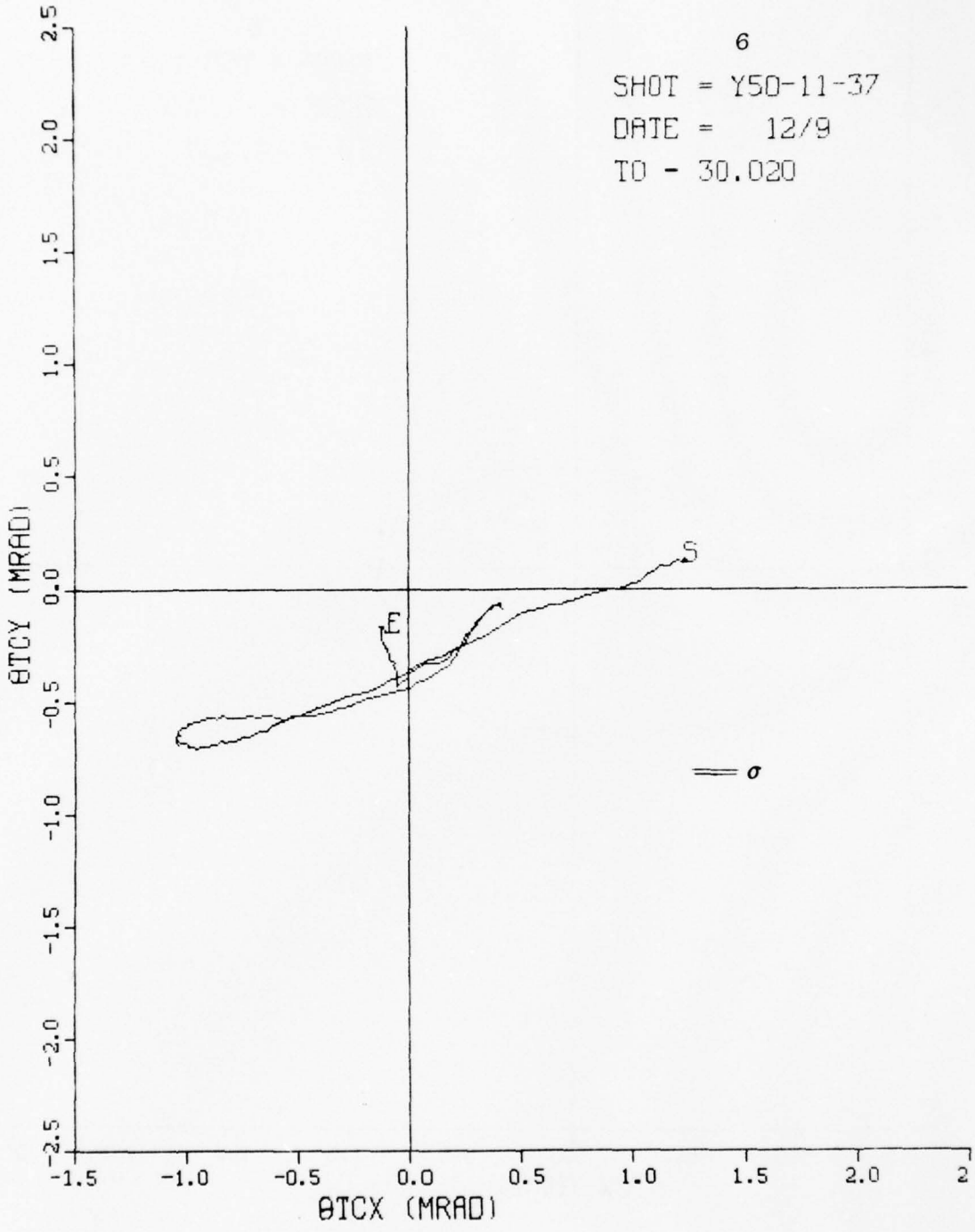

MUZZLE DISPLACEMENT

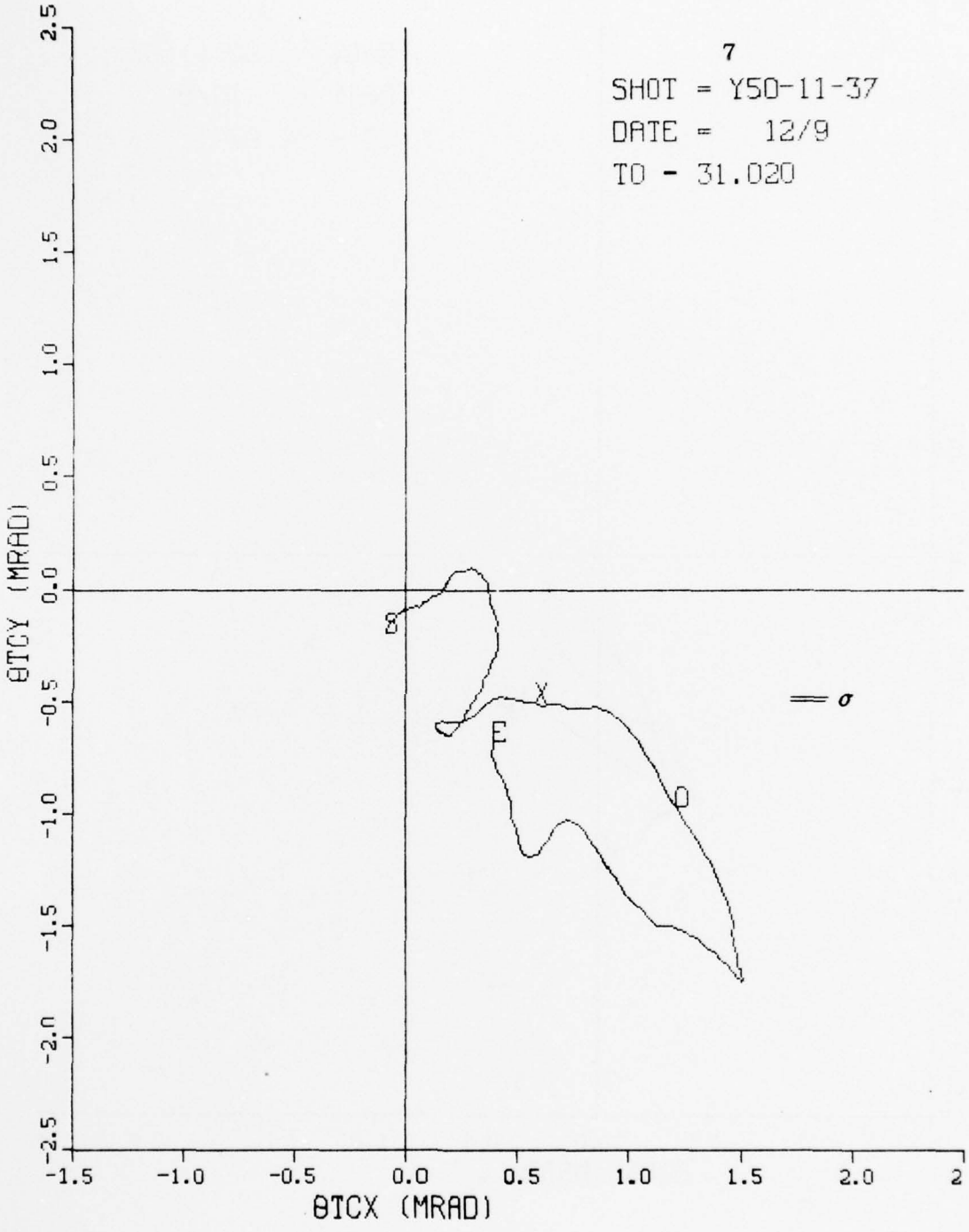

MUZZLE DISPLACEMENT

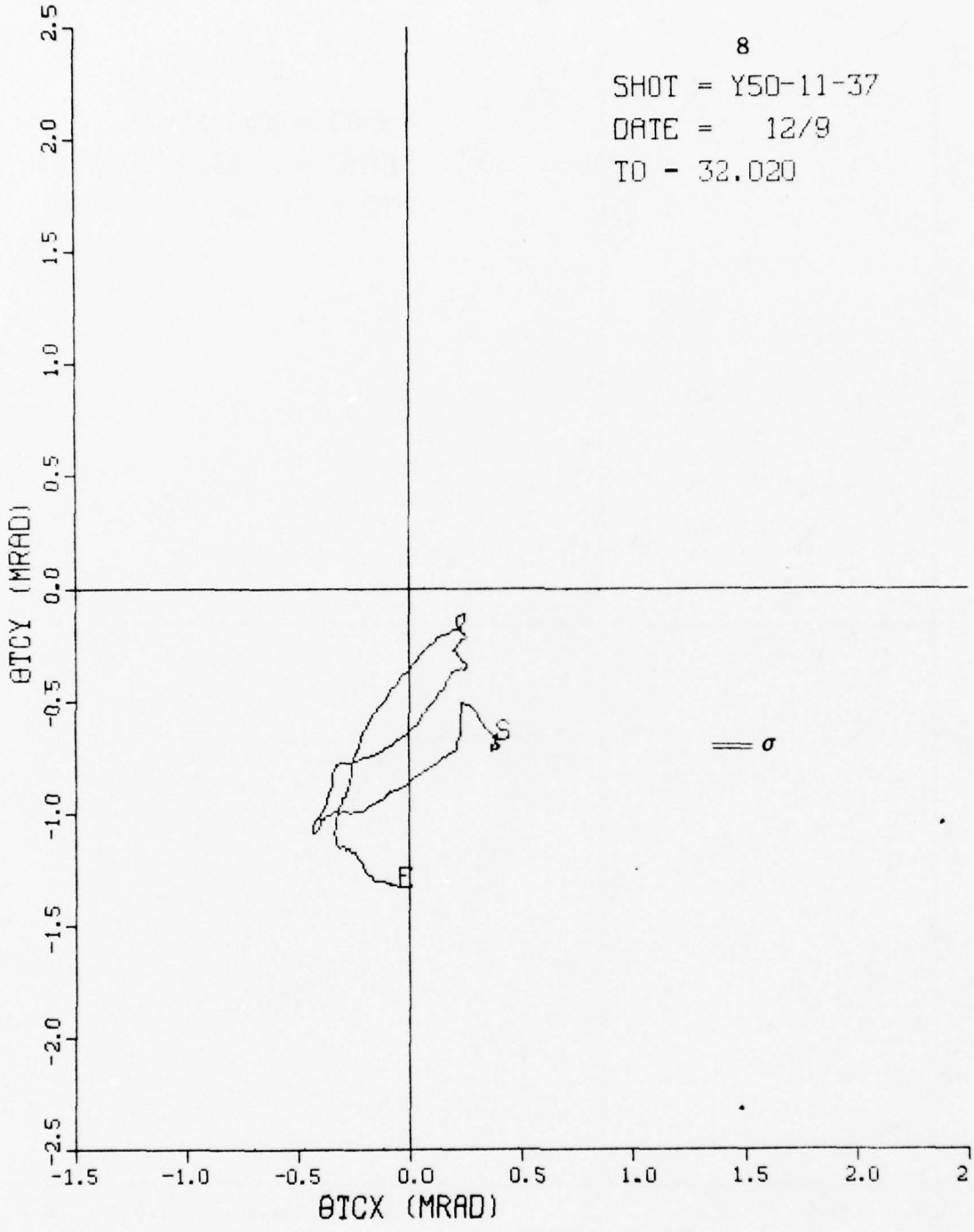

SHOT IDENTIFICATION: 049-11-24
DATE: 12/9/77
ROUND IDENTIFICATION: PROOF SLUG
DATA DROP-OUTS: NONE

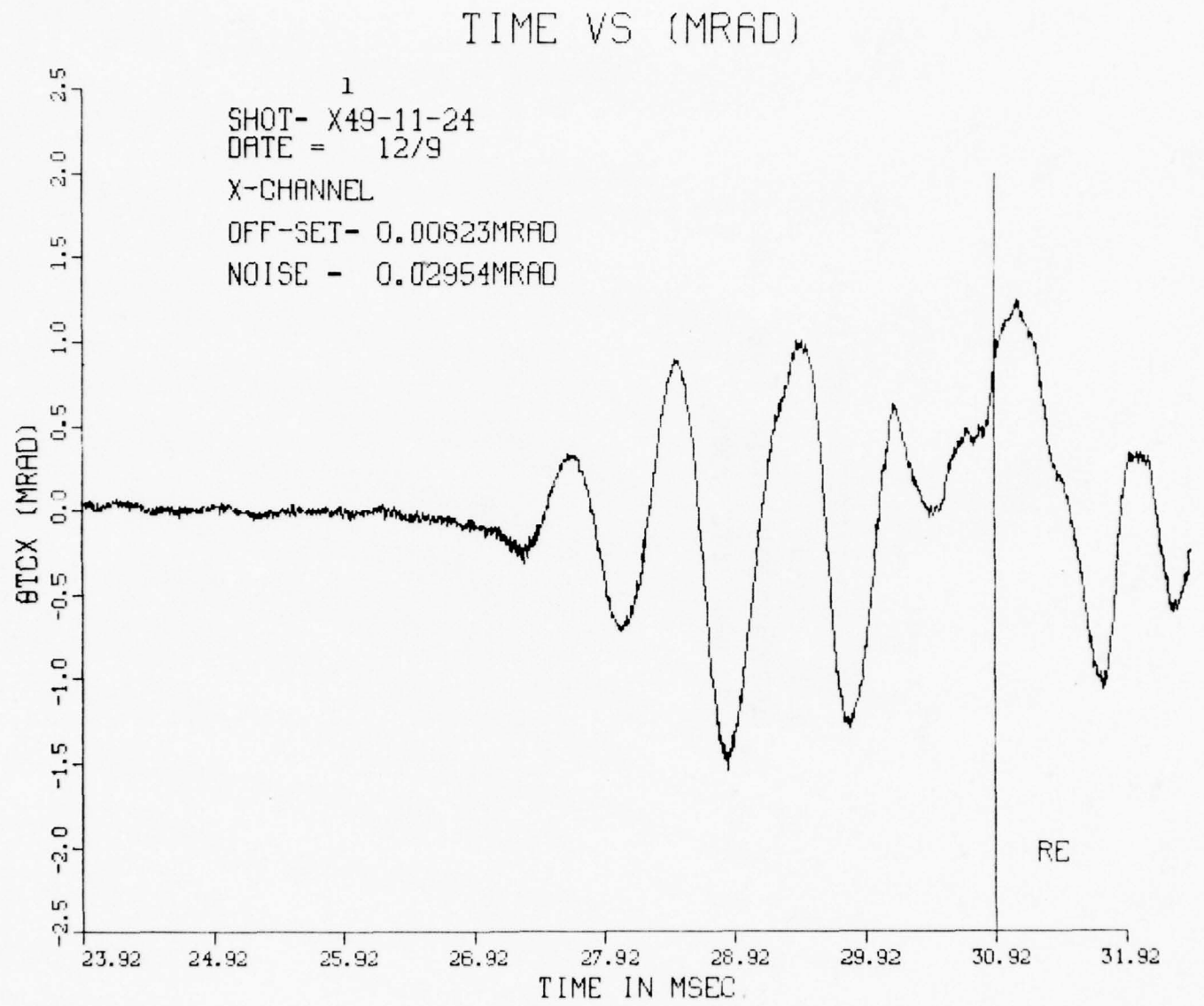
TIME VS (MRAD)
1
SHOT- X49-11-24
DATE = 12/9
X-CHANNEL
OFF-SET- 0.00823MRAD
NOISE - 0.02954MRAD
θTCX (MRAD)
2.5
2.0
1.5
1.0
0.5
0.0
-0.5
-1.0
-1.5
-2.0
-2.5
23.92
24.92
25.92
26.92
27.92
28.92
29.92
30.92
31.92
TIME IN MSEC
RE

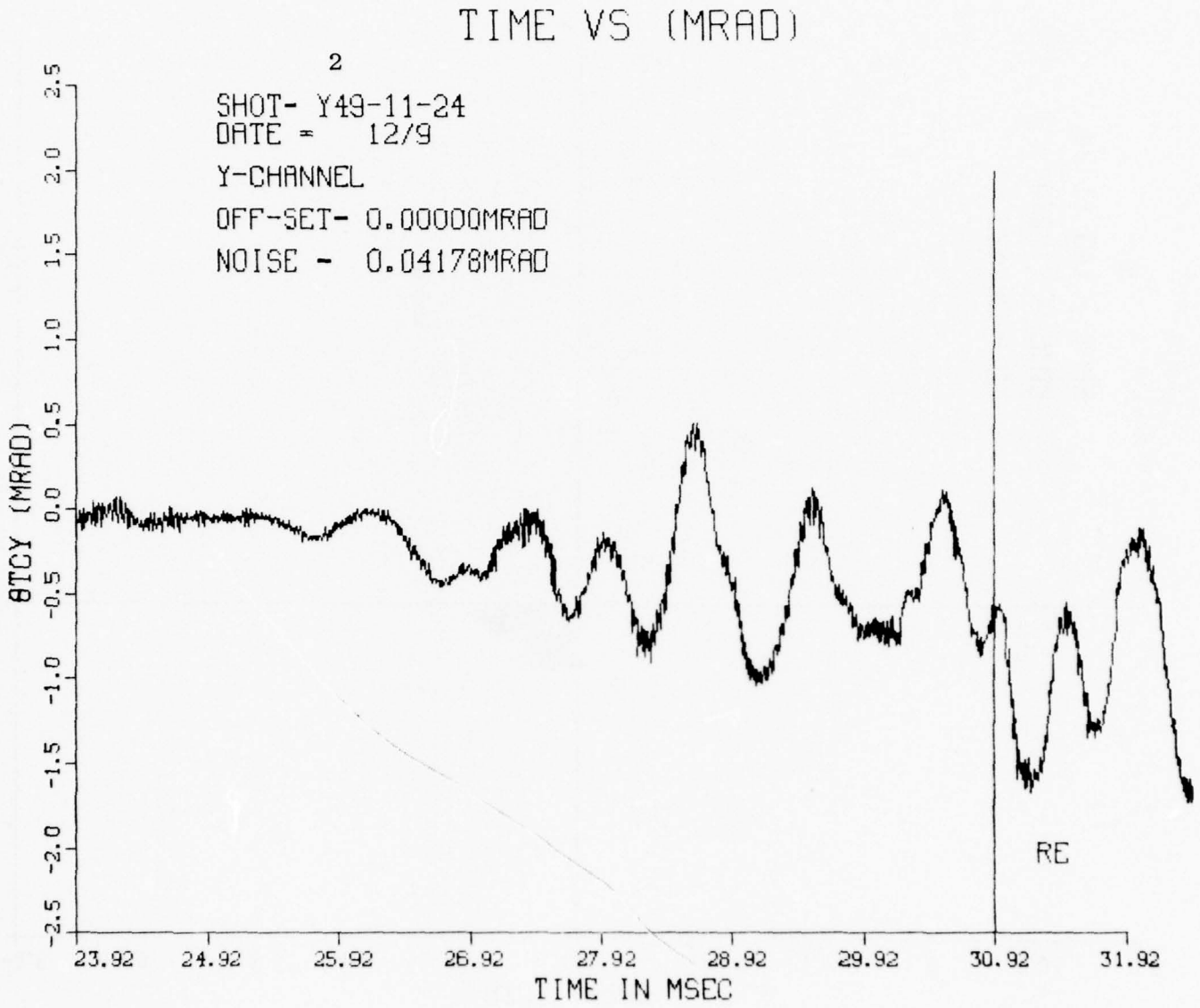
TIME VS (MRAD)
2
SHOT- Y49-11-24
DATE = 12/9
Y-CHANNEL
OFF-SET- 0.00000MRAD
NOISE - 0.04178MRAD
θTCY (MRAD)
2.5
2.0
1.5
1.0
0.5
0.0
-0.5
-1.0
-1.5
-2.0
-2.5
RE
23.92
24.92
25.92
26.92
27.92
28.92
29.92
30.92
31.92
TIME IN MSEC

MUZZLE DISPLACEMENT

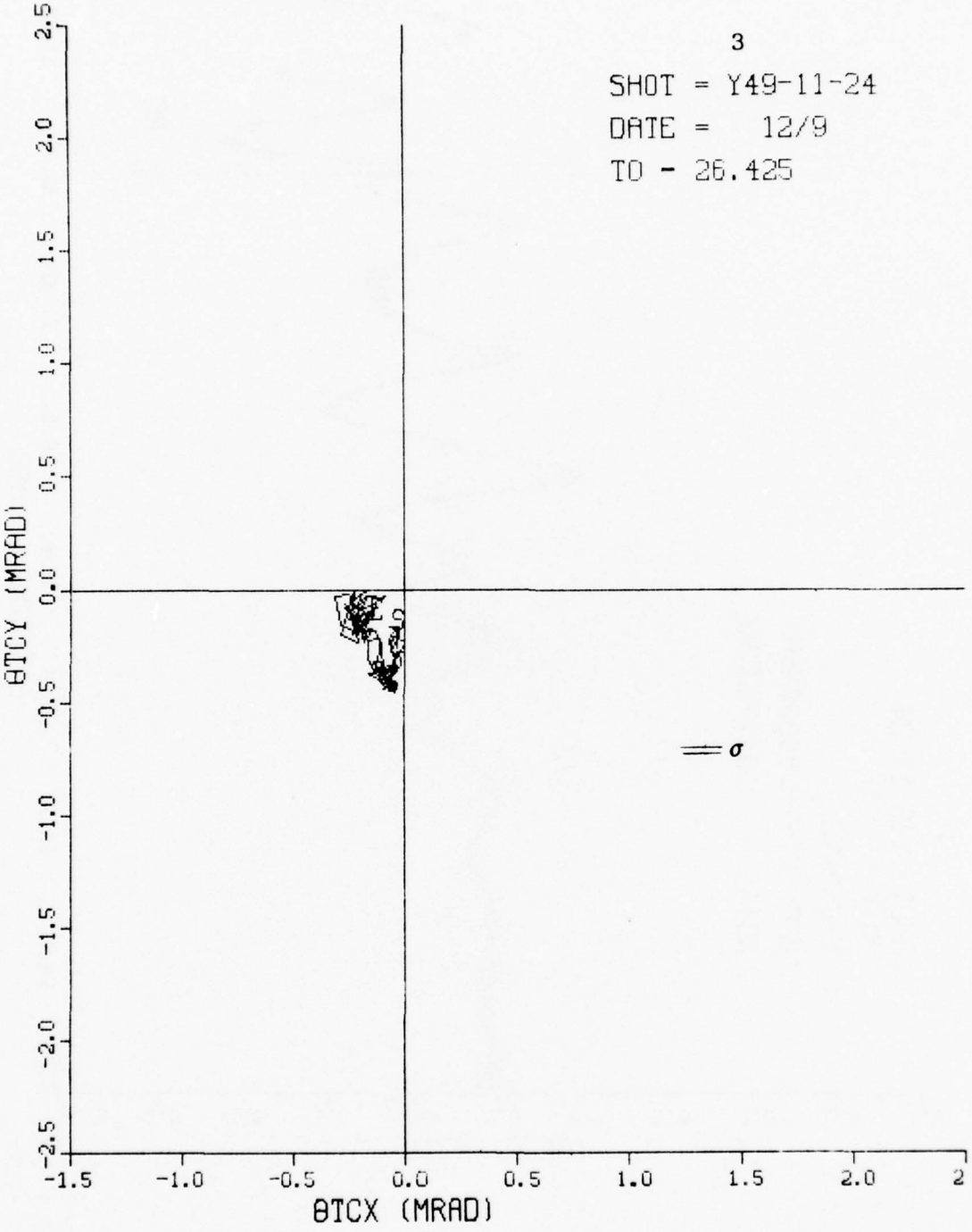

MUZZLE DISPLACEMENT

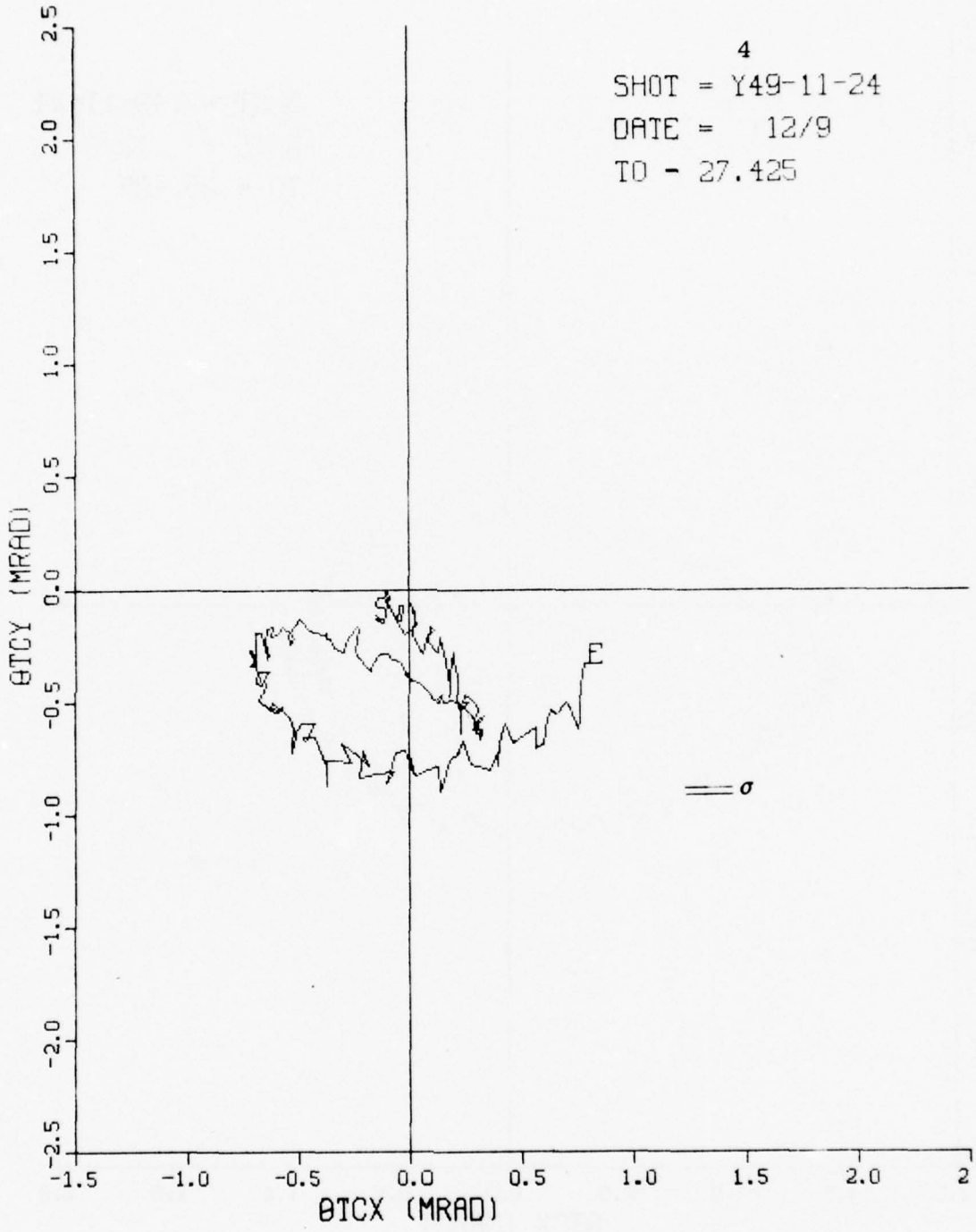

MUZZLE DISPLACEMENT

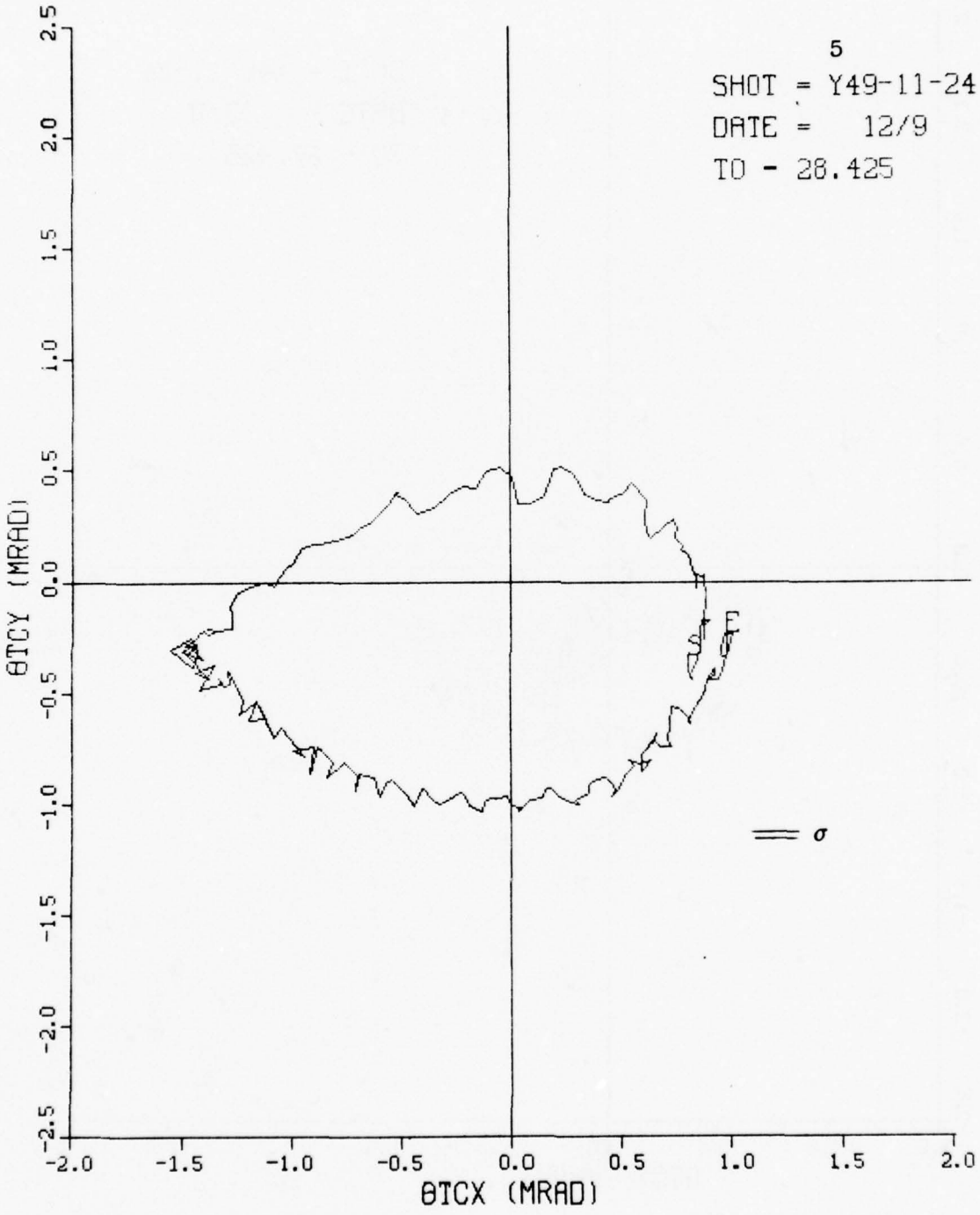

MUZZLE DISPLACEMENT

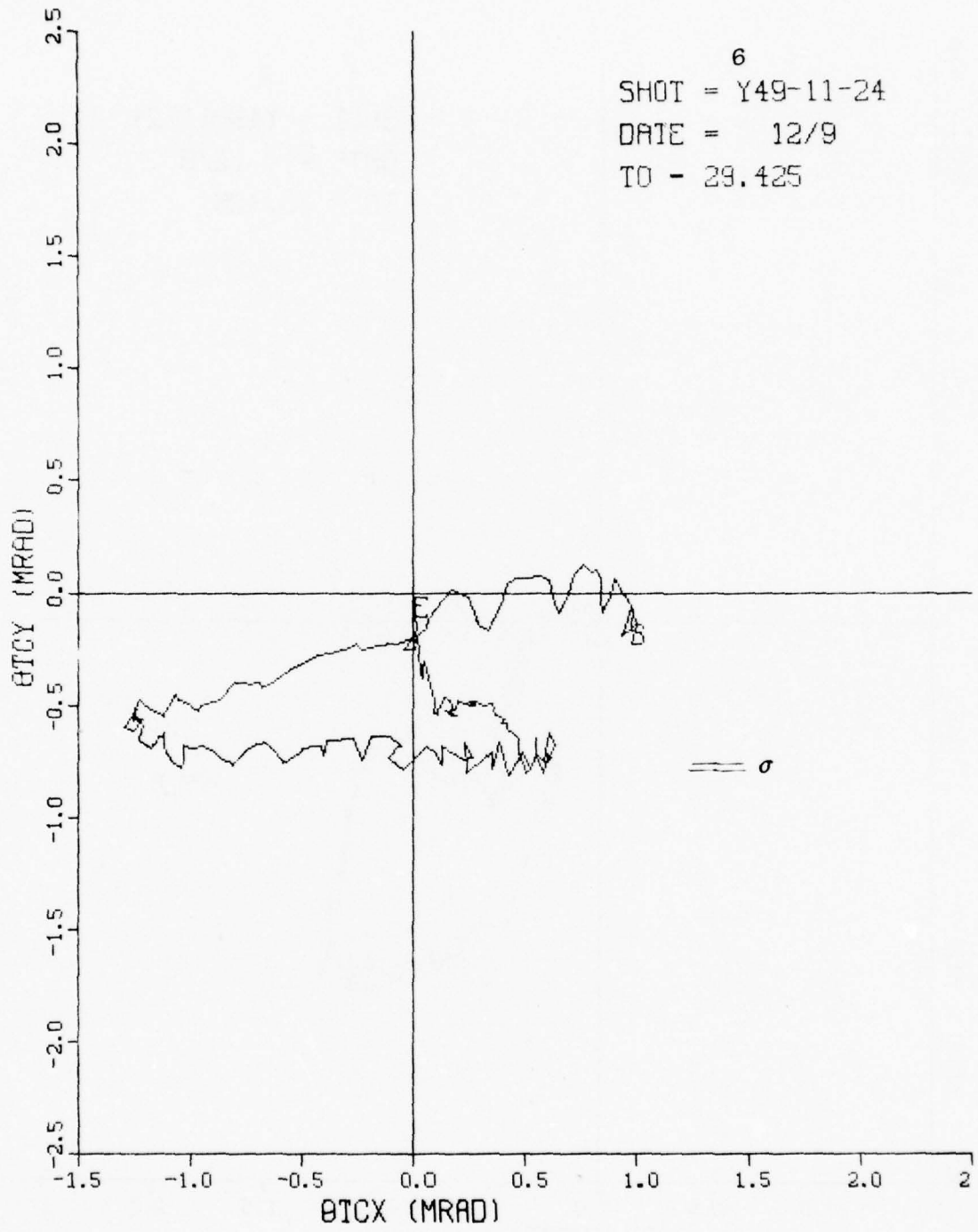

MUZZLE DISPLACEMENT

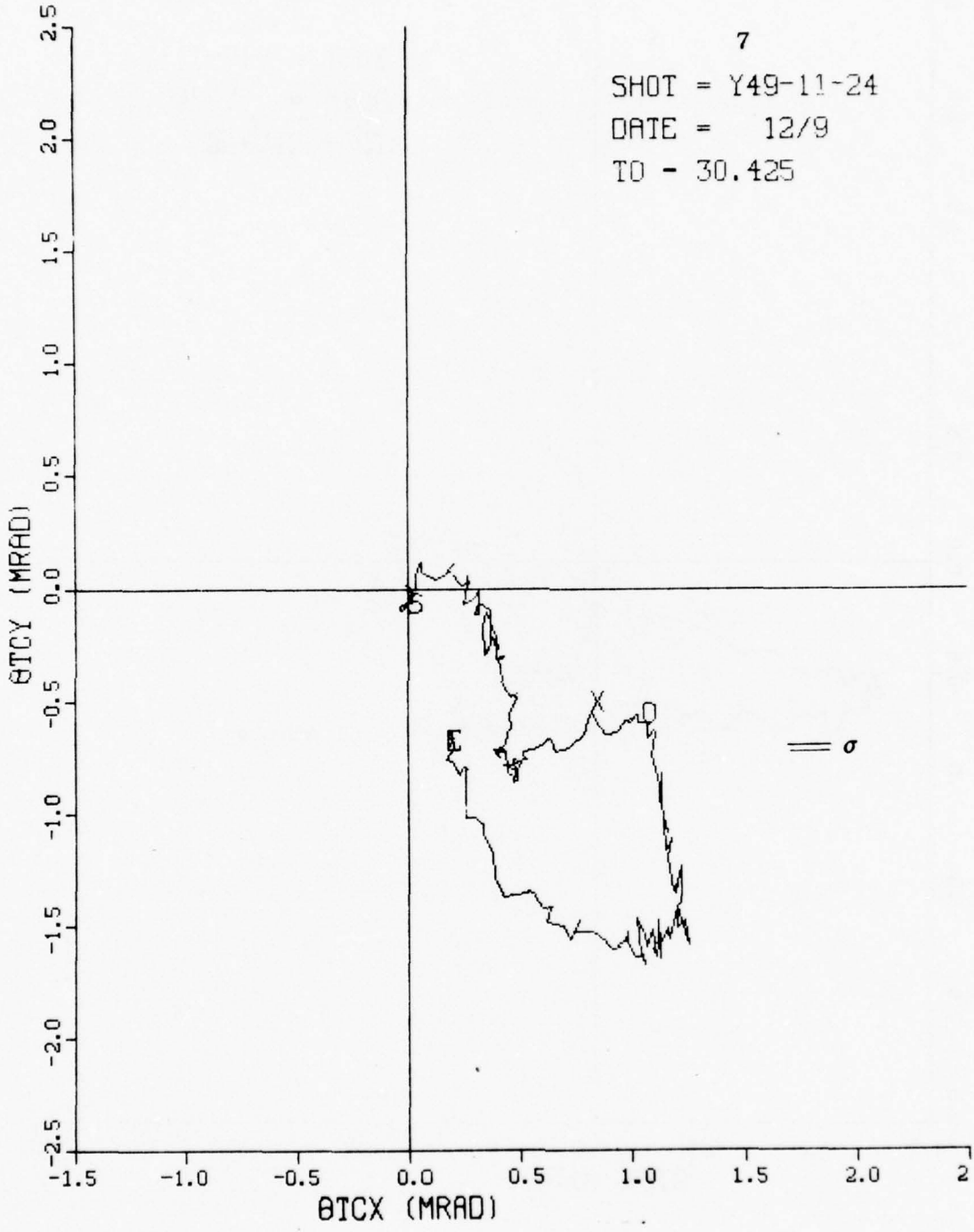

MUZZLE DISPLACEMENT

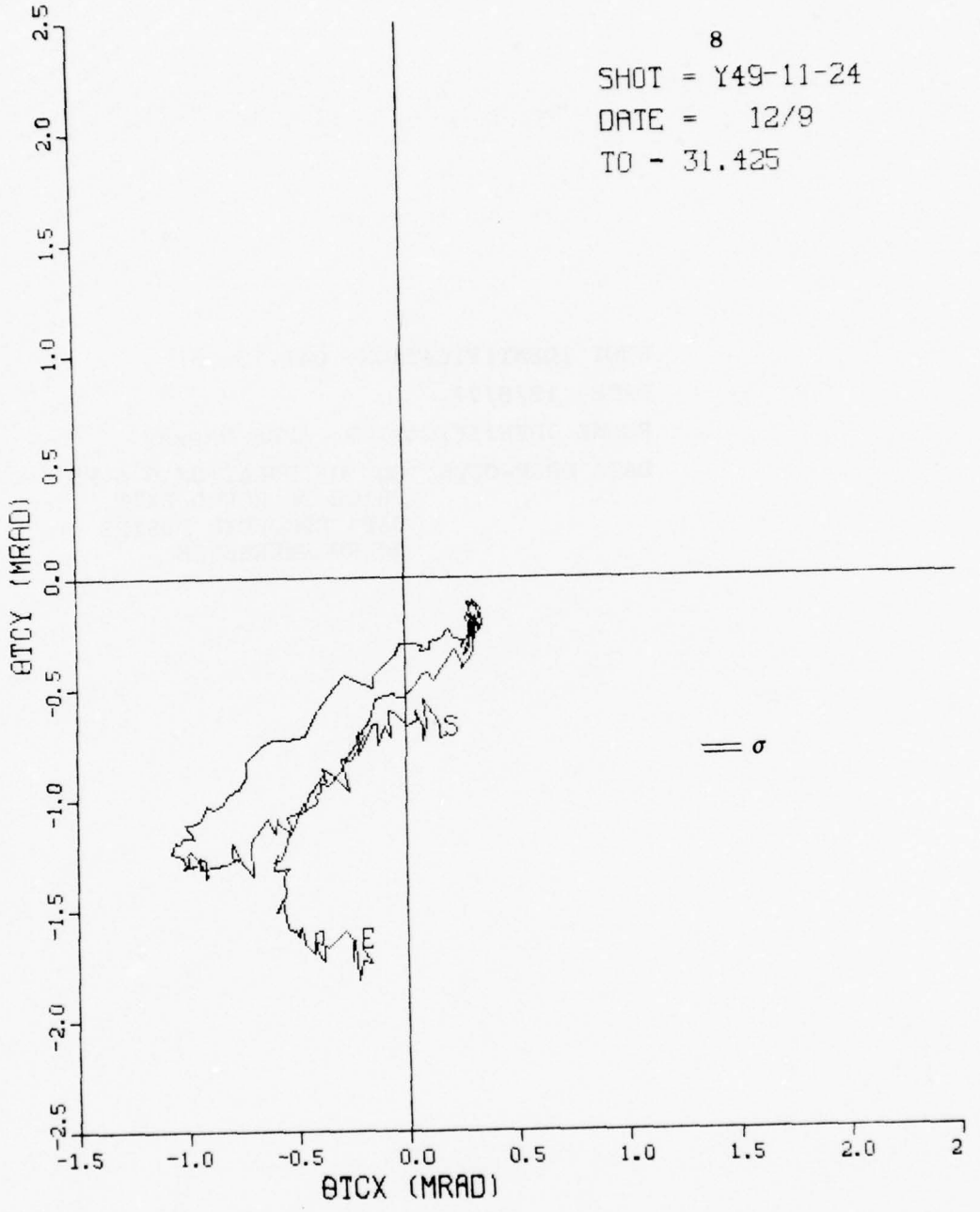

SHOT IDENTIFICATION: 041-13-36

DATE: 12/6/77

ROUND IDENTIFICATION: APDS M392A2

DATA DROP-OUTS: ONE OF DURATION 0.6 MS
PRIOR TO ROUND EXIT.
DATA RECORDED DURING
ROUND EMERGENCE

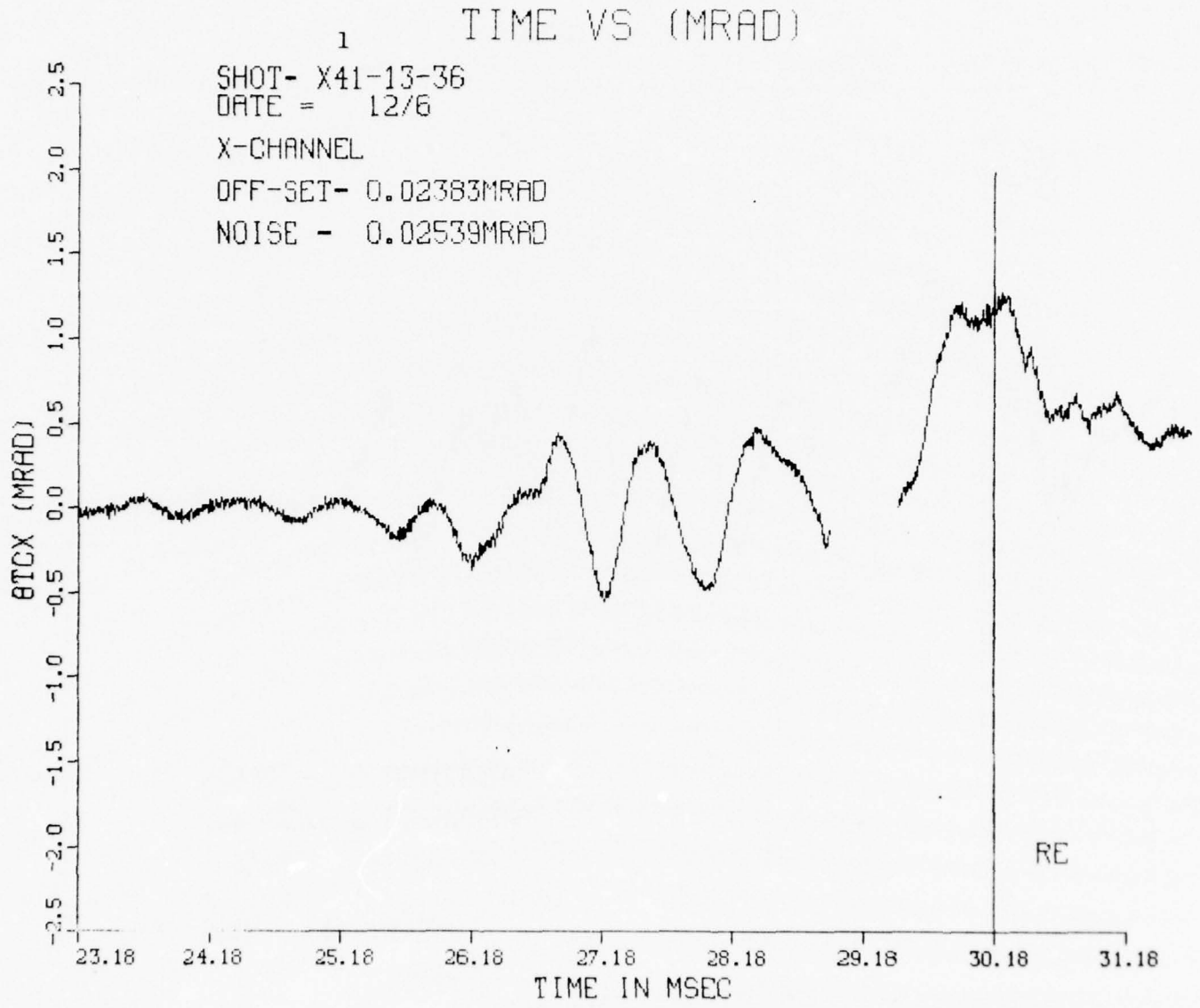
TIME VS (MRAD)
1
SHOT- X41-13-36
DATE = 12/6
X-CHANNEL
OFF-SET- 0.02383MRAD
NOISE - 0.02539MRAD
θTCX (MRAD)
2.5
2.0
1.5
1.0
0.5
0.0
-0.5
-1.0
-1.5
-2.0
-2.5
23.18
24.18
25.18
26.18
27.18
28.18
29.18
30.18
31.18
TIME IN MSEC
RE

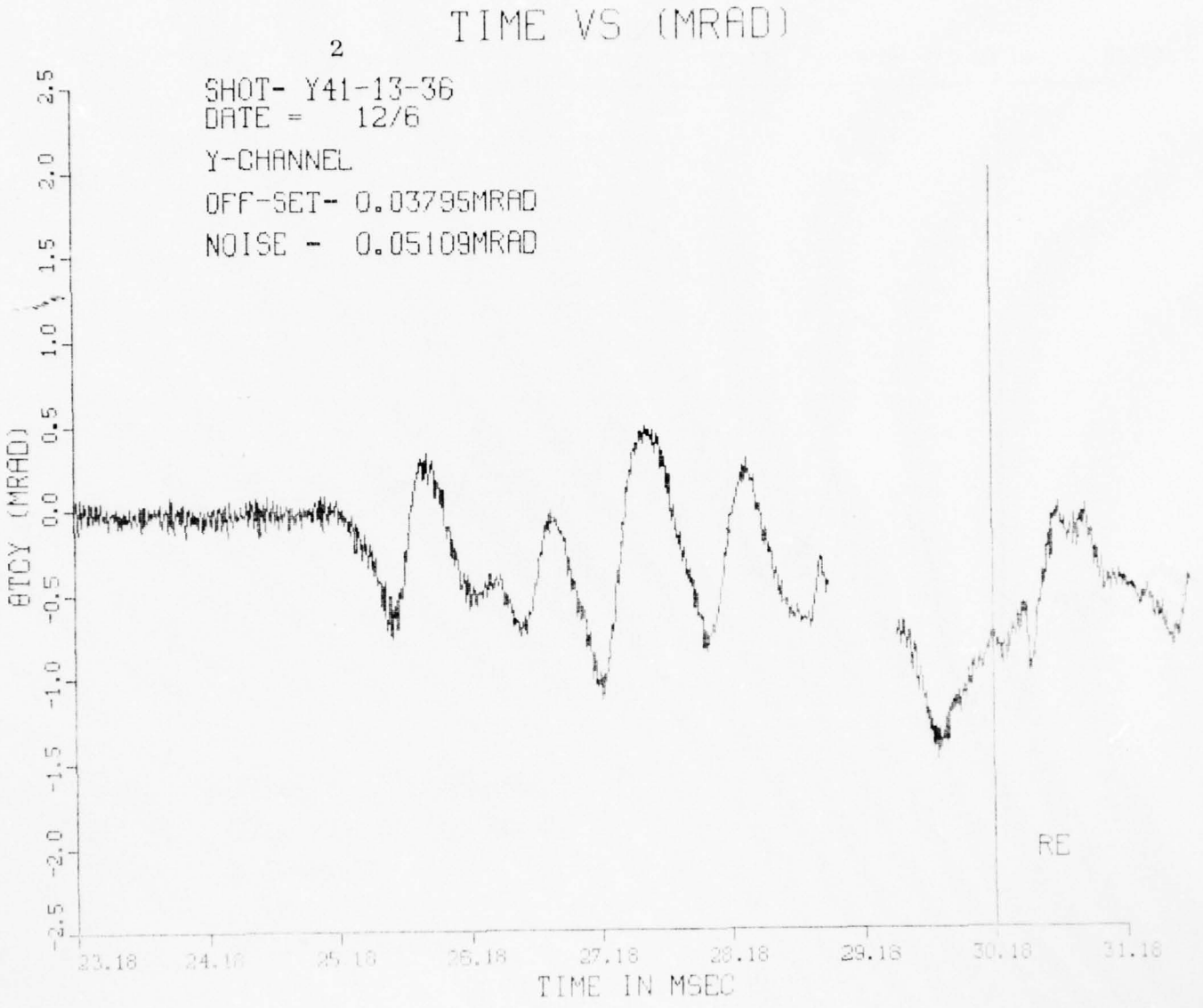
TIME VS (MRAD)
2
SHOT- Y41-13-36
DATE = 12/6
Y-CHANNEL
OFF-SET- 0.03795MRAD
NOISE - 0.05109MRAD
ATCY (MRAD)
2.5
2.0
1.5
1.0
0.5
0.0
-0.5
-1.0
-1.5
-2.0
-2.5
23.18
24.18
25.18
26.18
27.18
28.18
29.18
30.18
31.18
TIME IN MSEC
RE

MUZZLE DISPLACEMENT

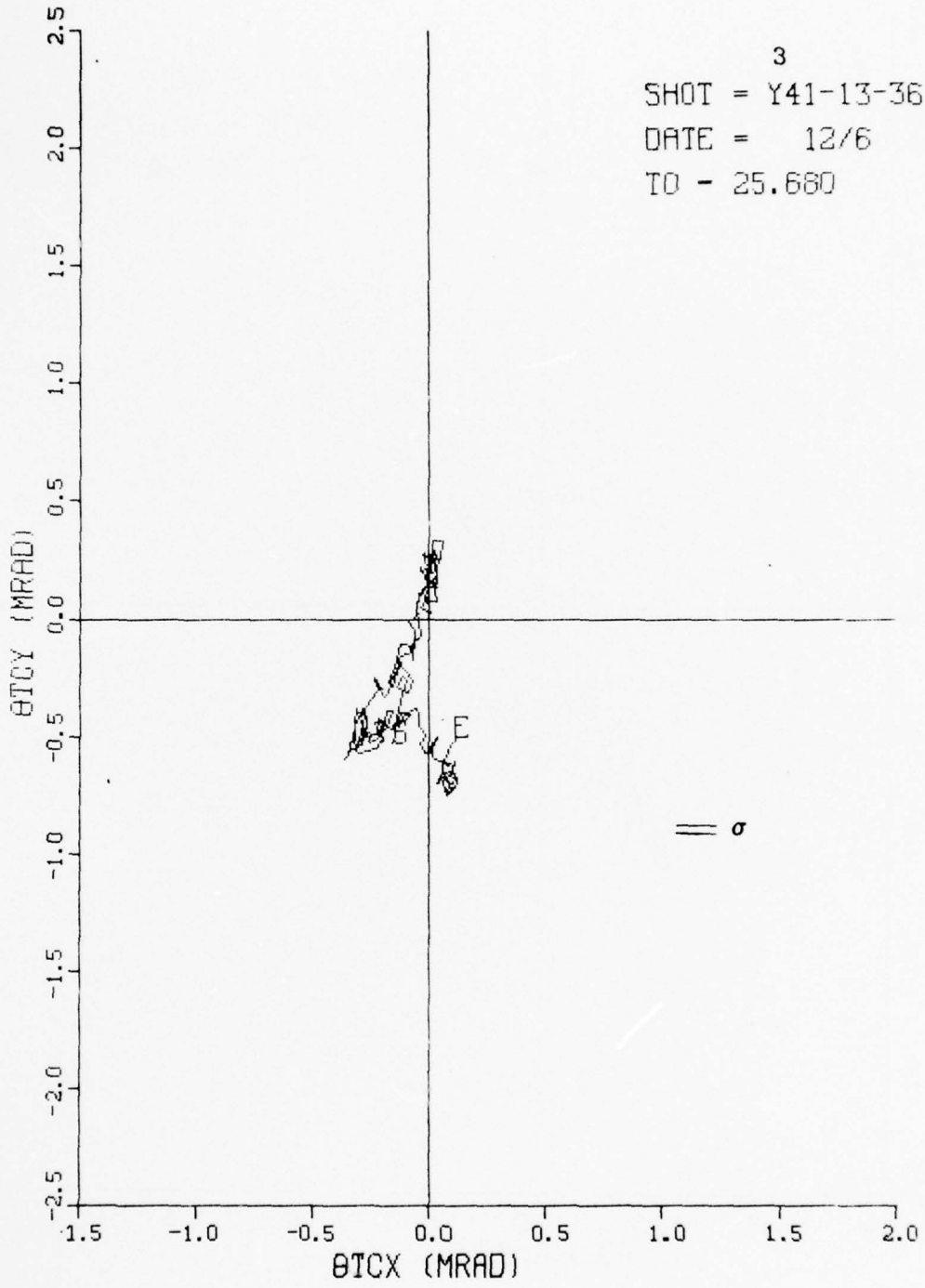

MUZZLE DISPLACEMENT

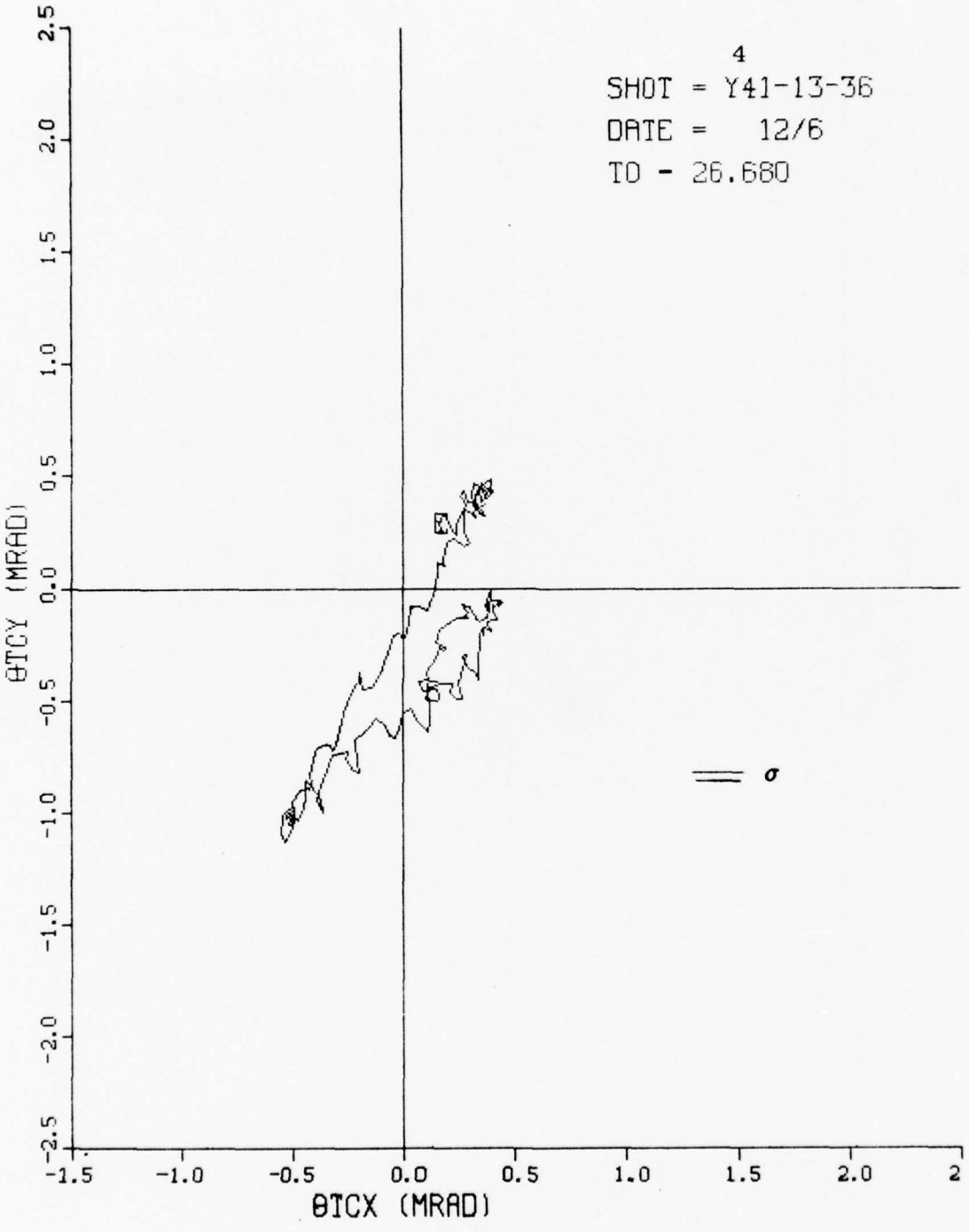

MUZZLE DISPLACEMENT

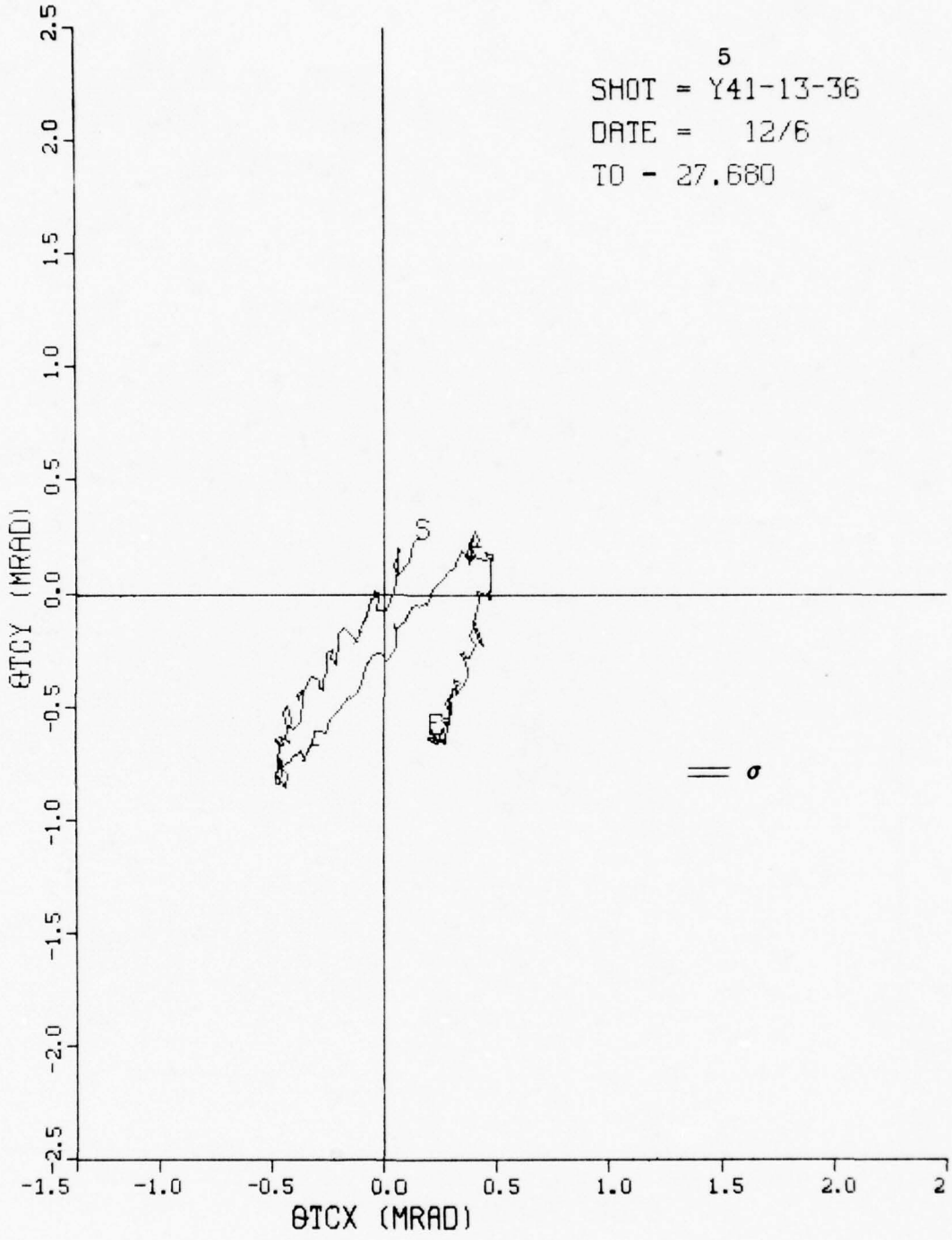

MUZZLE DISPLACEMENT

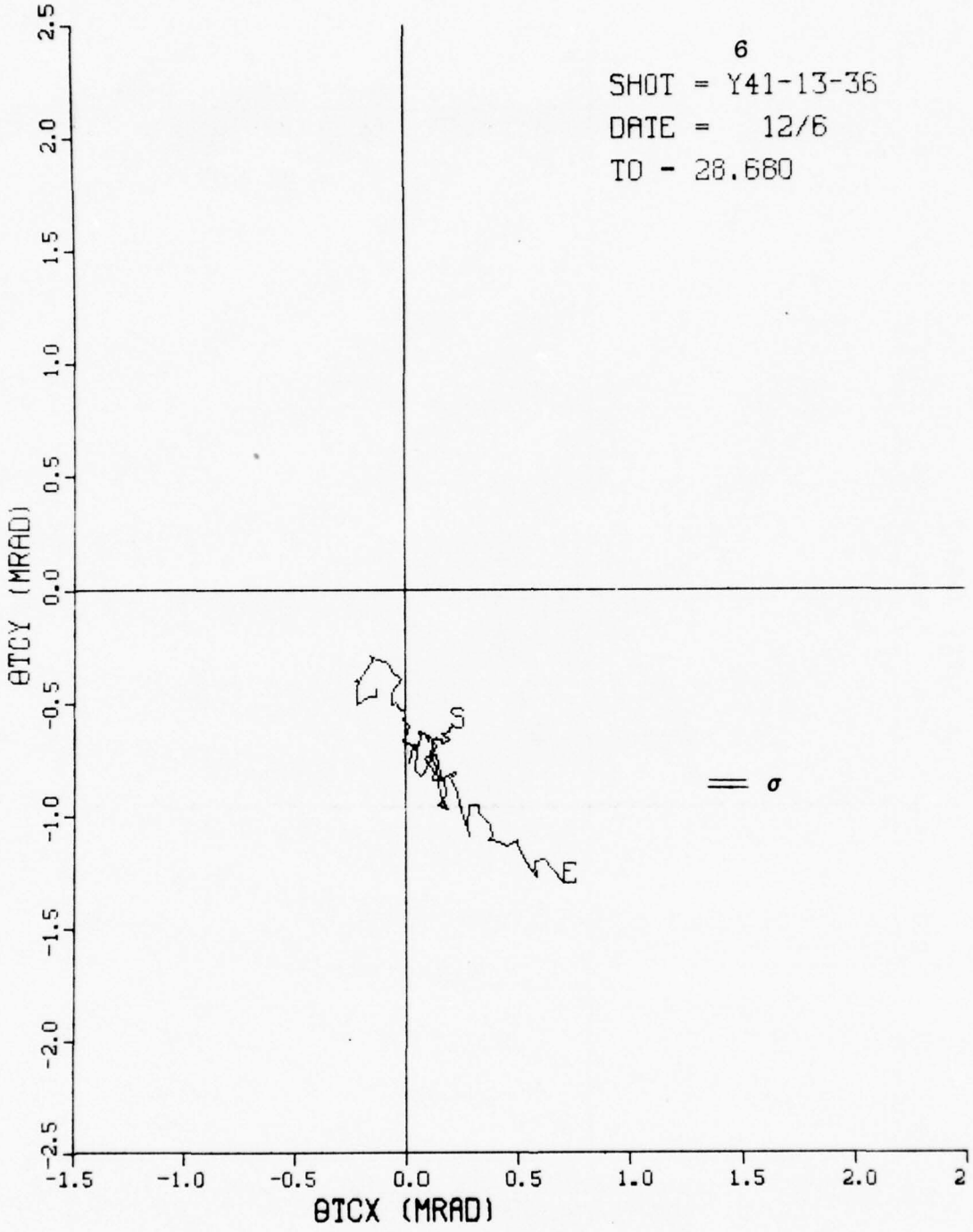

MUZZLE DISPLACEMENT

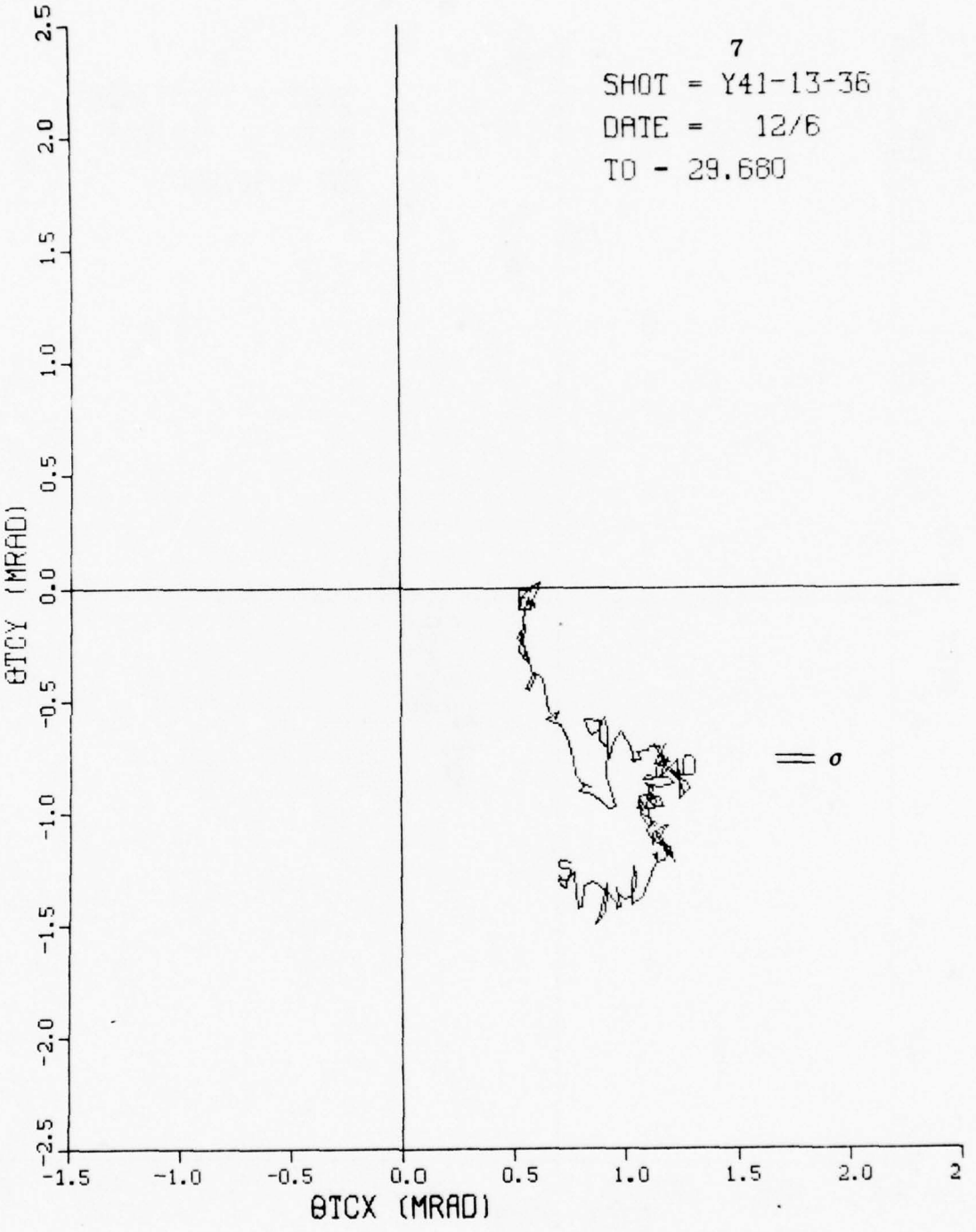

MUZZLE DISPLACEMENT

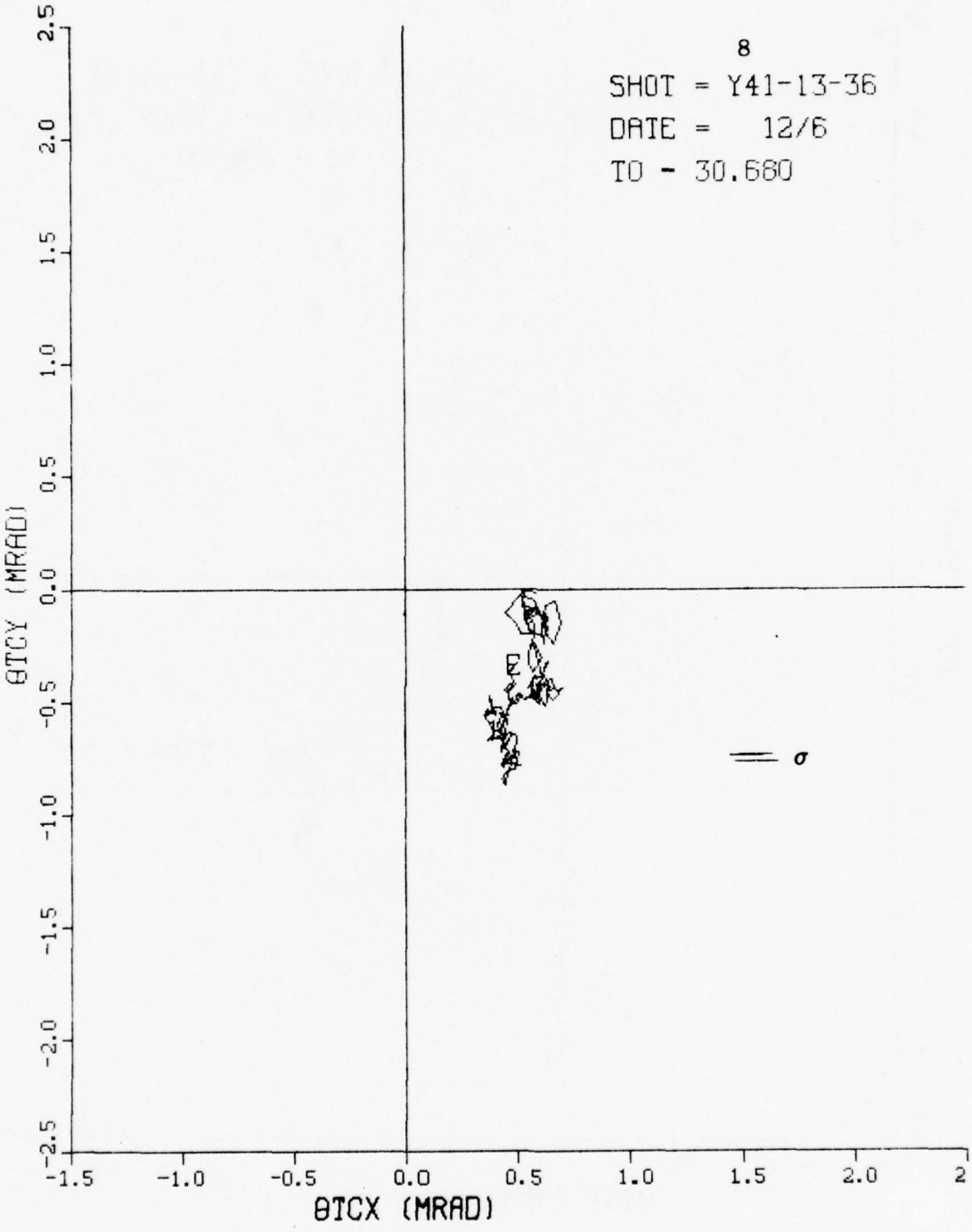

SHOT IDENTIFICATION: 042-09-56

DATE: 12/7/77

ROUND IDENTIFICATION: APDS M392A2

DATA DROP-OUTS: ONE OF DURATION 1.1 MS PRIOR TO ROUND EXIT; ONE AFTER ROUND EXIT OF DURATION 0.7 MS; DATA RECORDED DURING ROUND EMERGENCE

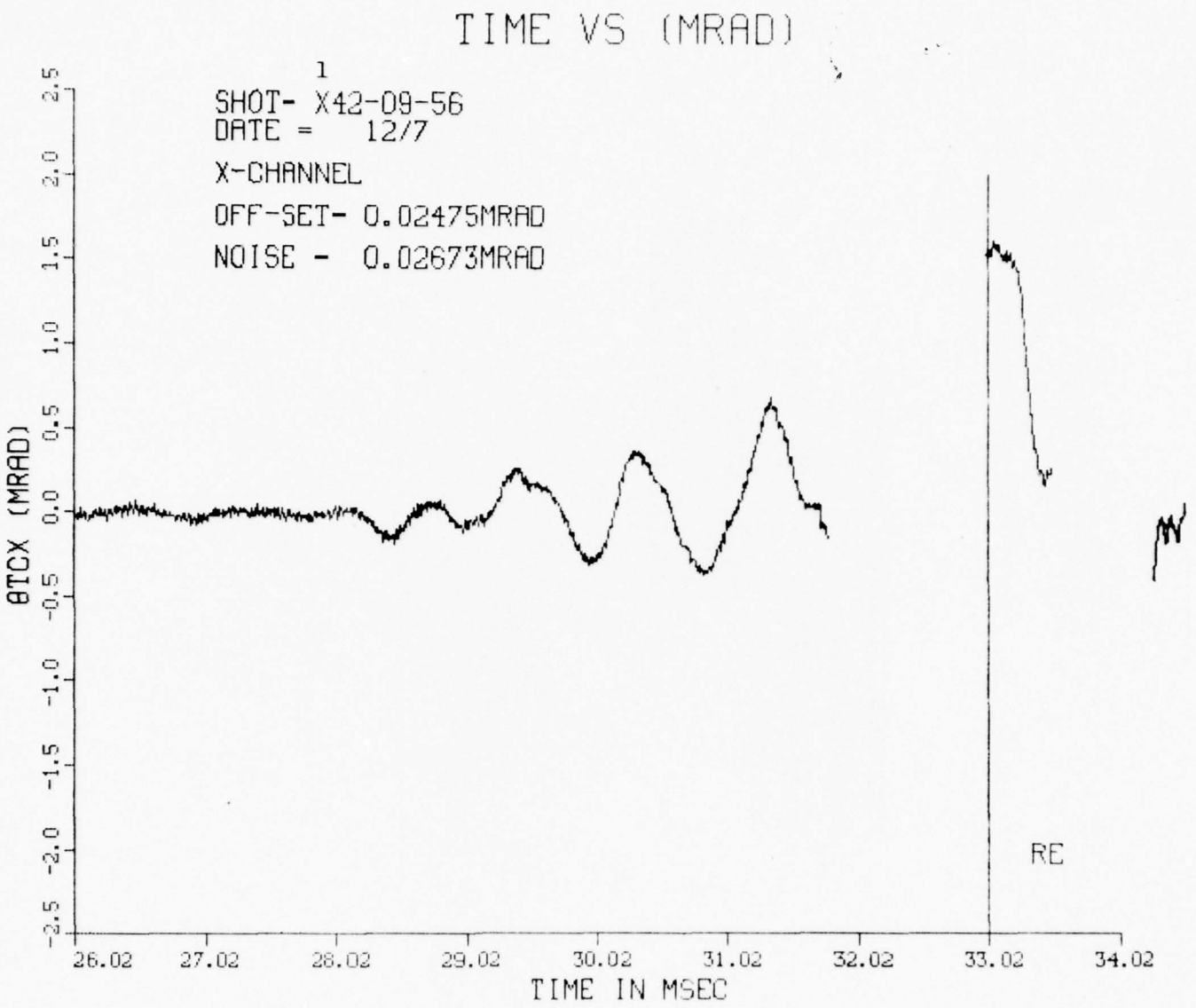
TIME VS (MRAD)
1
SHOT- X42-09-56
DATE = 12/7
X-CHANNEL
OFF-SET- 0.02475MRAD
NOISE - 0.02673MRAD
θTCX (MRAD)
2.5
2.0
1.5
1.0
0.5
0.0
-0.5
-1.0
-1.5
-2.0
-2.5
RE
26.02
27.02
28.02
29.02
30.02
31.02
32.02
33.02
34.02
TIME IN MSEC

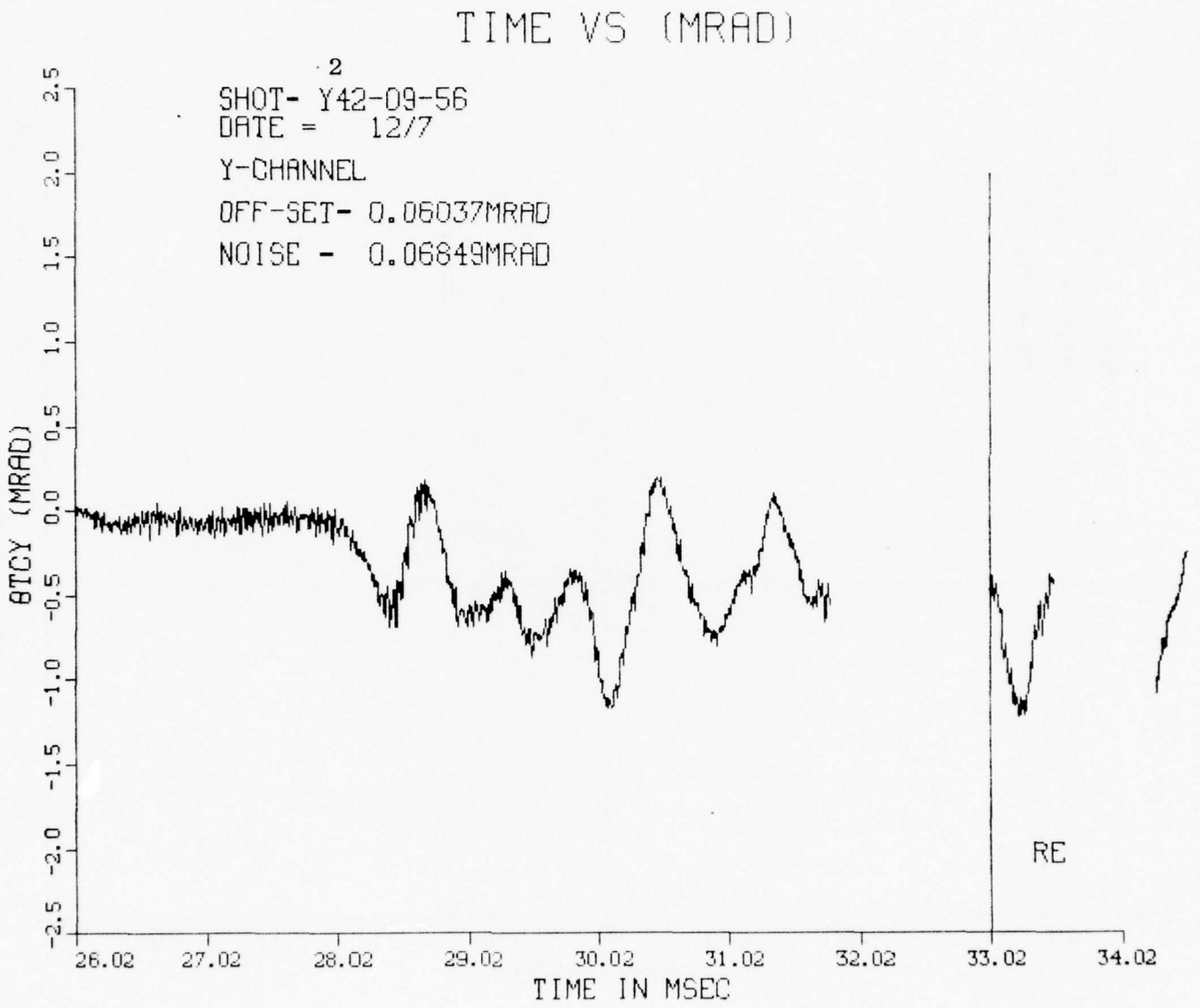
TIME VS (MRAD)
2
SHOT- Y42-09-56
DATE = 12/7
Y-CHANNEL
OFF-SET- 0.06037MRAD
NOISE - 0.06849MRAD
θTCY (MRAD)
2.5
2.0
1.5
1.0
0.5
0.0
-0.5
-1.0
-1.5
-2.0
-2.5
RE
26.02
27.02
28.02
29.02
30.02
31.02
32.02
33.02
34.02
TIME IN MSEC

MUZZLE DISPLACEMENT

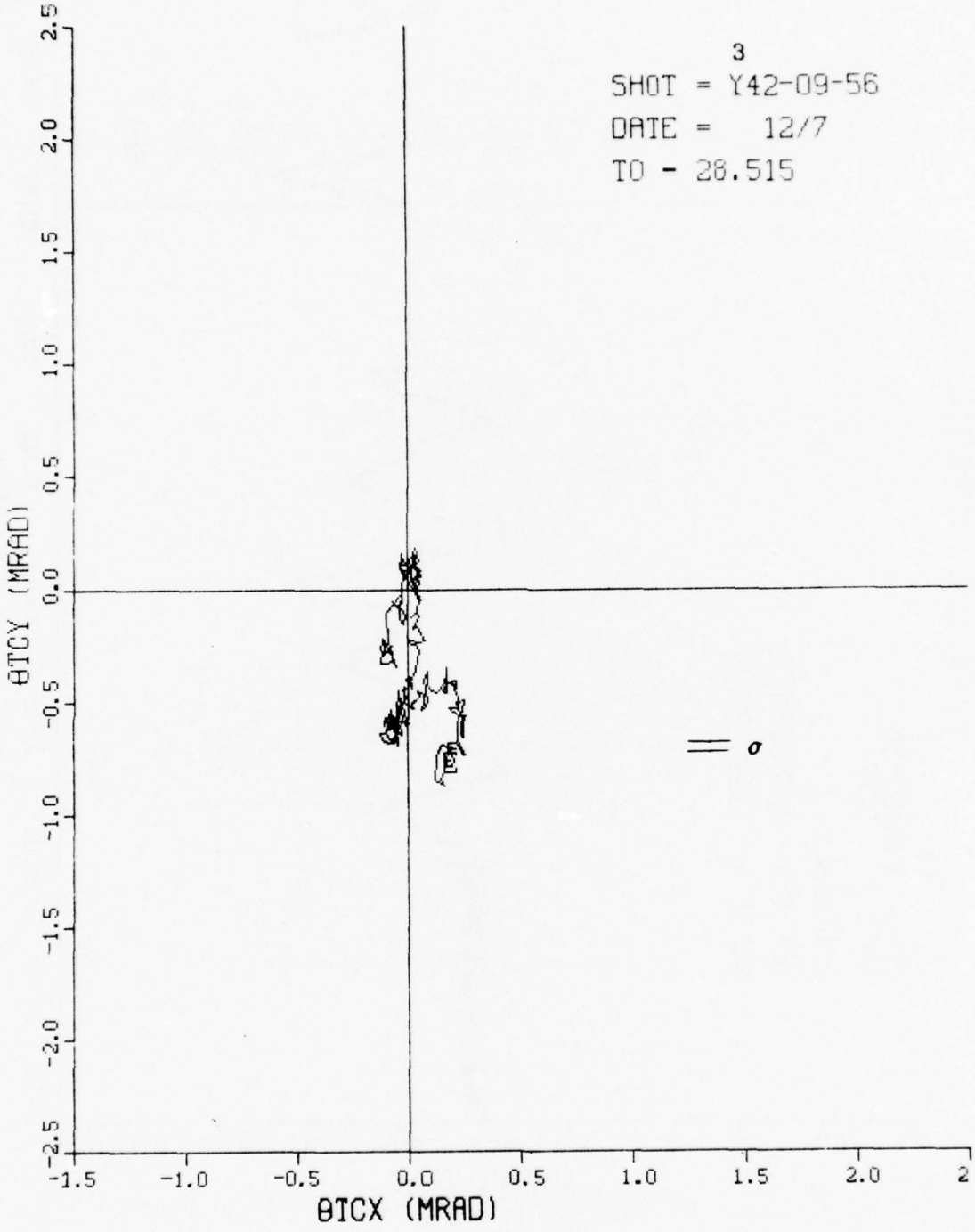

MUZZLE DISPLACEMENT

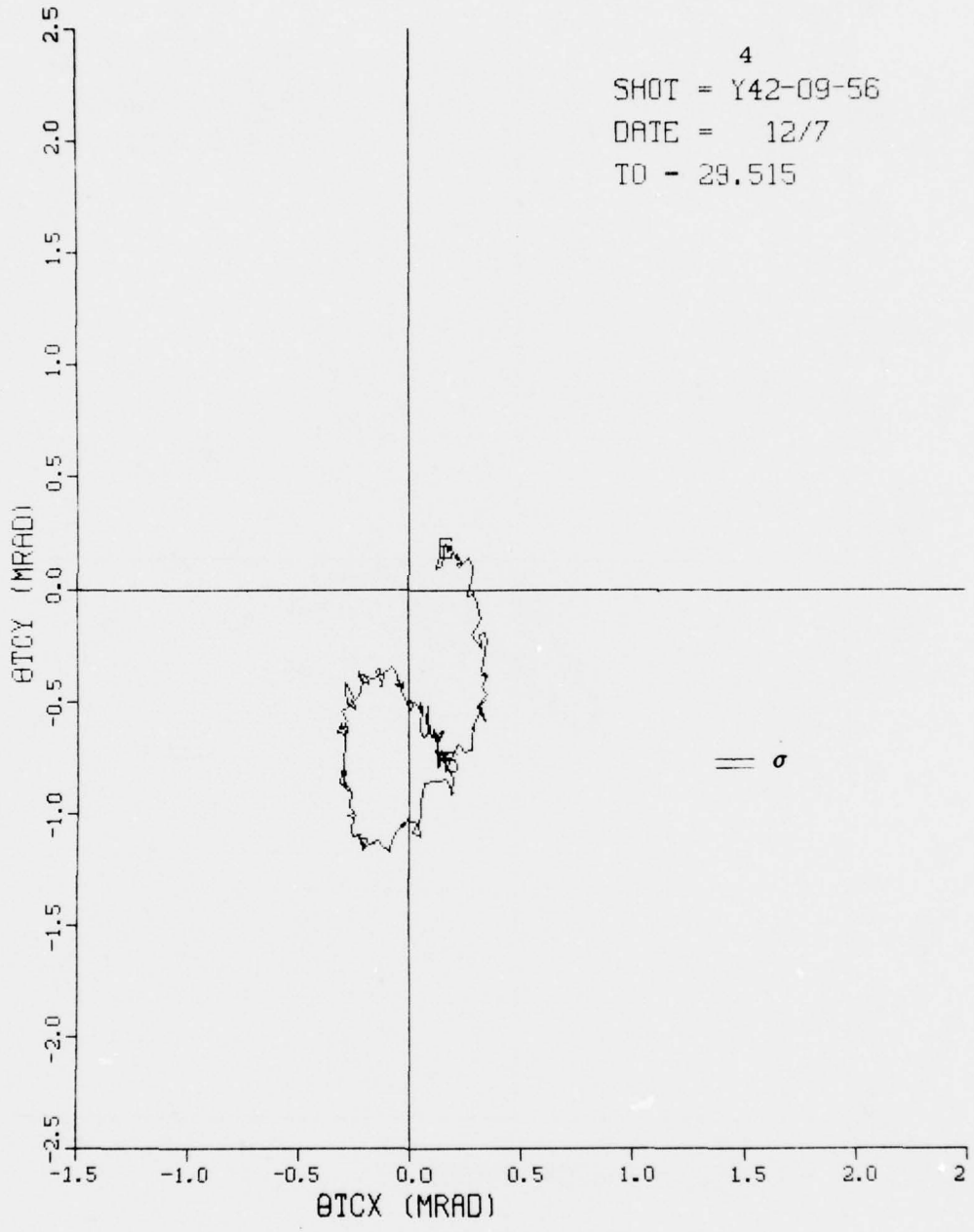

MUZZLE DISPLACEMENT

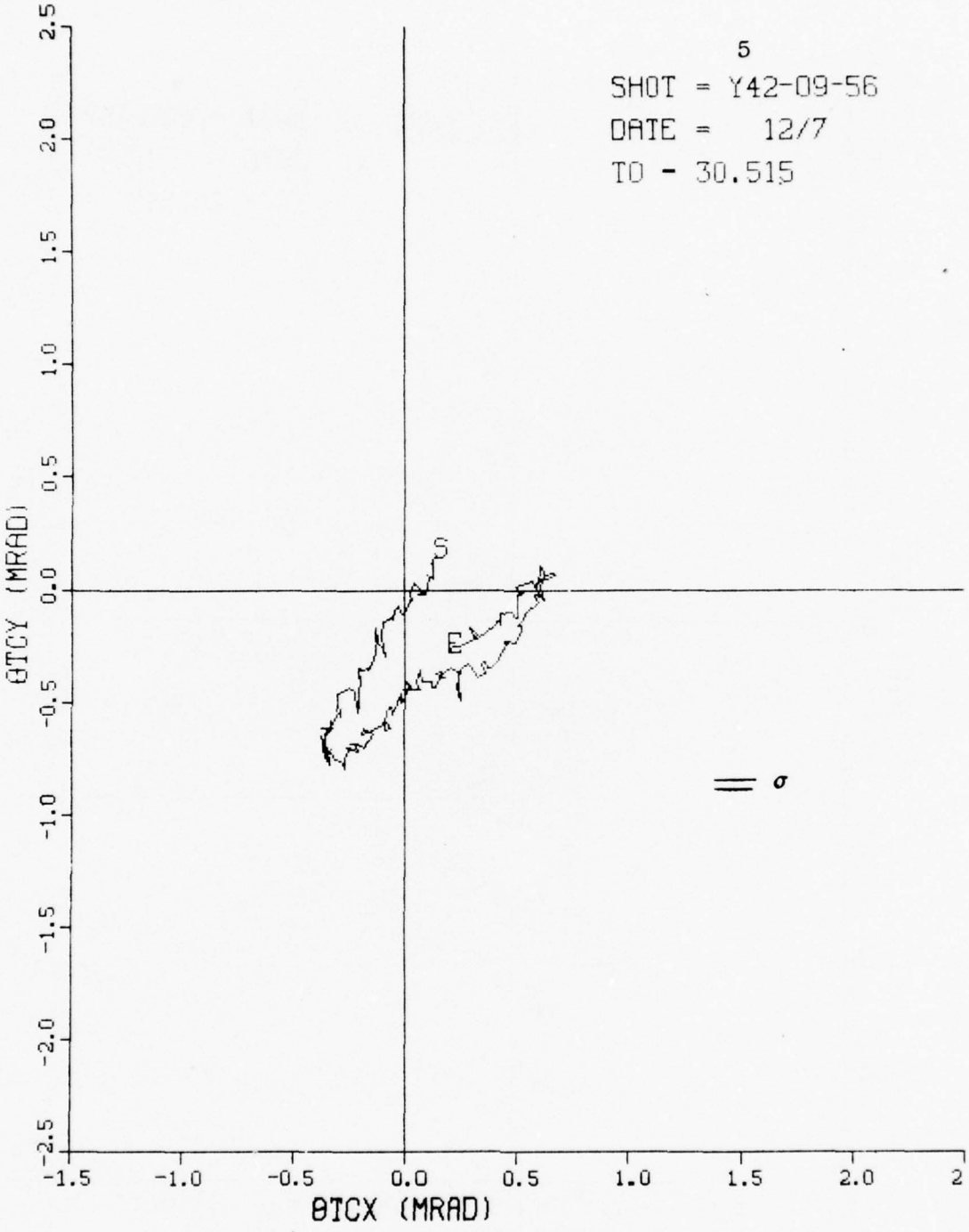

MUZZLE DISPLACEMENT

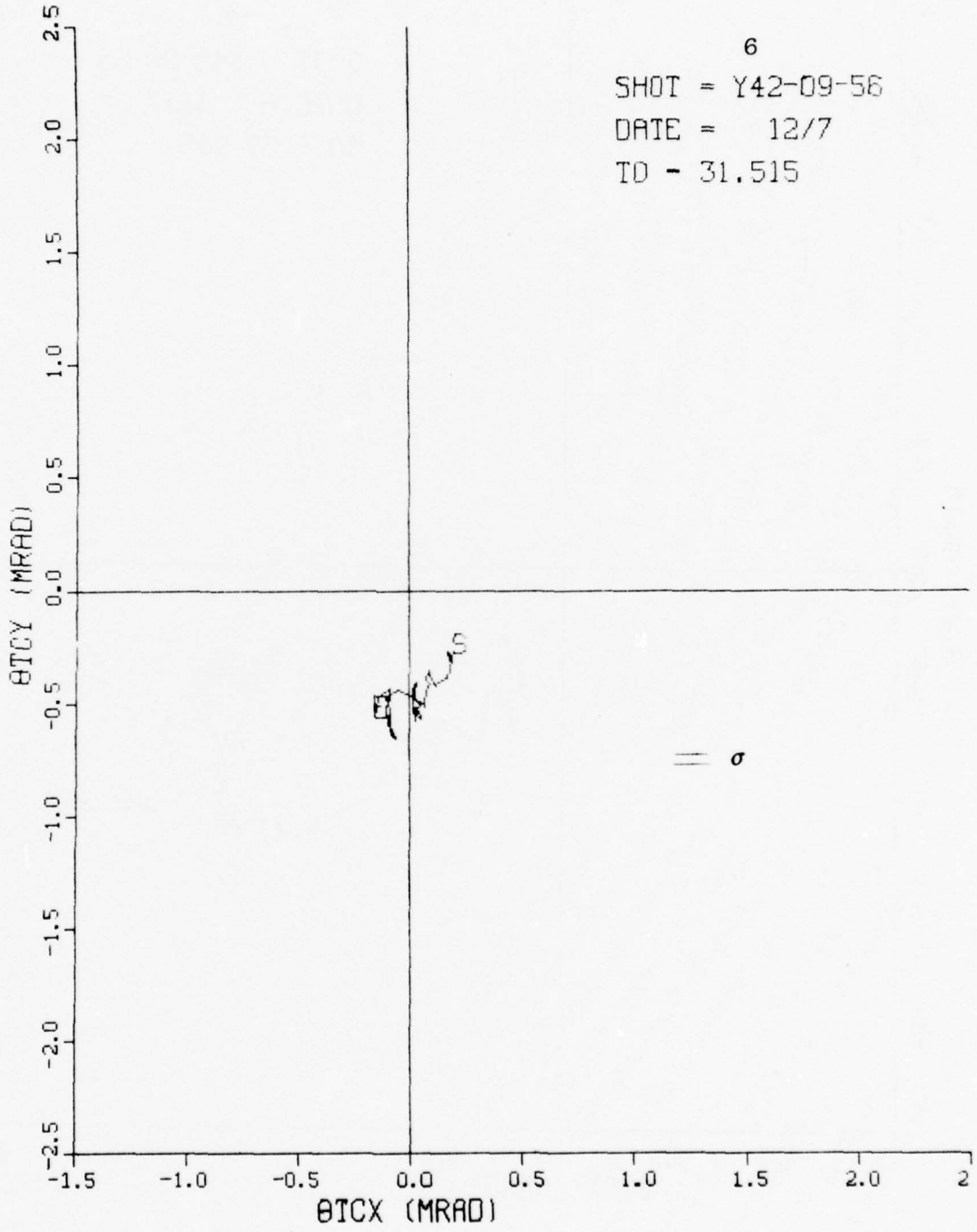

MUZZLE DISPLACEMENT

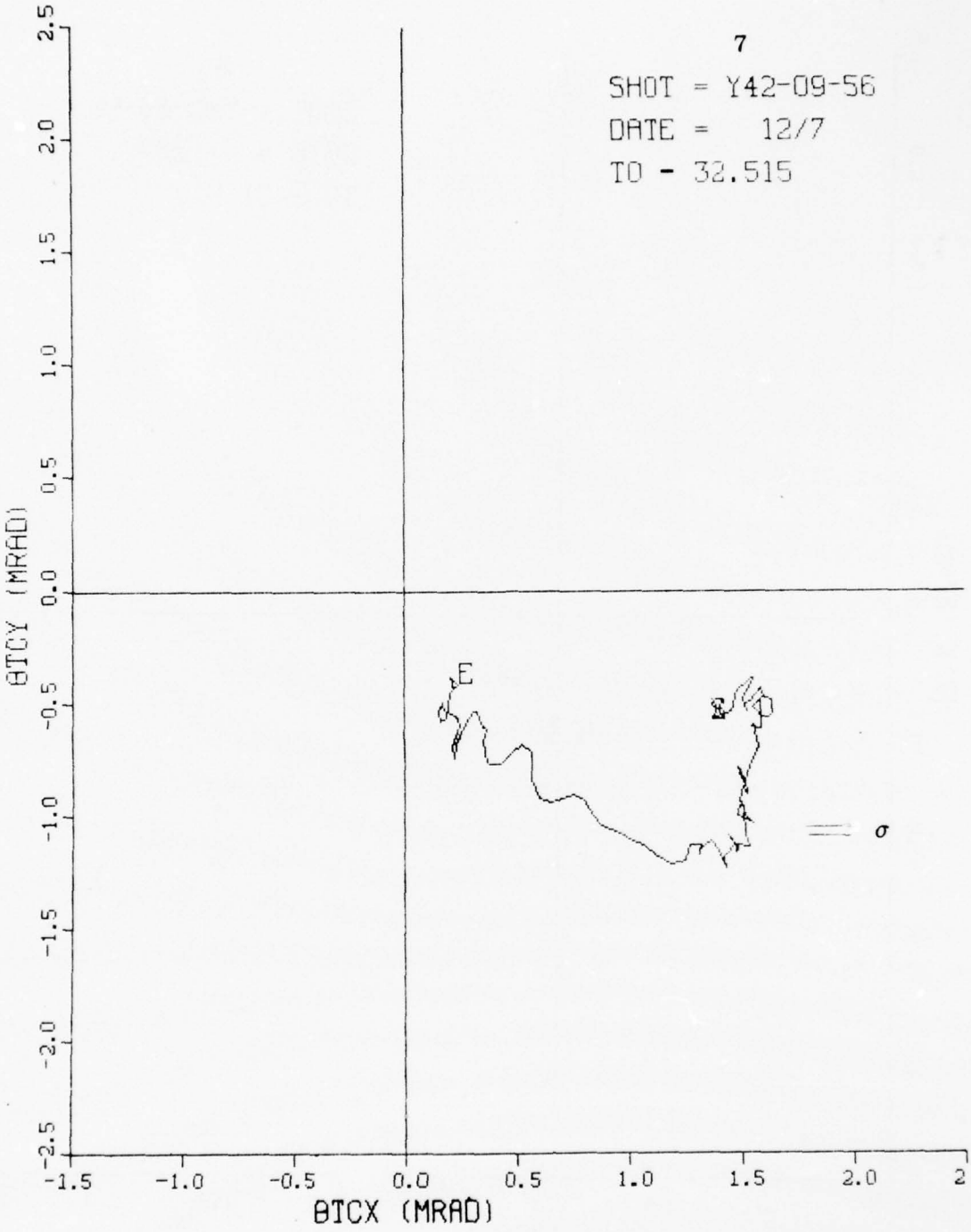

MUZZLE DISPLACEMENT

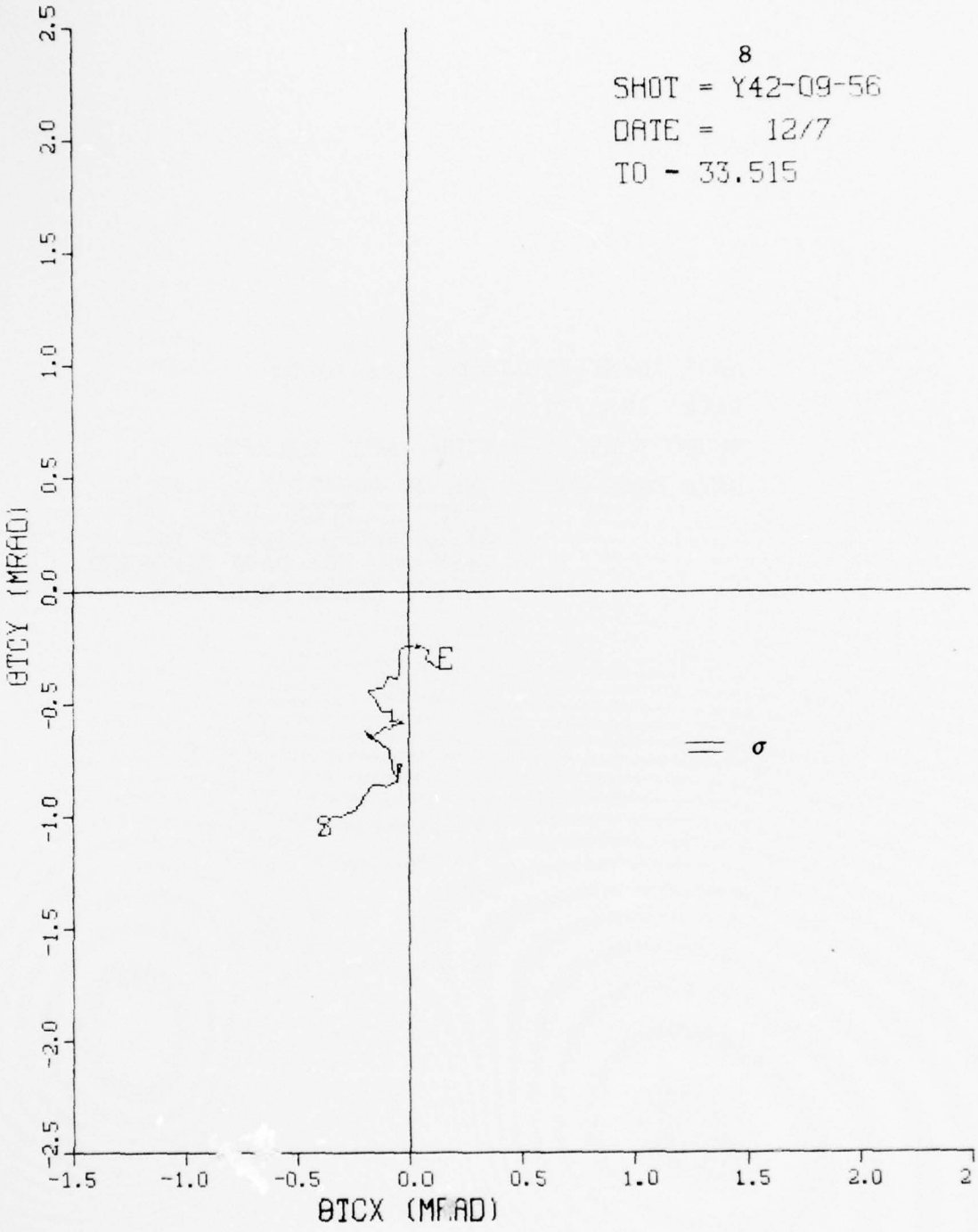

SHOT IDENTIFICATION: 045-10-56

DATE: 12/8/77

ROUND IDENTIFICATION: APDS M392A2

DATA DROP-OUTS: ONE OF DURATION 1.0 MS PRIOR TO ROUND EXIT; ONE AFTER ROUND EXIT OF DURATION 0.9 MS; DATA RECORDED DURING ROUND EMERGENCE

MUZZLE DISPLACEMENT

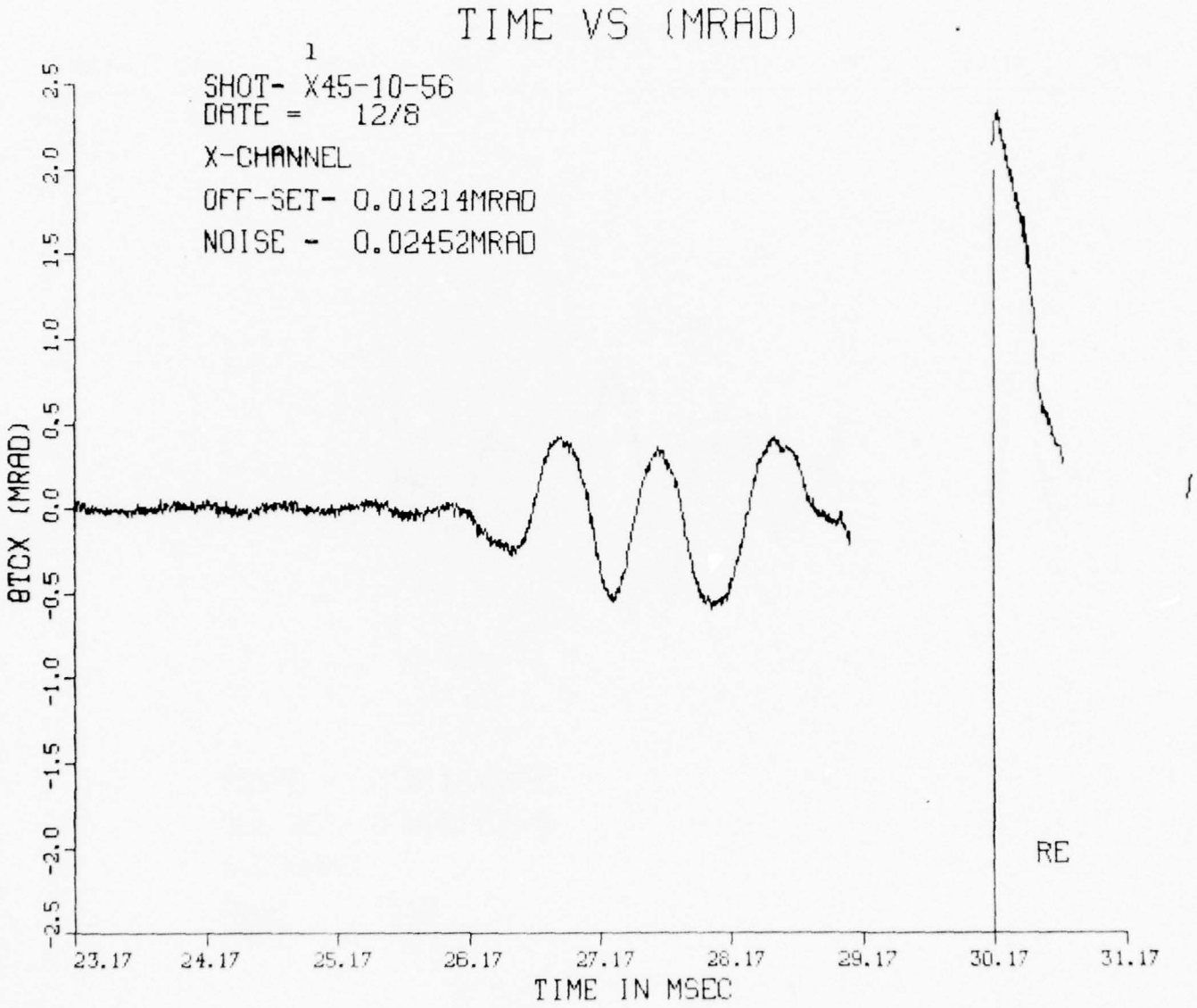
TIME VS (MRAD)
1
SHOT- X45-10-56
DATE = 12/8
X-CHANNEL
OFF-SET- 0.01214MRAD
NOISE - 0.02452MRAD
RE
BTCX (MRAD)
2.5
2.0
1.5
1.0
0.5
0.0
-0.5
-1.0
-1.5
-2.0
-2.5
23.17
24.17
25.17
26.17
27.17
28.17
29.17
30.17
31.17
TIME IN MSEC

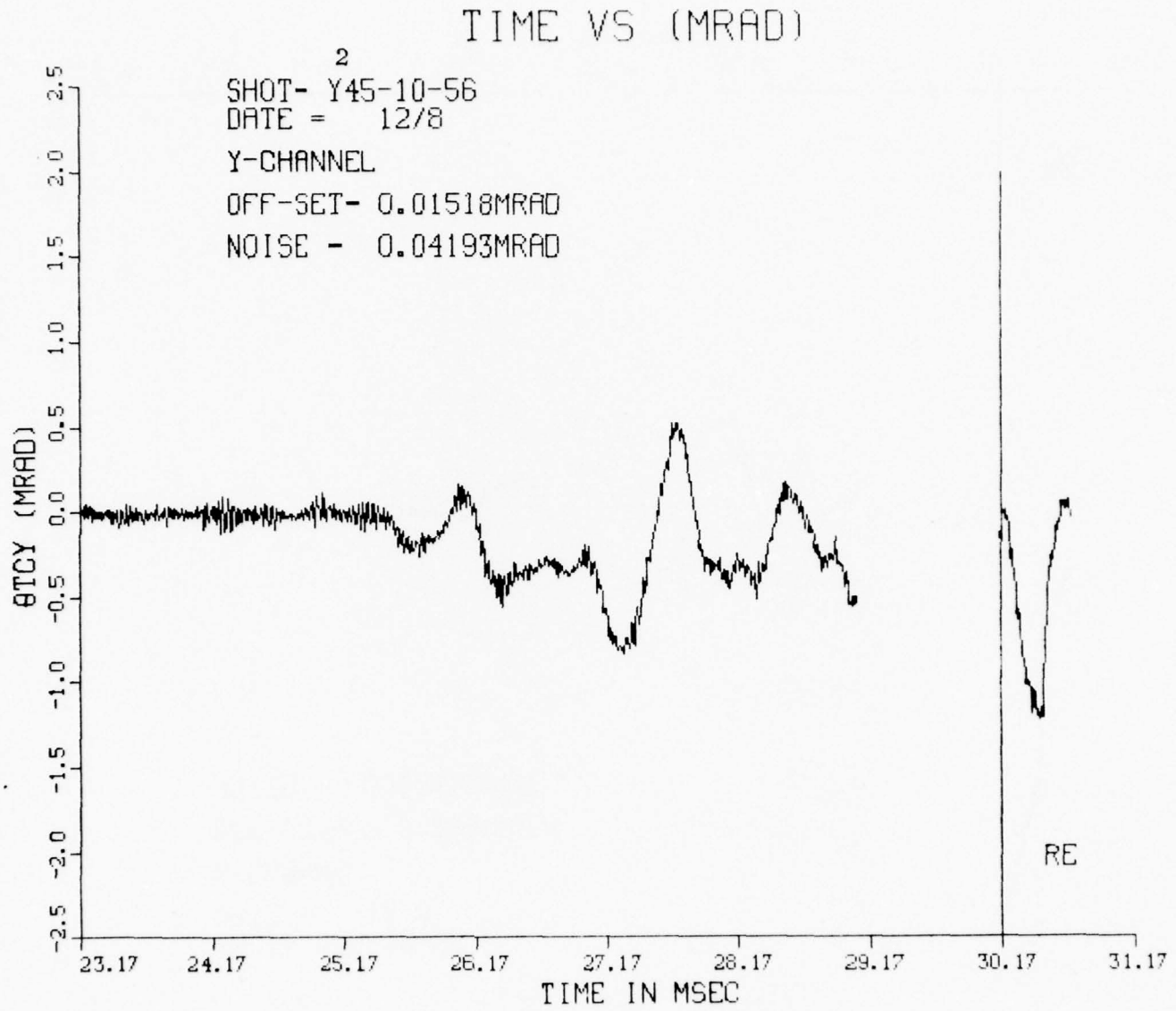
TIME VS (MRAD)
2
SHOT- Y45-10-56
DATE = 12/8
Y-CHANNEL
OFF-SET- 0.01518MRAD
NOISE - 0.04193MRAD
θTCY (MRAD)
2.5
2.0
1.5
1.0
0.5
0.0
-0.5
-1.0
-1.5
-2.0
-2.5
RE
23.17
24.17
25.17
26.17
27.17
28.17
29.17
30.17
31.17
TIME IN MSEC

MUZZLE DISPLACEMENT

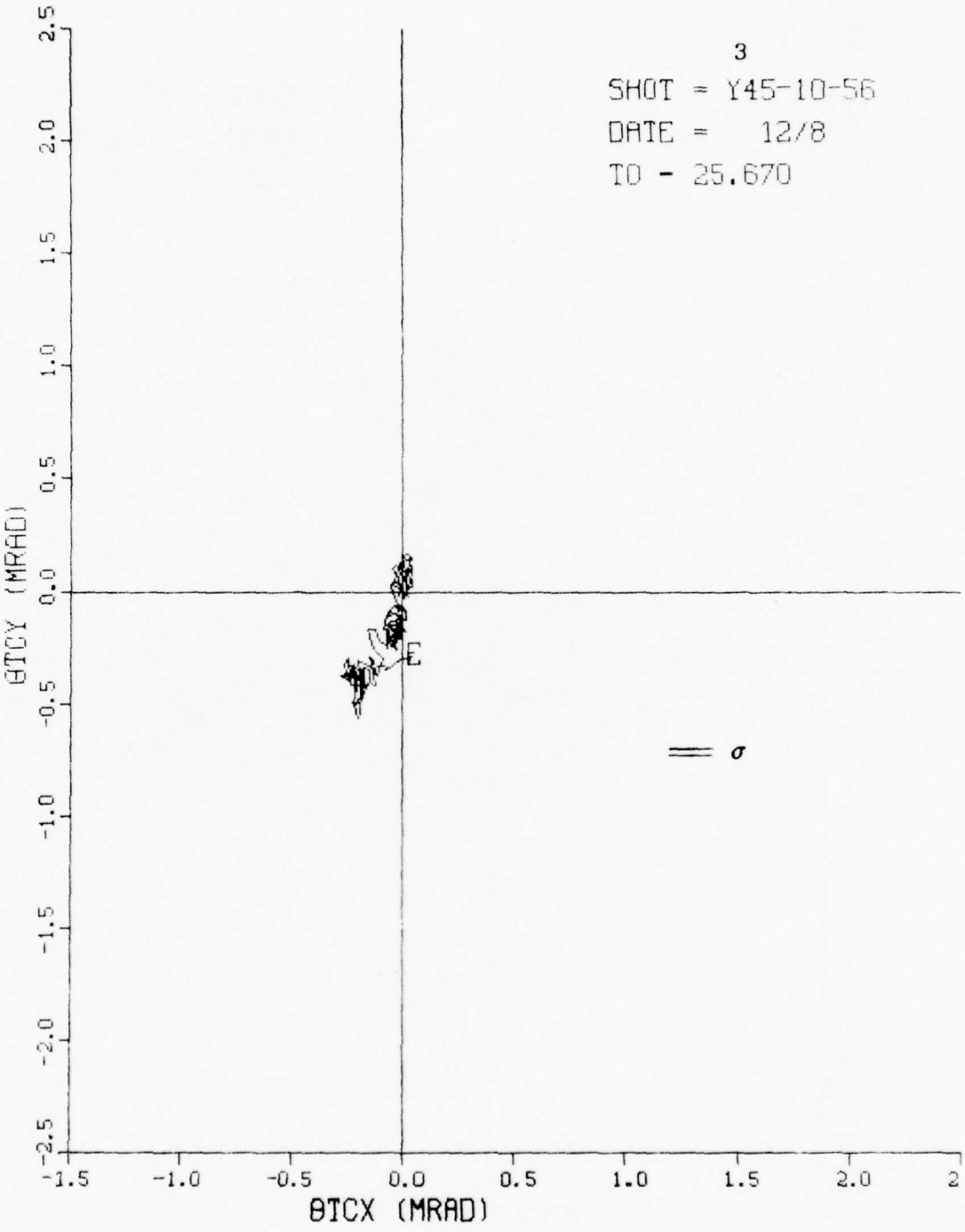

MUZZLE DISPLACEMENT

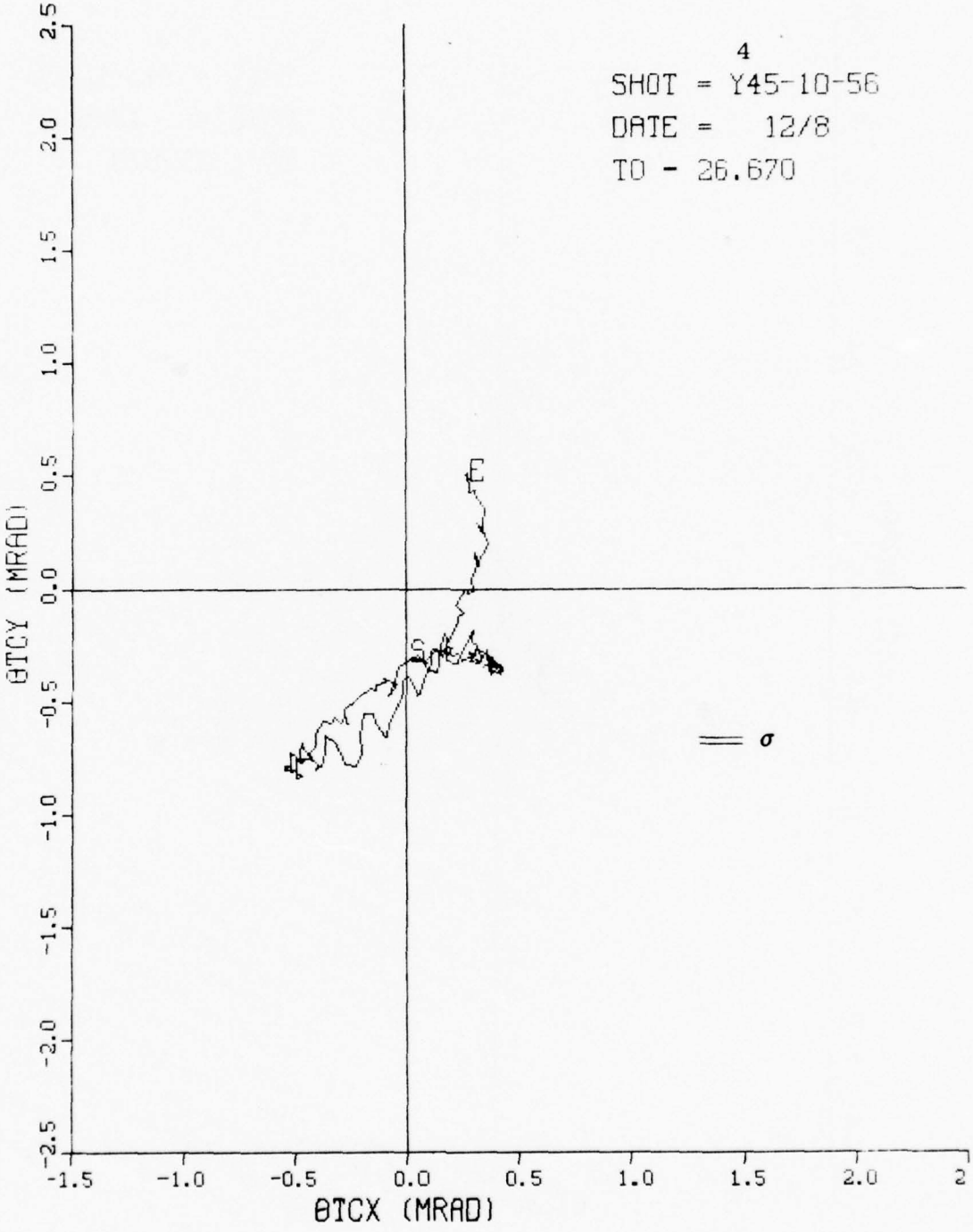

MUZZLE DISPLACEMENT

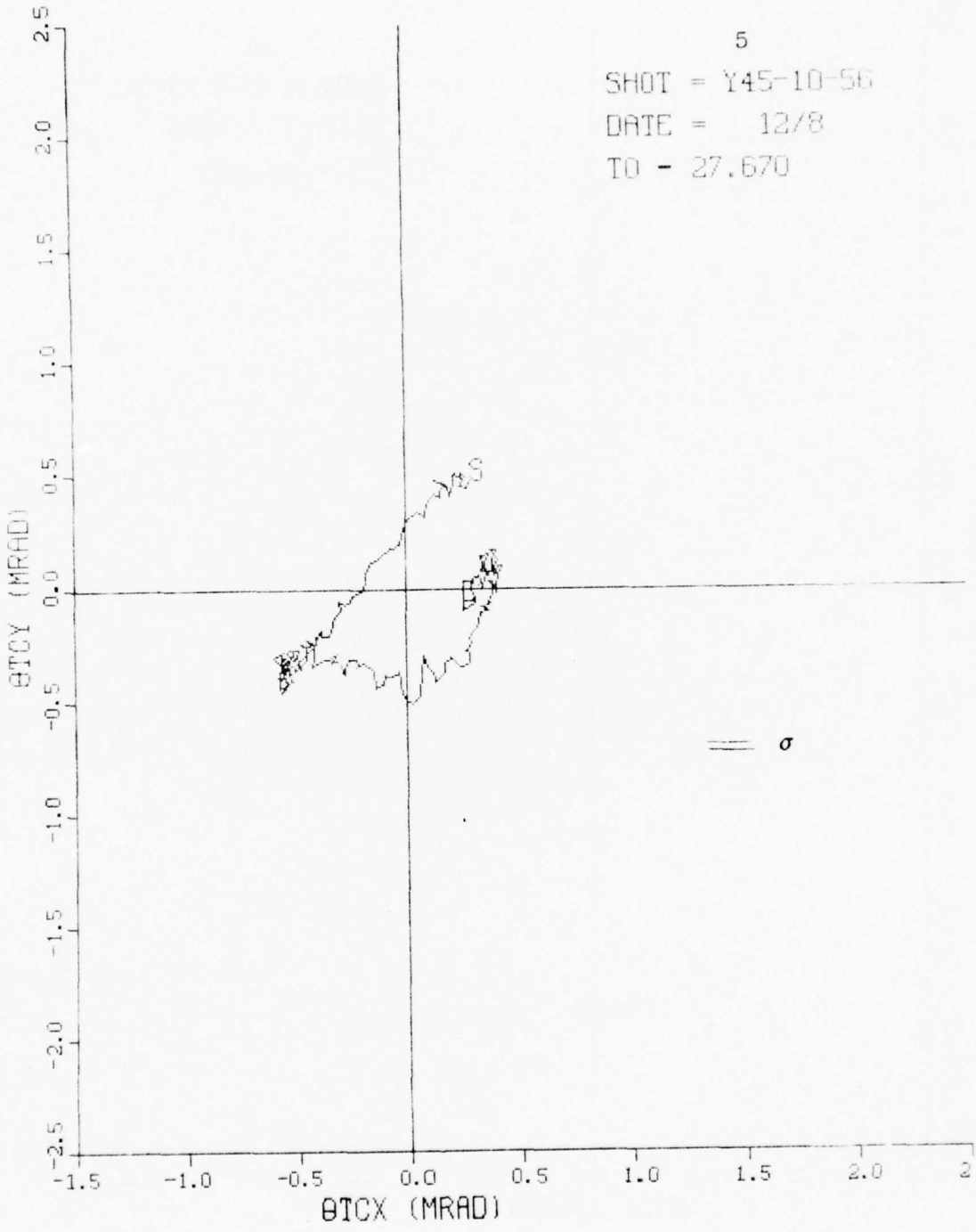

MUZZLE DISPLACEMENT

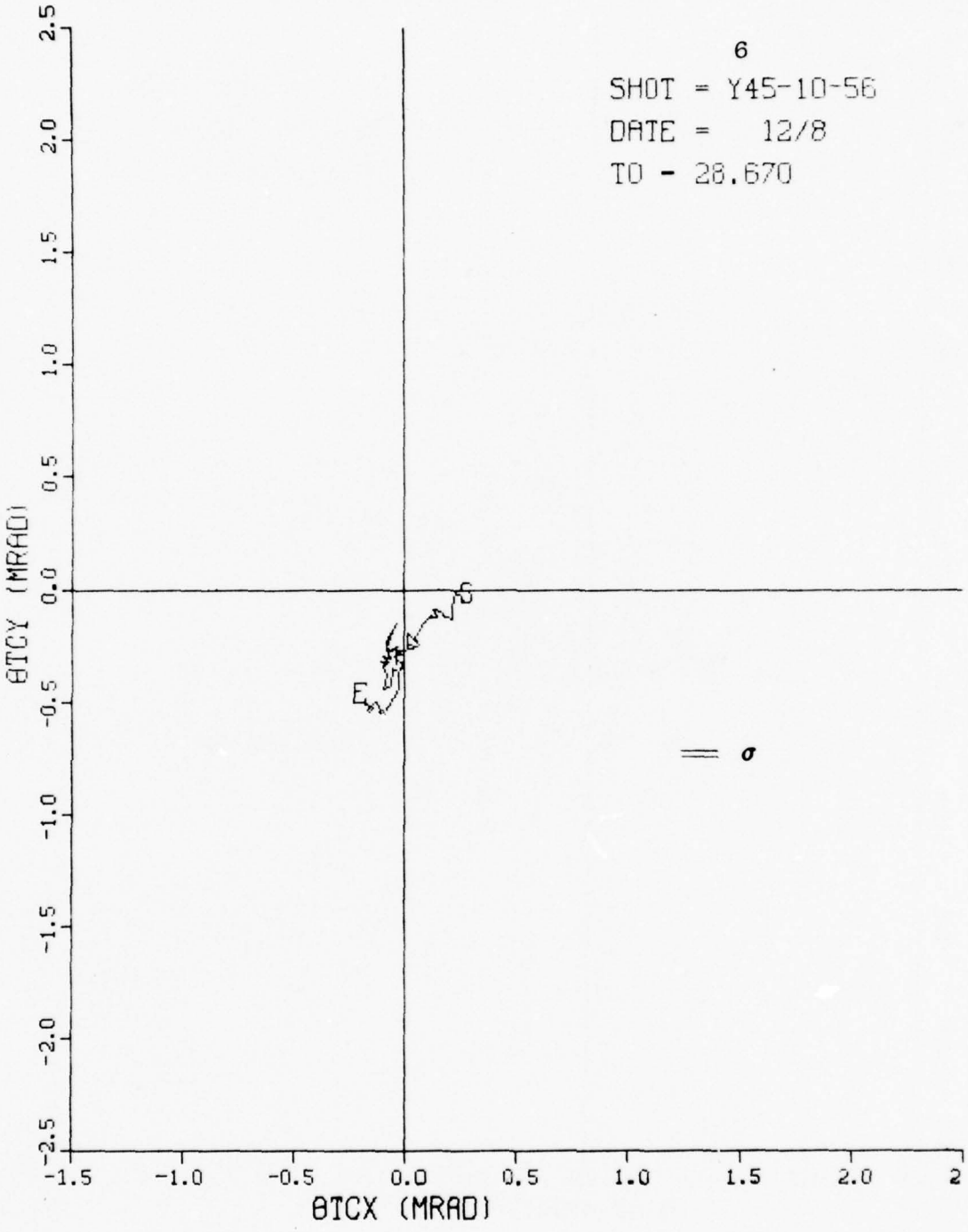

MUZZLE DISPLACEMENT

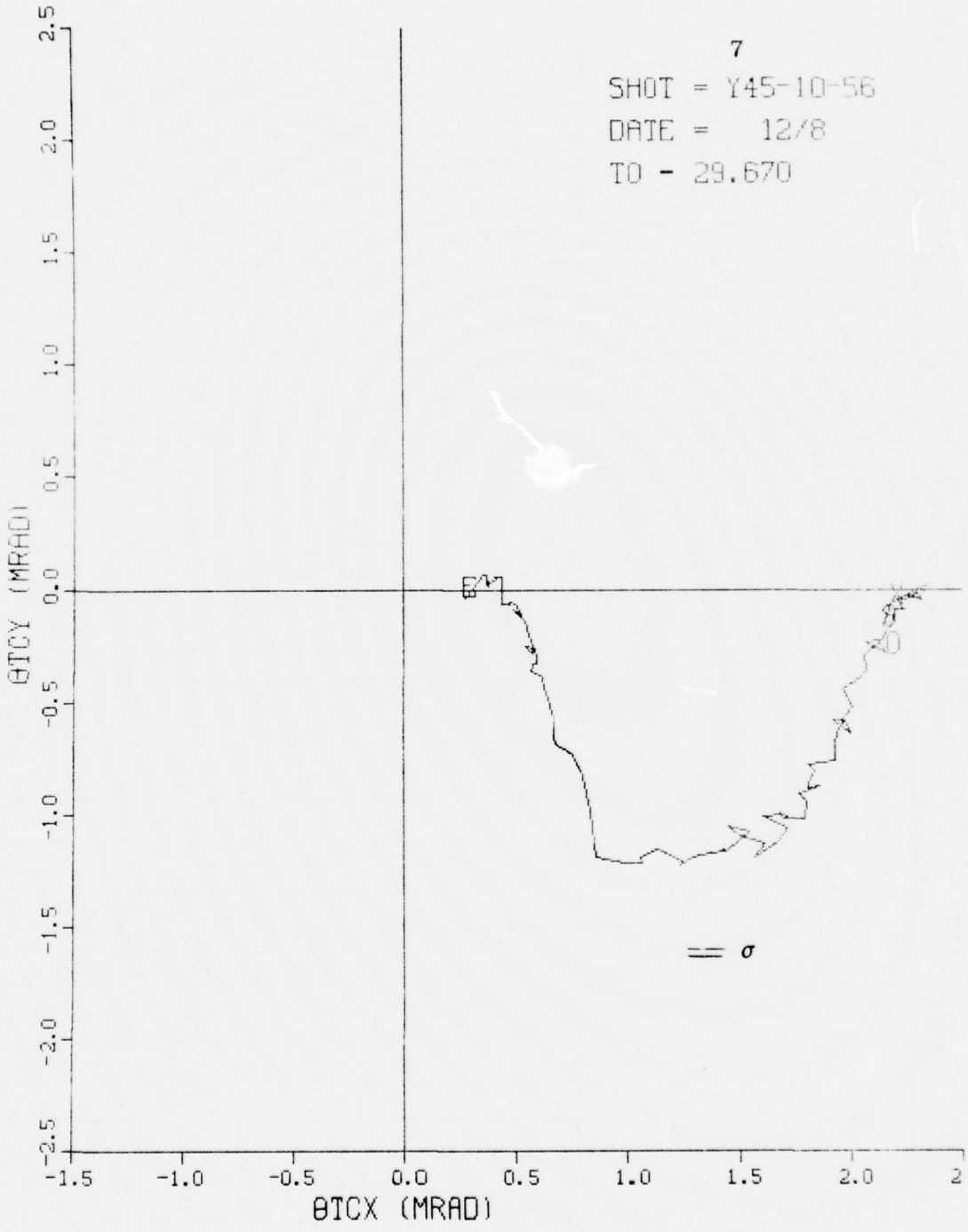

MUZZLE DISPLACEMENT

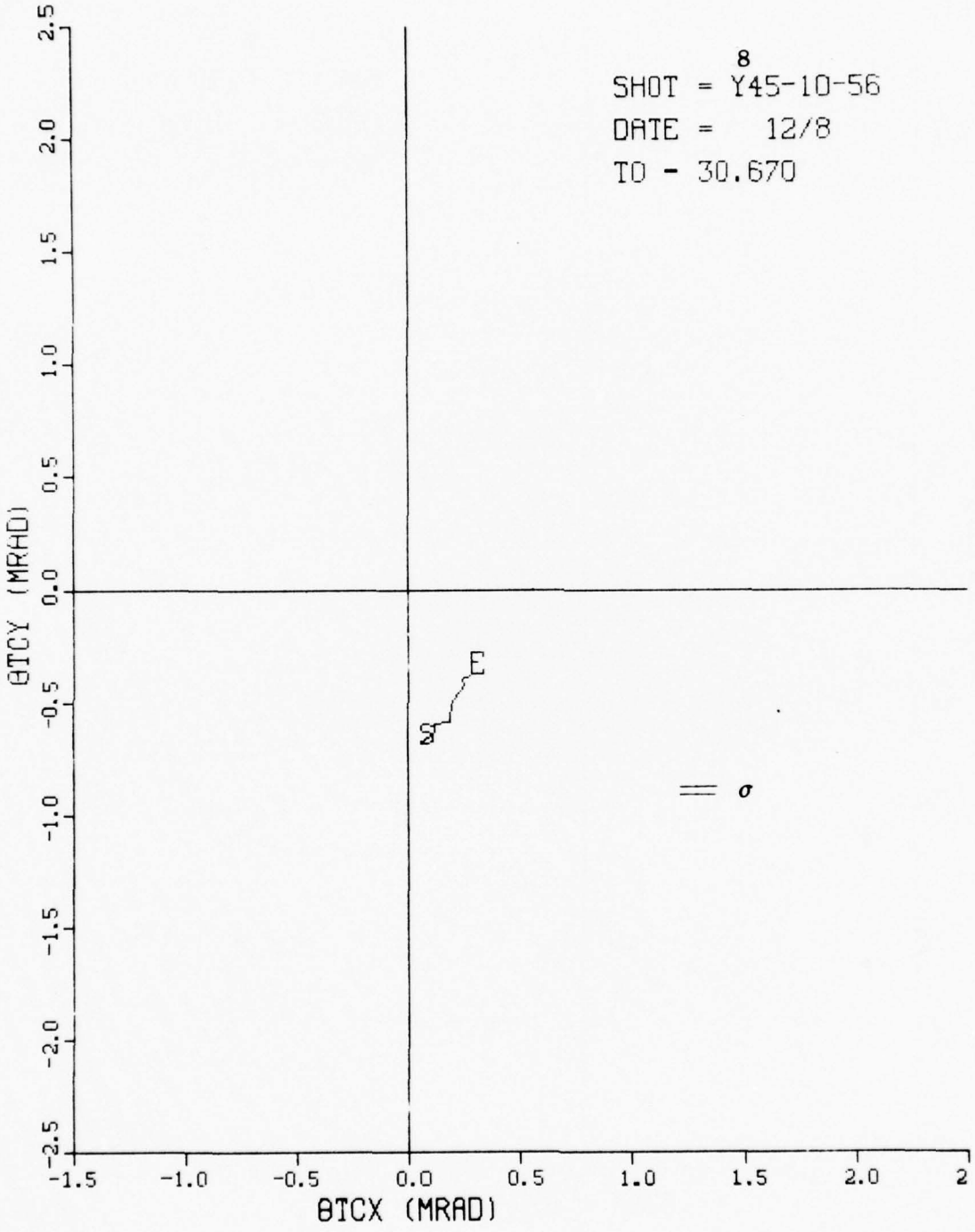

SHOT IDENTIFICATION: 046-13-55

DATE: 12/8/77

ROUND IDENTIFICATION: APDS M392A2

DATA DROP-OUTS: ONE PRIOR TO AND INCLUDING ROUND EMERGENCE; ONE AFTER ROUND EXIT OF DURATION 1.1 MS; NO DATA RECORDED DURING ROUND EMERGENCE

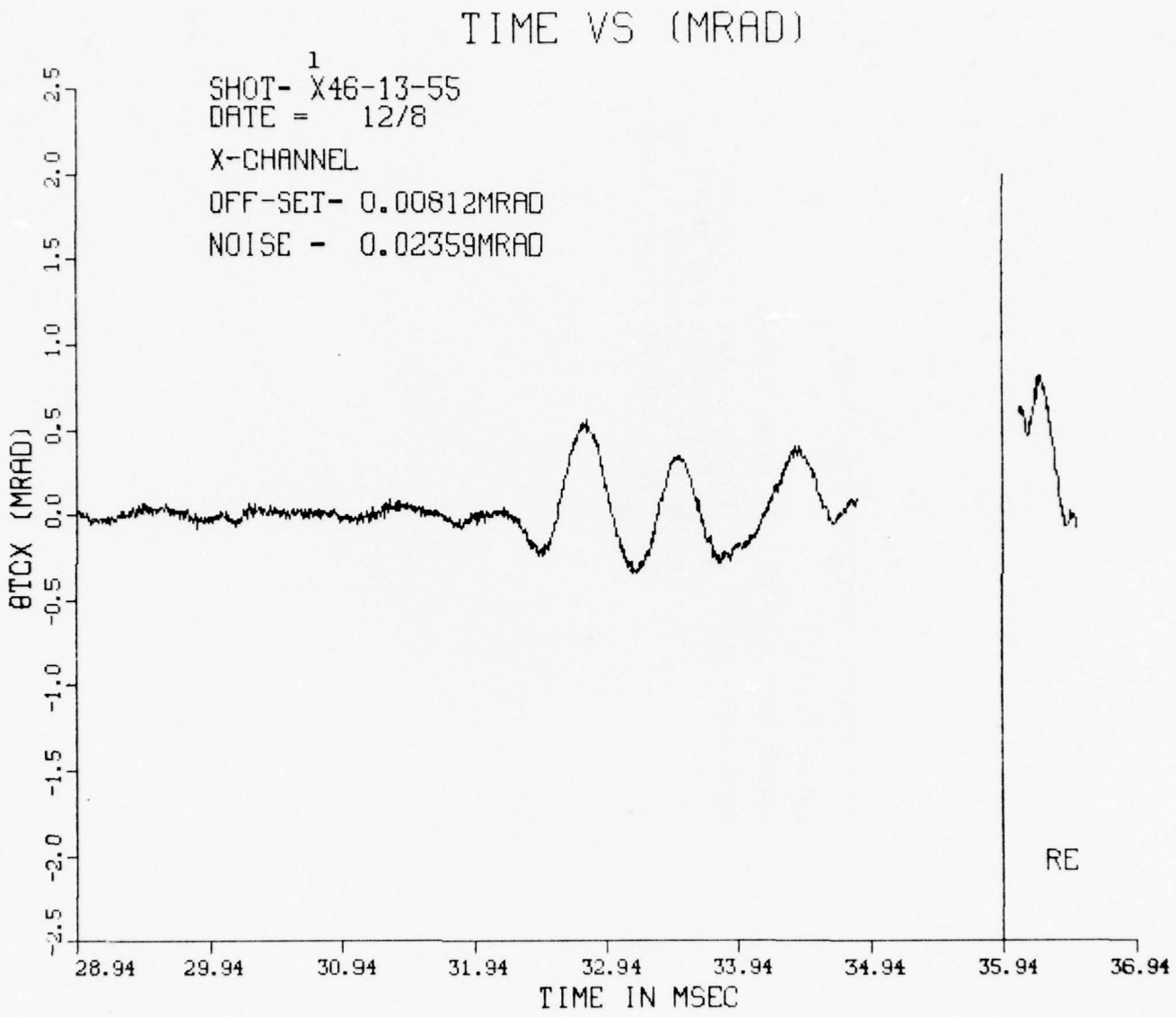
TIME VS (MRAD)
1
SHOT- X46-13-55
DATE = 12/8
X-CHANNEL
OFF-SET- 0.00812MRAD
NOISE - 0.02359MRAD
θTCX (MRAD)
2.5
2.0
1.5
1.0
0.5
0.0
-0.5
-1.0
-1.5
-2.0
-2.5
RE
28.94
29.94
30.94
31.94
32.94
33.94
34.94
35.94
36.94
TIME IN MSEC

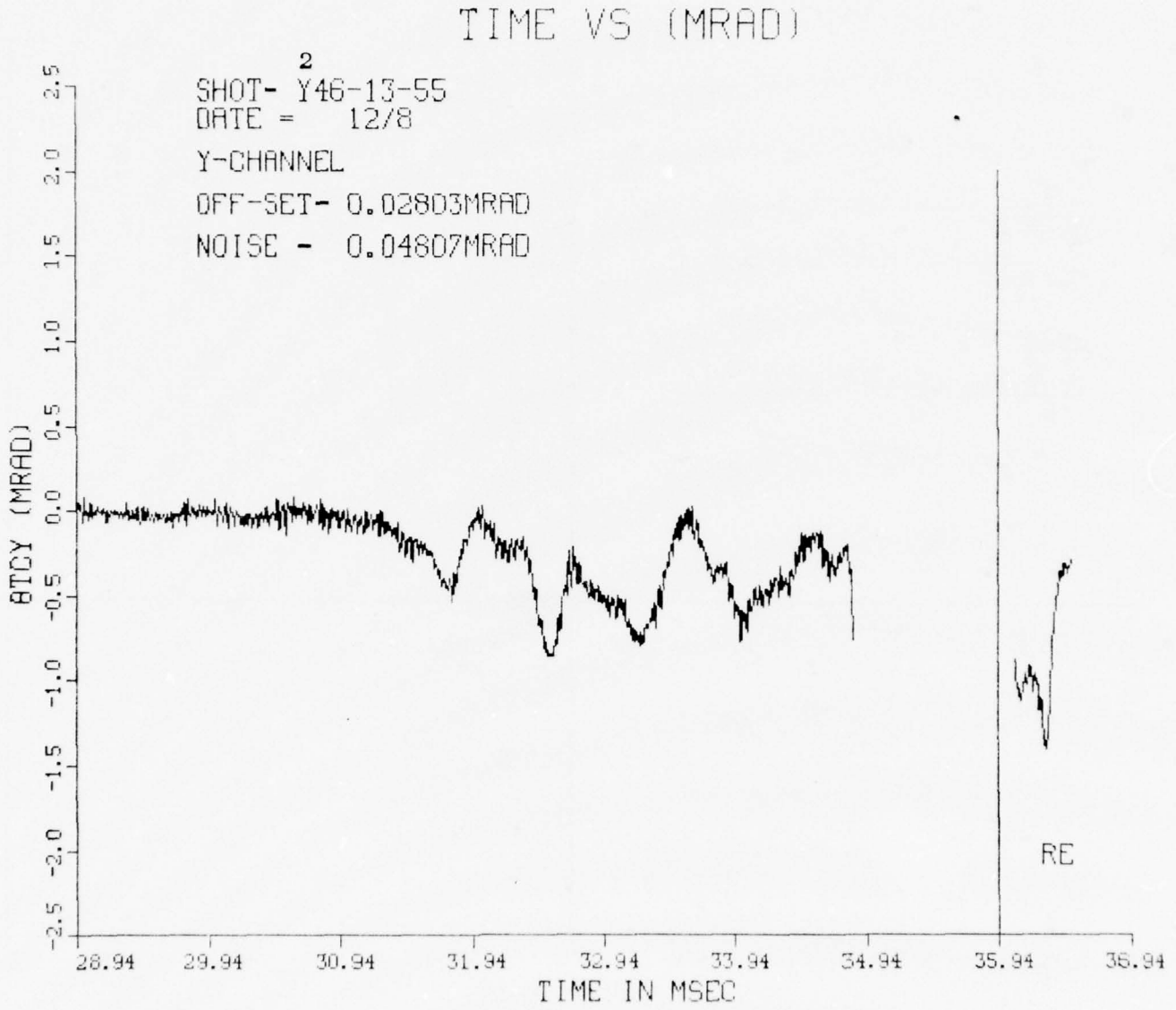
TIME VS (MRAD)
SHOT- Y46-13-55
DATE = 12/8
Y-CHANNEL
OFF-SET- 0.02803MRAD
NOISE - 0.04807MRAD
ΔTCY (MRAD)
2.5
2.0
1.5
1.0
0.5
0.0
-0.5
-1.0
-1.5
-2.0
-2.5
28.94
29.94
30.94
31.94
32.94
33.94
34.94
35.94
36.94
TIME IN MSEC
RE

MUZZLE DISPLACEMENT

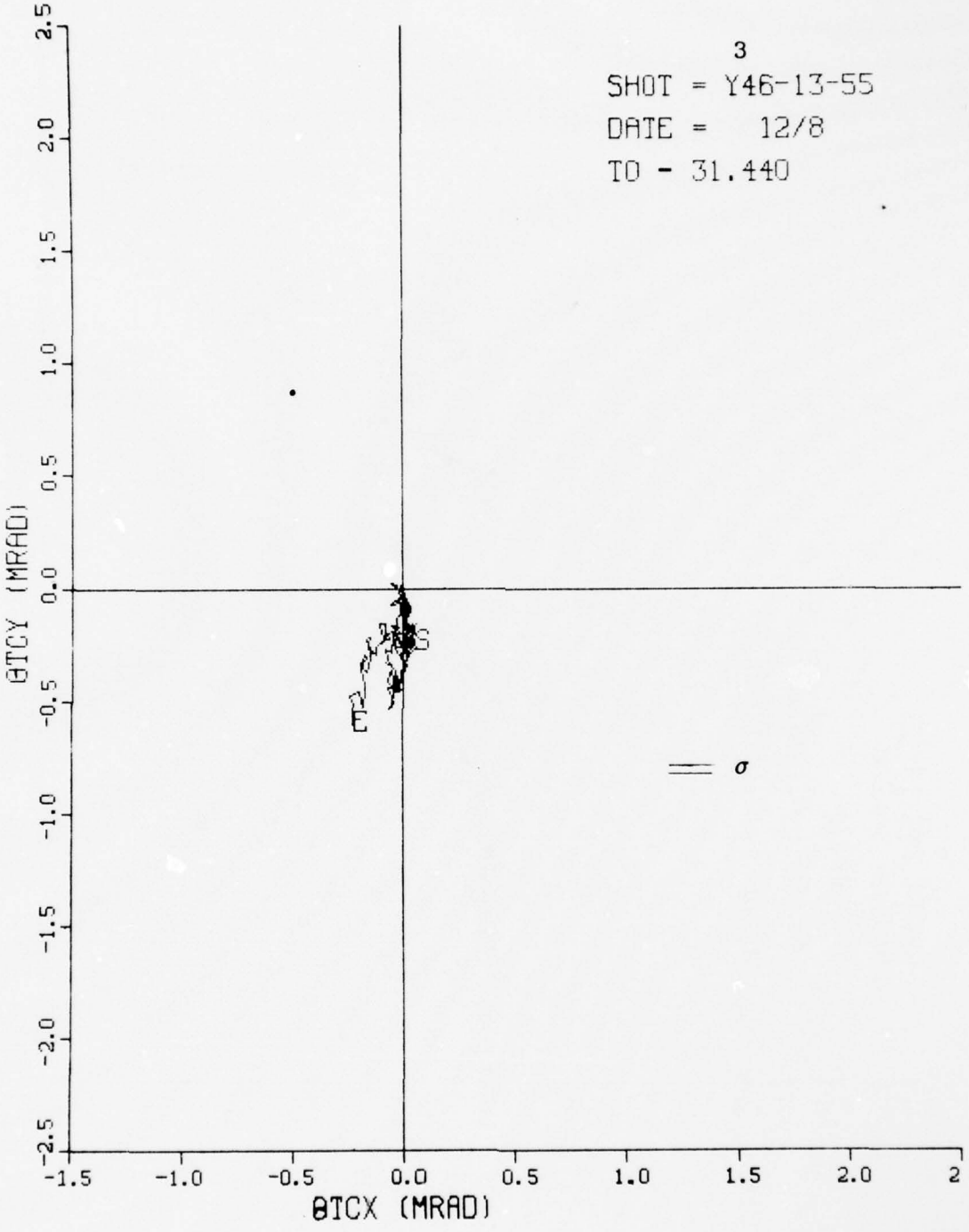

MUZZLE DISPLACEMENT

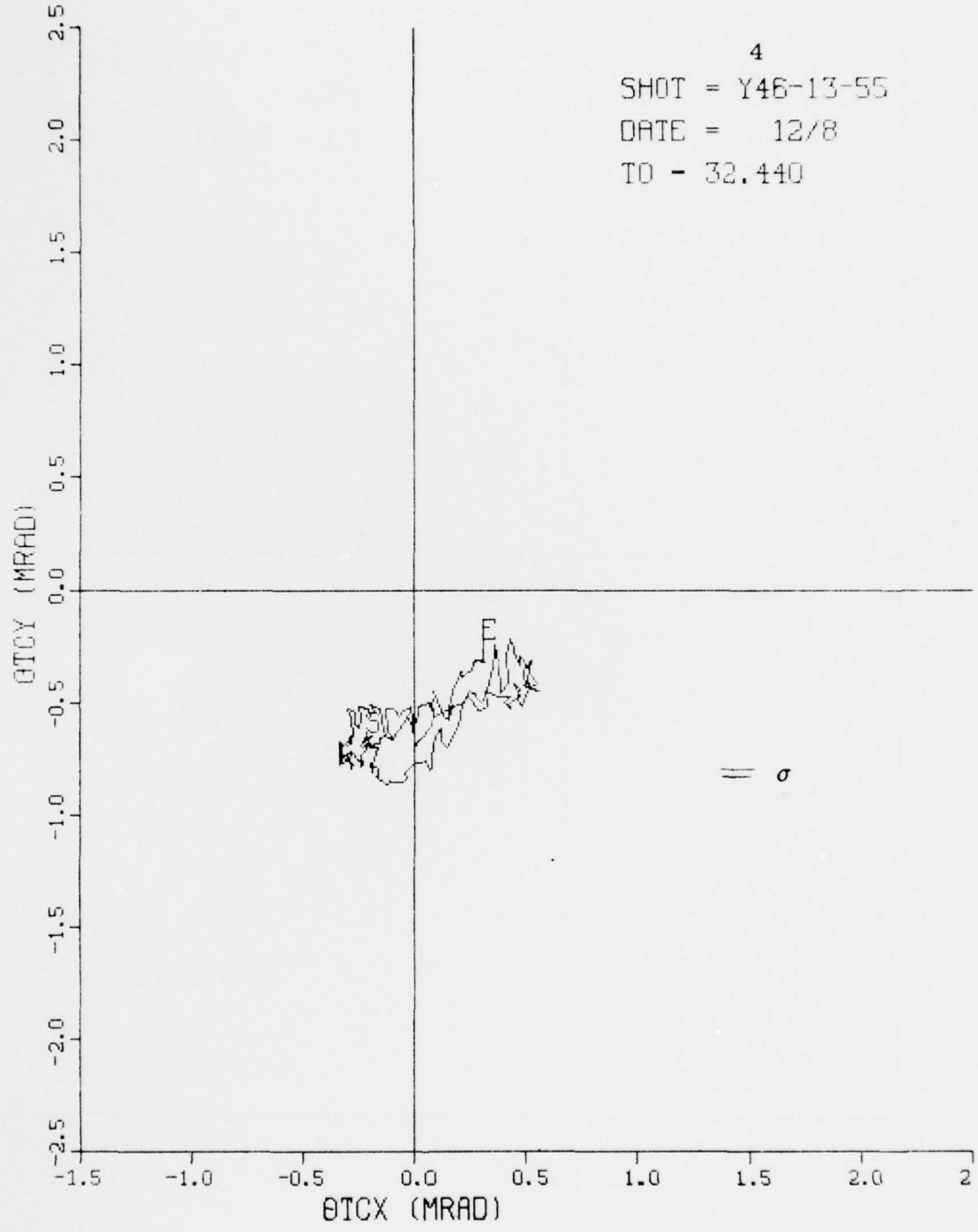

MUZZLE DISPLACEMENT

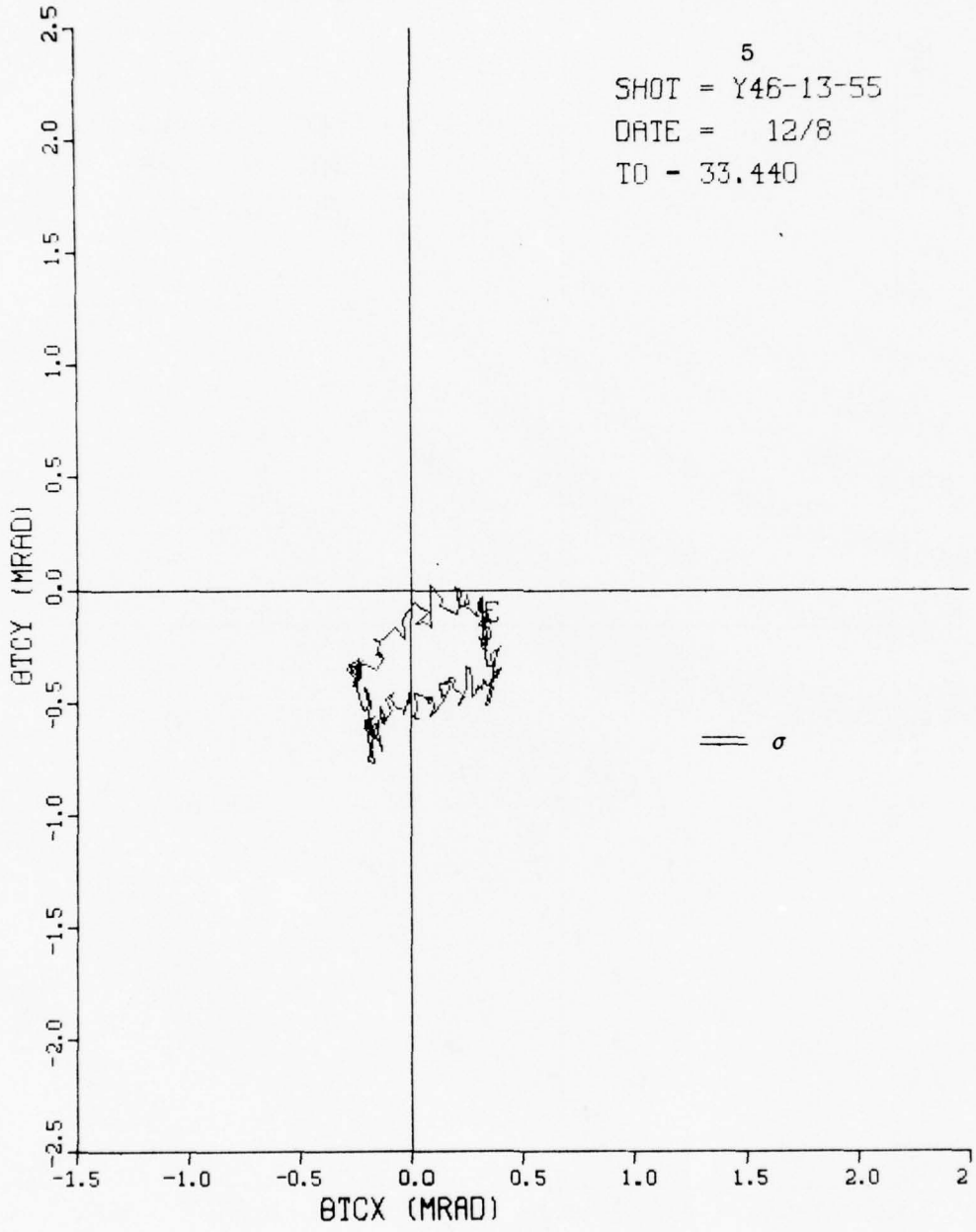

MUZZLE DISPLACEMENT

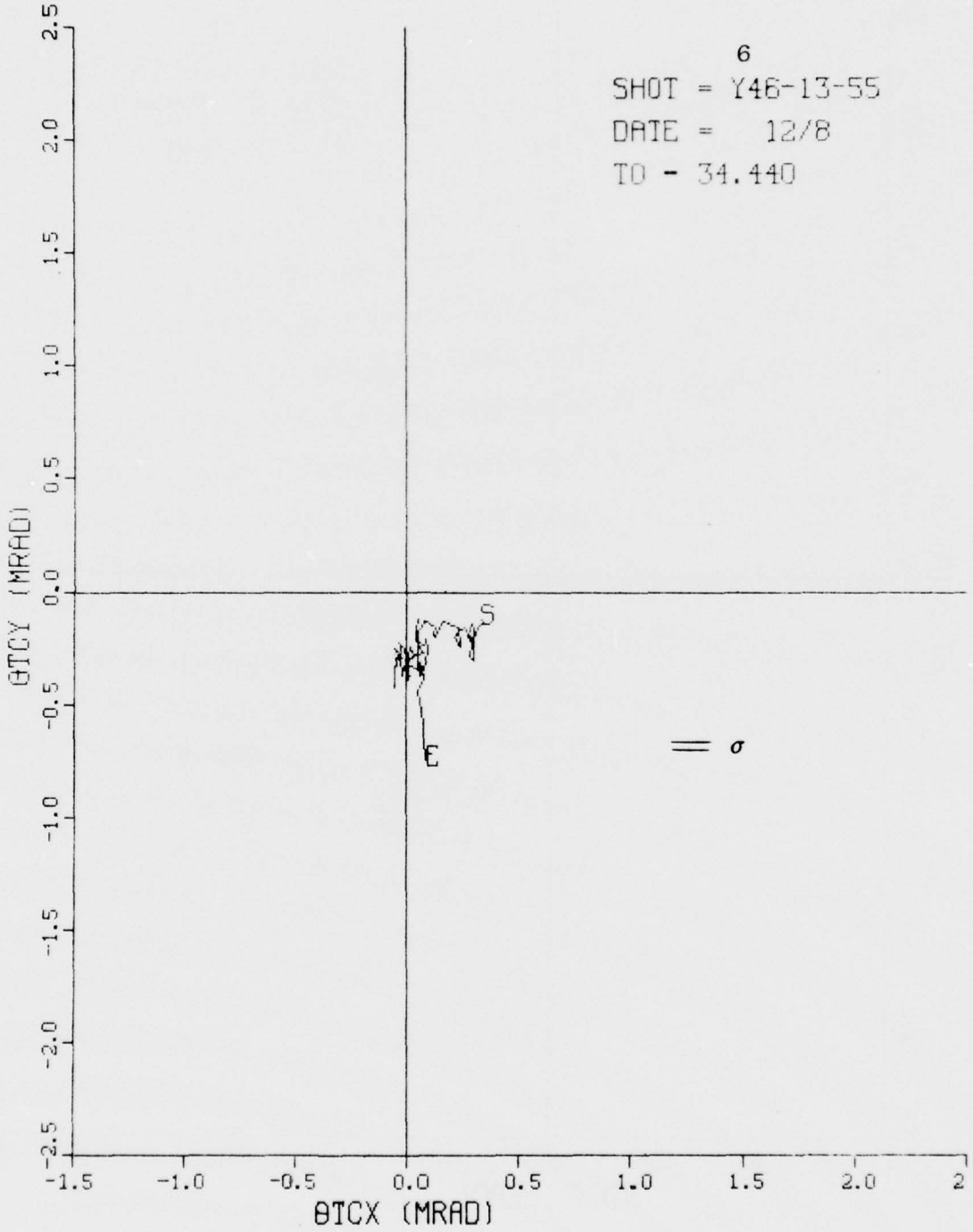

MUZZLE DISPLACEMENT

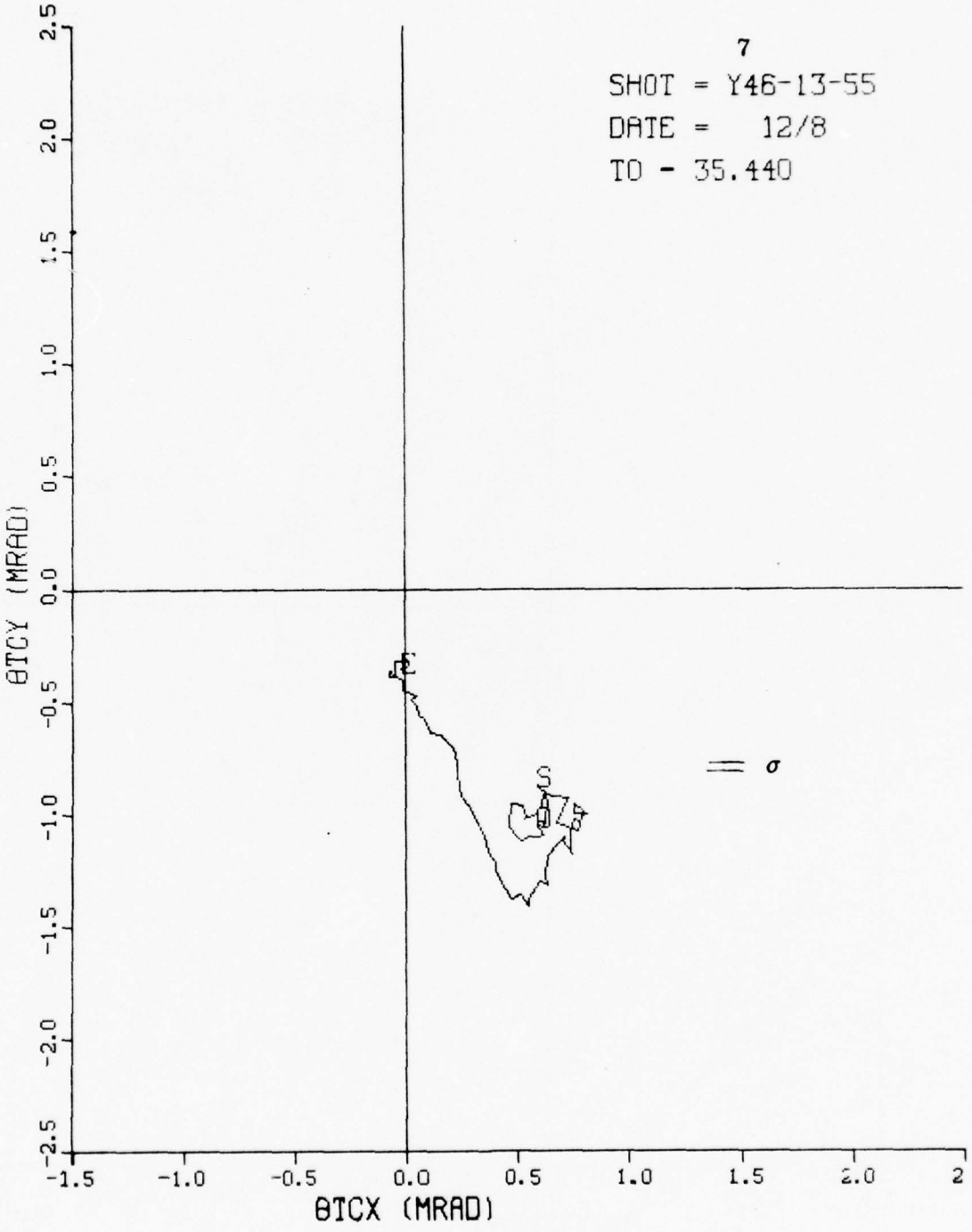

SHOT IDENTIFICATION: 048-15-07

DATE: 12/8/77

ROUND IDENTIFICATION: PROOF SLUG

DATA DROP-OUTS: ONE PRIOR TO AND INCLUDING ROUND EXIT OF DURATION 0.8 MS; ONE AFTER ROUND EXIT OF DURATION 0.15 MS; NO DATA RECORDED DURING ROUND EMERGENCE

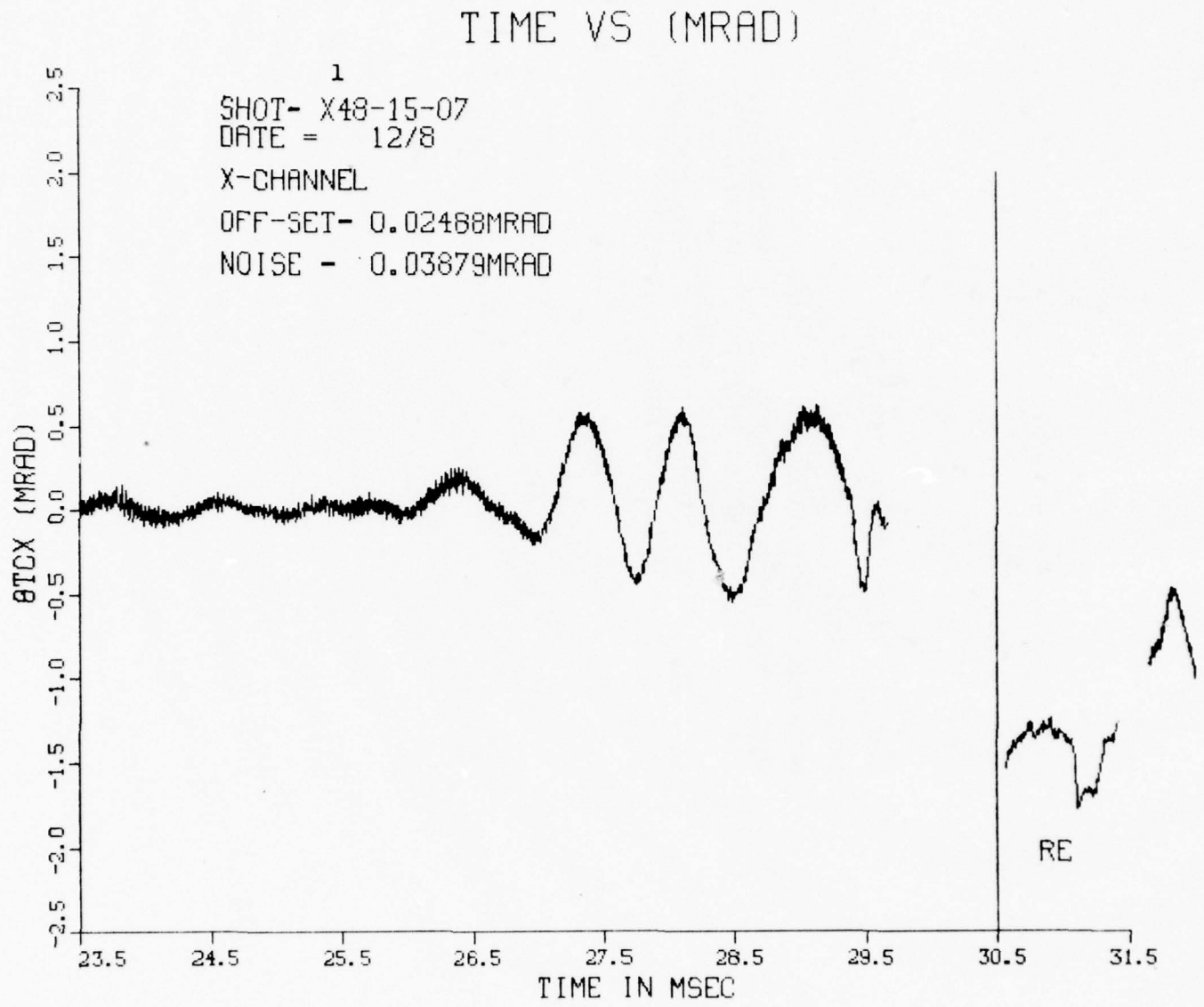
TIME VS (MRAD)
1
SHOT- X48-15-07
DATE = 12/8
X-CHANNEL
OFF-SET- 0.02488MRAD
NOISE - 0.03879MRAD
θTCX (MRAD)
2.5
2.0
1.5
1.0
0.5
0.0
-0.5
-1.0
-1.5
-2.0
-2.5
23.5
24.5
25.5
26.5
27.5
28.5
29.5
30.5
31.5
TIME IN MSEC
RE

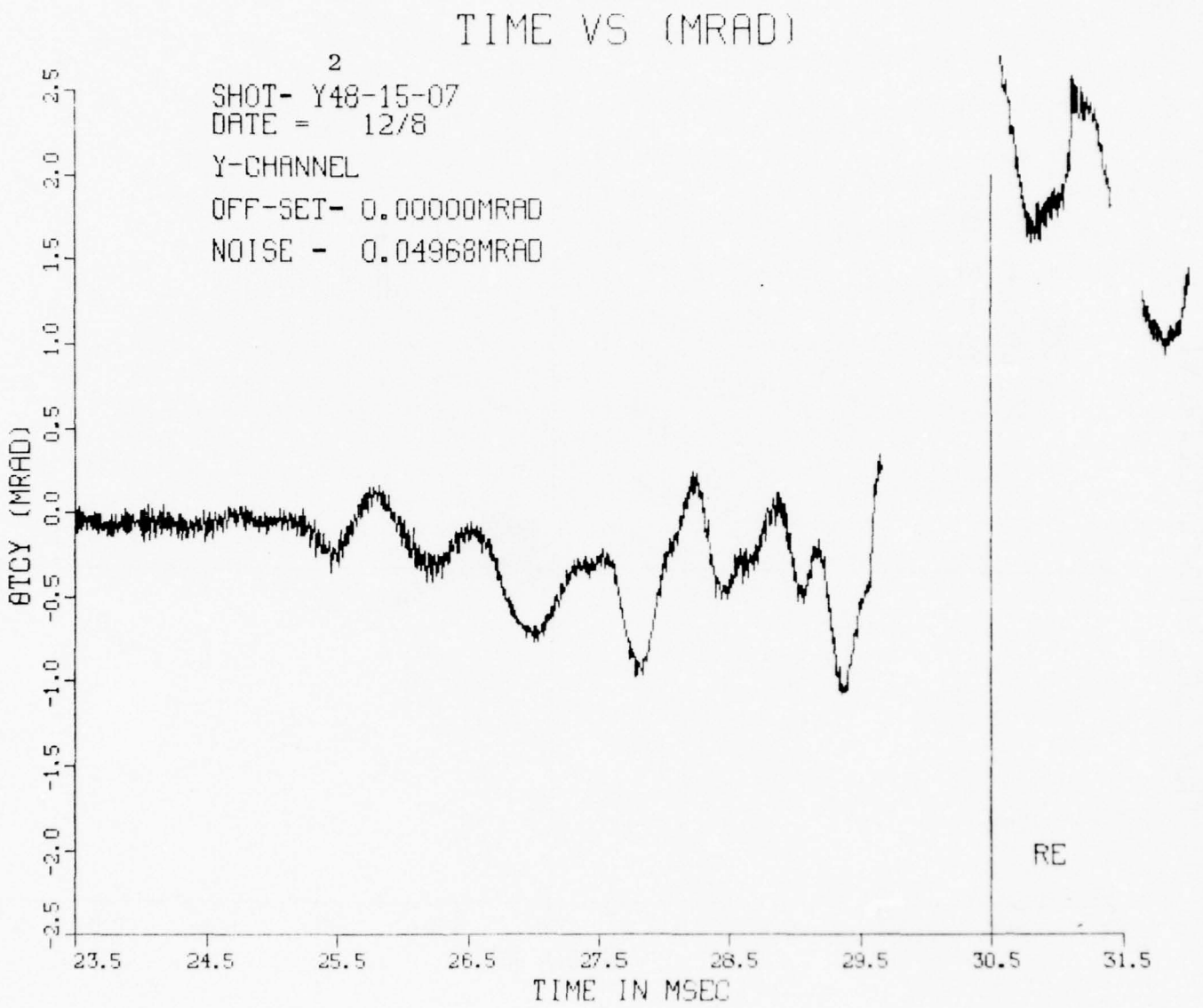
TIME VS (MRAD)
2
SHOT- Y48-15-07
DATE = 12/8
Y-CHANNEL
OFF-SET- 0.00000MRAD
NOISE - 0.04968MRAD
θTCY (MRAD)
2.5
2.0
1.5
1.0
0.5
0.0
-0.5
-1.0
-1.5
-2.0
-2.5
23.5
24.5
25.5
26.5
27.5
28.5
29.5
30.5
31.5
TIME IN MSEC
RE

MUZZLE DISPLACEMENT

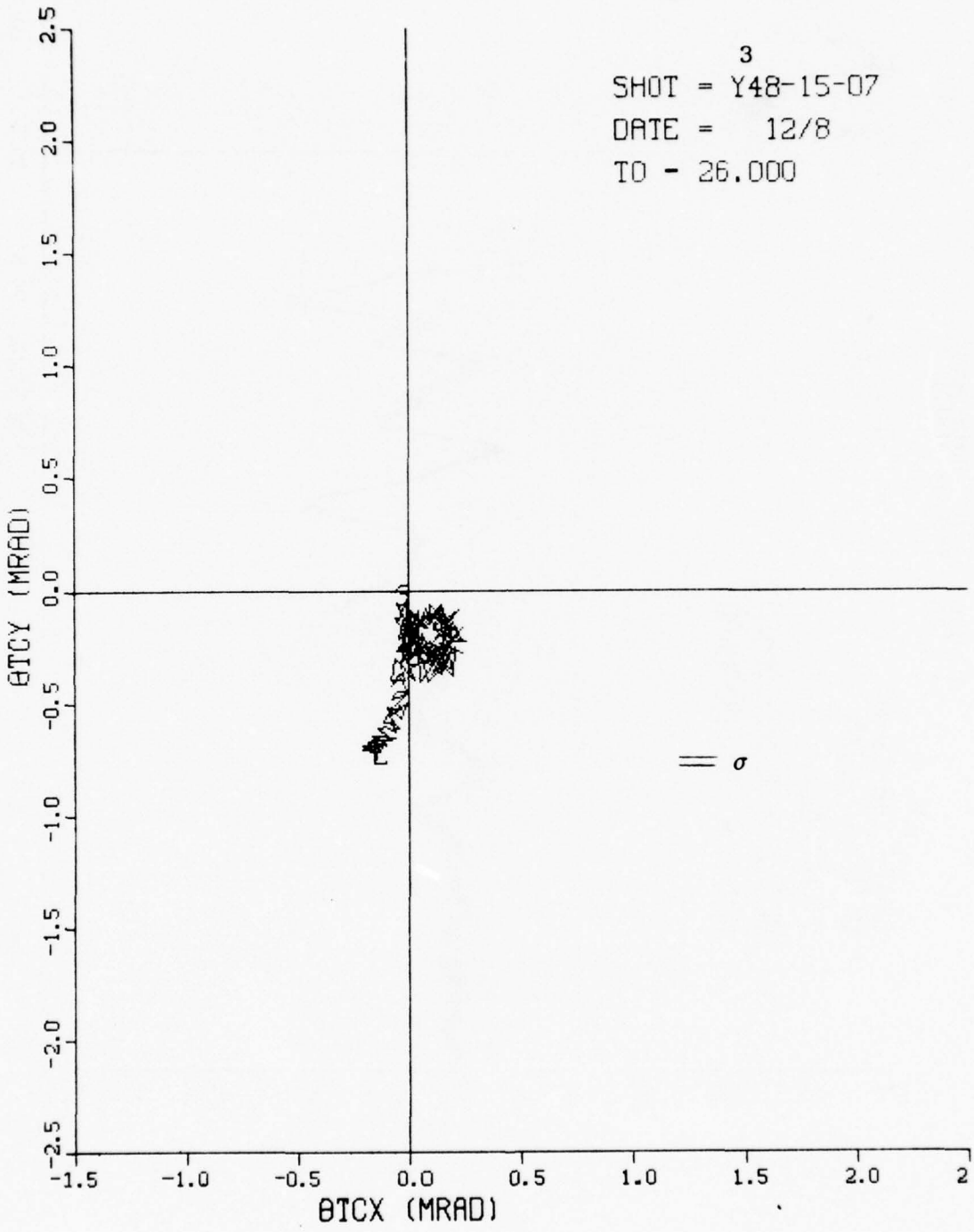

MUZZLE DISPLACEMENT

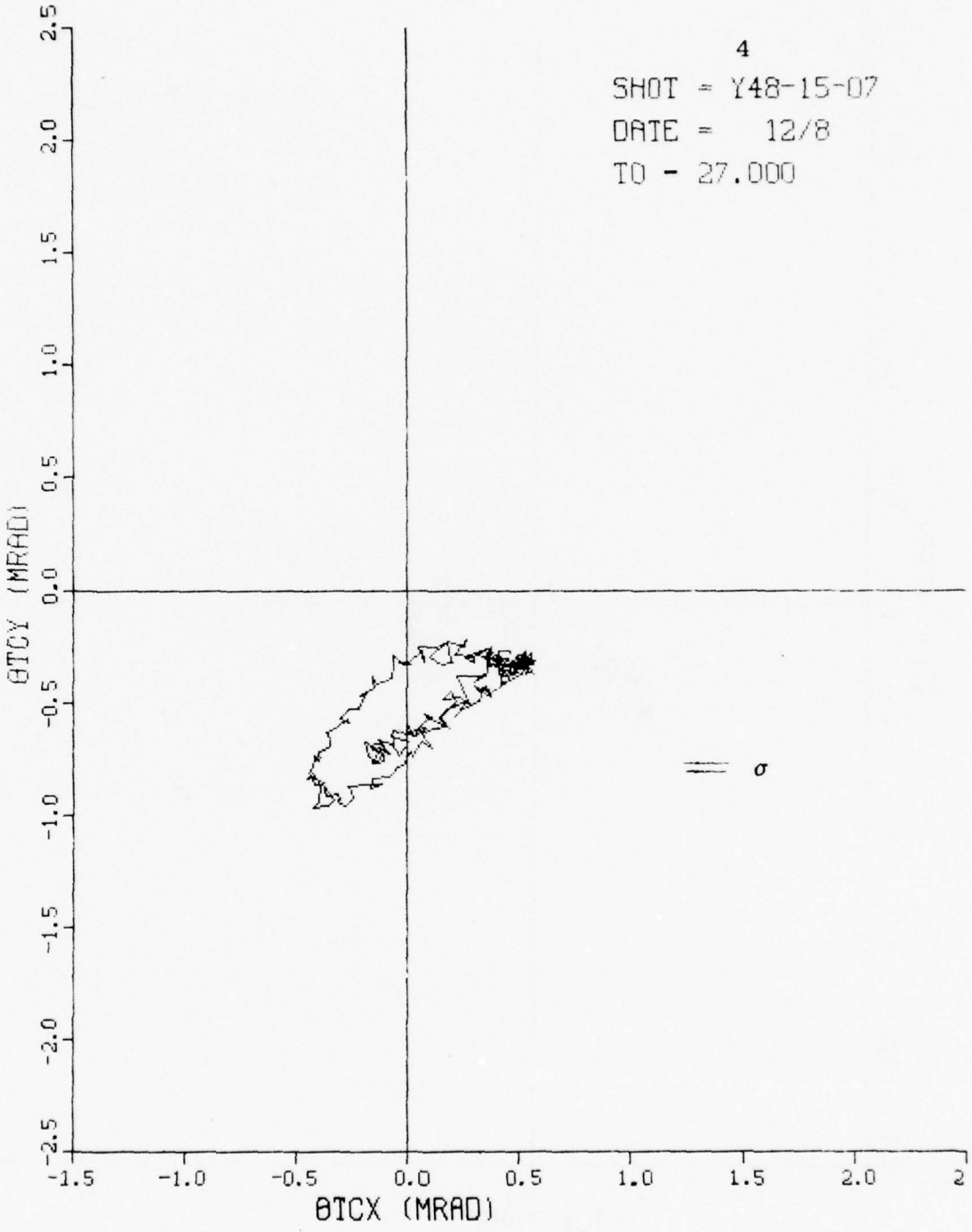

MUZZLE DISPLACEMENT

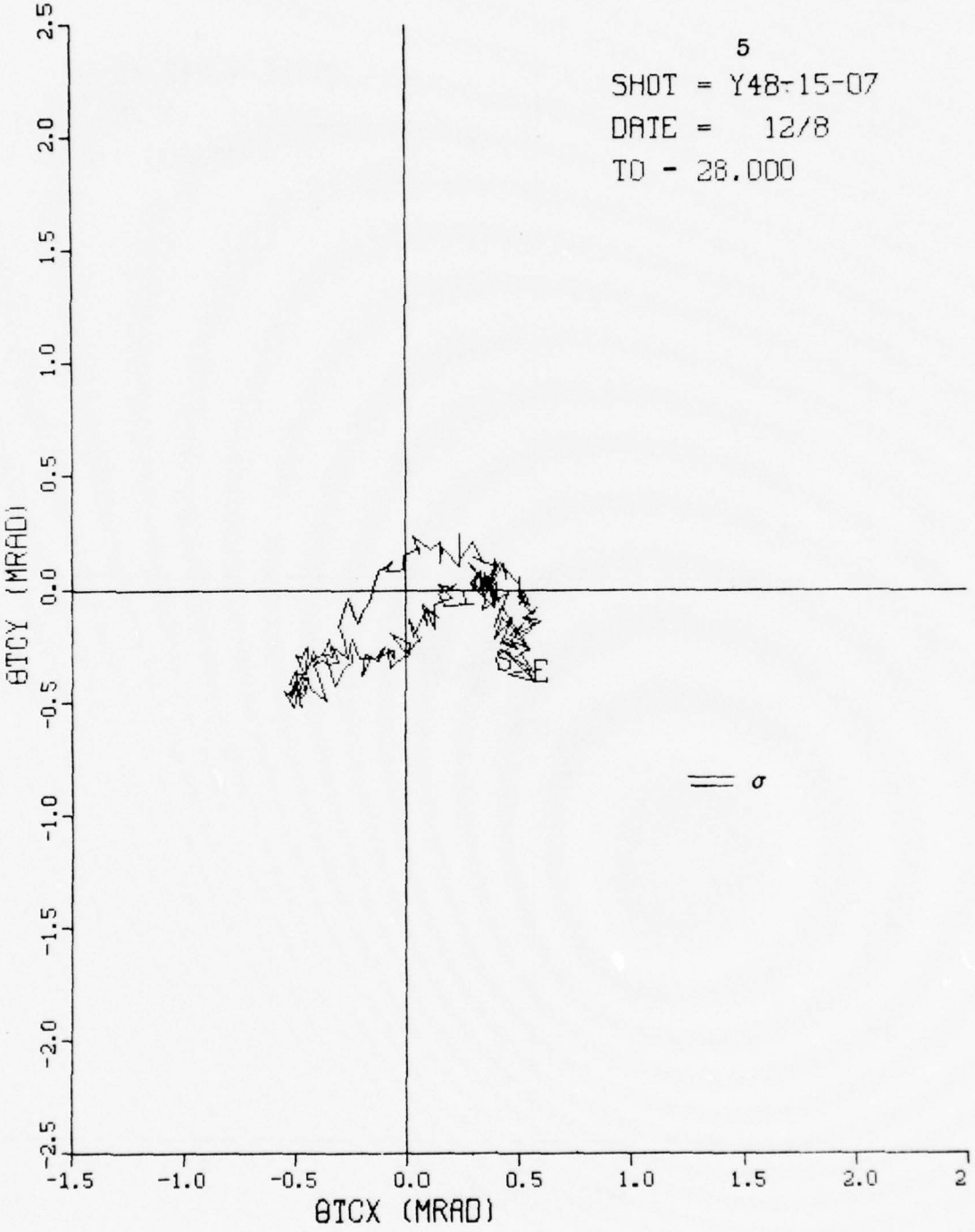

MUZZLE DISPLACEMENT

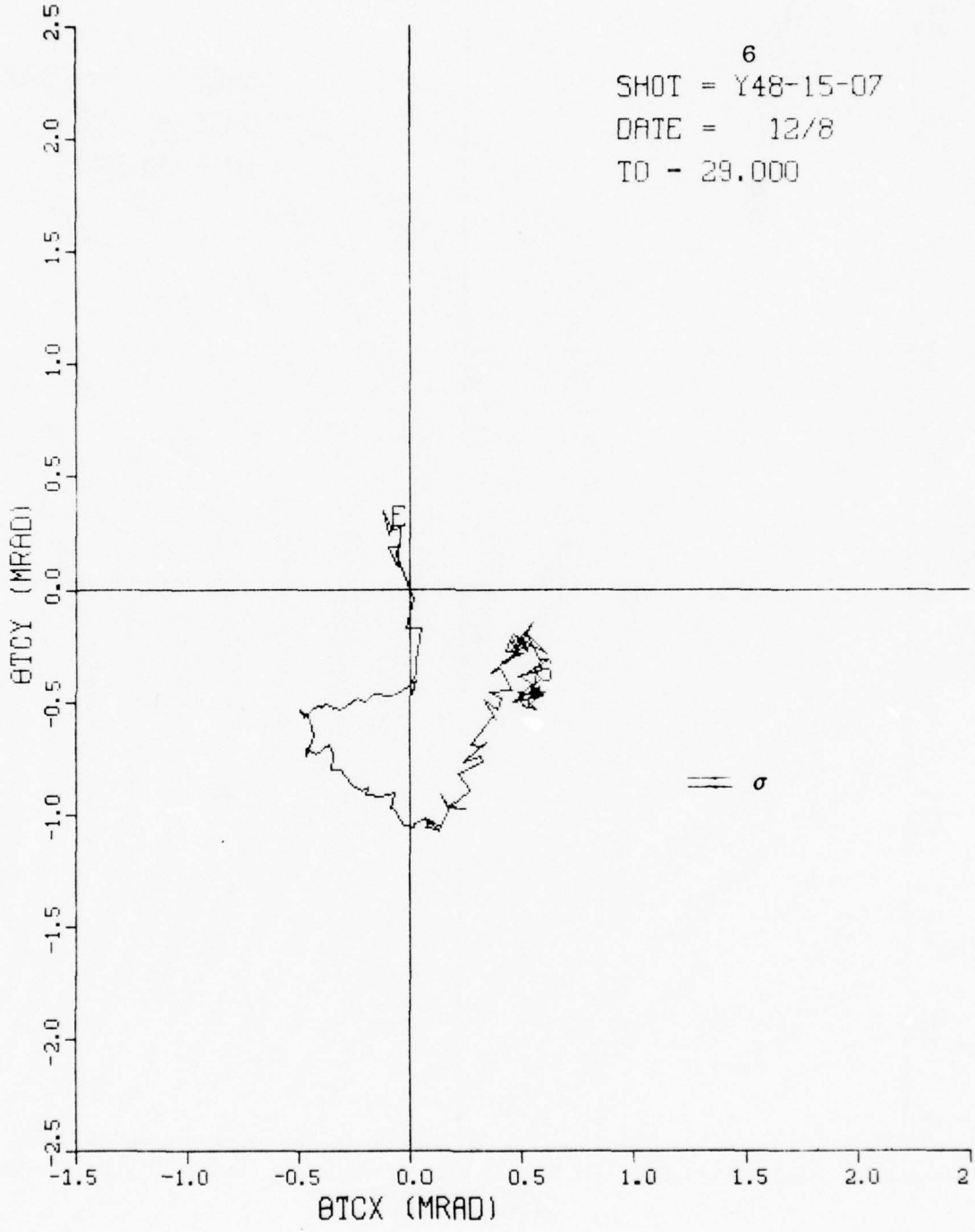

MUZZLE DISPLACEMENT

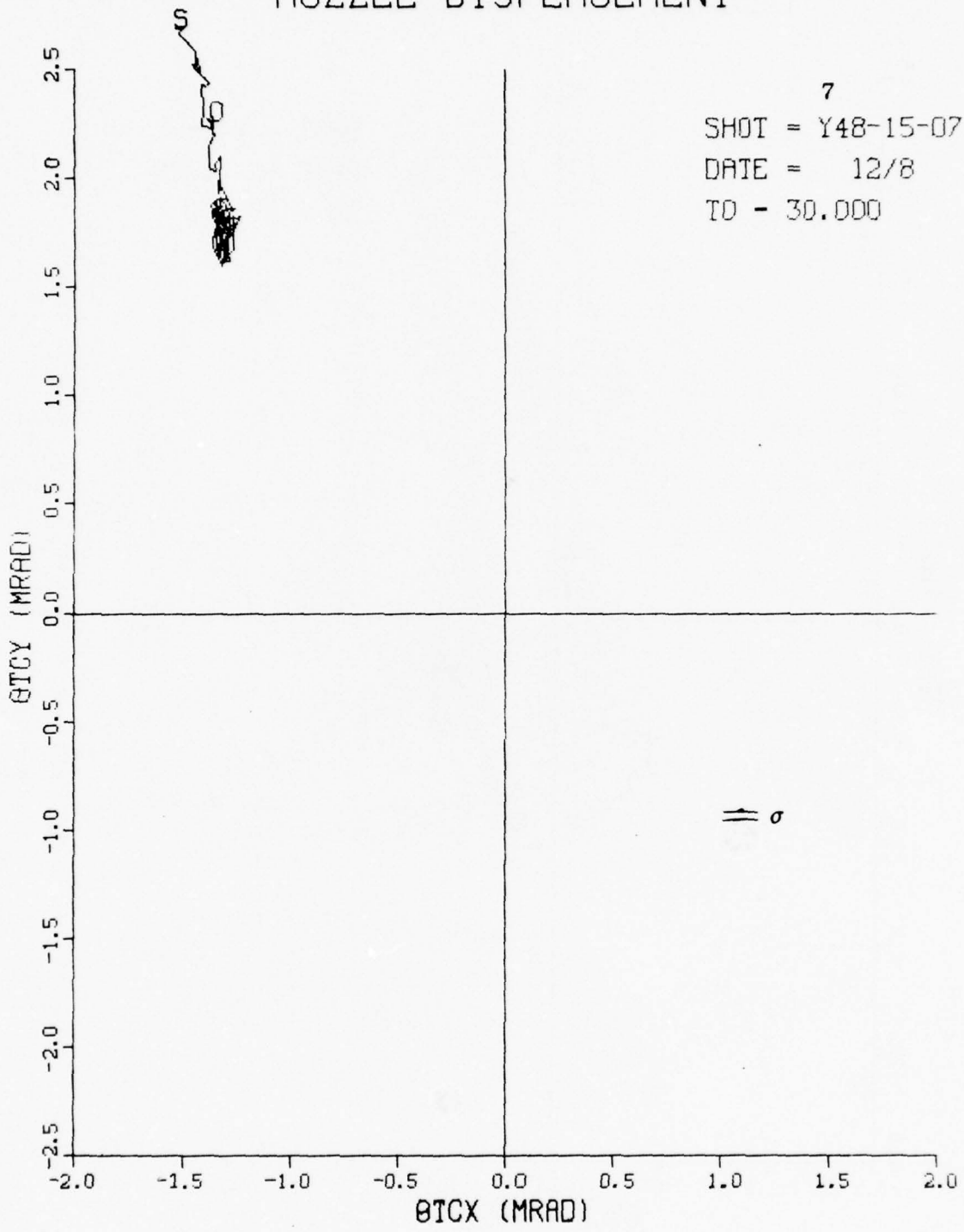

MUZZLE DISPLACEMENT

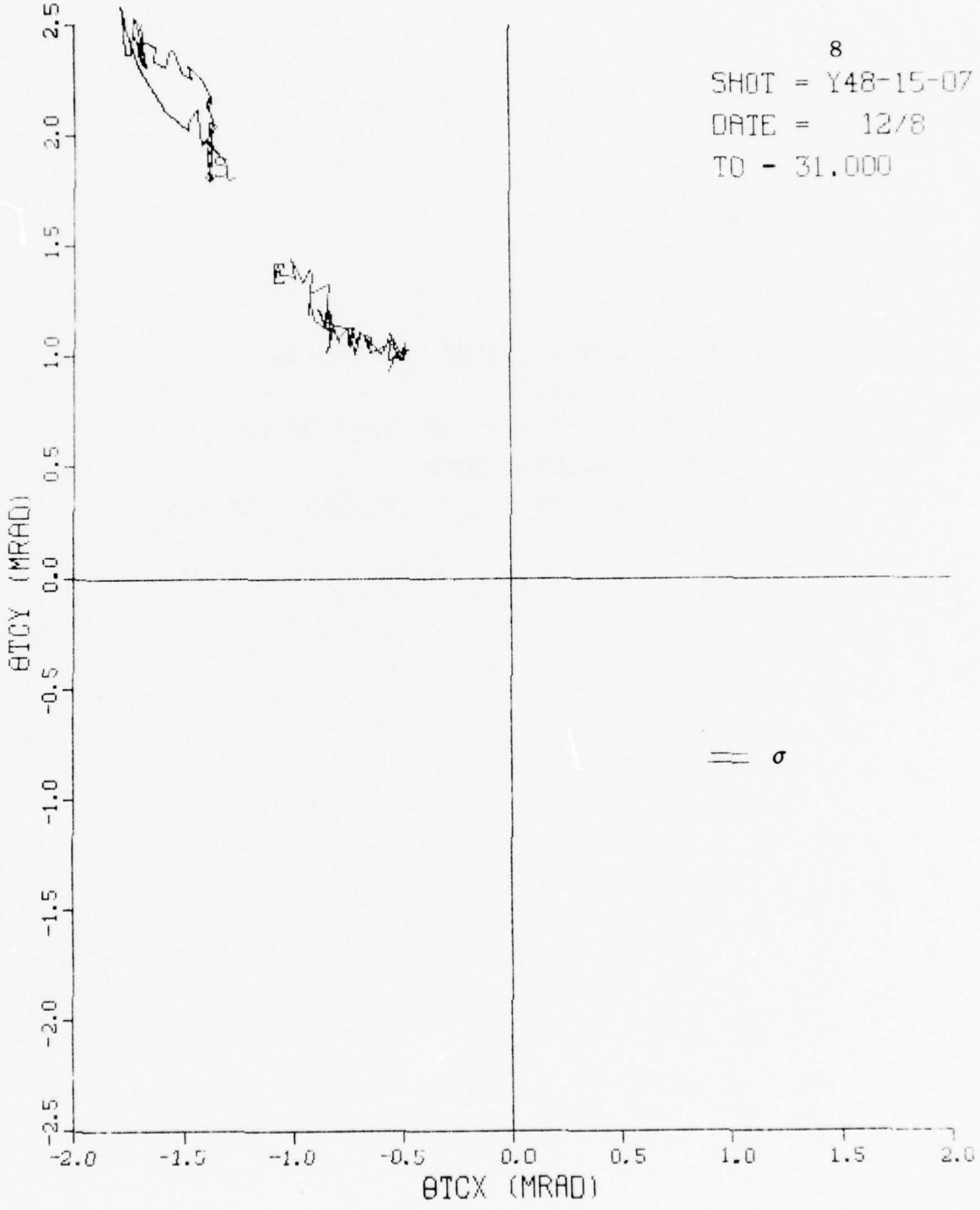

SHOT IDENTIFICATION: 047-10-38

DATE: 12/9/77

ROUND IDENTIFICATION: APDS 392A2

DATA DROP-OUTS: NONE

NOTE: THIS SHOT INVALID; SEE TEXT

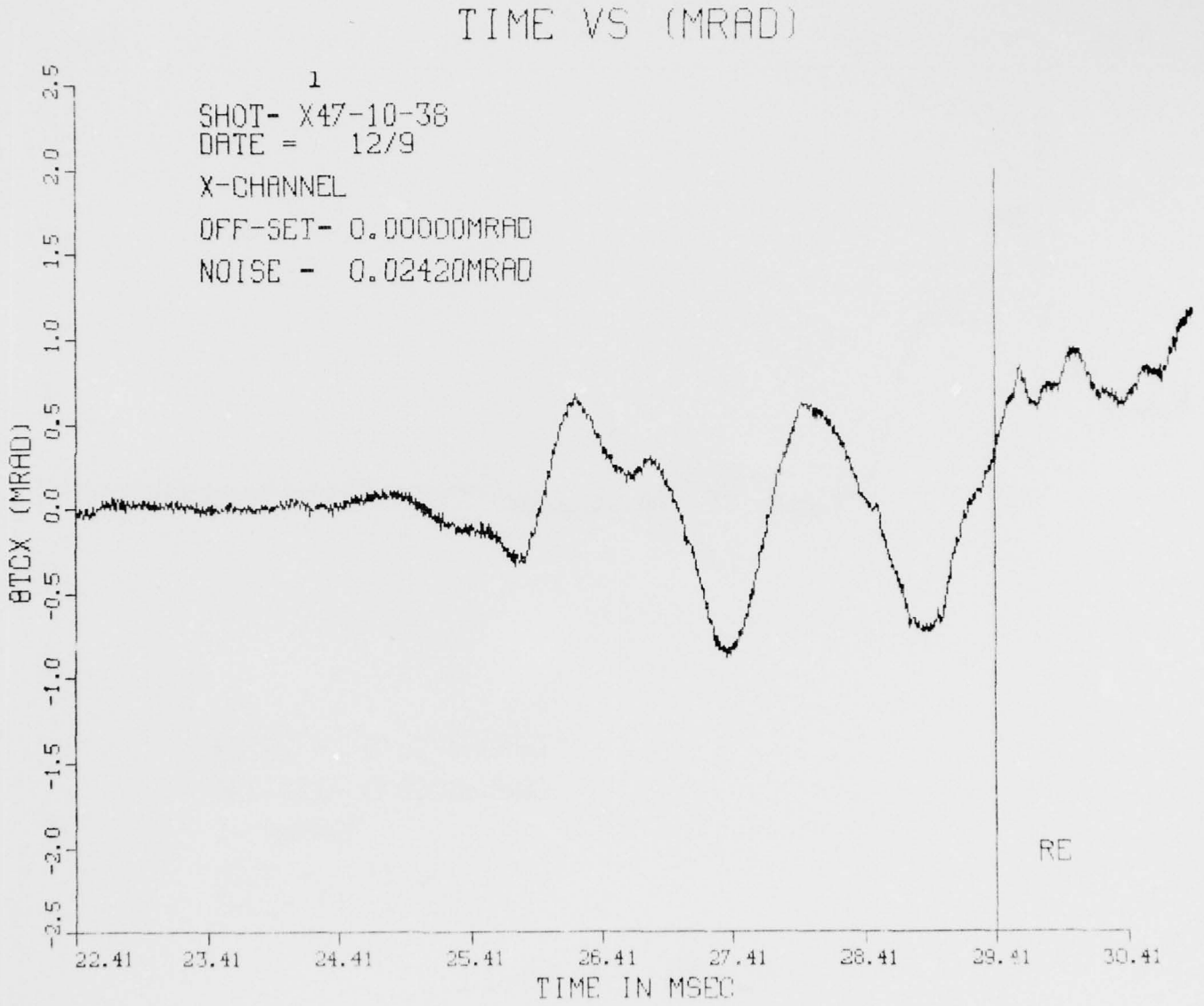
TIME VS (MRAD)
1
SHOT- X47-10-38
DATE = 12/9
X-CHANNEL
OFF-SET- 0.00000MRAD
NOISE - 0.02420MRAD
BTCX (MRAD)
2.5
2.0
1.5
1.0
0.5
0.0
-0.5
-1.0
-1.5
-2.0
-2.5
RE
22.41
23.41
24.41
25.41
26.41
27.41
28.41
29.41
30.41
TIME IN MSEC

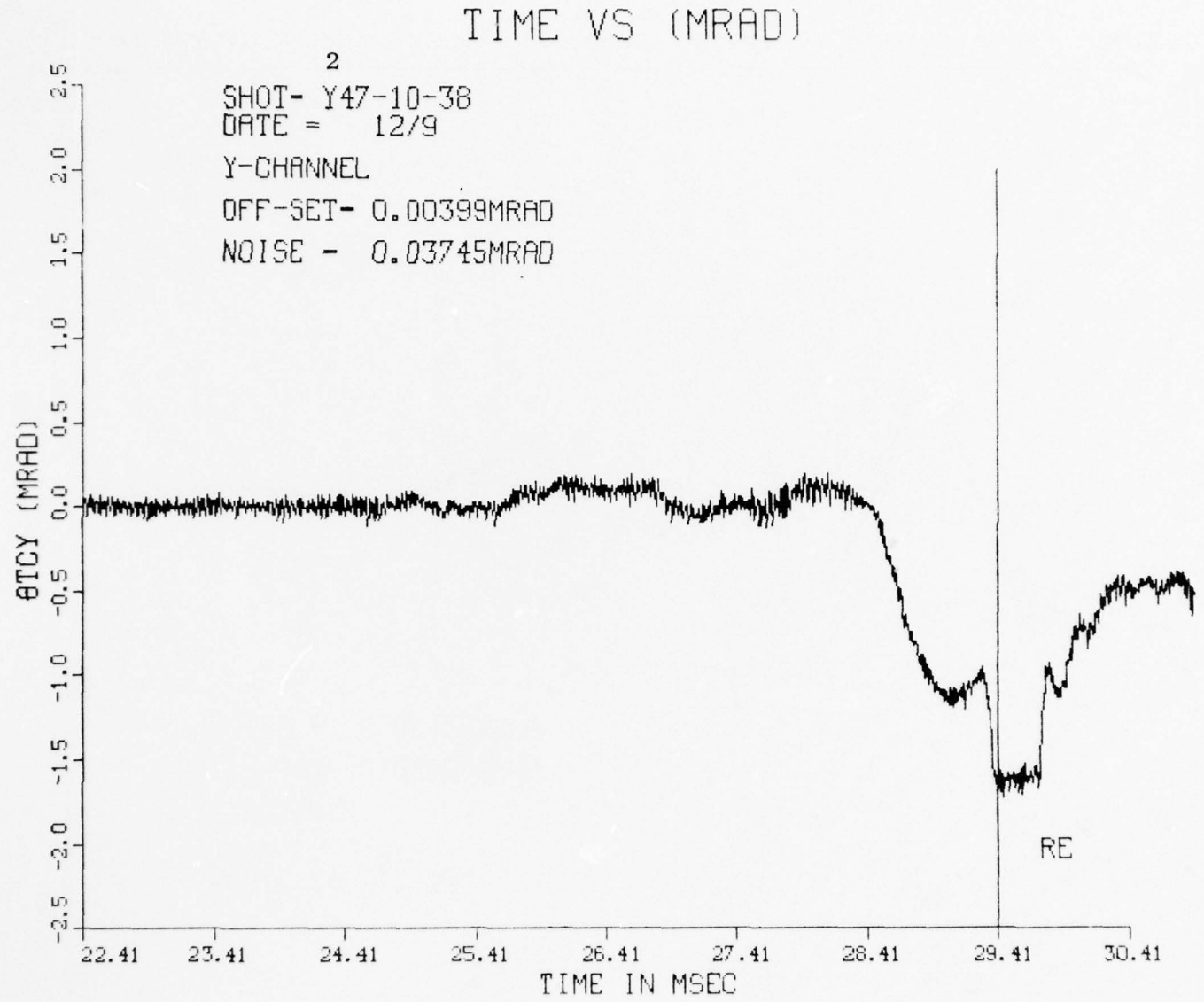
TIME VS (MRAD)
2
SHOT- Y47-10-38
DATE = 12/9
Y-CHANNEL
OFF-SET- 0.00399MRAD
NOISE - 0.03745MRAD
θTCY (MRAD)
2.5
2.0
1.5
1.0
0.5
0.0
-0.5
-1.0
-1.5
-2.0
-2.5
RE
22.41
23.41
24.41
25.41
26.41
27.41
28.41
29.41
30.41
TIME IN MSEC

MUZZLE DISPLACEMENT

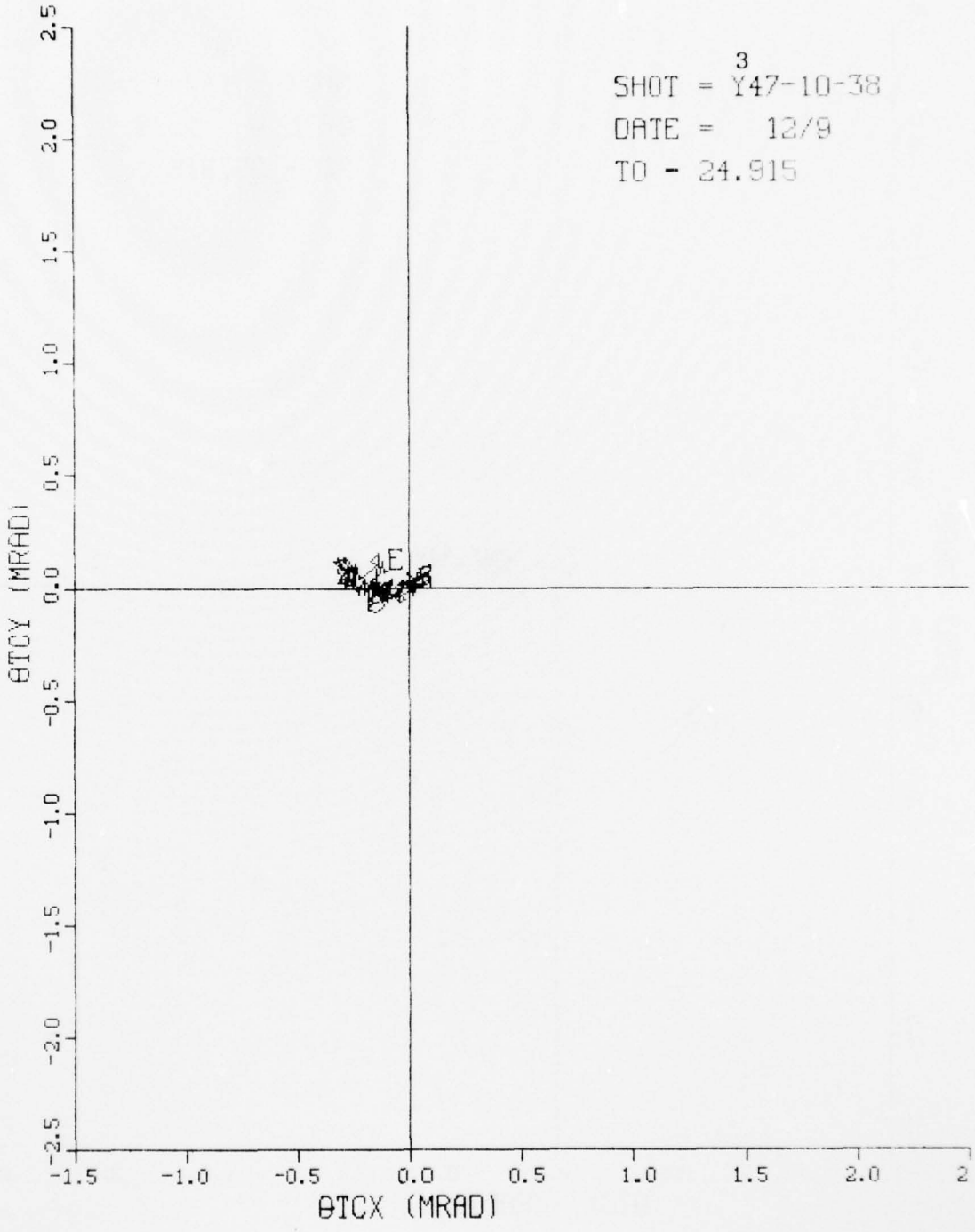

MUZZLE DISPLACEMENT

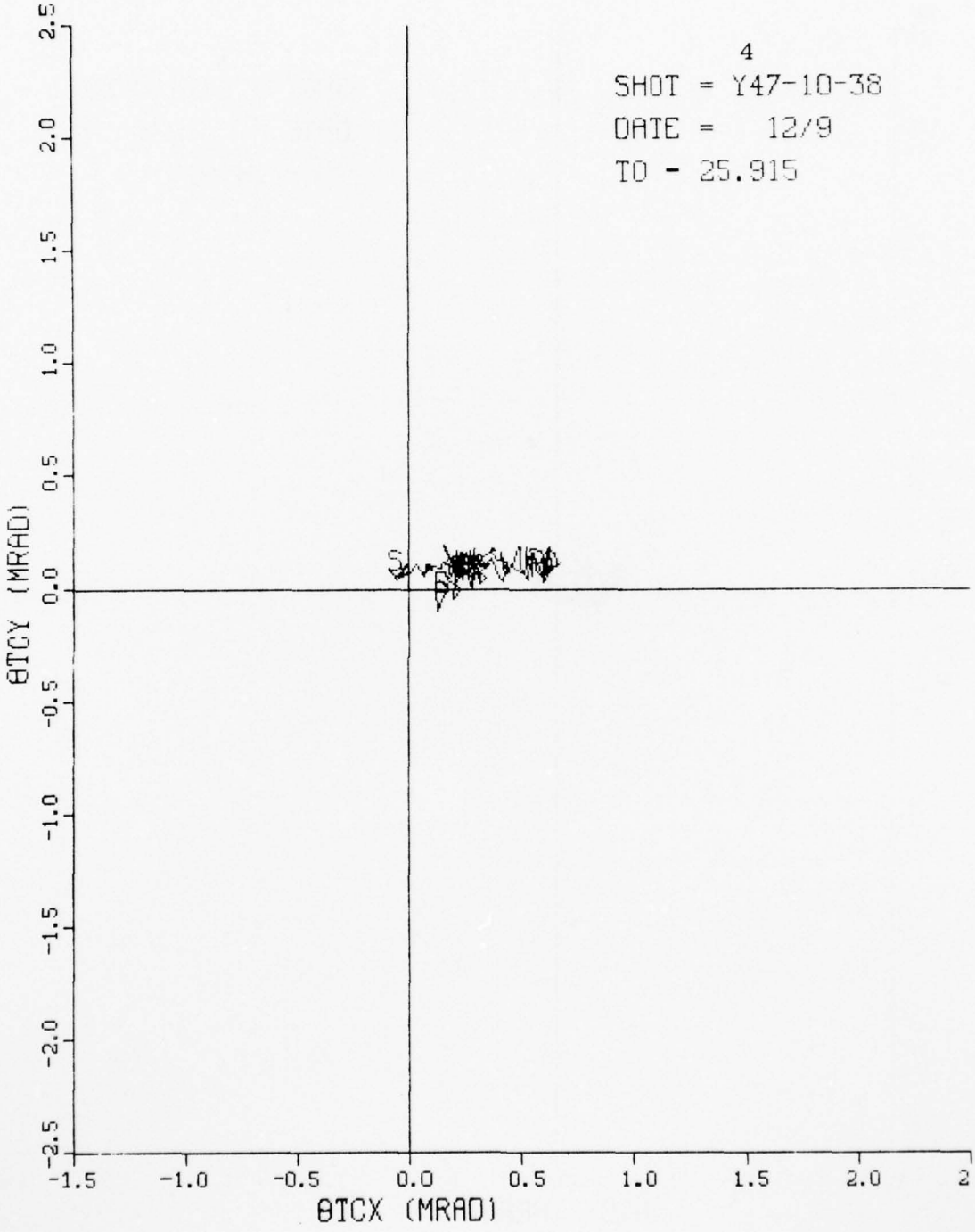

MUZZLE DISPLACEMENT

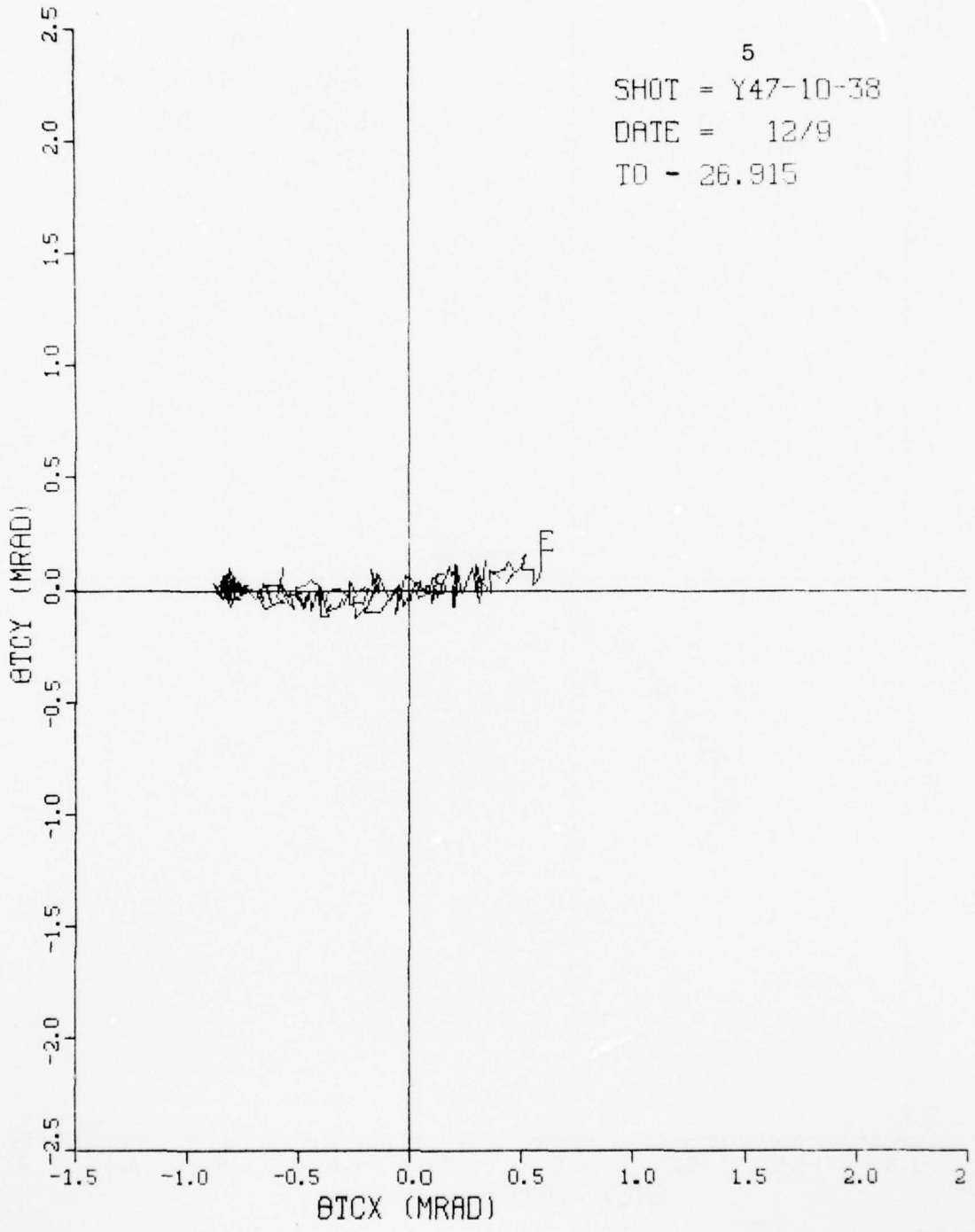

MUZZLE DISPLACEMENT

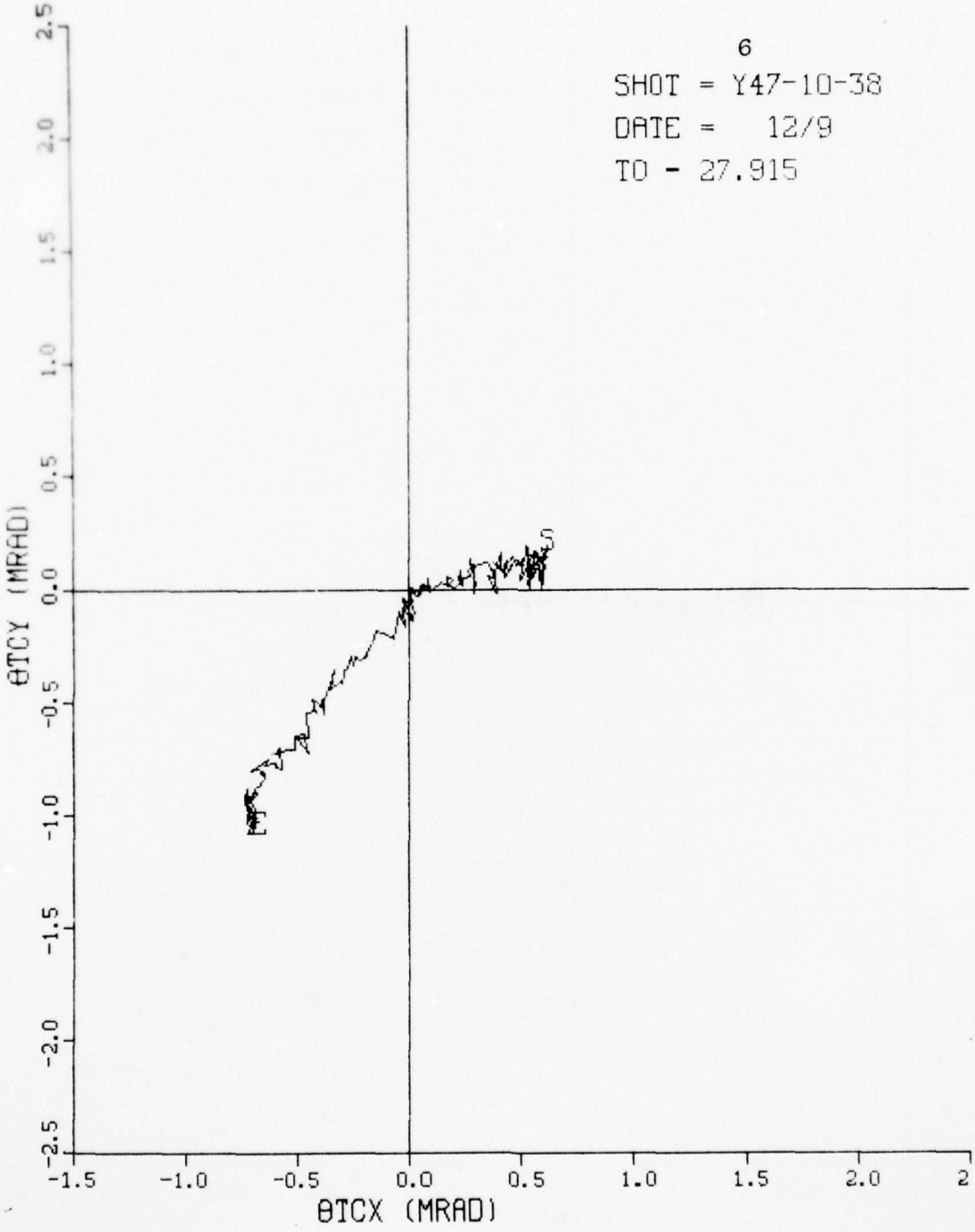

MUZZLE DISPLACEMENT

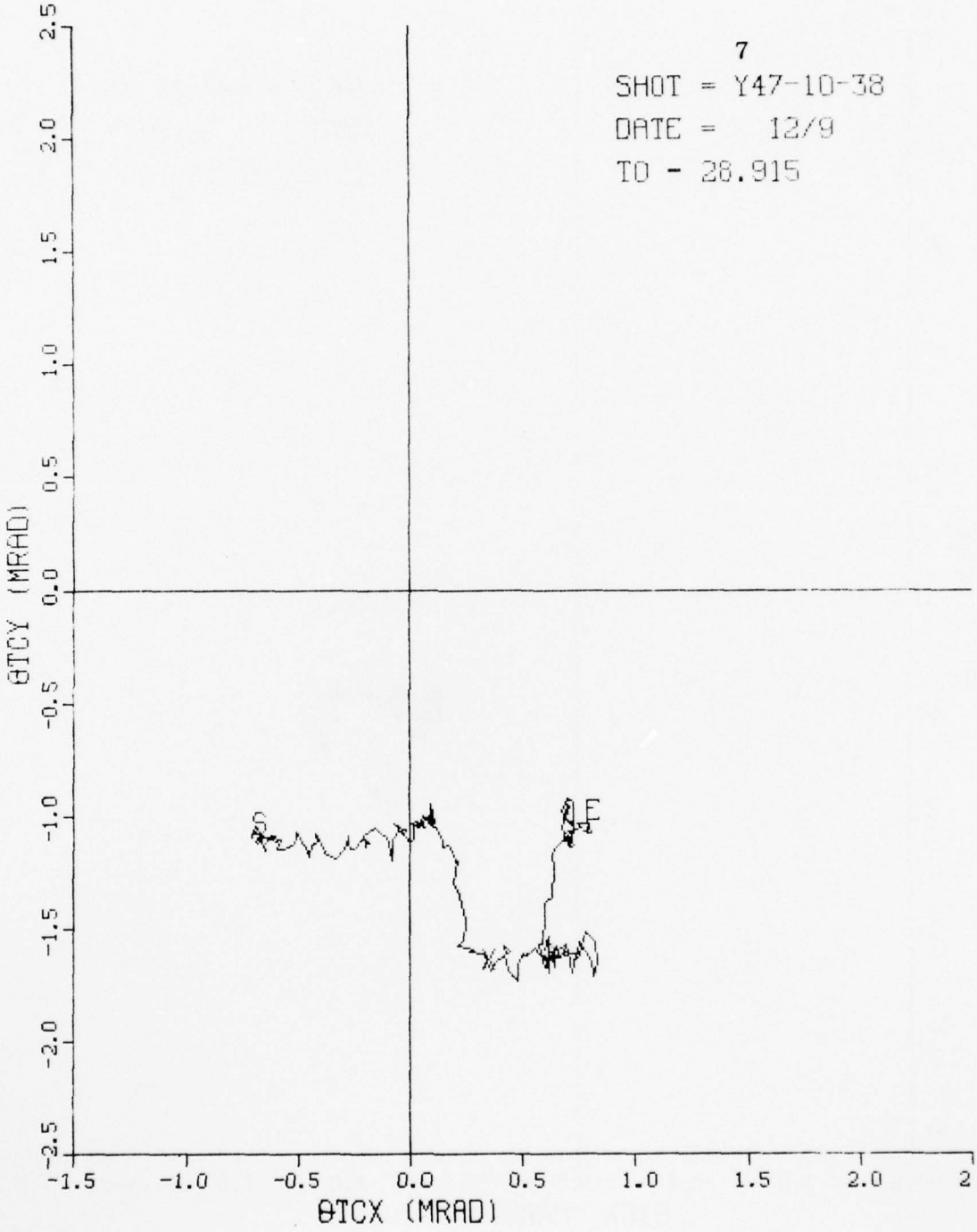

MUZZLE DISPLACEMENT

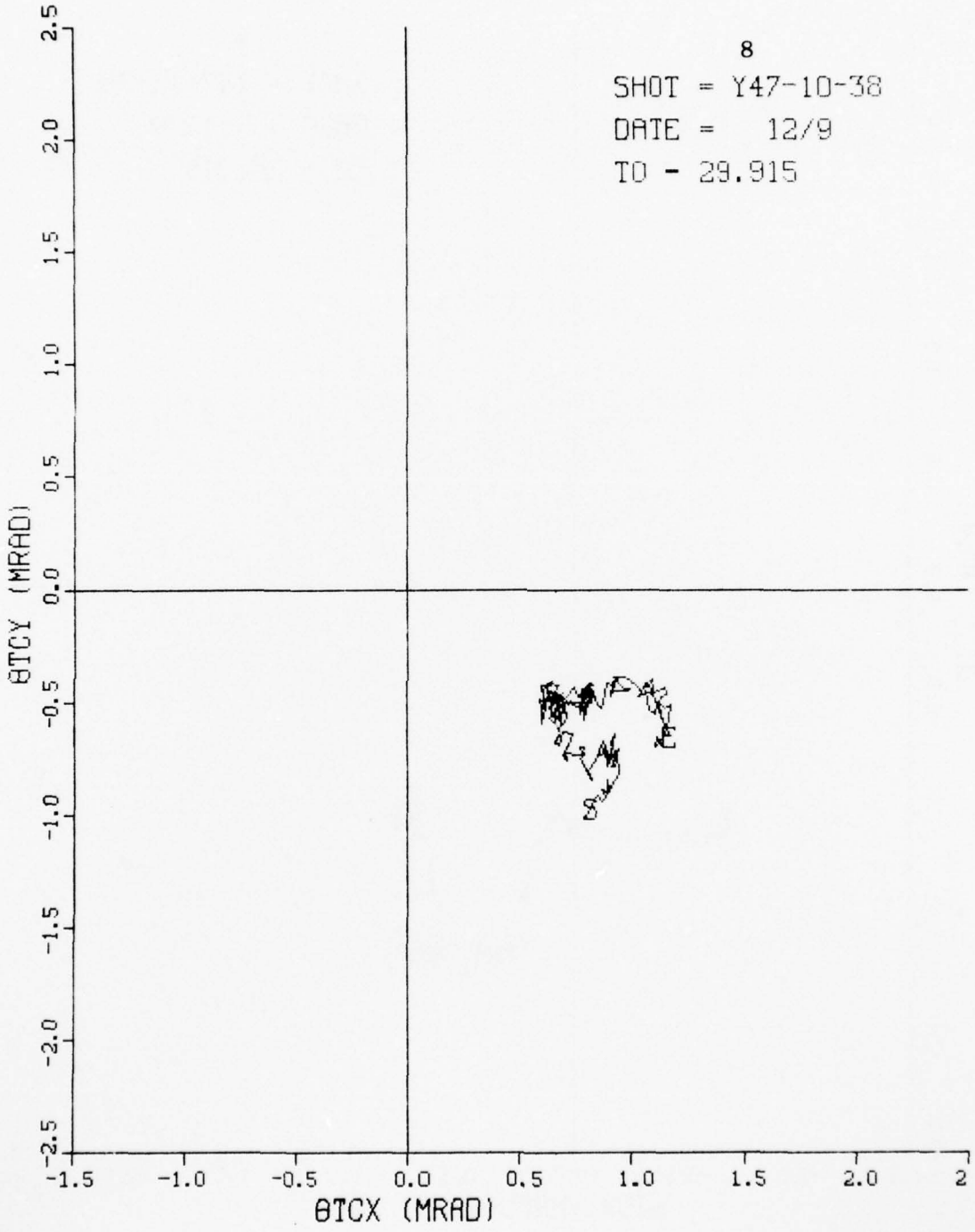

7.3 ANALYSIS OF THE DATA

7.3.1 Angular Deflection vs Time

As indicated by the graphical data, the motion of the muzzle during the transit of the round down the tube is complex. However, a prominent feature of the motion is its oscillatory character, as shown in Graphs 1 and 2 for each firing set. The period of oscillation in both the X- and Y-direction for all firings is the same and is in the range 0.8 ms to 1 ms, implying a dominant frequency on the order of 1 kHz to 1.3 kHz. This is well above the natural frequency of bending motion of the gun tube and raises the question as to the mechanism causing the high frequency motion of the muzzle mirror. Since the MDMS senses only angular motion of the mirror along the X- and Y-axes, the observed motion is interpreted as due primarily to tube bending. Thus, one asks if there is a mechanism which can account for the observed oscillations, which are a characteristic feature of muzzle motion.

It is hypothesized that one of the dominant forces acting on the tube is the reaction of the tube to the accelerating shell being forced to rotate by the rifling grooves. It is assumed that this is a major driving force on the tube. This hypothesis is examined below and is shown to predict a torquing force which produces a bending moment with the frequency observed in these tests. The results of the analysis strongly suggest that the postulated mechanism, which is certainly real, is a significant factor in causing tube bending during round transit.

As the shell is propelled down the tube, it is constrained to rotate in the direction prescribed by the spiral rifling grooves. This produces a torque on the tube which acts in the opposite direction of shell rotation and forces the tube to bend in the direction of the torque. Figure 37 (a) indicates the forces acting on the shell, with the force components resolved parallel and perpendicular to the direction of the rifling grooves. The reaction forces on the tube are indicated

in Figure 37 (b). The torquing force is F_T, acting at right angles to the tube axis and causes the tube to twist in a counter-clockwise direction, if the shell rotation is clockwise.

The forcing function for the X-component of tube motion can be expressed as

$$F_{TX} = F_T \cos(\omega_s t), \tag{28}$$

where ω_s is the angular rotation rate of the shell in radians per second and t is the time. Let v(t) be the velocity of the shell in the tube as a function of time, and let R be the number of revolutions per meter made by the shell due to the

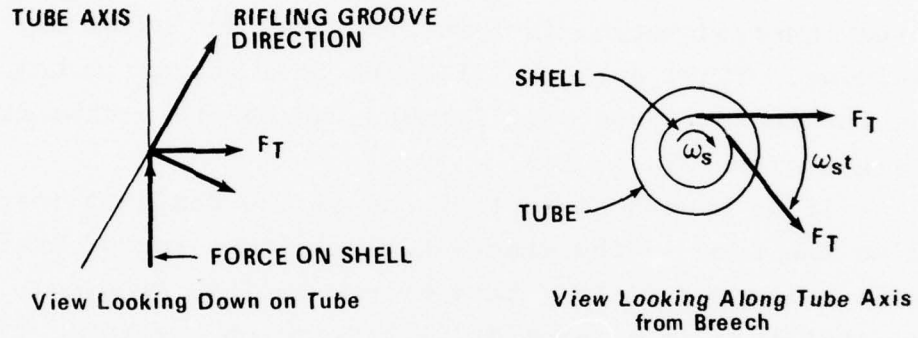

a) FORCES ON SHELL

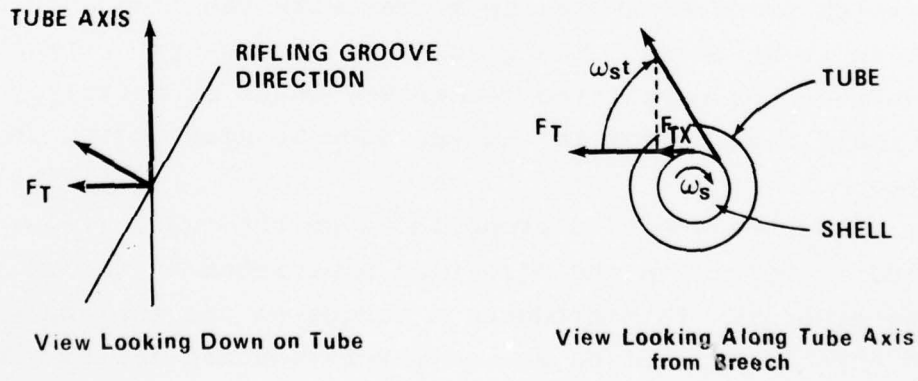

b) FORCES ON TUBE

Figure 37. Resolution of Forces on Shell and Tube. F_T is the Torquing Force and ω_s is the Angular Rotation Rate of Shell

rifling. Then

$$\omega_S(t) = 2\pi R\, v(t). \tag{29}$$

The X-component of the torquing force is, therefore,

$$F_{TX}(t) = F_T(t) \cos \left[2\pi R\, v(t)\, t \right] . \tag{30}$$

In Figure 38 the solid line is a plot of shell velocity in the tube of a 105 mm gun as a function of time. The measured data from which this curve was plotted was communicated to the author by Mr. William Frey of BRL. This is taken as a typical velocity-time profile of a shell in a 105 mm gun tube. The muzzle velocity in this case was about 1470 m/sec, consistent

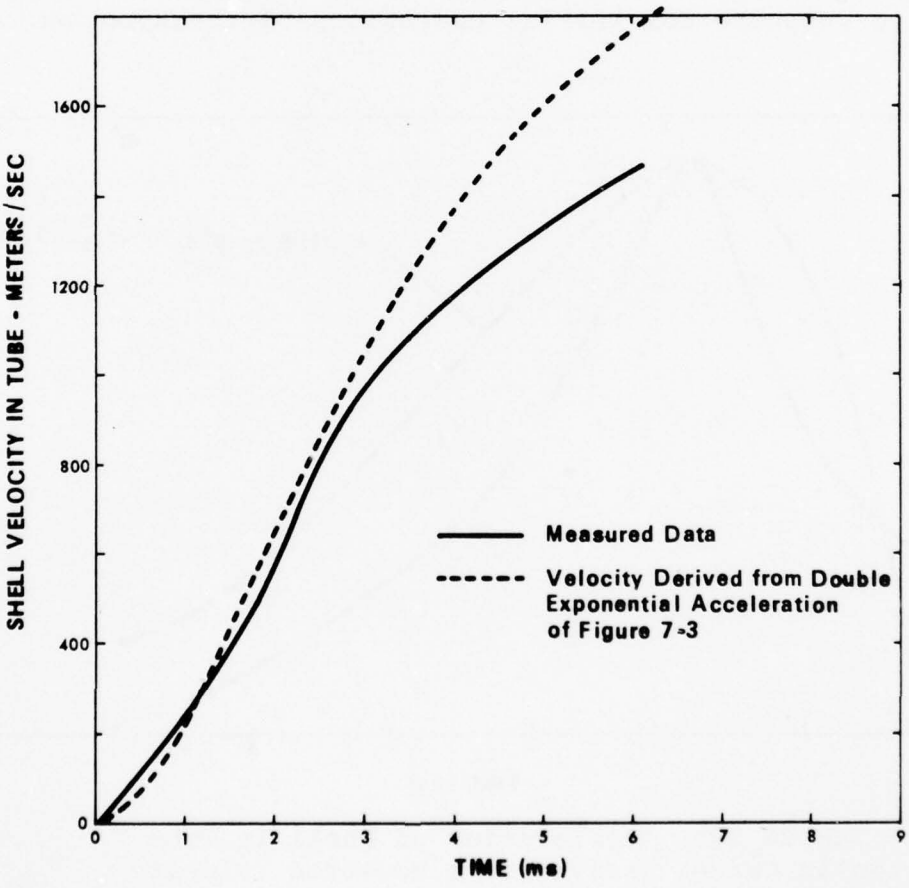

Figure 38. Velocity of Shell in Tube of 105 mm Tank Gun

with the values shown in Table 17 obtained during these tests. This curve was differentiated to give the acceleration of the shell as a function of time, $A_o(t)$, and the result is plotted as the solid line in Figure 39.

For an initial test of the hypothesis, the acceleration curve of Figure 39 was approximated by a double exponential function of the form

$$A_o(t) = A_o \left[\exp(-t/\tau_2) - \exp(-t/\tau_1) \right], \qquad (31)$$

where τ_1 and τ_2 are, respectively, the rise and fall time of the function. The dashed curve in Figure 39 is a plot of Eq. (31) with τ_1 = 1.76 ms, τ_2 = 1.8 ms and A_o = 5.2 x 10^4 m/sec^2. While this is not a good approximation to the actual acceleration, it is adequate for initial evaluation of the hypothesis

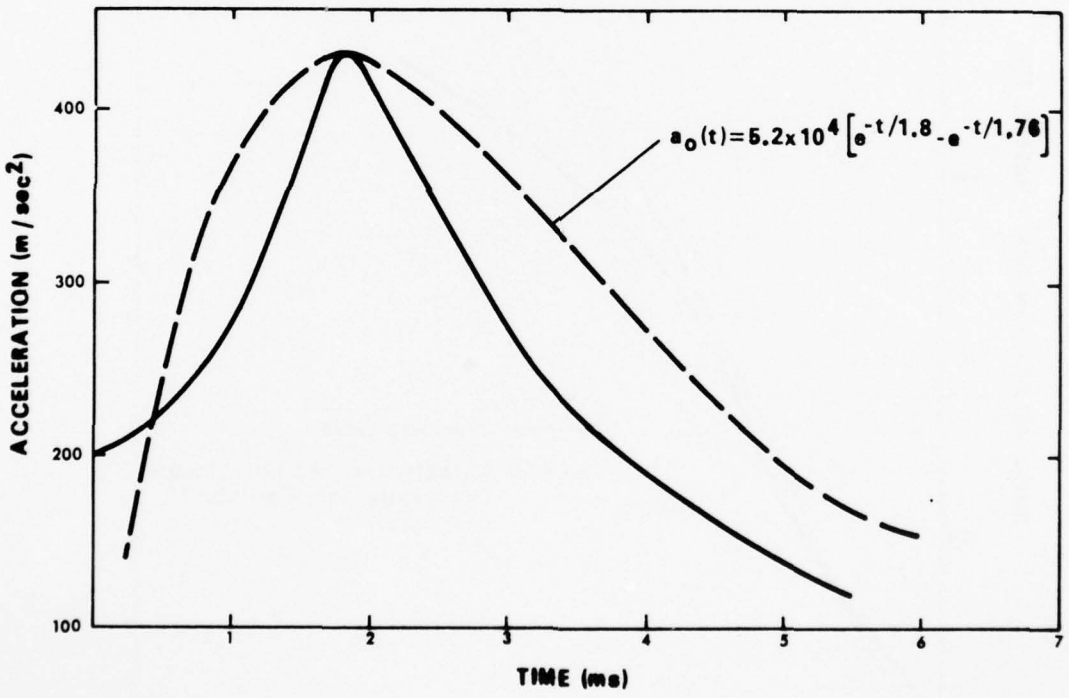

Figure 39. Acceleration of Shell in Tube
Solid Curve: Derived from Measured Velocity
Dashed Curve: Assumed Acceleration

and has the advantage that the double exponential can be easily treated analytically. A more accurate approximation will be made later.

On integrating Eq. (31), the velocity of the shell becomes:

$$v(t) = A_o \left[\tau_2 - \tau_1 + \tau_1 \exp(-t/\tau_1) - \tau_2 \exp(-t/\tau_2)\right]. \quad (32)$$

This equation is plotted in Figure 38 as the dashed line. Note that the approximation to the measured velocity is reasonably good to about 3 ms; thereafter the velocity predicted by this expression increasingly exceeds the measured velocity.

When Eqs. (31) and (32) are substituted into Eq. (30), the X-component of the torquing force can be expressed as

$$F_{TX}(t) = K \left[\exp(-t/\tau_2) - \exp(-t/\tau_1)\right] \bullet$$
$$\cos \left\{ 2\pi R A_o \times 10^{-3} \left[\tau_2 - \tau_1 + \tau_1 \exp(-t/\tau_1) \right.\right.$$
$$\left.\left. - \tau_2 \exp(-t/\tau_2)\right] t \right\}. \quad (33)$$

Here K is a constant and the unit of time is the millisecond. This is the forcing function which drives the muzzle along the X-axis. The time dependence of this function is of interest.

For a 105 mm tank gun, the rifling rotates the shell in a clockwise direction one revolution in 18 calibers. Thus, the shell travels a distance 0.105 m x 18 = 1.89 m in executing one revolution. This gives $R = (1.89)^{-1} = 0.53$ revolutions/m.

A normalized plot of the right-hand side of Eq. (33) is shown in Figure 40. The parameters used in making this plot are summarized below:

$$\tau_1 = 1.76 \text{ ms},$$
$$\tau_2 = 1.8 \text{ ms},$$
$$A_o = 5.2 \times 10^4 \text{ m/sec},$$
$$R = 0.53 \text{ rev/sec}.$$

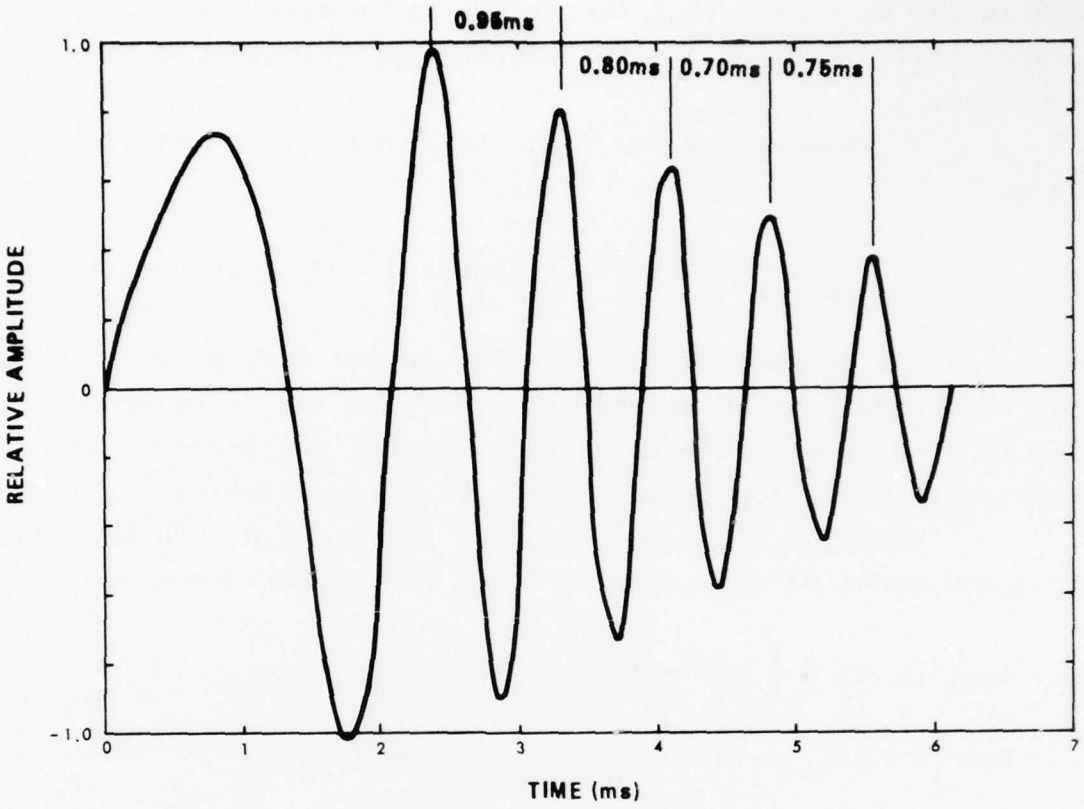

Figure 40. Forcing Function Based on Double Exponential Acceleration of Shell in the Tube as in Eq. (31) and Shown in Figure 41

The plot represents the normalized force on the gun tube which drives the muzzle in the X-direction. The driving force exhibits a damped oscillatory character with a period in the range 0.75 ms to 0.95 ms. This is to be compared muzzle motion shown in graphs 1 and 2 of each firing set, which also exhibit oscillatory motion with a period of the magnitude predicted by this analysis.

A similar calculation was made using an approximation to the acceleration function which more closely fits the measured acceleration shown in Figure 39. The following expressions were used to fit this curve on either side of the maximum:
For $0 \leq t \leq 1.7$ ms,

$$A_o(t) = 150 + 50 \exp(t/\tau_1) \text{ m/sec}^2, \qquad (34)$$

AD-A059 726 EG AND G INC ALBUQUERQUE N MEX F/G 19/6
MUZZLE DEFLECTION MEASUREMENT SYSTEM.(U)
JUL 78 R M BLAKNEY DAAK11-77-C-0051
UNCLASSIFIED EG/G-AG-1340 ARBRL-CR-00376 NL

3 OF 3
AD
A059726

END
DATE
FILMED
12-78
DDC

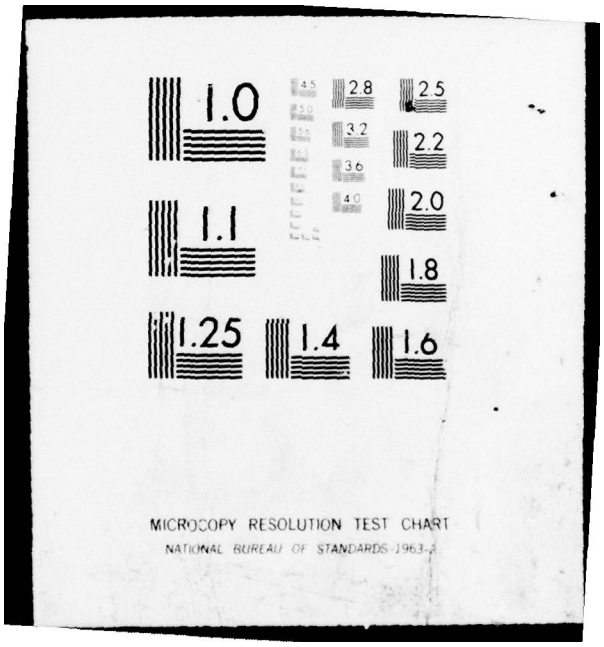
1.0
1.1
1.25
1.4
1.6
1.8
2.0
2.2
2.5
2.8
3.2
3.6
4.0
4.5
5.0
5.6
MICROCOPY RESOLUTION TEST CHART
NATIONAL BUREAU OF STANDARDS-1963-A

$$v(t) = 150t + 50\tau_1 \left[\exp(t/\tau_1) - 1 \right] \text{ m/sec.} \qquad (35)$$

For $t \geq 2$ ms,

$$A_o(t) = 860 \exp(-t/\tau_2) \text{ m/sec}^2, \qquad (36)$$

$$v(t) = 1898 - 2630 \exp(-t/\tau_2) \text{ m/sec.} \qquad (37)$$

These expressions closely approximate the measured acceleration and velocity of the shell in the tube, except in the time interval 1.7 ms < t < 2 ms around the peak acceleration. As before, the unit of time is the millisecond. The time constants in these expressions are:

$$\tau_1 = 0.983 \text{ ms}$$

$$\tau_2 = 2.754 \text{ ms}$$

Following the procedures previously employed, Eqs. (34) through (37) were substituted into Eq. (30), with R = 0.53 rev/m, and the resulting expressions were evaluated to give the normalized driving force. The result is shown in Figure 41. Note that for this case, the period of oscillation is in the range 0.9 ms to 1.1 ms, somewhat longer than in the previous example. This agrees well with the results measured with the MDMS. The slightly longer period is primarily the result of the lower acceleration for $t \geq 2$ ms used in this case, as compared to the double exponential approximation.

The time required from the start of shell motion to round exit is approximately 6 ms. During this period, four to five well defined oscillations are predicted by the above analysis. This agrees reasonably with the observed muzzle motion as shown in graphs 1 and 2 for each firing.

The purpose of this analysis has been to give an explanation of the characteristic oscillatory nature of the muzzle motion of the 105 mm tank gun during firing. The results support the hypothesis stated earlier, namely, that the forces

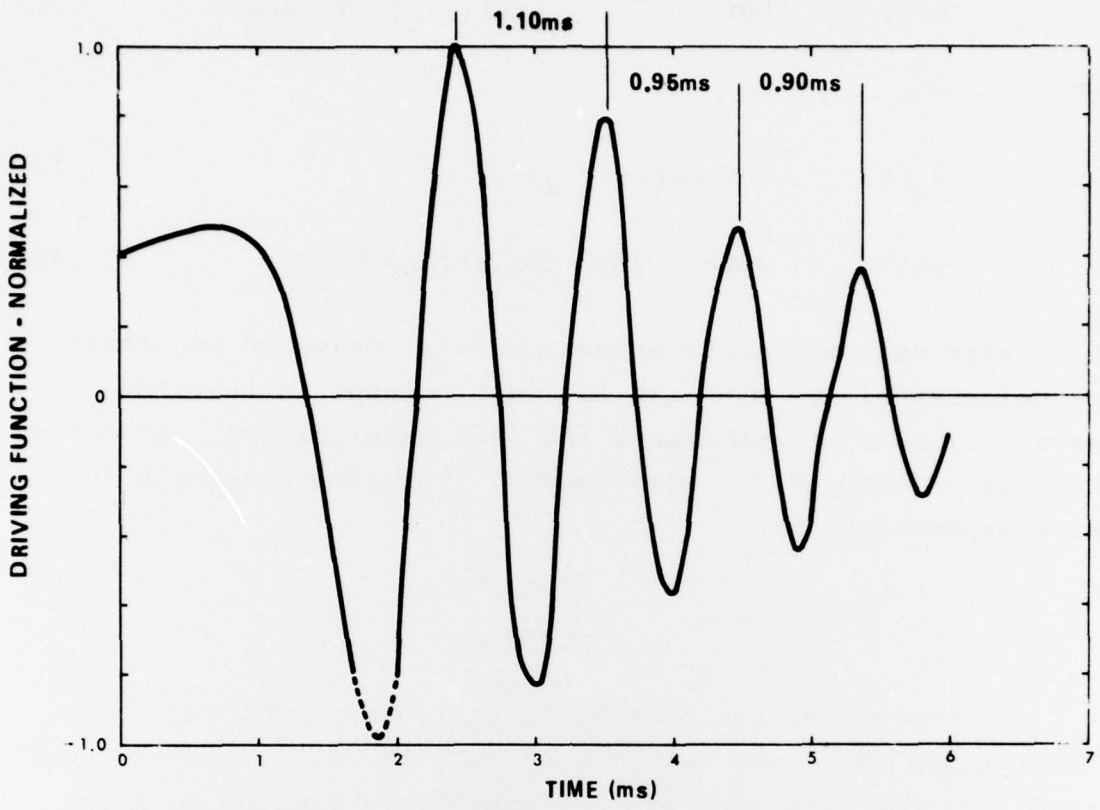

Figure 41. Normalized Driving Function for the Muzzle for a 105 mm Tank Gun Based on Measured Velocity Data (Figures 38 and 39)

on the tube are a reaction to the forced rotation of the accelerating shell, which gives rise to a torque on the tube. The time dependence of the torque has been shown to predict the observed period of oscillatory muzzle motion along the X- and Y-axes. It is assumed that the magnitude of the torque is sufficient to bend the tube with the observed amplitude. A more comprehensive analysis of the actual forces generated would be required to test this assumption, taking into account the actual elastic and dynamic properties of the tube. However, the results obtained in this study, both experimental and analytical strongly suggest that the mechanism proposed is an important factor in producing the observed muzzle motion.

7.3.2 Polar Representation of Muzzle Motion

The time variation of muzzle motion along the X- and Y-axes (Graphs 1 and 2) indicates that the path of the muzzle in the X-Y plane is quite complex. The patterns made by the muzzle in this plane are shown in Graphs 3 through 8 in the firing sets. The plots represent the path taken by the muzzle in one millisecond intervals, starting with Graph 3, which begins 4.5 ms prior to round emergence. Succeeding graphs show the pattern of muzzle deflection in contiguous one millisecond intervals.

Because the time resolution in these plots is much higher than for Graphs 1 and 2, small, rapid displacements of the muzzle can be resolved which complicate the patterns. Further complication is introduced by system noise. As a result, it is difficult to follow the gross motion of the muzzle in some instances. As an aid to visualizing this motion, Figure 42 was prepared from Graphs 3 through 8, which shows the smoothed pattern for each shot. The scale of the traces in this figure is only approximate. In preparing this figure, any ambiguities encountered in the polar plots were resolved by the use of Graphs 1 and 2. The figure provides a guide to more detailed examination of Graphs 3 through 8.

In the following discussion, some general observations on the character of these patterns will be made to point out some of the features of the patterns and how they compare among the several shots. The complexity of the patterns defy quantitative analysis, so that the following remarks are necessarily qualitative.

Examination of Figure 42 shows that for most of the shots, the direction of muzzle motion for the first three or four milliseconds is generally counter-clockwise, as one would expect from the clockwise spin of the shell. An exception to this is shot 046-13-55, where in the second and third frames (second and third milliseconds), the motion is clockwise. From the fourth to the sixth frames, the direction of motion of the muzzle in all shots is less regular.

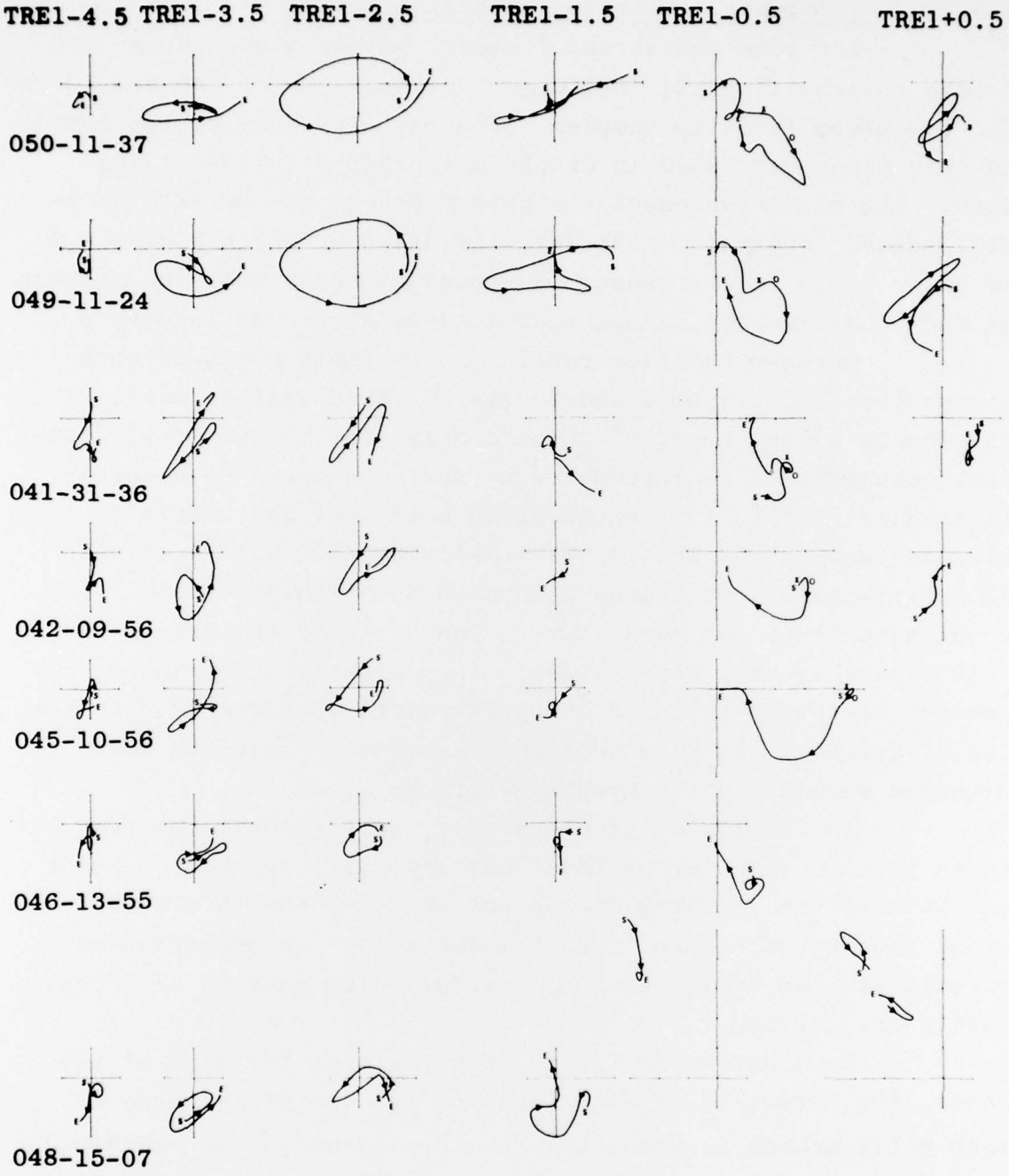

Figure 42. Smoothed Muzzle Mirror Motion-Summary (Scale Approximate)

With the exception of shots 050-11-37, 049-11-24 and 048-15-07, the data in the fourth and sixth frames are incomplete because of data drop-outs. The fifth frame (Graph 7 in the firing sets) is centered in time on the time of round emergence. The events of round emergence and round exit were captured by the data in five shots (050-11-37, 049-11-24, 041-13-36, 042-09-56 and 045-10-56) and are indicated in the plots by the letters X (round emergence) and O (round exit). As indicated in Section 7.2, the round exit interval for these shots may not all be valid; however, the time of round emergence is probably valid for all cases. It is interesting to note that the direction of muzzle motion during round emergence is clockwise. The exception to this is shot 041-13-36, where the general motion is in the opposite direction. In this case, however, the muzzle appears to execute a small, clockwise loop during round emergence. In shots 042-09-56 and 045-10-56, round emergence occurs just after the trace begins; prior to this was a period of data drop-out. The plots indicate that the muzzle was rapidly changing direction during round emergence. In general, the data seem to indicate that the muzzle is executing a rapid angular displacement while the round is leaving the muzzle.

A tabulation of the angular position of the muzzle at the time of round emergence is given in Table 18. For five of the shots, good data was obtained during this event; for the other two shots tabulated, the muzzle angle at round emergence is estimated. Round emergence occurred in a drop-out region for shot 046-13-55 approximately 0.15 ms prior to the beginning of recorded data in frame five. At the beginning of the recorded data, the muzzle was pointing down and to the right. By extrapolating the traces in Graphs 1 and 2 to the time of round emergence, the estimated angles of the muzzle at the time of round emergence were obtained. A similar estimate was made for shot 048-15-07, where round emergence occurred in a drop-out region about 0.1 ms prior to the beginning of recorded data. Note that with the exception of shot 048-15-07, the muzzle direction was

TABLE 18

Muzzle Angles at Round Emergence

Shot ID	θ_{TCX} (mrad)	θ_{TCY} (mrad)
050-11-37 12/9/77	+0.6	-0.5
049-11-24 12/9/77	+0.8	-0.6
041-13-36 12/6/77	+1.2	-0.8
042-09-56 12/7/77	+1.5	-0.5
045-10-57 12/8/77	+2.3	0
046-13-55 12/8/77	+0.7 (EST)	-0.9 (EST)
048-15-07 12/8/77	-1.6 (EST)	+2.0 (EST)

generally down and to the right at round emergence. For this shot, however, the muzzle was pointing high and to the left.

From this limited sample, the variance of the muzzle pointing angles at the time of round emergence are estimated to be σ_x = 1.2 mrad, σ_y = 1.3 mrad and $\sigma = (\sigma_2^2 + \sigma_y^2)^{\frac{1}{2}}$ = 1.8 mrad. This indicates a 1.8 m radius contribution to the dispersion pattern at one kilometer for this source.

A comment is in order concerning the observed noise in the two channels of the MDMS. Table 19 gives the RMS noise as computed from the first two milliseconds of the data. This period occurred from 7 ms to 5 ms prior to round exit, so that the noise values may contain some contribution due to the beginning of motion of the round in the breech. In the table, σ_x and σ_y are RMS noise in milliradians for the x and y channels, respectively, and $\sigma = (\sigma_x^2 + \sigma_y^2)^{\frac{1}{2}}$ represents the uncertainty in the polar plots.

As the table indicates, the noise in the y-channel is significantly higher than that in the x-channel. This is

TABLE 19

RMS Noise for Each Firing

Shot ID	X-Channel σ_x (mrad)	Y-Channel σ_y (mrad)	$\sigma = (\sigma_x^2 + \sigma_y^2)^{\frac{1}{2}}$ (mrad)
050-11-37	0.022	0.029	0.036
049-11-24	0.030	0.042	0.052
041-13-36	0.025	0.051	0.057
042-09-56	0.027	0.068	0.073
045-10-56	0.025	0.042	0.049
046-13-55	0.024	0.048	0.054
048-15-07	0.039	0.050	0.063
047-10-38	0.024	0.037	0.044

visually evident in Graphs 1 and 2 in the firing sets, which also show that the magnitude of the noise does not appear to change throughout the recorded data for any one shot. A further observation from Table 19 is that the noise in the y-channel is much more variable from shot to shot than that in the x-channel.

A different noise level in the two channels is not unexpected, since the two channels use different electronic componnents, although of the same type. The noise generated by two components of the same type can be different. What is surprising is the variability of the noise in the y-channel. The fact that the noise does not appear to change in magnitude during the course of a firing tends to rule out microphonics as a cause of the variability. Further, there seems to be no obvious correlation between the noise level and the type of round (see Table 13, Chapter 6). It is also difficult to imagine a mechanical noise source which partitions most of its energy in the y-direction. A source of noise which may make an important contribution is the data recording system used during the tests. It would be worthwhile in some future measurement program to interchange the x- and y-channels electrically to

see if the noise levels in the x- and y-directions are interchanged. This could be most easily done by interchanging the pin connections at the PSD.

The RMS uncertainty in the polar plots (Graphs 3 through 8) is indicated by the separation of the two straight lines, labeled σ, in the lower right quadrant of each plot. With this σ as a guide, one can make some distinction between noise-produced structure in the plots and structure that represents small amplitude, high frequency muzzle motion. Spikes and sharp corners are obviously noise produced. It appears that there is some high frequency structure in most of the curves of graphs 3 through 8. It should be noted, however, that most of this structure approaches in amplitude the resolution capability of the MDMS, which is about 0.1 mrad.

7.4 SUMMARY AND CONCLUSIONS

The angular motion of the muzzle mirror on a 105 mm tank gun has been measured with the EG&G Muzzle Deflection Measurement System. The basic measurement resolved the motion along two perpendicular axes in a plane normal to the gun tube axis, with the direction of the positive x-axis taken to the right in azimuth and the positive y-axis taken as up in elevation. The measurement technique is sensitive only to angular displacements of the muzzle mirror; the unit of angular displacement was the milliradian. Resolution of the measurement was 0.1 mrad.

Data were presented in two graphical formats: 1) Angular deflection along the x- and y-axes as a function of time; and 2) polar plots in which the x-deflection was plotted against the y-deflection. The latter plots were presented in six, consecutive one millisecond segments in order to make it easier to see the complex pattern of muzzle motion.

For all shots, the x- and y-deflections in time exhibited an oscillatory character in which the period was between 0.8 ms and 1.0 ms, corresponding to a frequency between 1 kHz and 1.3 kHz. It was postulated that the observed motion

of the muzzle mirror was the result of tube bending due to torquing forces on the tube generated in reaction to the accelerating shell which is forced to rotate by the rifling grooves. An analysis based on this hypothesis was performed, using measured data on the velocity of the shell in the tube as a function of time. The results of the analysis predicted accurately the observed periods of the oscillatory muzzle motion. The conclusion is that this mechanism does in fact cause the tube to bend and results in angular deflections of the muzzle as high as 1.5 mrad to 2 mrad prior to round exit.

The polar plots of muzzle deflection show a complex pattern which in the early stages indicate a general counterclockwise motion, consistent with the torque produced by a clockwise rotating shell. During the course of the measurements, the events of round emergence and round exit from the tube were recorded; these events are marked on the appropriate plots. With this information, one can determine the pointing angle of the tube at round exit. The data from seven firings showed a variance of 1.8 mrad in the muzzle angle at the time of round exit, indicating a contribution to dispersion at one kilometer of ±1.8 m from this source.

The polar plots also indicated the existence of small amplitude, high frequency motion of the muzzle mirror. The amplitude of the disturbances approaches the limiting resolution of the MDMS but is sufficiently larger than the noise to suggest that these motions are real.

7.5 ACKNOWLEDGEMENTS

The author wishes to recognize with appreciation the contributions made by several people in the successful completion of this work. At EG&G, Mr. James P. Furaus did an outstanding job in the design of the mechanical components of the MDMS. In particular, the mechanical interfacing of the MDMS and the test gun was perfect, even though Mr. Furaus has never seen the gun. Mr. John R. Stiles (formerly with EG&G) of the Miletus

Corporation performed the design of the electronic systems and worked diligently with the author in the calibration of the MDMS. Thanks are also due to Mr. John Wheatley for his helpful consultations and for valuable support, along with Mr. Henry Alvidres, during the field measurement program.

The author is also grateful to the COR, Mr. Harry Rogers, of BRL for the smooth administration of contractual matters. Particular appreciation is due Mr. William Frey of BRL for his technical support during this work and for his invaluable aid during the field test.

Additionally, the author and the COR are grateful to Dr. Rurick Loder, Mr. James Pilcher, Capt. David Ross and others of the BRL for graciously incorporating the MDMS test into the complex and high priority M392A2 Test program. The invaluable support of these people during the test is acknowledged with thanks. Appreciation is particularly extended to Ms. Caledonia Henry for her efforts in digitizing the data and providing data cards in the format required.

DISTRIBUTION LIST

No. of Copies	Organization
12	Commander Defense Documentation Center ATTN: DDC-TCA Cameron Station Alexandria, VA 22314
1	Commander US Army Materiel Development and Readiness Command ATTN: DRCDMD-ST 5001 Eisenhower Avenue Alexandria, VA 22333
1	Commander US Army Materiel Development and Readiness Command ATTN: DRCDE-L 5001 Eisenhower Avenue Alexandria, VA 22333
1	Commander US Army Materiel Development and Readiness Command ATTN: DRCDE-DW 5001 Eisenhower Avenue Alexandria, VA 22333
1	Commander US Army Materiel Development and Readiness Command ATTN: DRCPP-SP 5001 Eisenhower Avenue Alexandria, VA 22333
1	Commander US Army Aviation Research and Development Command ATTN: DRSAV-E 12th and Spruce Streets St. Louis, MO 63166
1	Director US Army Air Mobility Research and Development Laboratory Ames Research Center Moffett Field, CA 94035
1	Commander US Army Electronics Research and Development Command Technical Support Activity ATTN: DELSD-L Fort Monmouth, NJ 07703
1	Commander US Army Communications Rsch and Development Command ATTN: DRDCO-SGS Fort Monmouth, NJ 07703
1	Commander US Army Missile Research and Development Command ATTN: DRDMI-R Redstone Arsenal, AL 35809
1	Commander US Army Missile Materiel Readiness Command ATTN: DRSMI-AOM Redstone Arsenal, AL 35809
1	Commander US Army Tank Automotive Research & Development Cmd ATTN: DRDTA-UL Warren, MI 48090
1	Commander US Army Armament Materiel Readiness Command ATTN: DRSAR-LEP-L, Tech Lib Rock Island, IL 61299
4	Commander US Army Armament Research and Development Command ATTN: DRDAR-TSS (2 cys) DRDAR-LC, Dr. J. Frasier DRDAR-LCU-D, Mr. A.Novak Dover, NJ 07801

DISTRIBUTION LIST

No. of Copies	Organization
5	Commander US Army Armament Research and Development Command ATTN: DRDAR-SC, Mr. D. Gyrog DRDAR-SCF, Mr. R. Volz Mr. K. Pfleger Mr. J. Heberley DRDAR-SE Dover, NJ 07801
2	Commander US Army Watervliet Arsenal USAARRADCOM ATTN: DRDAR-LCB, Mr. Simkins Mr. G. Friar Watervliet, NY 12189
3	Project Manager, M60TD ATTN: DRCPM-M60TD-T Mr. E. Weslea Mr. G. Karavias DRCPM-M60TD, MAJ D. Derrah Warren, MI 48090
2	Project Manager XM1 Tank System ATTN: DRCPM-GCM-S Warren, MI 48090
1	Director US Army TRADOC Systems Analysis Activity ATTN: ATAA-SL, Tech Lib White Sands Missile Range NM 88002
1	President US Army Armor/Engineer Board ATTN: ATZK-AE-AR, CPT R.Lewis Fort Knox, KY 40121
1	Commander US Army Armor Center ATTN: ATZK-CD-MS, CPT L. Main Fort Knox, KY 40121
1	Commandant US Army Armor School ATTN: Combat Developments Fort Knox, KY 40121
5	HQDA (DAMA, Advanced Concepts Team, Mr. C. Church) Washington, DC 20310
1	EG&G, Washington Analytical Services Center, Inc. Albuquerque Group 9733 Coors Road, P.O. Box 10218 Albuquerque, NM 87114
1	Falcon Research & Development ATTN: Dr. R. Blakney 2350 Alamo S.E. Albuquerque, NM 87106

Aberdeen Proving Ground

Dir, USAMSAA
ATTN: Dr. J. Sperrazza
DRXSY-B, Mr. G. Zeller
Mr. R. Conroy
Mr. W. Clifford
DRXSY-T, Mr. P. Reid
DRXSY-D, Mr. J. Kramar

Cdr, USATECOM
ATTN: DRSTE-SG-H
DRSTE-CM-R, LTC K.Nelson

Cdr, USAMTD
ATTN: STEAP-MT, Mr. J.Sova,Jr.
Mr. R. Lenert
Mr. T. Wagner
CPT D. Brown
Mr. B. Sissom

Dir, USAHEL
ATTN: W. McJilton

Cmdt, USAOC&S
ATTN: ATSL-CD

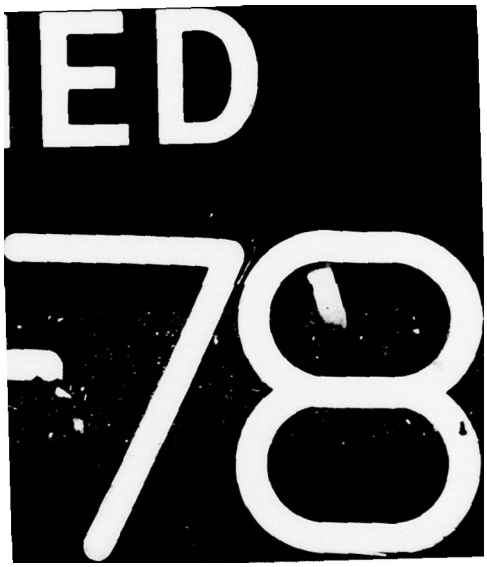
ED
78